UNIVERSITY OF BELGRADE

FACULTY OF TECHNOLOGY AND METALLURGY

Akram Ariebi Halap

STRUCTURE AND WELDABILITY OF A HIGH STRENGTH MARINE GRADE Al-Mg ALLOYS

PhD Thesis



Belgrade 2014

UNIVERSITY OF BELGRADE

FACULTY OF TECHNOLOGY AND METALLURGY

Akram Ariebi Halap

STRUCTURE AND WELDABILITY OF A HIGH STRENGTH MARINE GRADE Al-Mg ALLOYS

PhD Thesis



Belgrade 2014

УНИВЕРЗИТЕТ У БЕОГРАДУ

ТЕХНОЛОШКО-МЕТАЛУРШКИ ФАКУЛТЕТ

Akram Ariebi Halap

СТРУКТУРА И ЗАВАРЉИВОСТ Al-Mg ЛЕГУРА ВИСОКЕ ЧВРСТОЋЕ ЗА БРОДОГРАДЊУ

Докторска дисертација



Београд 2014

Supervisor:

_____

Dr. Endre Romhanji, Full Professor

University of Belgrade, Faculty of Technology and Metallurgy

Co-supervisor:

_____

Dr. Miljana Popović, Associate Professor

University of Belgrade, Faculty of Technology and Metallurgy

Committee members:

_____

Dr. Vencislav Grabulov, Scientific Advisor

Institute of Materials Testing, Belgrade

_____

Dr. Tamara Radetić, Scientific Advisor

University of Belgrade, Faculty of Technology and Metallurgy

Candidate:

_____

Akram Ariebi Halap

Date of the defense:

_____

Mentor:

_____

Dr. Endre Romhanji, redovni profesor

Univerzitet u Beogradu, Tehnološko metalurški fakultet

Ko-mentor:

_____

Dr. Miljana Popović, vanredni profesor

Univerzitet u Beogradu, Tehnološko metalurški fakultet

Članovi komisije:

_____

Dr. Vencislav Grabulov, naučni savetnik

Institut za ispitivanje materijala, Beograd

_____

Dr. Tamara Radetić, naučni savetnik

Univerzitet u Beogradu, Tehnološko metalurški fakultet

Kandidat:

_____

Akram Ariebi Halap

Datum odbrane: _____

STRUCTURE AND WELDABILITY OF A HIGH STRENGTH MARINE GRADE Al-Mg ALLOYS

Non-heat treatable Al-Mg alloys (5xxx series) draw the most of their strength from a work hardening and solid solution strengthening. However, with an increase in the Mg content over 3.5%, the Al-Mg alloys became prone to toward different forms of corrosion in certain environments. Deterioration of the corrosion properties is caused by sensitization - precipitation of Mg from supersaturated solid solution in the form of anodic β (Al_3Mg_2) phase at the grain boundaries during the exposure to elevated temperatures in a 60-200 °C range. Due to the high mobility of Mg atoms in Al matrix, the precipitation processes might occur at room temperature albeit with extremely low rate.

Degradation of the corrosion properties of AA 5083 alloy, containing 4-5 wt% Mg, in certain environments limits its application as a material of choice for structural components of marine vehicles. The extent of susceptibility toward different forms of corrosion depends on environment, materials chemistry, fabrication and thermo-mechanical processing. Attempts to mitigate susceptibility toward different forms of corrosion while increasing Mg content to improve the alloy strength lead to modification of AA5083 by Zn additions and design of new alloy types such as AA 5059. In this study, the effect of thermo-mechanical treatment on corrosion properties of Zn modified Al-5.1wt%Mg-0.7wt%Mn alloy plates was investigated.

In order to develop optimal thermo-mechanical regime for the studied alloy, that would provide desired combination of mechanical and corrosion properties (described by ASTM standard as H321 state), the effect of multiple processing parameters was evaluated. The specimens underwent varied amount of cold work (16-55 % reductions), while final annealing was conducted in 220-280 °C temperature range for 1 - 3 hrs. Characterization of mechanical (hardness measurements and tensile test) and corrosion properties (IGC, exfoliation and pitting susceptibilities) and their correlation to microstructure (light microscopy, SEM and TEM) was conducted for different stages of the processing as well as for various processing conditions.

It has been established that there is a joint effect of final annealing temperature and prior cold deformation on the intergranular corrosion (IGC) susceptibility

determined by NAML test (ASTM standard G67). In a tested range of final annealing temperatures of 220-280 °C, the temperature increase improved the IGC resistance, as well as the previous cold work. Material annealed at 220 °C was sensitive to IGC independently on the previous cold deformation (although the IGC susceptibility decreased with deformation). After annealing at 240 °C and pre-deformation over 30 %, the IGC condition changed from sensitive to resistant. The deformation effect vanished after annealing temperature of 260 °C and higher. Variation in the annealing time had lesser effect, but, generally, increase from 1h to 3h resulted in improved IGC resistance.

The test performed for evaluation of exfoliation and pitting forms of corrosion (ASTM G66 standard) have shown detrimental exfoliation corrosion level for the material that underwent high cold rolling deformations (~50 %) and annealing at 220 °C. However, with increase in annealing temperature the exfoliation was not developed as a general IGC was also suppressed. Pitting corrosion was not detected at a harmful level at all, but moderate pitting attack was observed after annealing at higher temperatures, i.e. states that had high IGC resistance.

Correlation of the results of corrosion testing with mechanical properties (yield strength, elongation) showed that the optimum thermo-mechanical regime, that yielded to material properties required for the H321 state, corresponded to 42 % cold reduction and annealing for 2 h at 240 °C. Further treatment, i.e. sensitization for 7 days at 100 °C, of the alloy resulted in the IGC resistant state. Although, increase in sensitization time or temperature lead to IGC susceptible states, this is significant result since "7 days / 100 °C" represents a benchmark corresponding to sensitization level in a service-life of a ship.

Electrical resistivity measurements combined with microstructural characterization and EDS showed that IGC response of the alloy plates was controlled by morphology and distribution of grain boundary precipitation, while precipitated fraction had lesser effect. Characterization of specimens annealed at 2 h at 240 °C showed that Zn addition of 0.5 wt % resulted in precipitation of ternary Al-Mg-Zn phase enriched with small amounts of Cu at grain boundaries. While variation in the amount of the cold work did not affect the chemical composition of the precipitates, different deformation substructures were created, which, in turn, influenced kinetics and mechanism of the precipitation. Nearly continuous coverage of the grain boundaries by the precipitates was a signature of the IGC susceptible state. In the specimens that

underwent higher degree of the cold work (over 30-40%) and showed superior corrosion resistance, the grain boundary precipitation was in the form of discrete particles as well as precipitation in grain interiors occurred. Characterization of the surfaces of the alloy exposed to the nitric acid showed that in IGC susceptible material corrosion was localized at the grain boundaries with nearly continuous coverage while matrix grain's interiors were intact. In the IGC resistant material, corrosion attack was uniform – both grain interiors and grain boundaries were corroded, however, overall mass loss was low.

Weldability assessment was performed on the samples with 42 % deformation, annealed at 240 °C/2h (state H321 and H116). Experimentally arc welding tests were performed using inert gas shield welding process TIG, MIG, pulsed TIG and pulsed MIG process. AlMg4.5Mn alloy with the addition of zirconium rod and wire was used as filler material. The mechanical and technological properties of welded joints were determined by ultimate tensile strength, bending angle up to cracking and hardness profile of the welded joint cross section. Microstructural analysis was performed by optical metallography, susceptibility to hot cracking was evaluated using a modified FISCO-test and corrosion resistance by applying NAML & ASSE tests.

The results of experimental welding showed that the present parent material is suitable for welding using TIG, MIG, TIG-P and MIG-P welding procedures and other parameters of welding technology which have been performed during experimental welding.

Key words: Al-Mg alloys; AA5083-H321; thermo-mechanical processing; β-phase precipitation; intergranular corrosion (IGC) susceptibility; exfoliation and pitting corrosion; sensitization; AA5083-H116; MIG and MIG-Pulse; TIG and TIG-Pulse.

Research field: Metallurgy/Metallurgical Engineering

Specific field: Thermo-mechanical Treatment, Physical Metallurgy

UDC number: 620.179.2:691.771:623.8

СТРУКТУРА И ЗАВАРЉИВОСТ Al-Mg ЛЕГУРА ВИСОКЕ ЧВРСТОЋЕ ЗА БРОДОГРАДЊУ

Алуминијум-магнезијум легуре које не ојачавају термичком обрадом, или преципитацијом секундарних фаза, свој капацитет ојачавања остварују захваљујући растварању легирних елемената у чврстом раствору, пре свега Mg атома, као и хладном деформацијом. Међутим, када је концентрација Mg атома преко 3.5%, ове легуре постају осетљиве према корозији. Развој корозионе осетљивости везан је за сензитизацију – преципитацију Mg-а из пресићеног чврстог раствора у виду анодне β (Al_3Mg_2) фазе по границама зрна на температурама 60-200 °C. Услед високе покретљивости Mg атома процес преципитације се одвија и на собној температури, с тим што је брзина преципитације веома ниска.

Ова карактеристика Al-Mg легура са вишим садржајем Mg-а, упркос веома добрим механичким особинама и доброј заварљивости (легуре типа AA5083), у великој мери ограничава њихову примену у области бродских конструкција или пак морских платформи. Осетљивост Al-Mg легура према корозији зависи од средине, састава легуре и начина прераде, тј. процеса термо-механичке прераде. Унапређења механичких особина праћена су повећањем концентрације Mg-а, што истовремено повећава и осетљивост ка корозији. Настојања да се овај проблем ублажи, резултовала су модификацијом типичне или најпознатије легуре за бродске конструкције AA5083 додатком Zn-а, и стварањем нових типова легура. У овом раду је испитиван утицај параметара термо-механичке прераде на корозиона и механичка својства, као и на заварљивост Zn-ом модификоване легуре типа Al-5.1wt%Mg-0.7wt%Mn.

Да би се развио оптималан термо-механички режим прераде испитиване легуре, ради обезбеђења механичких и корозионих карактеристика дефинисаних специфичним стањем H321 за примену у бродоградњи, дефинисана је мултипараметарска прерада испитиваног материјала. Материјал је подвргнут различитим степенима хладне деформације ваљањем (16-55 %), међуфазном жарењу на 350 °C, и завршном жарењу на различитим температурама у опсегу 220-280 °C у времену 1-3 h. Карактеризација механичких особина (тврдоћа и затезне особине), корозионе карактеристике (осетљивост на интергрануларну

корозију - IGC, ексфолијацију и питинг корозију) и њихову корелацију са микроструктуром (откривену оптичком, скенирајућом и трансмисионом електронском микроскопијом) вршена је у различитим фазама процесирања.

Добијени резултати показали су да постоји спрегнути утицај температуре завршног жарења и претходне хладне деформације на осетљивост према интергрануларној корозији (IGC), која је одређена путем NAML теста (ASTM стандард G67). Повећање температуре завршног жарења у испитиваној температурној области 220-280 °C, као и повећање претходног степена хладне деформације, праћено је повећањем отпорности на IGC. Тако, узорак жарен на 220 °C био је осетљив на IGC независно од претходне деформације (иако осетљивост ка IGC опада са деформацијом). После жарења на 240 °C и претходне деформације од 30 %, узорак је био отпоран на IGC. Утицај деформацције практично је нестао после завршног жарења на 260 °C и више. Утицај времена жарења је био мање изражен, али је консеквентно доприносио побољшању корозионе стабилности испитиване легуре.

Тест испитивања склоности ка ексфолијацији и питинг корозији (ASTM G66) показао је недозвољени ниво ексфолијације код узорака који су деформисани до високих степена деформације (~50 %) и завршно жарени на 220 °C. Међутим, са даљим повишењем температуре, ексфолијација се није јављала, с тим што је и општа осетљивост према интергрануларној корозији (IGC) сузбијена. Питинг корозија није откривена на штетном нивоу (према стандарду), али је извесна питинг корозија запажена код узорака жарених на високим температурама, у стању које је показало високу отпорност према IGC.

Корелација механичких особина (граница течења, затезна чврстоћа, издужење) и корозионе осетљивости испитиване легуре показала је да за добијање H321 стања, режим ТМП треба да се базира на завршној деформацији 35-40 % и завршном жарењу на 240 °C/2h. Даља испитивања показала су да је после сензитизације на 100 °C/7 дана, легура била отпорна на IGC, што је од посебног значаја ако се узме у обзир да се наведени услови сензитизације сматрају еквивалентом сензитизације за радни век бродова.

EDS испитивања микроструктуре и мерења електричне проводљивости довела су до сазнања да је осетљивост на IGC контролисана пре свега морфологијом и дистрибуцијом преципитата по границама зрна , док је сам удео

преципитата од секундарног значаја. Испитивања код узорака жарених на 240 °C /2h показала су да додатно легирање са 0.5 % Zn-a резултује преципитацијом тројне фазе Al-Mg-Zn и мање количине Cu по границама зрна. Степен хладне деформације није утицао на састав издвојених фаза, али је креирањем различите дислокационе субструктуре утицао на кинетику и механизам преципитације. Издвајање континуираног филма по границама зрна био је знак осетљивости структуре на IGC. Узорци који су деформисани са вишим степенима деформације (30-40 %) показали су одличну корозиону отпорност, и у њиховој структури преципитати су били у дискретној форми по границама зрна, а такође су били запажени по унутрашњости кристалних зрна.

Оцена заварљивости је обављена на узорцима са степеном деформације од 42 % жареним на 240 °C/2h (стање H321 и H116). Експериметално заваривање је обављено електролучним поступцима у атмосфери заштитног инертног гаса и то са нетопивом (TIG поступак) или топивом електродом (MIG поступак), и истим поступцима применом пулсирајућег лука (TIG-P и MIG-P поступак).

Êàî äîäàòíè ìàòåðè¼àë ¼å êîðèøžåíà øèïêà èëè æèöà îä ÀlMg4.5Mn ëåãóðå ñà äîäàòêîì Zr. Ìåõàíè÷êî-òåõíîëîøêå îñîáèíå çàâàðåíîã ñïî¼à ñó îäðå èâàíå èñïèòèâàœåì çàòåçíå ÷âðſòîžå, óãëà ñàâè¼àœà äî ïî¼âåå ïðñëèíå è ïðîìåíå òåðäîžå êðîç ïðåñåê çàâàðåíîã ñïî¼à. Ìèêðîſòðóêòóðíà àíàëèçà ¼å îáàâšåíà ïðèìåíîì îïòè÷êå ìèòàëîãðàôè¼å, ñêëîíîſò êà ïî¼àâè òîïëèõ ïðſëèíà ¼å îöåœåíà ïðèìåíîì îïàèôèêîâàíîã FISCO–òåſòà, à êîðîçèîíà îòïîðíſò ïðèìåíîì NAML и ASSE òåſòà. Äîáè¼åíè ðåçóëòàòè åêſïåðèìåíòàëíîã çàâàðèâàœà ïîêàçàëè ſó äà ¼å, ïðåäìåòíè îſíîâíè ìàòåðè¼àë ó ſòàœó Í321, ïîãîäàí çà çàâàðèâàœå óêîëèêî ſå ïðèìåíå ÒIG, ÌIG, ÒIG-P è ÌIG-P ïîſòóïöè çàâàðèâàœà, óç îſòàëå ïàðàìåòðå òåõíîëîãè¼å çàâàðèâàœà êî¼è ſó áèëè ïðèìœåíè êîä åêſïåðèìåíòàëíîã çàâàðèâàœà.

Кључне речи : Al-Mg легуре; AA5083 - H321; Термо- механички третман; преципитација β – фазе; сензитизација структуре; интергрануларна корозија (IGC); ексфолијација и питинг корозија; AA5083 – H116; MIG и MIG пулсирајући; TIG и TIG пулсирајући.

Научна област : Металургија/Металуршко инжењерство

Ужа научна област : Термомеханичка прерада метала , Физичка металургија

УДК број: 620.179.2:691.771:623.8

ACKNOWLEDGMENT

First of all, I thank God for His mercy on me.

I would like to thank my supervisor Prof. Endre Romhanji for his excellent support, guidance, encouragement and most importantly his friendship throughout this thesis. He continually helped me out to develop my ability.

I sincerely thank my co-adviser, Dr Vencislav Grabolov, for his instructions, helpful discussions, meetings and encouragement in welding work.

I also thank Dr. Miljana Popović and Dr. Tamara Radetić for thier numerous stimulating discussions and comments at all stages of this challenging work, and also many thanks to Prof. Veselin Vaščić for his assistance with corrosion analysis experiments. Especial thanks are extended to Mr. Nebojša Stajić, Mr. Milovan Blagojević and Mr Zlatibor for their assistance in preparing the samples.

In addition, I would like to express my sincere thanks to all academic and technical members of the Department of Metallurgical Engineering, Faculty of Technology and Metallurgy, University of Belgrade for help during my work on this thesis.

I would like to express my gratitude to the Ministry of Higher Education in Libya for PhD scholarship and financial support.

IMPOL SEVAL Aluminium Mills a.d. Sevojno for the supply of materials for this study is greatly acknowledged. I would like also to thank Goša Institute and military- technical Institute Žarkovu for helping me on mechanical testing of weldments.

I give this work to the spirit of my father, may ALLAH give him a pleasant place in Paradise, this thesis is dedicated to my mother, sisters and brothers for their unending love, sacrifice and support throughout my education.

Last but not least, I would like to express sincere appreciation and love to my loving supportive wife, daughters and son who shared this journey with me from the beginning to the end. Without them these past five years would be boring and pointless.

Thank you all !!!

Table of Contents

I Abstract i
II Acknowledgements vii
III Table of Contents viii
IV List of Figures xiii
V List of Tables xviii
VI List of Acronyms and Abbreviations xix
CHAPTER 1 1
========== 1
1. Introduction 1
CHAPTER 2 3
========== 3
2. Theoretical Background 3
2.1. Aluminium and Aluminium Alloys 3
2.1.1. Classification of Aluminum Alloys 4
2.1.2. Temper Designation of Non-heat Treatable Alloys 5
2.2. Aluminum-Magnesium alloys 6
2.2.1. Chemistry of Al-Mg Alloys 7
2.2.2. Processing of Al-Mg Alloys 8
2.3. Corrosion of Al-Mg Alloys 9
2.3.1. Corrosion in general 9
2.3.1.1. Pitting Corrosion 10
2.3.1.2. Intergranular Corrosion (IGC) 10
2.3.1.3. Stress Corrosion Cracking SCC– definition 11
2.3.1.4. Exfoliation 11
2.3.2. Sensitization 11
2.4. Welding of aluminum and its alloys 14
2.4.1. TIG welding 16
2.4.1.1. Process principles 16
2.4.2. MIG welding 17
2.4.2.1. Process principles 17
2.4.3. Pulsed gas metal arc welding 18
2.4.4. Welding energy and heat input 20

2.4.5. Mechanical Properties for 5xxx series Aluminium Alloy sheet and Plate Butt Welds (As-Welded Condition) 21
2.4.5.1. Aluminium oxide film 21
2.4.5.2. Heat affected zone (HAZ) 23
2.4.5.3. The parent alloy 23
2.4.6. Welding of 5083 aluminum 24
2.4.6.1. Structure of the welds 24
2.4.6.2. Mechanical properties of welded 5083 aluminum 25
2.4.7. Aluminium alloy filler wires 26
2.4.8. Weldability of aluminum 5083 26
2.4.9. Corrosion of 5083 welds 27
2.4.10. Testing Methods for Welded Joints 28
2.4.11. Susceptibility of hot cracks - FISCO test 28
CHAPTER 3 30
========== 30
3. Experimental Part 30
3.1. Material 30
3.2. Thermo-mechanical treatment 31
3.2.1. Cold rolling 31
3.2.2. Thermal treatment 31
3.3. Testing methods 33
3.3.1. Mechanical testing 33
3.3.1.1. Tensile test 33
3.3.1.2. Hardness measurements 34
3.3.2. Electrical resistivity measurements 34
3.3.3. Corrosion testing 34
3.3.3.1. Nitric Acid Mass Loss Testing 35
3.3.3.2. ASSET Test (ASTM G66) 35
3.3.4. Microstructure characterization 36
3.3.4.1. Optical (light) microscopy 36
3.3.4.2. Scanning Electron Microscopy (SEM) 36
3.3.4.3. Transmission Electron Microscopy (TEM) 37
3.4 Welding procedure 38
3.4.1 Material characterization 40

3.4.2 Testing Methods for Welded Joints 41
3.4.2.6. Tensile testing 41
3.4.2.7. Bending testing 42
3.4.2.8. Hardness measurements 42
3.4.2.4 Electrical Resistivity 43
3.4.2.5 Corrosion testing 43
3.4.2.5.1 NAMLT Test (ASTM G67) 43
3.4.2.5.2 ASSET Test (ASTM G66) 43
3.4.2.6 Metallographic observations 43
3.4.2.6.1 Macrostructure of Welded Parts 44
3.4.2.6.2 Microstructure of Welded Parts 44
CHAPTER 4 46
---------- 46
4. Results 46
4.1. Work hardening and ductility of the tested alloys in cold rolling 46
4.1.1. Mechanical properties of the cold rolled material 46
4.1.2 Mechanical properties after the thermo-mechanical processing 48
4.1.2.1 Hardness (HB) of the material 48
4.1.2.2 Tensile properties 50
4.1.3 Electrical resistivity 52
4.1.4 Corrosion Properties 55
4.1.4.1 Intergranular Corrosion – NAML Test 55
4.1.4.2 Exfoliation and Pitting Corrosion (G66 – ASSET TEST) 58
4.1.5 Microstructural characterization 64
4.1.5.1 Microstructure of the cold rolled sheets 64
4.1.5.2 Grain size 67
4.1.5.3 Intergranular corrosion - microstructure 68
4.1.6 Grain boundary phase 72
4.2 Welding Results 75
4.2.1 Radiographic Testing 75
4.2.2 Tensile Testing 75
4.2.3 Bending results 78
4.2.4 Hardness measurements 79
4.2.5 Electrical Resistivity 80

4.2.6 Corrosion test results 82
4.2.6.1 Intergranular Corrosion 82
4.2.6.2 Exfoliation and Pitting Corrosion 82
4.2.7 Metallographic observations results 85
4.2.7.1 Macrostructure of Welded Parts 85
4.2.7.2 Microstructure of Welded Parts 87
CHAPTER 5 90
========== 90
5. Discussion 90
5.1 Thermo-mechanical processing 90
5.1.1 Mechanical properties 90
5.2. Corrosion Resistance and Microstructure 91
5.2.1. Intergranular Corrosion 91
5.2.2. Exfoliation and Pitting Corrosion 95
5.3. Welding and Weldability 98
5.3.1. Tensile properties test 98
5.3.2. Bending test 98
5.3.3. The hardness 99
5.3.4. Electrical resistivity 99
5.3.5. Corrosion Resistance 99
5.3.5.1. Intergranular Corrosion (G67 – NAML TEST): 99
5.3.5.2. Exfoliation and Pitting Corrosion (G66 – ASSE TEST) 100
5.3.6. Metallographic observations 100
5.3.6.1. Macrostructure of Welded Parts 100
5.3.6.2. Microstructure of Welded Parts 101
CHAPTER 6 102
========== 102
6 Conclusions 102
CHAPTER 7 I
========== I
7 Appendix I
7.1 Appendix I (Mechanical properties) I
7.2 Appendix II Corrosion V
7.3 Appendix III Optical Microscope XXI

7.4 Appendix IV Welding..... XXIV
7.4 Appendix V Papers published as a result of this thesis XXXVIII
Биографија ..... a
Прилог 1. ..... b
Прилог 2. c
Прилог 3. ..... d

List of Figures

Figure 2.2.1 The binary Al-Mg equilibrium diagram [12]..... 7
Figure 2.3.1 The effect of [Al (Mn, Fe, Cr)] on the corrosion behavior of AA5083 aluminum alloy in 3.5 wt. % NaCl solution [33]..... 10
Figure 2.4.1 Principle of TIG Welding [56]..... 16
Figure 2.4.2 Typical GMAW Process Connections [57]..... 18
Figure 2.4.3 Typical Pulse GMAW current cycle Pattern [58]..... 19
Figure 2.4.4 Heat input influences cooling rate [59]..... 21
Figure 2.4.5 Possible flaws and defects within the aluminium oxide film [54]..... 23
Figure 2.4.6 FISCO test for hot cracks..... 29
Figure 3.3.1 Schematics of a tensile test specimen..... 33
Figure 3.4.1 Material processing of welded samples..... 38
Figure 3.4.2 Jigging of plates to maintain flatness..... 40
Figure 3.4.3 Method of cutting test-pieces from procedure approval plate..... 41
Figure 4.1.1 Engineering stress-strain curves of the material in as-received state and after cold rolling reductions in a range 8-85%..... 46
Figure 4.1.2 Plot of the average strength parameters, $R_{0.2}$ and Rm, elongation and hardness (HB) as a function of the cold reduction %..... 48
Figure 4.1.3 Hardness of the sheets cold rolled and annealed at 220-280 °C for 2h as a function of the % rolling reduction..... 49
Figure 4.1.4 Hardness of the sheets cold rolled and annealed at 220-280 °C for 2h as a function of the annealing temperature..... 50
Figure 4.1.5 Effect of the annealing time on the hardness of the sheets deformed with 16.7% (a) and 42.6% (b) cold reduction and annealed in 220-280 □C temperature range..... 50
Figure 4.1.6 Effect of the final annealing temperature on the strength of the alloy. Annealing time was 2h. Prior the annealing specimens were deformed with 16.7% or 42% cold rolling reduction. (Red lines mark minimum strength parameters for attaining H321 state..... 51
Figure 4.1.7 Effect of the final annealing temperature on the elongation. Annealing time was 2h. Prior the annealing specimens were deformed with 16.7% or 42% cold rolling reduction. (Red lines mark minimum strength parameters for attaining H321 state..... 52

Figure 4.1.8 Electrical resistivity of the sheets cold rolled and annealed at 220-280 °C for 2h as a function of the % rolling reduction. “0” corresponds to the electrical resistivity of the specimens that underwent initial cold rolling and intermediate annealing..... 53
Figure 4.1.9 Electrical resistivity of the sheets cold rolled and annealed at 220-280 °C for 2h as a function of the annealing temperature. “0” corresponds to the electrical resistivity of the specimens that underwent initial cold rolling and intermediate annealing..... 54
Figure 4.1.10 Effect of the annealing time on the electrical resistivity of the specimens deformed with 16.7% (a) and 42.6% (b) cold reduction and annealed in 220-280 °C temperature range 54
Figure 4.1.11 Electrical resistivity of the specimens deformed 16.7% and 42% at different stages of the thermo-mechanical processing and sensitization. 55
Figure 4.1.12 Intergranular corrosion susceptibility (IGC) determined by Nitric Acid Mass Loss Test (NAMLT) following the ASTM G67 standard as a function of the % cold rolling reduction. 56
Figure 4.1.13 Intergranular corrosion susceptibility (IGC) determined by Nitric Acid Mass Loss Test (NAMLT) following the ASTM G67 standard as a function of the annealing temperature..... 57
Figure 4.1.14 Effect of the annealing time on the IGC susceptibility of the specimens deformed with 16.7% (a) and 42.6% (b) cold reduction and annealed in 220-280 °C temperature range..... 57
Figure 4.1.15 Effect of sensitization treatment on IGC susceptibility of alloy (a) 7 days and (b) 25 days..... 58
Figure 4.1.16 Variation in a response toward exfoliation and pitting corrosion as function of the cold rolling reduction and annealing temperature (Face1)..... 60
Figure 4.1.17 Variation in a response toward exfoliation and pitting corrosion as function of the cold rolling reduction and annealing temperature (Face2)..... 61
Figure 4.1.18 Ratings of different levels of exfoliation corrosion (according to ASTM G66 standard)..... 62

Figure 4.1.19 The degree of pitting corrosion (according to ASTM G66 standard) identified at samples cold rolled with different reductions (up to 55%) and subsequently annealed in the range of temperatures from 220°C to 280°C..... 62
Figure 4.1.20 Samples surfaces after exfoliation and pitting testing for different cold rolling deformation and different annealing temperatures at annealing time 2 hours. 64
Figure 4.1.21 Microstructure of samples cold rolled to 16.7% (a) and 42% (b) and subsequently annealed at 240°C/2h 65
Figure 4.1.22 Bright field TEM micrographs of the deformation substructure of: a) 16 % thickness reduction, 110]za.; b) 42 % thickness reduction, [110]za..... 66
Figure 4.1.23 Back scattered SEM micrographs showing distribution of constituent particles after cold rolling. Bright particles are mostly $Al_6(Mn,Fe)$. (a) and (b) 16.7% cold reduction. (c) and (d) 42% cold reduction. 66
Figure 4.1.24 Grain microstructure of the specimens deformed to 16.7% (a & b) and 54% (c & d) and annealed at 220°C/2h and 280°C/2h, respectively. 67
Figure 4.1.25 Mean grain size aspect ratio of the samples cold rolled to 16.7%, 30% and 54% and subsequently annealed in the temperature range 220°C-280°C for 2h. 68
Figure 4.1.26 LOM micrographs of the microstructure after orthophosphoric acid etch: (a) 42% deformation and annealing 2h/260°C (IGC resistant); (b) 42% deformation and annealing 2h/240°C (IGC resistant); (c) 42% deformation and annealing 2h/220°C (IGC susceptible); 69
Figure 4.1.27 Secondary electron SEM micrographs showing morphology of the surface parallel to LT plane. Specimens were deformed 16% and annealed for 2h at 240°C (IGC susceptible). Specimens were immersed in the nitric acid for: (a) 2h - (b) 24h. 71
Figure 4.1.28 Secondary electron SEM micrographs of the surface morphology at higher magnifications: a) Specimen deformed 16 % and annealed for 2h at 240°C (IGC susceptible) after immersion 24h in the nitric acid. b) Specimen deformed 42% and annealed for 2h at 240°C 71

Figure 4.1.29 Secondary electron micrographs showing morphology of the surface parallel to LT plane. Specimens were deformed for 42% and annealed for 2h at 240°C (IGC resistant). Specimens were immersed in the nitric acid for: (a) 2h - Below surface layer of flat gra 72
Figure 4.1.30 Bright field TEM micrographs of the precipitated β-phase at the grain boundaries: (a, b) Specimen deformed 16% and annealed 2h at 240°C (IGC susceptible state). The precipitated grain boundary phase forms continuous or semicontinuous film. (c, d) Specimen deformed 42% and annealed 2h at 240°C (IGC resistant state). Subgrains network was formed during annealing. The precipitated grain boundary phase is observed at the high angle grain boundaries and triple junctions while subgrain boundaries are precipitate free. 73
Figure 4.1.31 EDS spectra and corresponding bright field TEM micrographs of the precipitated grain boundary phases: (a) Specimen deformed 16% and annealed 2h at 240°C (IGC susceptible state). (b) Specimen deformed 42% and annealed 2h at 240°C (IGC resistant state). 74
Figure 4.2.1 Comparison strength values with welded joints 78
Figure 4.2.2 Micro-Hardness of the welded samples. 79
Figure 4.2.3 Vickers Hardness of the welded samples. 80
Figure 4.2.4 Electrical resistivity variation for different welding process..... 81
Figure 4.2.5 Electrical resistivity variation for different welding process..... 81
Figure 4.2.6 Results of Intergranular Corrosion (G67) testing for different welded samples 82
Figure 4.2.7 Exfoliation and pitting corrosion of H116 samples (a.) TIG, (b.) TIG Pulse, (c.) MIG (d.) MIG Pulse 84
Figure 4.2.8 Exfoliation and pitting corrosion of H321 samples (a.) TIG, (b.) TIG Pulse, (c.) MIG (d.) MIG Pulse..... 85
Figure 4.2.9 Macrographs of 5083H116 : (a) TIG welded, (b) TIG-Pulse welded, (c.) MIG (d.) MIG Pulse. 86
Figure 4.2.10 Macrographs of 5083H321 : (a) TIG welded, (b) TIG-Pulse welded, (c) MIG welded, (d) MIG-Pulse welded. 87
Figure 4.2.11 Microstructure of Base Metal, Weld Metal and Heat Affected Zone of etched 5083 samples MIG welded..... 88

Figure 4.2.12 Microstructure of Base Metal, Weld Metal and Heat Affected Zone of etched 5083 samples TIG welded 89
Figure 7.1.1 Hardness variation with cold rolling reduction for different annealing temperatures and different annealing time. I
Figure 7.1.2 Hardness variation with annealing temperature for different cold rolling reductions and different annealing time II
Figure 7.1.3 Electrical resistivity variation with cold rolling reduction for different annealing temperatures and annealing times. III
Figure 7.1.4 Electrical resistivity variation with annealing temperature for different cold rolling reductions and annealing times. IV
Figure 7.2.1 Intergranular Corrosion variation with cold rolling reduction for different annealing time and different annealing temperatures. V
Figure 7.2.2 Intergranular Corrosion variation with annealing temperature for different cold rolling reductions and different annealing time. VI
Figure 7.2.3 Exfoliation and Pitting variation with annealing temperatures for different cold rolling reductions and different annealing time (Face 1).XV
Figure 7.2.4 Exfoliation and Pitting variation with annealing temperatures for different cold rolling reductions and different annealing time (Face 2).XVI
Figure 7.2.5 Ratings of different levels of exfoliation corrosion (according to ASTM G66 standard)..... XVII
Figure 7.2.6 The degree of pitting corrosion (according to ASTM G66 standard) identified at samples cold rolled with different reductions (up to 55%) and subsequently annealed in the range of temperatures from 220°C to 280°C..... XVIII
Figure 7.2.7 Samples surfaces after exfoliation and pitting testing for different cold rolling deformation and different annealing temperatures at annealing time 2 hours XXI
Figure 7.3.1 Optical images of 5083-H321 samples XXIII

List of Tables

Table 2.2.1 Classification of wrought aluminum alloys [8]..... 4

Table 2.4.1 Principal processes for the welding of aluminium [3]..... 14

Table 3.1.1 Chemical compositions of the studied alloy and Standard AA5083 and AA5059 alloys (weight percent). 30

Table 3.3.1 Dimension of the samples for tensile test. 33

Table 3.4.1 Welding parameters of the welded samples 39

Table 3.4.2 Dimension of tensile test sample as standard EN 895[90] 42

Table 4.1.1 Mechanical properties of as-received and cold rolled sheets 47

Table 4.1.2 Corrosion stability of the specimens deformed with a different cold rolling reductions and annealed for 2 hours in the temperature range 220-280 °C for three sets of specimens. 59

Table 4.2.1 Desination of welded samples..... 75

Table 4.2.2 Mechanical behaviour of the base metal 76

Table 4.2.3 Mechanical behaviour of welded samples..... 76

Table 4.2.4 Bending test results of the welded samples 78

Table 4.2.5 Corrosion stability for welded Samples..... 83

Table 5.1.1 Properties of the AA 5083 required by ASTM standard for H321 state. 90

Table 5.2.1 Average Composition of the Precipitated Grain Boundary Phases and Aluminum Matrix (Weight Percent) from EDS Data.[106] 93

Table 7.2.1 Corrosion stability after 17.6% deformation, different final annealing and time. VIII

Table 7.2.2 Corrosion stability after 20% deformation, different final annealing and time. IX

Table 7.2.3 Corrosion stability after 25% deformation, different final annealing and time. X

Table 7.2.4 Corrosion stability after 30.5% deformation, different final annealing and time. XI

Table 7.2.5 Corrosion stability after 35% deformation, different final annealing and time. XII

Table 7.2.6 Corrosion stability after 42.6% deformation, different final annealing and time. XIII

Table 7.2.7 Corrosion stability after 54.2% deformation, different final annealing and time. XIV

List of Acronyms and Abbreviations

Al	Aluminium
Mg	Magnesium
5XXX	Aluminium Magnesium Alloy
β (Al_3Mg_2)	Beta phase
°C	Degree Celsius
AA5083	Aluminum Alloy
wt%	Weight percent
Zn	Zinc
AA5059	Aluminum Alloy
Mn	Manganese
ASTM	American society for testing and materials
H321	Some work hardening impacted by Shaping but less than required for H32 temper
Hr	Hour
IGC	Intergranular corrosion
SEM	Scanning Electron Microscope
TEM	Transmission electron microscope
NAMLT	Nitric acid metal loss test
G66	Visual Assessment of Exfoliation Corrosion Susceptibility of Aluminum Alloys
G67	Determining the Susceptibility to Intergranular Corrosion of Aluminum Alloys by Mass Loss After Exposure to Nitric Acid
EDS	Energy Dispersive Spectrometry
AlMgZn	Aluminum alloy
Cu	Copper
MIG	metal inert gas welding
MIG-P	metal inert gas welding Pulse
TIG	Tungsten Inert Gas welding
TIG-P	Tungsten Inert Gas welding Pulse
H116	Some work hardening impacted by Shaping but less than required for H11 temper
SCC	Stress Corrosion Cracking
Fe	Iron
Si	Silicon
Cr	Chromium
µm	Micrometer
pH	Negative logarithm (base 10)
NaCl	Sodium chloride
AA5182	Aluminum Alloy
HAZ	Heat Affected Zone

GMAW	Gas Metal Arc Welding
Mm	Millimeter
TAGS	Tungsten Active Gas welding
GTAW	Gas Tungsten Arc Welding
CO_2	Carbon dioxide
MAG	Metal Active Gas welding
Q	Heat input
E	Energy
ν	work (KJ)
η	efficiency factor for GMAW
Al_2O_3	Aluminum Oxide
MPa	Mega Pascal
H_2O	Water
H^+	Hydrogen ion
e^-	Electron
OH^-	Hydroxyl anions
Al^{+3}	Aluminium ion
Cl^-	Chlorine
Br^-	Bromine ion
I^-	An iodide ion
ER5356	Aluminum Welding Wire for MIG Welders
AWS	American Welding Society
FISCO	Tests of susceptibility to hot cracking
Ti	Titanium
Zr	Zirconium
r%	Rolling Reduction percentage
L-T orientation	Longitudinal-Transparence
min	Minute
ρ	initial true strain rate
Kg	Kilogram
SiC	Silicon Carbide
KHz	kilo Hertz
HNO_3	Nitric acid
Mg	Milligram
cm	Centimeter
IHC	Input Heat Coefficient
s	Seconds
ASSET	Method for Visual Assessment of Exfoliation Corrosion Susceptibility of AA5xxx Series Al alloys
NH_4Cl	Ammonium chloride
NH_4NO_2	Ammonium nitrite

$C_4H_{12}N_2O_6$	ammonium tartrate
H_2O_2	Hydrogen peroxide
U	Volt
I	Current
kV	Kilo volt
$Lmin^{-1}$	Liter per minute
HI	Heat input
mL	Milliliter
HBF4	Fluor boric acid
R0.2	Yield Strength
Rm	Ultimate Strength
ε	Elongation
HB	Brinell Hardness
Pm	force Newton
FL	Fusion Line
HV	Vickers Hardness
OM	Optical Microscope
WM	Weld Metal

CHAPTER 1

1. Introduction

Aluminum alloys, such as alloys from AA 5xxx series, represent alternative to steel in a number of applications due to light weight, good weldability and formability, moderate strength and corrosion resistance in certain environments [1]. One of the most versatile of AA5xxx aluminum alloys, AA5083 and its derivate alloys has been widely used in automotive [2] and marine industries [3]. However, it is prone toward intergranular corrosion (IGC) and stress corrosion cracking (SCC) in certain environments due to high magnesium content. The extent of IGC and SCC susceptibility depends on environment, materials chemistry, fabrication and thermo-mechanical processing. Attempts to mitigate susceptibility toward different forms of corrosion while increasing Mg content to improve the alloy strength lead to modification of AA5083 by Zn additions and design of new alloy types such as AA 5059. In this thesis, the effect of thermo-mechanical treatment on corrosion properties of Zn modified Al-5.1wt%Mg-0.7wt%Mn alloy plates was investigated.

In order to develop optimal thermo-mechanical regime for the studied alloy, that would provide desired combination of mechanical and corrosion properties (described by ASTM standard as H321 & H116 state), the effect of multiple processing parameters was assessed.

The growing range of applications has added challenges for improvement of the welding processes. One of the aims of this work was evaluation of the application of different welding techniques (MIG, MIG-Pulse, TIG and TIG-Pulse) and its effect on the mechanical properties and corrosion resistance of the H321 and H116 welded joints.

This PhD thesis is divided into eight chapters. The literature review, presented in Chapter 2, provides outline of the characteristics of non-heat treatable 5xxx series Al alloys and current understanding of the corrosion response of high Mg 5xxx alloys. Detailed description of the experimental techniques utilized in this project is presented in Chapter 3. The key results are presented in Chapter 4. Chapter 5 discusses the influence of thermo-mechanical regime on mechanical properties, microstructure and corrosion resistance of the alloy as well as influence of the processing route of the base alloy on the weld microstructure. Chapter 6 summarizes the results and presents the conclusions of the thesis. In the Appendix (Chapter 7) all results, plots, tables and micrographs are presented as well as the peer-reviewed papers published to date as a result of this research. List of references is given in Chapter 8.

CHAPTER 2

2. Theoretical Background

2.1. Aluminium and Aluminium Alloys

Aluminium, the third most abundant element in Earth's crust and the most abundant structural metal, is very reactive and in nature exists in very stable compounds such as silicates and oxides. Hence, elementary aluminium was isolated from its ore bauxite only in the XIX century. The discovery was followed by intensive research and development of processes of aluminum production from its ore culminating with evolution of the Hall-Héroult and Bayer process that is in use even nowadays [4-6]. The advantages for aluminum that caused its fast adoption and replacement of more traditional metals and alloys can be summarized in following points [3,6]:

- A combination of high strength, low density, good formability and weldability resulted in its applications in automotive and aerospace industry.
- Good corrosion resistance in certain environments due to formation protective oxide film on the surfaces.
- High electrical conductivity allowed use in electrical power applications.
- Non-magnetic property eliminated arc blow problem associated with arc welding processes.
- High modulus of elasticity increased the resistance to impact loading and provided ability to absorb the loading energy.
- Good toughness resistance at low temperature provided advantage for use in cryogenic applications.
- Good formability facilitated their shaping by several ways of forming processes, such as deep drawing, extrusion and cold work forming.

- Non-poisonous and colorless corrosion products facilitated their use in chemical and food-processing industry.

- Low melting point made the cost of the aluminum recycling and re-processing cheaper than its extraction.

Disadvantages of aluminum and its alloys are poor fatigue and wear resistance as well as deterioration of mechanical and corrosion properties at elevated service temperatures that restrict its use for elevated temperature and high turbulence applications.

Nowadays, aluminum alloys are used in a broad range of applications – for electrical conductors, transport, and packaging as well as other applications such as high pressure gas cylinders, machined components, ladders and access equipment, sporting goods, road barriers and signs, furniture, lithographic plates, etc.

2.1.1. Classification of Aluminum Alloys

Aluminum alloys may be divided into two broad classes according to mode of manufacturing the final products: cast and wrought products. The alloys are classified further into families according to chemical composition and, finally, by temper designation [7,8].

Wrought aluminum alloys are the alloys produced from metal ingots through forming processes such as rolling, extrusion and forging. A system of four-digit numerical designations is devised for identification of the wrought aluminum alloys. The first digit indicates the alloy group while the last two digits identify the aluminum alloy or aluminum purity. The second digit indicates the modification on the original alloy or impurity limits [8,9]. Table 2.2.1 shows the classification of wrought aluminum alloys.

Table 2.2.1 Classification of wrought aluminum alloys [8].

Aluminum, 99.9 percent minimum and greater	1XXX
Copper	2XXX
Manganese	3XXX
Silicon	4XXX
Magnesium	5XXX
Magnesium and Silicon	6XXX
Zinc	7XXX
Other element	8XXX
Unused series	9XXX

Wrought aluminum alloys are further grouped into heat treatable and non-heat treatable alloys. The former are subjected to thermal treatment at elevated temperature, i.e. aging, and major strengthening mechanism is precipitation hardening while the later strengthening mechanisms are solid solution and work hardening. The alloys from the series 2XXX (Aluminum-Copper-Magnesium), 6XXX (Aluminum-Magnesium-Silicon) and 7XXX (Aluminum-Zinc-Magnesium) groups belong to heat treatable group. Non-heat treatable alloys include all the various grades of pure aluminum and alloys from 3XXX (Aluminum-Manganese), 4XXX (Aluminum-Silicon) and 5XXX (Aluminum-Magnesium) groups.

2.1.2. Temper Designation of Non-heat Treatable Alloys

Commercial Al alloys are produced in different tempers and their designation according to temper includes "letter and digits" system [3]. Five basic tempers are identified by a letter:

- F – as fabricated. Wrought products in which the amount of strain hardening or the thermal treatments is not specified.
- O – annealed at temperature higher of recrystallization temperature. The alloy is fully recrystallized and is characterized by the lowest strength.
- H – work hardened. The letter 'H' is always followed by at least two digits to identify the amount of cold work and any heat treatments that have been carried out
- W – This is applied to alloys which precipitation harden at room temperature (natural ageing) after a solution heat treatment.
- T – thermally treated, i.e. aged. The 'T' is always followed by one or more digits to identify the specific heat treatment.

In the non-heat treatable wrought aluminum alloys, strength is attained by alloying – solid solution hardening and cold working – strain hardening. Those alloys are classified according to a thermo-mechanical processing and attained level of the work-hardening. The letter "H" is followed by a digit that indicates type of a heat treatment:

- H1 – strain hardened only.
- H2 – strain hardened and partially annealed.
- H3 – strain hardened and stabilized.
- H4 – annealed at temperature of paint baking painted.

The second digit after 'H' indicates the amount of strain hardening in the alloy. The maximum hardness is 8, while digits 1-7 correspond to strength between maximum and fully annealed temper O:

• Hx8 – the most heavily cold worked condition (deformation ≈75-80%).
• Hx4 –strength halfway between the annealed and fully hard condition (deformation ≈35-40%).
• Hx2 – H12 halfway between O and H14 (deformation ≈18%).

The third digit after 'H' is not mandatory and is used when the alloy requires special control to achieve the specific properties. Examples of such properties are exfoliation corrosion resistance, seam welded tube or additional working after the final temper has been achieved, e.g. by embossing. The full details of these designations are contained in the specification EN 515 'Aluminum and Aluminum Alloys – Wrought Products – Temper Designations' [10].

AA 5083 and its derivate alloys in H321 temper are marine grade alloys that are required to meet standards described by the ASTM B 928 Standard Specification for High Magnesium Alloy Sheet and Plate for Marine Service [10]. The purpose of the standard is to prevent cracking due to precipitation of anodic β- (Al_3Mg_2) at the grain boundaries that is cause of intergranular corrosion, exfoliation and stress corrosion cracking. In addition to required mechanical properties, the alloy must pass both ASTM G66 and G67 tests as well as metallographic examination. The G66 test specimen must not only pass the G66 with no signs of exfoliation, it must also exhibit a pitting corrosion rating of PB or better. This results in an alloy that is less susceptible to pit blistering. ASTM G67 requires mass loss during the Nitric Acid Mass Lost Test to be less than 15 mg/cm^2. If the alloy temper passes those tests, a photomicrograph is taken that is used as the comparison for metallographic examination for lot release [10].

2.2. Aluminum-Magnesium alloys

Wrought aluminum alloys of AA 5xxx series, i.e. Al-Mg alloys, belong to the group of non-heat treatable alloys. Main strengthening mechanisms of those alloys are work hardening and solid solution strengthening. Magnesium is the principal alloying element and the alloys of 5xxx series can contain from 0.5 wt% up to 12wt% of Mg. Increase in Mg content in an Al solid solution for 1wt% results in the yield strength increase of 16-19 MPa [11].

From the binary phase diagram (Figure 2.2.1) it can be seen that the maximum solubility of magnesium in aluminum is 17.4 wt% at eutectic temperature of 450 °C, while it drops to 1.9 wt% at room temperature. Hence, alloys with Mg content over 2 wt% form supersaturated solid solution at room temperature and there is a tendency toward decomposition and precipitation of equilibrium β phase. β phase (Al_3Mg_2 or Al_8Mg_5) is anodic with respect to the aluminum matrix and its precipitation is considered to be cause of different forms of intergranular corrosion (IGC) and stress corrosion cracking, particularly in alloys with over 3.5 wt% Mg [12,13].

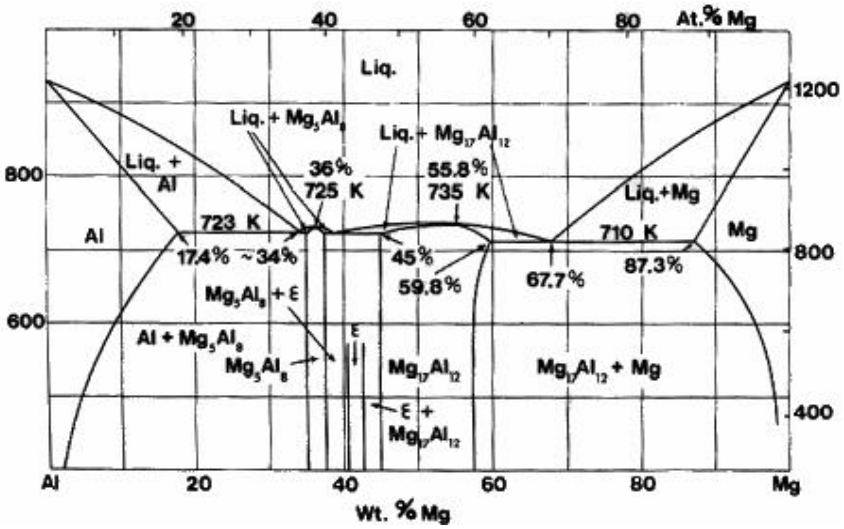


Figure 2.2.1 The binary Al-Mg equilibrium diagram [12]

Alloys from the AA 5xxx series have very broad range of applications, ranging from beverage cans to shipbuilding, due to moderate strength, good formability and weldability as well as good corrosion properties in the atmospheric conditions [2, 3]. One of the most versatile of alloys from the series is AA5083 has been used in shipbuilding industry. However, it is prone toward intergranular corrosion (IGC) and stress corrosion cracking (SCC) in certain environments due to high magnesium content.

2.2.1. Chemistry of Al-Mg Alloys

Binary Al-Mg alloys have very limited application, so the majority of commercial alloys contain other alloying elements such as Mn, Fe, Si, Cr, Cu etc. Commercial wrought alloys form 5xxx series contain up to 5.5wt% Mg, while content of the other alloying elements is in a 0.25-1wt% range.

Copper, silicon, manganese, magnesium, lithium and zinc are added to aluminum in a controlled amount to improve its mechanical properties, corrosion behavior, formability and weldability. On the other hand, nickel, chromium, titanium, zirconium and scandium are added to achieve specific properties. Generally, the added alloying elements can be classified into two types:

The alloying elements that improve mechanical and physical properties through solid solution strengthening and forming fine precipitate hardening phases. These include copper, manganese, zinc, magnesium, silicon and zirconium.

The elements initially present in aluminum as impurities such as iron (Fe) and silicon (Si) tend to form a relatively coarse cathodic constituent second phases owing to their limited solid solubility.

2.2.2. Processing of Al-Mg Alloys

Conventional fabrication of the wrought Al-Mg alloys includes primary and final processing. By primary processing is considered casting, homogenization anneal and hot deformation by rolling or drawing, while final processing includes cold deformation (by rolling or drawing) and annealing as well as welding processes. Depending on a thermo-mechanical regime during the final processing different types of temper can be attained.

In the as-cast state, microstructure of AA 5083 alloy types tends to be characterized by a coarse grains (200-400 μm) containing cored dendrites of α (Al)-solid solution surrounded by a network of coarse eutectic constituent particles of Al_6(Mn, Fe) and Mg_2Si type [14,15]. Microsegregations are almost always present and characterized by constituent particles in the interdendrite regions, dendrite cores enriched with peritectic forming elements (as well as lower levels of magnesium, while wide border between dendrite cores and interdendrite channels are enriched with Mg.

In the heavily alloyed Al-Mg alloys such as AA 5083 and its derivate, due to strong tendency of alloying elements to form segregations, homogenization anneal is a necessary processing step. Optimal homogenization treatment (520-560 °C) provides elimination of Mg microsegregations, due to the high diffusivity of Mg and controlled dissolution as well as precipitation of secondary phases (containing Mn, Fe, Cr, Cu etc). One of the goals homogenization is controlled particle size distributions, including fine

dispersoids and coarser constituents. Those dispersoids have a strong influence on the recrystallization kinetics and texture development during the hot rolling [16-19].

The hot rolling process is used to convert sheet ingots into coils with a gauge suitable for the cold rolling process. The optimum starting temperature for the hot rolling of Al-Mg alloys is in a range 460-500 °C [20].

Hot-rolled aluminum strip is cooled to room temperature and fed into the cold roll mill. The strip is passed several times between a series of rollers until it is gradually reduced to the desired gauge and wound up into a coil. Between cold and hot rolling intermediate thermal treatments may be applied.

Depending on desired temper and properties the final annealing is conducted in a wide temperature range.

The common methods used for joining aluminum and its alloys are the solid state bonding and fusion welding processes. AA5xxx aluminum alloys can be successfully joined with both processes [21-22]. Joining of aluminum and its alloys with fusion welding processes requires attention since the thermal coefficient of expansion for the aluminum is high. For this reason the heat input during joining has to be high to insure proper fusion, particularly for thick sections [7].

Welding involves the melting and fusion of the parent metals only is known as *autogenous* welding, but many processes involve the addition of a *filler metal* which is introduced in the form of a wire or rod and melted into the joint. Together with the melted parent metal this forms the weld metal [21].

2.3. Corrosion of Al-Mg Alloys

2.3.1. Corrosion in general

Aluminum and its alloys have good resistance to corrosion in neutral solutions, the atmospheric environment and even some acidic solutions, due to formation of a protective oxide film on their surfaces [23,24]. However, protective oxide layer generally dissolves in a low pH solutions ($pH \leq 4$) and high alkalinity solutions ($pH \geq 9$).

In acidic and high alkalinity solutions, the aluminum oxide film is attacked uniformly, resulting in general corrosion. In neutral solutions, the oxide film is attacked locally due to the corrosion potential difference between the impurities and the intermetallic particles and Al matrix leading to localized corrosion. The susceptibility of the aluminum toward localized corrosion increases with increase of chloride and oxygen

concentration, pH and solution flow rate, the presence of second phase precipitates, inclusions and grain boundary segregation and the effect of static fluctuating stress [25-27].

2.3.1.1. Pitting Corrosion

Pitting corrosion takes place on alloys that form passive films on their surfaces due to the breakdown of the protective films [24,25,27]. Pitting on aluminum alloy surface takes place in the neutral solutions of pH in the range of 4.5-8.5 pH [28]. Initiation of pitting requires the presence of oxygen, moisture, aqueous solutions and aggressive anions such as chloride, inclusions, second phases and mechanical damage sites [29]. The intermetallic particles are considered of pitting due to the difference in the corrosion potential between the particle and the aluminum matrix. Depending on the corrosion potential difference, the particles either corrode or promote dissolution of the surrounding aluminum matrix giving rise to pitting corrosion [30-32]. Pitting corrosion in the AA 5083 alloy is r related to the presence of iron-rich ($Al_6(Fe,Mn)$) and magnesium-rich (Mg_2Si and Al_3Mg_2) particles within the AA5083 alloy (Figure 2.3.1) .

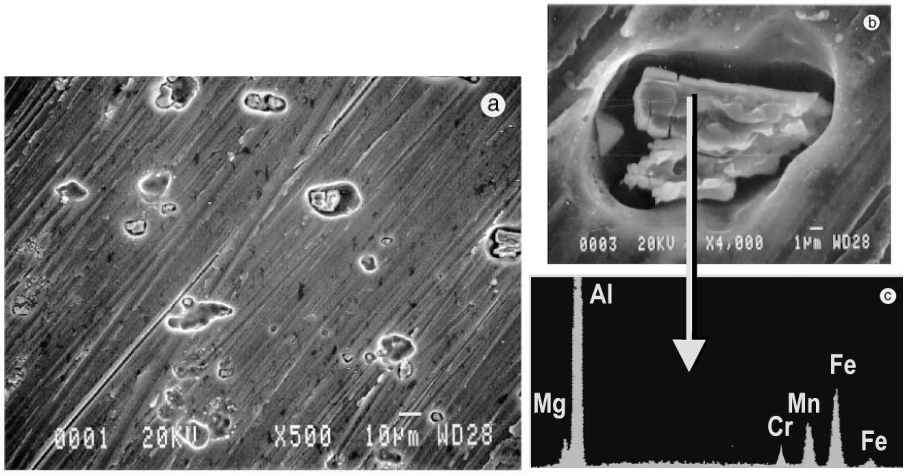


Figure 2.3.1 The effect of [Al (Mn, Fe, Cr)] on the corrosion behavior of AA5083 aluminum alloy in 3.5 wt. % NaCl solution [33].

2.3.1.2. Intergranular Corrosion (IGC)

The IGC corrosion takes place either at a grain boundaries or areas immediately adjacent due to the difference in the corrosion potential between the precipitated phase and the matrix. Depending whether the precipitated phase is anodic or cathodic with respect to the matrix, it can preferentially corrode or cause corrosion of the surrounding

matrix. The susceptibility of aluminum alloys to IGC increases with subjecting the alloy to excessive cold work and thermal cycles such those experienced during welding and heat treatment due to the change in the alloy microstructure [34]. Generally, non heat treatable AA5xxx aluminum alloys with Mg content over 3.5 wt% IGC are susceptible toward IGC due to precipitation of anodic β- phase at grain boundaries [35].

2.3.1.3. Stress Corrosion Cracking SCC– definition

SCC is a form of localized corrosion. It takes place in an intergranular or transgranular form. Initiation of SCC requires residual or applied stress and corrosive solutions. It is initiated by localized corrosion and once formed crack propagates within the velocity higher than the corrosion rate.

AA5xxx aluminum alloys are susceptible to SCC in NaCl-H_2O_2, NaCl, sea water and water vapor [5,6,33]. Susceptibility toward SCC in wrought alloys is highly anisotropic, with the direction transverse to rolling direction the most susceptible [36].

In AA5xxx aluminum alloys containing more than 3wt. % control of the heat input during welding, the alloy chemical composition and the thermo-mechanical processing can reduce the risk of the microstructure sensitization and increases its resistance to SCC [37].

2.3.1.4. Exfoliation

The exfoliation corrosion is a substrate attack that occurs in heavily cold worked that is characterized by flat and elongated grains. Selective intergranular attack takes place along the grain boundaries and due to the difference in specific volume of the corrosion product and the matrix detachment among the grains occurs, leading to separate layers of uncorroded metal [38].

2.3.2. Sensitization

AA 5083 and its derivate alloys are prone toward intergranular corrosion (IGC) and stress corrosion cracking (SCC) due to high magnesium content. At elevated temperatures, there is extensive solubility of Mg in the α (Al)-solid solution, but as temperature decreases, anodic β-phase (Al_3Mg_2) precipitates out by a complex sequence of reactions [39-41]. Due to the high mobility of Mg atoms in Al matrix, the precipitation processes occur even at room temperature albeit with extremely low rate.

The precipitation significantly accelerates at temperatures above 65°C. The process is known as sensitization and involves precipitation of Mg from supersaturated solid solution in the form of anodic β (Al_3Mg_2) phase at the grain boundaries. Sensitization effects are not common in alloys with a Mg content below 3.5 wt% since low supersaturation of the Al solid solution limits driving force for the precipitation of β (Al_3Mg_2) phase.

The β phase tends to form heterogeneously at grain boundaries and interfaces between Al_6(Mn,Fe) and Al matrix, but only the grain boundary precipitation is responsible for increased tendency toward IGC and SCC [42,43]. Deterioration of the corrosion properties occurs, in particular if the β–phase formed continuous film at the boundary. Preference of the β phase to precipitate at certain types of grain boundaries during sensitization anneal was reported in AA5182 [32] while precipitation of the β phase can affect grain boundary morphology as the presence of the film can introduce grain boundary faceting as observed in Al-6wt%Mg alloy [44,45].

Attempts to mitigate IGC and SCC susceptibility while increasing Mg content to improve the alloy strength lead to modification of AA5083 by Zn additions and design of new alloy types such as AA 5059 [46]. It has been reported that minor addition of Zn (0.68-0.7wt%) to the standard AA 5083 alloy (4.7wt%Mg) improved performance of the alloy during exfoliation testing due to the formation of more corrosion resistant τ ($Mg_{32}(Al,Zn)_{49}$) phase at the grain boundaries [23].

Kinetics and morphology of precipitation of β (Al_3Mg_2) phase is influenced not only by the chemical composition but, in a great extent, by processing of the alloy. Key factors that control precipitation of the β (Al_3Mg_2) phase in the Al-Mg alloys are considered to be sensitization temperature and time, since their increase increases fraction and continuity of the grain boundary β (Al_3Mg_2) phase [47,48]. However, a thermo-mechanical treatment has influence on β (Al_3Mg_2) phase morphology, distribution and amount of the precipitated phase, and it can alter corrosion response of Al-Mg alloys [49-51].

2.4. Welding of aluminum and its alloys

The common methods used for joining aluminum and its alloys are the solid state bonding and fusion welding processes. AA5xxx aluminum alloys can be successfully joined with both processes [52,53]. Usually, joining of aluminum and its alloys with fusion welding processes requires attention since the thermal coefficient of expansion for the aluminum is high. For this reason the heat input during joining has to be high to insure proper fusion, particularly for thick sections [54].

The principal processes used for the joining of aluminum are listed in Table 2.4.1 Welding that involves the melting and fusion of the parent metals only is known as *autogenous* welding, but many processes involve the addition of a *filler metal* which is introduced in the form of a wire or rod and melted into the joint. Together with the melted parent metal this forms the weld metal [3].

Table 2.4.1 Principal processes for the welding of aluminium [3].

Process	Application
Fusion welding	
Tungsten inert gas	High-quality, all position welding process that utilizes a non-consumable electrode; may be used with or without wire additions; may be manual, mechanized or fully automated; low deposition rate, higher with hot wire additions; straight or pulsed current.
Metallic arc inert gas shielded	High-quality, all position welding process that utilizes a continuously fed wire; may be manual, mechanized or fully automated; can be high deposition rate; twin wire additions; straight or pulsed current.
Manual metal arc	Limited application; uses a flux-coated consumable electrode; non- or lightly stressed joints; obsolescent.
Oxy-gas	Low-quality weld metal; unstressed joints; obsolescent.
Electron beam	High-quality, precision welding; aerospace/defense welding and electronic equipment; high capital cost; vacuum chamber required.
Laser welding	High-quality, precision welding; aerospace/defense and electronic equipment; high capital cost.
Electro-gas, electro-slag, submerged arc	Limited applications, e.g. large bus bars; porosity problems; largely obsolescent.

Welding with fusion and pressure	
Magnetically impelled arc butt welding	Butt joints in pipe; capital equipment required but lower cost than flash butt; fully automated.
Resistance and flash welding	
Spot, projection spot seam welding	Lap joints in sheet metal work, automotive, hollowware, aerospace industry; high capital cost; high productivity.
Weld bonding	Combination of spot welding through an adhesively bonded lap joint; automotive industry; very good fatigue strength.
High-frequency induction seam Flash butt welding	Butt joints; production of pipe from strip; high capital cost; high production rates. In line and mitre butt joints in sheet, bar and hollow sections; dissimilar metal joints, e.g. Al-Cu; high capital cost; high production rates.
Stud welding	
Condenser, capacitor discharge Drawn arc	Stud diameters 6mm max, e.g. insulating pins, pan handles, automotive trim and electrical contacts. Stud diameters 5–12mm.
Solid phase bonding	
Friction welding	Butt joints in round and rectangular bar and hollow sections; flat plate and rolled section butt welds (friction stir); dissimilar metal joints; capital equipment required.
Explosive welding	Field pipeline joints; dissimilar metal joints, surfacing.
Ultrasonic welding	Lap joints in foil; thin to thick sections; Al-Cu joints for electrical terminations.
Cold pressure welding	Lap and butt joints, e.g. Al-Cu, Al-steel, Al sheet and wire.
Hot pressure welding	Roll bonded lap joints, edge to edge butt joints.

Welding processes are essential for the manufacture of a wide variety of products, such as: frames, pressure vessels, automotive components and any product which have to be produced by welding. However, welding operations are generally expensive, require a considerable investment of time and they have to establish the appropriate welding conditions, in order to obtain an appropriate performance of the welded joint. There are a lot of welding processes, which are employed as a function of the material, the geometric characteristics of the materials, the grade of sanity desired and the application type (manual, semi-automatic or automatic). The following describes some of the most widely used welding process for aluminum alloys [55].

2.4.1. TIG welding

Tungsten arc inert gas shielded welding, EN process number 144 abbreviated to TIG, TAGS or GTAW (USA), is an arc welding process that uses a non-consumable tungsten electrode and an inert gas shield to protect the electrode, arc column and weld pool. The welding arc acts as a heat source only and the welding engineer has the choice of whether or not to add a filler wire. The weld pool is easily controlled such that unpacked root passes can be made, the arc is stable at very low welding currents enabling thin components to be welded and the process produces very good quality weld metal, although highly skilled welders are required for the best results. It has a lower travel speed and lower filler metal deposition rate than MIG welding, making it less cost effective in some situations.

TIG tends to be limited to the thinner gauges of aluminum, up to perhaps 6 mm in thickness. It has a shallower penetration into the parent metal than MIG and difficulty is sometimes encountered penetrating into corners and into the root of fillet welds.

2.4.1.1. Process principles

The basic equipment for TIG welding comprises a power source, a welding torch, a supply of an inert shield gas, a supply of filler wire and perhaps a water cooling system. A typical assembly of equipment is illustrated in Figure 2.4.1.

For welding most materials the TIG process conventionally uses direct current with the electrode connected to the negative pole of the power source. Welding on this polarity does not give efficient oxide removal. A further feature of the gas shielded arc welding processes is that the bulk of the heat is generated at the positive pole. TIG welding with the electrode connected to the positive pole [3].

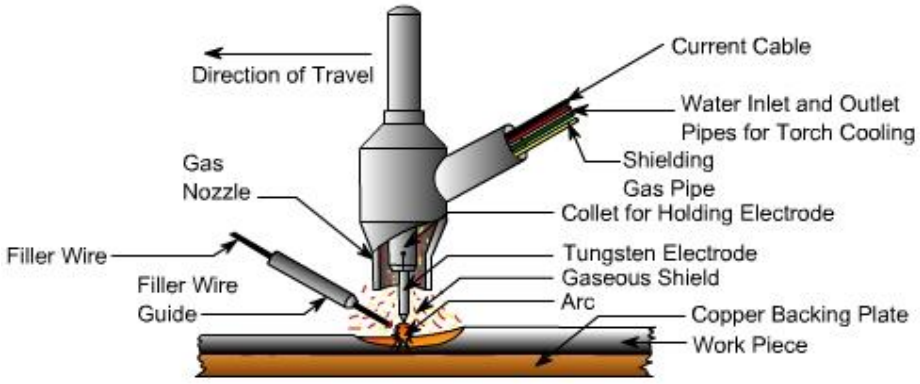


Figure 2.4.1 Principle of TIG Welding [56].

2.4.2. MIG welding

Metal inert gas welding (MIG) is a fusion welding process with a consumable wire electrode. Developed in the 1940s, it is now widely used in industrial applications and is also well understood from the scientific point of view.

The high cost of the inert gas limits its applicability to non-ferrous metals. For ferrous metals half inert gases like CO_2 may be used (MAG).

It is referred to as a semi-automatic process, since the wire length is automatically adjusted by the welding tool. This way high welding speeds can be achieved, and long continuous welds may be performed without stops.

Since it uses a gas shield to protect the welding pool during solidification, it is mostly used indoors. The gas also stabilizes the electric arc and assists in the transfer of the metal from the filler wire. Continuous current is normally used, in very few cases alternating current may also be used. Because of its versatility, MIG welding is one of the most widespread welding processes. Welding can either be done by hand or by a robot. All welding positions may be used, al- though since this is a fusion process the flat position is recommended.

In the present work, MIG welding was used in the context of the study of temperature and strain fields.

2.4.2.1. Process principles

In MIG/MAG welding method, an arc is established between a continuous fed filler wire (consumable) electrode and the work piece. The electrode is fed automatically from the machine, through a liner, then out of a contact tip in the MIG/MAG gun. The weld metal is protected from the atmosphere by a flow of an inert gas, or gas mixture. The contact tip is hot or electrically charged, when the trigger is pulled and melts the wire for the weld puddle Figure 2.4.2. After proper settings are made by the operator, the arc length is maintained at the set value, despite the reasonable changes that would be expected in the gun-to-work distance during normal operation. This automatic arc regulation is achieved in one of the two ways. The most common method is to utilize a constant-speed (but adjustable) electrode feed unit with a variable-current (constant-voltage) power source.

Welding currents of 50 amperes up to more than 600 amperes are commonly used at welding voltages of 15V to 32V [57]. As the gun-to-work relationship changes,

which instantaneously alters the arc length, the power source delivers either more current (if the arc length is decreased) or less current (if the arc length is increased). This change in current will cause an equivalent change in the electrode melt-off rate, thus maintaining the desired arc length.

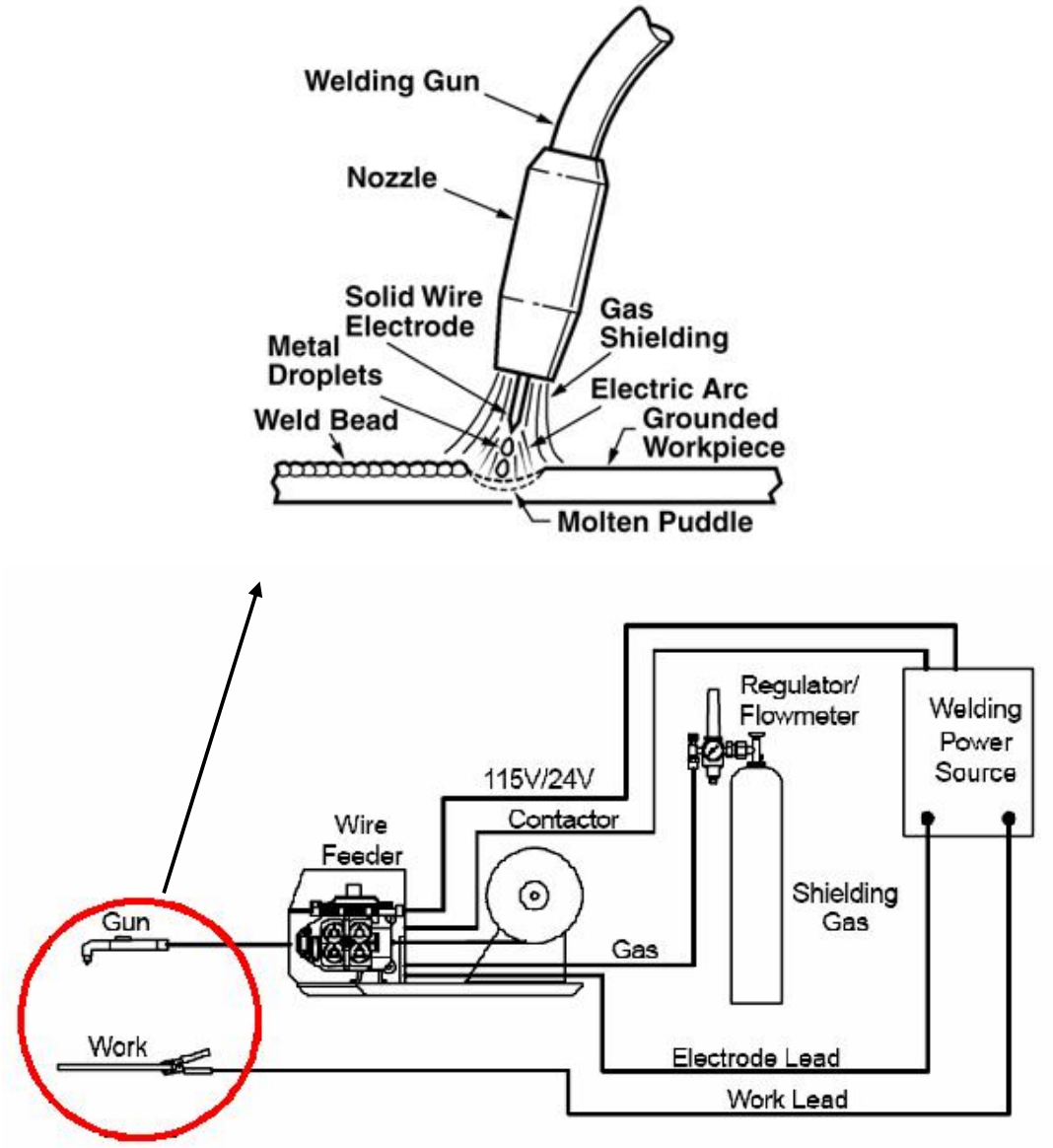


Figure 2.4.2 Typical GMAW Process Connections [57].

2.4.3. Pulsed gas metal arc welding

Pulsed arc welding is a variation of the gas metal arc welding GMAW process. With pulsed GMAW, the welding power source(s) provides a dual level welding current and provides substantially improved weld deposition control especially for out-of-

position welding applications. Both the background and the pulsed peak welding currents can be controlled separately so that the actual average welding current may be set more precisely than with the use of conventional GMAW power sources.

In pulsed spray gas metal arc welding the current is varied between a high (peak) and low (background) value. The low level of current is below the non-pulsing transition current while the high on the peak current level is well into the spray arc region, i.e. if the upper current were continuous, it would provide spray transfer and if the lower current were continuous it would produce globular transfer. Metal is transferred to the work during the peak current levels. Figure 2.4.3 illustrates the pulsed GMAW welding current cycle pattern. In the spring of 1983, most of the "off-the-shelf" pulsed arc power sources manufactured in the United States appeared to use pulse in either 60 or 120 pulses per second [58].

However, one manufacturer has recently begun manufacturing a pulse GMAW power source covering an approximate range of 50-250 pulses per second.

When using argon or argon rich mixtures or 75% helium/25% argon gas shielding with the pulsed GMAW process, a spray transfer occurs above the transition current value for a given electrode and diameter involved. As the current density at the electrode is increased, the end of the filler wire (electrode] will form into a droplet because of the "pinch effect" [58].

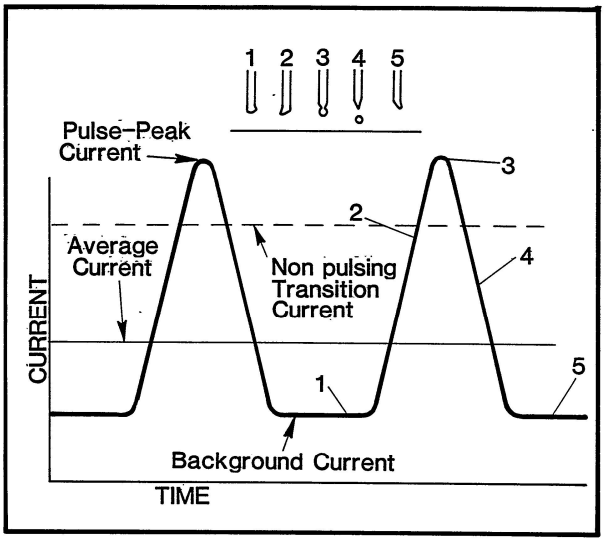


Figure 2.4.3 Typical Pulse GMAW current cycle Pattern [58].

The advantages of the pulse and "pulse short-circuiting" modes of gas metal arc welding are as follows:

- Permits the welder to make a one-side, full penetration, out-of position weld using the manual GMAW process.
- Provides cooler arc and less distortion.
- Minimizes weld spatter and undercutting.
- Permits the out-of-position welding of thin sheet materials, e.g. .063 inch thicknesses of aluminum alloy sheet.
- Permits spray transfer welding at average currents below those normally possible.
- Provides improved arc control for out-of-position welding and more effective welding of thin gauge material, with all the advantages of spray transfer, i.e. minimizes excessive weld puddle fluidity.
- Permits use of larger diameter electrode wires which cost less, feed easier and also have a lower surface-to-volume ratio which reduces the possibility of weld porosity and, in some cases, weld cracking.
- Provides precision control of current to assure bead shape and root penetration approaching GTAW quality.

2.4.4. Welding energy and heat input

In GMAW a sufficient amount of power (energy transferred per unit time) and energy density is supplied to the electrode and this cause melting. Heat input is a relative measure of the energy transferred per unit length of weld. It is an important characteristic because it influences the cooling rate, which may affect the mechanical properties and metallurgical structure of the weld and the HAZ Figure 2.4.4.

Heat input is typically calculated as the ratio of the power (i.e., voltage x current) to the velocity of the heat source as follows: [59]

$$Q = \frac{60EI}{1000V}\eta$$

Q = Heat input (kJ/mm)

E =Welding voltage (volts)

I = welding current (amps)

V = Travel speed (mm/min)

η = efficiency factor for GMAW is 0.8 [35].

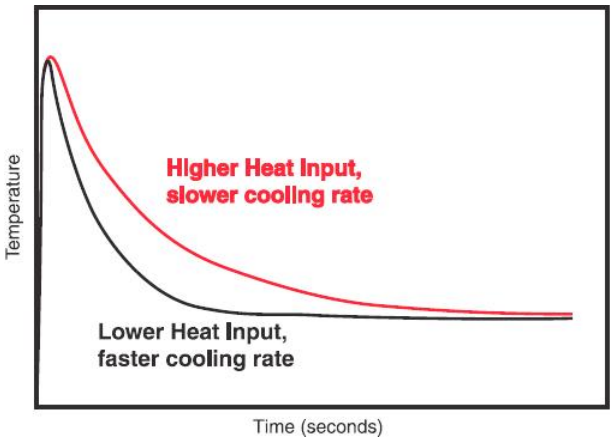


Figure 2.4.4 Heat input influences cooling rate [59].

The above equation is useful for comparing different welding procedures for a given welding process.

Heat input increases, the rate of cooling decreases for a given base metal thickness. These two variables interact with others such as material thickness; specify heat, density and thermal conductivity [59].

The thermal diffusivity of the base material plays a large role in the HAZ, if the diffusivity is high, the material cooling rate is high and the HAZ is relatively small. Conversely, a low diffusivity leads to slower cooling and a larger HAZ [60].

2.4.5. Mechanical Properties for 5xxx series Aluminium Alloy sheet and Plate Butt Welds (As-Welded Condition)

The non-heat treatable 5000 series aluminum alloys depend upon chemical composition and cold working or strain hardening for their mechanical properties. Welding primarily affects these alloys by annealing. When welding heat input is increased, the width of the heat-affected-zone (HAZ) is increased. Significant changes in-weld metal strength occurs as heat input varies by welding techniques. It has been reported that yield strength (MPa) could vary from 240MPa for stringer type weld beads to 207 MPa for tide weave type weld deposits. The mechanical properties of a weld decrease with increased total heat input.

2.4.5.1. Aluminium oxide film

The passive film (Al_2O_3) forms from reaction of aluminum with oxygen and aqueous solutions. It forms according to the following reaction:

$4\ Al + 3\ O_2 \longrightarrow 2\ Al_2O_3$

$2Al(s) + 3H_2O\ (l) \rightarrow Al_2O_{3(s)} + 6H^+_{(aq)} + 6e^-$

The thickness of the oxide film in air and aqueous solutions at room temperature is about 2-3 nm and increases with oxidation at temperatures below 425˚C to 20 nm [61].

The formed film is characterized by its ability to self-repair once scratched or mechanically damaged. With anodizing, the thickness of the oxide film can reach 10-20 μm [62].

The film contains two layers known as inner and outer oxide layers. The inner layer has an amorphous structure and it is thinner and less permeable than the outer hydrated oxide layer. The thickness of the inner layer increases with increase of the oxygen pressure and the solution temperature.

The oxide film does dissolve in both acidic and high alkalinity solutions according to the reactions:

$Al_2O_3(s) + 6H^+_{(aq)} \rightarrow 2Al^{3+}_{(aq)} + 3H_2O_{(l)}$ in acidic solution.

$Al_2O_3(s) + 3H_2O_{(l)} + 2OH^-_{(aq)} \rightarrow 2Al(OH)_4^-{}_{(aq)}$ in alkaline solution.

On the contrary, in neutral solutions, the oxide film is stable and functions as a barrier between the aluminum substrate and the surrounding environment. Thus, it inhibits passage of electrons and protects the aluminum substrate from the attack of aggressive solutions. Unfortunately, the aluminum oxide film does contain flaws and or defects caused by the heat treatment and the fabrication processes [61]. The latter tend to create roughness and cracks within the oxide film giving accessibility to the surrounding solution aggressive species such as Cl^-, Br^-, I^- ion that penetrate through the defective locations within the oxide film to the aluminum substrate and attack the substrate locally causing pitting [24,62,63].

Further, the impurities picked up from the lubricant during rolling processes may have a different chemical behavior from the surrounding areas, resulting in initiation of localized corrosion in the form of pitting that is driven by the corrosion potential variation [62]. Figure 2.4.5 demonstrates possible flaws and defects that may exist within the aluminum oxide film.

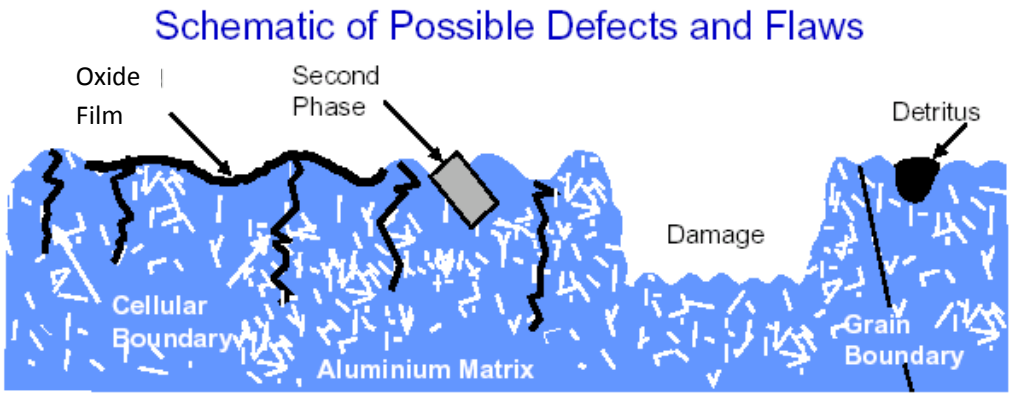


Figure 2.4.5 Possible flaws and defects within the aluminium oxide film [54].

2.4.5.2. Heat affected zone (HAZ)

The HAZ is a part of the base alloy which is metallurgically affected by the heat of welding, without possessing solid to liquid transformation. The HAZ is generated in all welding processes due to the effect of the heat generated from welding. In some cases, it can be observed by the naked eye in arc welds rather than in the friction stir welds, due to the variation in the heat input between the two processes [64].

In fusion welding processes, the width of the HAZ is governed by the material, welding parameters and the welding process. With a higher material thermal diffusivity and a higher cooling rate, a smaller HAZ is expected and vice versa. The heat input increases with the increase in the current, voltage and the process efficiency. The efficiency is variable from one process to another. It is approximately 0.8 for shielded arc welding process, 0.4-0.6 for the tungsten arc welding process and 0.95 for the submerged arc welding [65].

$$Q = \frac{E \times I}{S \times 60} \div 1000$$

Where, Q is the heat input (kJ/mm), E is the applied voltage (V), I is the applied current (A), and (S) is the welding speed (mm/min) [66].

In the case of the friction stir welding, the HAZ width is influenced by the tool size and rotation speed.

2.4.5.3. The parent alloy

The parent alloy is the part of the component that is not metallurgically affected by the welding process. It represents the original alloy microstructure.

2.4.6. Welding of 5083 aluminum

Arc welding is the most widely used process in the shipbuilding, aerospace, pipeline, pressure vessel, automotive and structural industries. With a pulsed power supply, the metal transfer from the tip of the electrode wire to the work piece during GMAW is controlled [67-69].

The weld penetration, bead geometry, deposition rate and overall quality of the weld are also affected to a large extent by the welding current, arc voltage (as determined by the arc length), travel speed, electrode extension, electrode orientation (or gun angle) and the electrode diameter. Excessive arc voltages or high arc lengths promote porosity, undercut and spatter, whereas low voltages favor narrow weld beads with higher crowns. The travel speed affects the weld geometry, with lower travel speeds favoring increased penetration and deposition rates. Excessively high travel speeds reduce penetration and deposition rate, and may promote the occurrence of undercut at the weld toes [70]. The mechanical properties of the welded joint, the weld geometry, occurrence of flaws and level of residual stress after welding depend mainly on the joining process, welding consumable and procedure employed.

2.4.6.1. Structure of the welds

The filler metal and the melted-back base metal form an admixture. The properties of the weld, such as strength, ductility, resistance to cracking and corrosion resistance, are strongly affected by the level of dilution. The dilution, in turn, depends on the joint design, welding process and parameters used. Joint preparations such as single or double V-grooves are often preferred to square edge joint preparations when welding crack susceptible material with non-matching filler metal [71].

The thermal cycle experienced by the metal during welding results in various zones that display different microstructures and chemical compositions. The fusion zone (composite zone or weld metal) melts during welding and experiences complete mixing to produce a weld with a composition intermediate between that of the melted-back base metal and the deposited filler [70].

Most welds contain discontinuities or flaws that may be design or weld related, with the latter category including defects such as undercut, slag or oxide inclusions, porosity, overlap, shrinkage voids, lack of fusion, lack of penetration, craters, spatter,

arc strikes and under fill. Metallurgical imperfections such as cracks, fissures, chemical segregation and lamellar tearing may also be present.

Aluminium welds are also very susceptible to hydrogen-induced porosity. The weld pool may dissolve large amount of hydrogen from the arc atmosphere. On solidification, the solubility of hydrogen decreases and the entrapped hydrogen forms gas porosity. Typical sources of hydrogen contamination are lubricant residues, moisture and the hydrated surface oxide on the base metal or filler wire surface. These defects act as stress concentrations and may lead to rapid fatigue crack initiation if the weld is exposed to fluctuating stresses of sufficient magnitude [71,72].

Most weld flaws can be removed by grinding, machining and/or flush polishing, thereby improving the mechanical properties, corrosion resistance and fatigue properties of the joint. Subsurface flaws, which are more prevalent during SA-GMAW than FA-GMAW, are more difficult to detect and correct.

2.4.6.2. Mechanical properties of welded 5083 aluminum

Aluminium alloys 5083, produced via ingot casting, and cold working, contain precipitates that interact with moving dislocations, thus increasing strength at room temperature. When these alloys are welded, however, the precipitates dissolve and/or coarsen, reducing the mechanical strength significantly. This reduction in mechanical properties can be attributed to annealing and recrystallization, grain growth and precipitate dissolution and/or over ageing; and uncontrolled grain boundary precipitation on cooling [73].

The HAZ of 5083 aluminum alloy is completely annealed and recrystallized during welding. The effect of any prior work hardening is lost when such an alloy is exposed to a temperature above 343°C for only few seconds. A reduction in hardness is therefore observed in the HAZ [73]. The degree of softening is mainly affected by the heat input, the welding technique, the size of the work piece and the rate of cooling. Low heat input levels reduce the time at temperature and increase the cooling rate, thereby minimizing the degree of softening in the HAZ. Pulsed GMAW has the advantage of ensuring good penetration and adequate fusion at lower average heat input levels [70]. The amount of grain growth is reduced and the width of the HAZ minimized.

2.4.7. Aluminium alloy filler wires

In general, for welding 5000 series aluminum alloy sheet and plate, the Plans (Drawings) will, unless otherwise specified, permit the fabricator to use interchangeably ER 5183, 5356 or 5556 per ASTM/AWS 5.10, "Specification for Aluminium and Aluminium Alloy Bare Welding Rods and Electrodes."

The prefix ER is used by AWS to denote "Electrode/Rod" to cover both the gas metal arc welding GMAW or the gas tungsten arc welding GTAW process.

The weld is a composite or alloy of the filler material and the base material. This composite largely determines the mechanical properties of the weld. Also, the gas metal arc process does leave an annealed condition weld area. Weld joint configuration, weld filler wire types and welding techniques are other variables that must be considered.

High magnesium gas metal arc filler wires such as ER 5183, 5356 and 5556 generally produce strong ductile welds [71].

Usually the "as welded" tensile strengths of the 5000 series aluminum magnesium alloy welds are equal to the strength of the annealed base material. The only way to strengthen "as welded" tensile strength in 5000 series aluminum is to cold work, e.g. roll-planishing, which is not practical in a shipyard setting.

All aluminum alloy filler materials when opened were kept in a dry warm storage box.

2.4.8. Weldability of aluminum 5083

Pure aluminum exhibits high electrical conductivity, about 62% of that of pure copper. Very little resistance heating occurs during welding, and high heat inputs are therefore necessitated when joining aluminum and its alloys to ensure complete fusion. Incomplete fusion may also result from the presence of a hydrated aluminum oxide layer that forms spontaneously on exposure to air or water due to the strong chemical affinity of aluminum for oxygen. This layer melts at about 2050°C, significantly above the melting range of aluminum. In order to prevent poor fusion, the aluminum oxide layer needs to be removed prior to or during welding. Suitable fluxes, chemical or mechanical cleaning methods, or the cleaning action of the welding arc in an inert atmosphere (cathodic cleaning) can be used to remove the oxide [70]. The high thermal expansion coefficient of aluminum (about twice that of steel) may result in distortion and high levels of residual stress in the welds, and precautions need to be taken to control distortion to within acceptable limits.

There are four approaches regarding assessment of weldability of aluminum alloys: resistance of the material to the formation of cracks (hot and cold), reduction of mechanical properties in HAZ, reduction of corrosion susceptibility and increasing porosity.

The weldability of aluminum, defined as the resistance of the material to the formation of cracks during welding, is affected by the physical properties, chemical composition and prior temper state of the material [70,71]. As long as dilution is controlled to a minimum, these alloys can, however, be welded successfully using non-matching filler metal.

A dissimilar filler metal with a lower solidus temperature than the base metal is generally employed so that the hardenable base metal is allowed to completely solidify and develop some strength along the fusion line before weld solidification stresses develop. Contraction stresses, which could cause cracking, are relieved by the plasticity of the still liquid filler metal, preventing the formation of cracks [71].

2.4.9. Corrosion of 5083 welds

The passive oxide films, spontaneously formed on aluminum alloy surfaces, are however, susceptible to localized breakdown at the exposed surface or at discontinuities, which result in high dissolution rates of the underlying metal (pitting corrosion). The chemical composition of the weld metal and HAZ and the presence of inclusions, precipitates and second phases in the welded joint, however, produce slightly different electrode potentials in the presence of an electrolyte. Selective or localized corrosion is therefore possible when the base metal and the weld metal or second phases possess significantly different electrode potentials. A galvanic effect can be created, with the more active region corroding preferentially to protect the more noble region with which it is in contact [70,71,74].

Welds produced by the GMAW process appear to be less resistant to pitting corrosion in salt water solutions than solid state friction stir welds, as reported by Moggiolino and Schmid [75]. Preferential attack occurs in the narrow interface between the weld bead and the HAZ, or between the HAZ and the base metal. As a result of the high peak temperatures experienced by the high temperature HAZ adjacent to the fusion line, grain coarsening, recrystallization and partial dissolution of intermetallic strengthening precipitates occurring during welding.

2.4.10. Testing Methods for Welded Joints

Destructive testing (DT) and non destructive testing (NDT) are the main testing methods used to determine the presence of cracks, fusion defects, inclusions and pores. In the field of NDT for Al-alloy visual inspection, radiographic examination, die penetration are usually applied, while for the Mechanical testing the main tests used for Al alloys are Bending test, Tensile test, Hardness test and sharpy test.

Macro and Micro structure examination usually used for determination of phase transformation and appearance of micro structure compounds.

There are many technological tests for assessment of cracks susceptibility of Al alloy weldments. The most used are FISCO test and Warenstain test.

The Corrosion tests used for Al-Mg alloys are Intergranular Corrosion (IGC) and Exfoliation Corrosion

2.4.11. Susceptibility of hot cracks - FISCO test

Pair of test pieces are clamped firmly with uniform bolting moment in a FISCO tester as shown in Figure 2.4.6 to form a joint with one of the following preparations: square butt single V groove with broad root face, single U groove with vertical sides, the root gap being from 1 to 4 mm. Three to four test beads, each 40 to 50 mm long, are deposited from left to right, one after the other or after the cooling of each bead to a temperature lower than 50 °C. No crater filling is used. The specimen is kept clamped in the clamping FISCO tester for approximately 5 to 10 minutes (in some cases for several days). The evaluation of the cracking is usually carried out visually, after fracture of the weld seams by bending the welded plates, either by hammering or by pressing.

Measured values were the length of detected hot cracks and overall length of weldment. After measuring the length of revealed hot cracks on FISCO test samples, a part (percentage) of cracks in overall length of weldments was calculated.

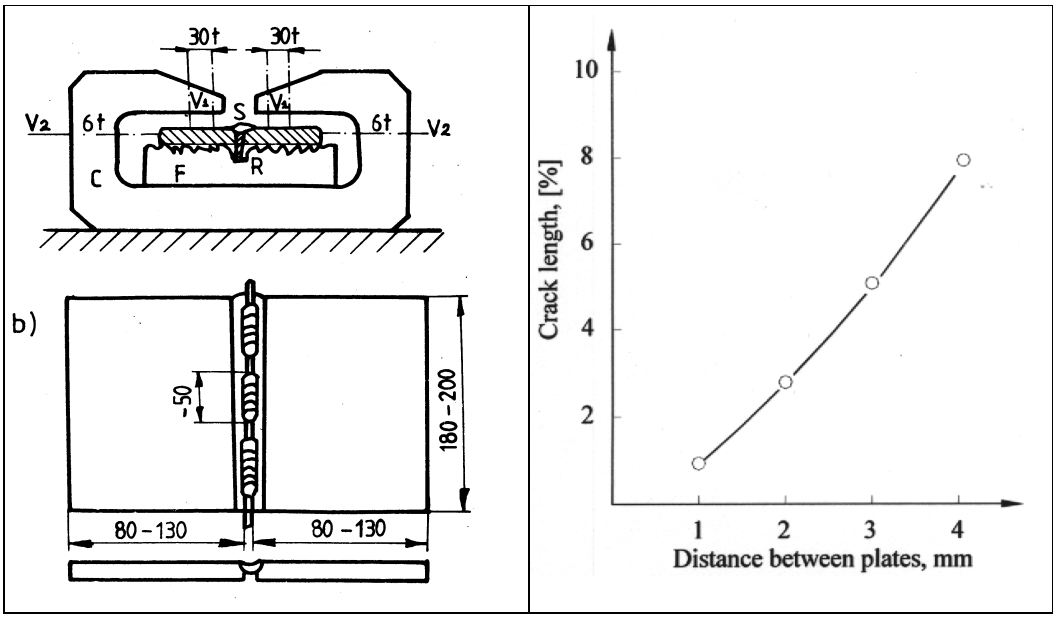


Figure 2.4.6 FISCO test for hot cracks

CHAPTER 3

3. Experimental Part

3.1. Material

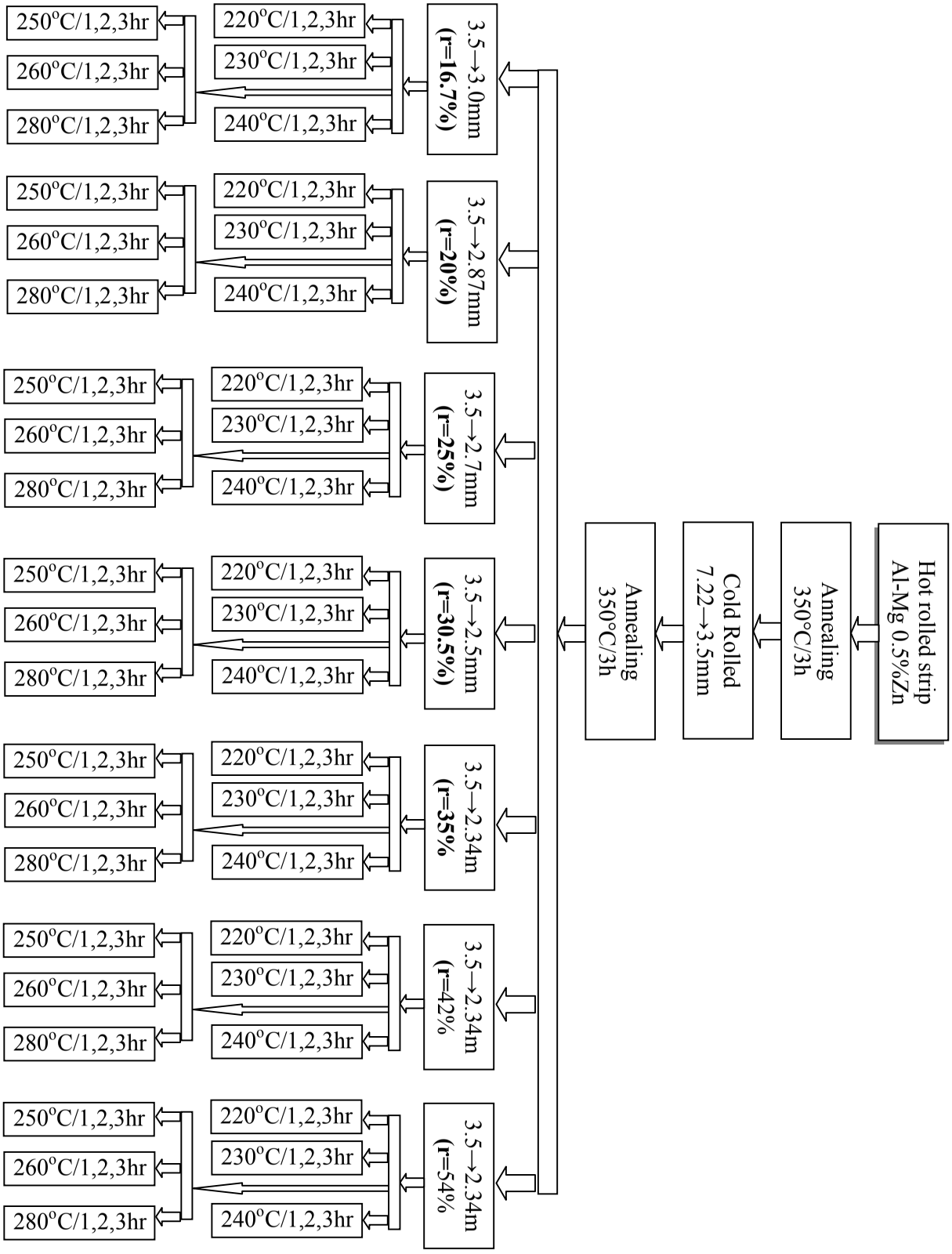
The studied alloy was a modified Al-Mg alloy of an AA 5083 type. The chemical composition of the alloy is given in Table 3.1.1. Magnesium (Mg) and Zinc (Zn) levels were higher than in the standard AA5083 alloy; actually, the composition was within the lower limits of an AA5059 alloy (Table 3.1.1)

Table 3.1.1 Chemical compositions of the studied alloy and Standard AA5083 and AA5059 alloys (weight percent).

Alloy	Mg	Mn	Cu	Fe	Si	Zn	Cr	Ti	Sr	Zr
Study	5.13	0.718	0.013	0.337	0.108	0.513	0.008	0.025	0.003	0.0202
AA5083	4-4.9	0.4-1	0.1	0.4	0.4	0.25	0.05-0.25	0.15	0.005	0.05
AA5059	5-6	0.6-1.2	0.25	0.5	0.45	0.4-0.9	0.25	0.2	0.05	0.05-0.25

The material, supplied by IMPOL-SEVAL Rolling Mill, was industrially cast and hot rolled (HR) to 7.4 mm thick plates. Further processing of the alloy was conducted in the in laboratory conditions with a goal to develop schedule for attaining the H321 state in the 5083 type alloys, which is defined in US Standard : B 928/B 928M-04a standard [76].

Figure 3.2.1 Chart of the lab processing route of the as-received specimens



3.2. Thermo-mechanical treatment

Chart of the lab processing route of the as-received industrially hot rolled 7.4 mm thick plates is presented in Figure 3.2.1.

The processing involved laboratory cold rolling to the plate thickness of 3.5 mm followed with an intermediate annealing at 350 °C for 3 h. Subsequent cold rolling involved reductions in the range 15-50%. Final annealing was conducted at various temperatures in the range 220-280 °C for 1h, 2h and 3h.

In order to evaluate effect of sensitization treatment on susceptibility of selected states toward intergranular corrosion (IGC), selected specimens were annealed at 100 °C and 150 °C for 7 and 25 days. Selection of the states was based on the results of IGC testing after the final anneal.

3.2.1. Cold rolling

Range of cold rolling reductions was selected to evaluate effect of deformation degree on mechanical properties, microstructure and, consequently, corrosion properties of the alloy in order to define optimal thermo-mechanical treatment for attaining H321 state.

3.2.2. Thermal treatment

In order to produce fully recrystallized microstructure and accomplish complete dissolution of β (Al_2Mg_3) phase, that was eventually present in the microstructure of the as-received material, intermediate annealing was performed at 350 °C for 3 h.

Final annealing was performed at various temperatures (220-280 °C) and times (1-3h) in order to induce different extent of recovery in the microstructure. Moreover, in that temperature range, precipitation of β (Al_2Mg_3) phase occurs as the temperatures are beyond the β solvus for an alloy of given composition [76]. Amount of precipitated phase as well as precipitation mechanism was dependant on the annealing conditions.

In order to cause/simulate sensitization of the alloy, annealing at 100 °C and 150 °C was performed. Times selected for the treatment were sufficient to achieve sensitization effect, i.e. IGC susceptibility according to literature [77,78].

Thermal treatment was conducted in air-circulating furnace, brand name. After all annealing treatment stages (intermediate, final and sensitization) specimens were cooled in the air.

3.3. Testing methods

3.3.1. Mechanical testing

3.3.1.1. Tensile test

Evaluation of an effect of different cold reductions on strenght and ductility of the alloy was performed by tesile testing on as-recived and cold rolled specimens as well as selected states after the final annealing.

Uniaxial tensile testing was performed on servo-hydraulic testing machine INSTRON Model 1332 at the room temperature. Tensile testing was conducted at constant cross head velocity of 3 mm/min, giving an initial true strain rate of $\dot{\varepsilon}_1 = 6.7\times10^{-3}/\ s^{-1}$.

Table 3.3.1 Dimension of the samples for tensile test.

Nomenclature	Designation	Dimension (mm)
Width	W	20
Radius of fillet	R	13
Over-all length	L	210
Length of reduced section	A	70
Width of grip section	C	12.5
Gage length	G	30

The tensile test specimens were transverse to the rolling direction (L-T orientation). The tensile test samples had a dog-bone geometry (Figure 3.3.1). The dimensions of the specimens (Table 3.1.2) were according to ASTM E8 standard [89].

Load, crosshead displacement, and gage length strain were measured as raw data. The engineering stress-strain as well as true stress-strain curves were extracted from the test data. For each state, corresponding to different % reduction, were performed at least two tensile tests.

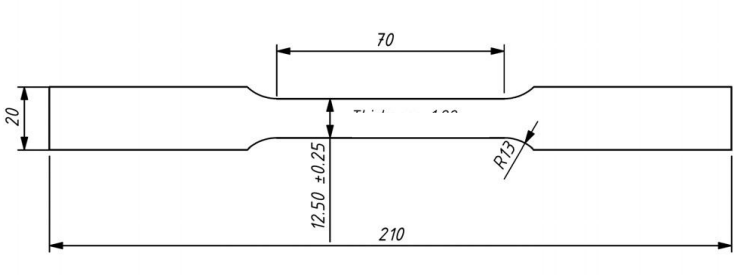


Figure 3.3.1 Schematics of a tensile test specimen.

3.3.1.2. Hardness measurements

Hardness measurements (Brinell) were conducted for all processing conditions (% reduction, annealing temperature and time of annealing).

Since the alloy was in the border line region for a loading weight selection, measurements were performed with two weights and results were compared. The measurements using the weight 250 kg were performed in VEB (Werkstoffprüfmaschinen Leipzig) instrument while measurements using the weight 100 kg were performed in HB portable device with a 2.5mm diameter ball.

Specimens for the hardness measurements were prepared by grinding the surface down to 240 SiC paper. Measurements were performed at least 5 times for each specimens and averages were used as a data points.

3.3.2. Electrical resistivity measurements

In order to evaluate the effect of different thermo-mechanical treatments on microstructure, electrical resistivity measurements were conducted. Electrical properties such as electrical resistivity are very sensitive to the presence of defects in a crystalline material. In alloys, changes in electrical resistivity can be used to detect changes in a solute content in the alloy matrix, i.e. to follow precipitation/dissolution processes [89-91]. In this work, electrical resistivity measurements were employed to follow changes in the Mg solute content in the Al matrix due to the precipitation during different thermo-mechanical treatments.

The conductivity / resistivity measurements were performed using Foerster Sigmatest 2.069 equipment with operating frequency of f = 120 kHz.

3.3.3. Corrosion testing

Major forms of corrosion in Al-Mg alloys with magnesium content over 3.5 wt% are: intergranular corrosion (IGC), stress corrosion cracking (SCC), pitting and exfoliation corrosion. They are caused by a precipitation of β- (Al_2Mg_3) phase that is more anodic than aluminium matrix. Susceptibility of the Al-Mg alloy toward these forms of corrosion depend strongly on the microstructure developed during thermo-mechanical treatment.

In this study susceptibility toward IGC as well as pitting corrosion and exfoliation was evaluated.

3.3.3.1. Nitric Acid Mass Loss Testing

Nitric acid mass lost test (NAMLT) according to ASTM G67-93 standard [92] represents quantitative measurement of susceptibility toward IGC of Al-Mg alloys. The NAMLT procedure consists of immersion of the specimens into concentrated nitric acid (HNO_3) at 30 °C for 24 h. The mass of the specimen was measured before and after the immersion into the acid and calculated difference, the mass lost, is correlated to IGC susceptibility.

According the standard, if the mass loss is below 15 mg/cm^2, the specimen is considered resistant toward IGC. On the hand, the mass loss greater of 25 mg/cm^2 characterizes IGC susceptible states. In the intermediate range 15-25 mg/cm^2, a further metallographic examination is required to asses extent of IHC.

Specimens for the NAMLT had dimensions of 50 mm (along the longitudinal direction) x 6mm while thickness was 3mm and less depending on % reduction. According the standard the specimen thickness must be less than 25mm. Specimens were immersed in 5% NaOH at 80 °C for 1 min, then washed in concentrated nitric acid for 30 s, rinsed with distilled water, and allowed to air dry. At least 3 specimens were tested for each state.

3.3.3.2. ASSET Test (ASTM G66)

Susceptibility toward exfoliation and pitting corrosion was determined by a visual inspection following the ASSET method described in ASTM G66 standard [93].

The specimens were cut and all the surfaces were machined to the final dimensions 40 mm by 100 mm. The 40 mm dimension was parallel to the longitudinal direction, i.e. rolling direction, of the plate. The thickness of the specimens varied, depending on the % reduction. Specimens thicker than 2.5 mm were machined with minimum milling of 10% of the original thickness.

Prior to the test, specimens were etched for 1 min in 5 wt% sodium hydroxide (NaCl) solution at 80 ºC, rinsed in water, immersed for 30 seconds in concentrated nitric acid (HNO_3) at room temperature, rinsed with distilled water, and allowed to air dry. Afterwards specimens were fully immersed vertically into the test solution at 65 ± 1°C for 24 hours.

The test solution contained ammonium chloride (NH_4Cl), ammonium nitrite (NH_4NO_2), ammonium tartrate ($C_4H_{12}N_2O_6$), and hydrogen peroxide (H_2O_2). A standard

pH of the solution was between 5.2-5.4. A fresh solution was used at the start of each new test. The quantity of solution was always sufficient to provide a volume-to-exposed sample surface area ratio at least 100 L/m^2.

Exfoliation and pitting corrosion susceptibility was ranked by visual inspection, according to ASTM G66 standard, using the following letters to describe the degree of pitting corrosion: N - no appreciable attack or A, B and C level (A and B are acceptable, C is susceptible). In case of exfoliation corrosion (beside N) the ratings are as follows: A, B, C and D (A and B are acceptable, C and D are susceptible). Combination of two letters was used in many cases when the surface morphology could not be described by one letter due to mixed or boundary type surface appearance with respect to standard photographs given in ASTM G66 standard.

3.3.4. Microstructure characterization

3.3.4.1. Optical (light) microscopy

Microstructure characterization by optical microscopy was performed using Olymus BHM optical microscope with a digital image capture system. Magnification range of the microscope was 5-1000X.

Specimens were sectioned in the longitudinal (L), long-transverse (T) and short-transverse (S) directions and cold mounted into a epoxy resin. Specimen preparation for the metallographic characterization involved mechanical grinding by silicon-carbon paper (600 - 2000 μm) followed by fine polishing with 10, 3, 1 and 0.5 μm diamond paste.

Specimens used for grain size characterization were electrolyticaly etched in Barkers reagent, at U =15V I =3 amp. Characterization was conducted in polarized ilumination while grain size was determined by linear intercept method.

Precipitation of the β (Al_2Mg_3) phase at the grain boundaries was revealed by etching in 10% orthophosphoric acid at 50 °C for 20 s.

3.3.4.2. Scanning Electron Microscopy (SEM)

Scanning electron microscopy characterization was conducted in JEOL JSM-6610LV microscope at 20 kV. The SEM was equipped with Oxford INCA energy dispersive X-ray spectroscopy (EDS) system.

Characterization of distribution and identification of constituent particles was performed in SEM/EDS for selected states, i.e. 16% and 42% reductions. Specimens were prepared by fine mechanical polishing following the procedure for metallographic characterization described in the section 3.3.4.1.

For selected states (16% and 42% reductions + annealing 2h/240 °C), surface morphology after exposure to a nitric acid for various times (τ=2, 6, 24h) was characterized.

3.3.4.3. Transmission Electron Microscopy (TEM)

Thin foils for the TEM characterization were prepared from specimens that underwent 16 and 42 % reductions by cold rolling and were subsequently annealed for 2h at 240 °C. Those two states were selected on the basis of very different corrosion response.

TEM specimens were prepared by mechanical thinning, dimple grinding and ion milling. Ion milling was conducted at 5 keV and incidence angle of 5° till perforation while further cleaning was done at 1 and 0.5 keV. The specimen holder was cooled with liquid nitrogen during the ion-milling to avoid any overheating. Specimens were characterized in JEOL 100 CX and Phillips CM200 microscopes, at 100keV and 200keV, respectively. CM200 was equipped with EDS detector.

Ion-milling is non-traditional preparation method for metallic specimens. However, there are reports [42,94] of dissolution and amorphisation of anodic β (Al_3Mg_2) phase if the specimens were prepared by traditional electro-polishing. Since morphology and composition of the precipitated β (Al_3Mg_2) phase were crucial for this work, specimens were ion-milled.

3.4 Welding procedure

Flat aluminium sheets (with initial dimensions of 200 mm long, 100 mm wide and 4.5 mm thick) of aluminium alloy 5083 which was produced according to the processing shown in Figure 3.4.1 were supplied for examination. These samples were welded in a horizontal position using four different types of welding processes (TIG, pulsed TIG, MIG and pulsed MIG). All welds were performed with a square edge preparation. The aluminium filler wires was used, namely AWS A5.10/ER5183 (Al-Mg) with 1.2mm thickness.

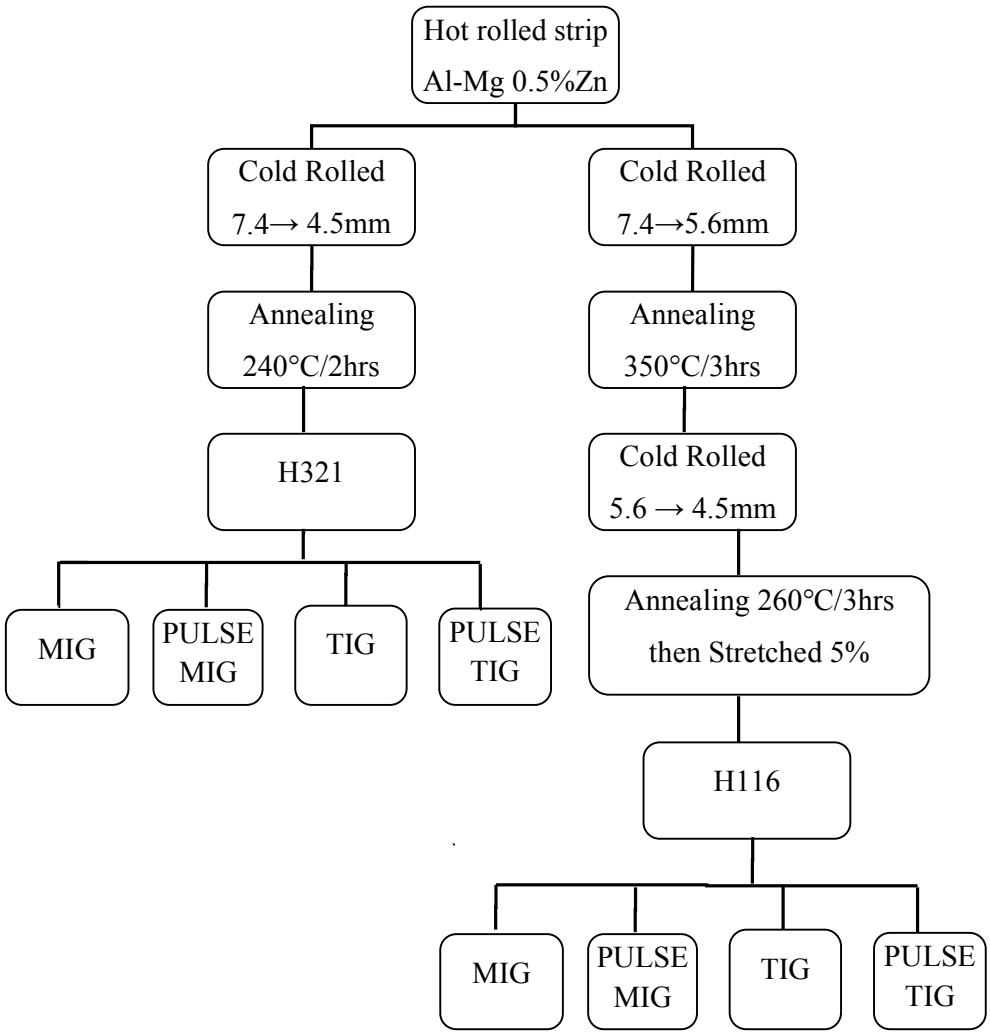


Figure 3.4.1 Material processing of welded samples

MIG welding was undertaken with AA 5183 filler rod of 1.2 mm diameter, shielding was provided by argon gas at a flow rate of 15 $L.min^{-1}$ and a mechanised

process was employed. The welding current, arc voltage and travel speed determine the heat input (HI) during welding. This relationship is shown in equation (1);

$$HI = \eta \frac{V \cdot I}{\nu} \qquad \text{eq.(1)}$$

where: V is the arc voltage (V), I is the welding current (A), ν is the travel speed, and η is the arc efficiency factor (typically in the region of 0.7 to 0.8 for GMAW). The welding parameters were selected to ensure a spray transfer mode for all the welds, and are given in Table 3.4.1.

Table 3.4.1 Welding parameters of the welded samples

Specimen No.	Voltage Volts	Current amp.	Time sec.	Wire Speed m/min	Speed mm/min	Heat Input kJ/mm
M1-1	20	127	44	6.8	218.18	0.6985
M3-1	20	127	43	6.8	223.26	0.6826
MP1-1	21.5	127	30	8	320	0.51197
MP3-1	21.5	127	30	8	320	0.51196
MP3-2	21.5	127	30	8	320	0.51197
T1-1	14.5	220	45	-	213.33	0.89718
T1-2	14.5	220	55	-	174.55	1.09656
T3-1	14.5	220	40	-	240	0.7975
TP1-1	13.5	200	66	-	145.45	1.11375
TP3-1	13.5	200	65	-	175.39	0.92368

Pass Length is 190 mm and for MIG welding gap length is 3mm

Used jigs and fixtures Figure 3.4.2 shows the jig and fixture used to hold and retain the components in the correct alignment. The use of rigid restraints will give increased levels of residual stress and may increase the risk of cracking. Jigs need to be designed to provide good access for welding, to be rigid and robust, to be foolproof in use and to be well maintained to ensure that wear is taken into account and tolerances are achieved.



Figure 3.4.2 Jigging of plates to maintain flatness.

3.4.1 Material characterization

In order to analyse the welded samples and to quantify the material properties that may influence, the microstructures of the as-welded specimens were analysed, the hardness was measured and tensile and bending tests were performed. The corrosion resistance was evaluated using immersion test and exfoilation and pitting corrosion tests.

As-welded samples were tested using radiographic eximination in order to identify volume defects in welded joints and then sectioned and machined to produce tensile and bending specimens, with dimensions shown schematically in Figure 3.4.3. Samples were removed for microstructural examination in the long transverse (LT) direction. Samples were prepared for microstructural analysis and etched using Keller's reagent as described in ASTM standard E340 [88]. The metallographic samples were examined with an inverted optical microscope (with Image-Pro PLUS 5.1™ or IMAGEJ™ image analysis software).

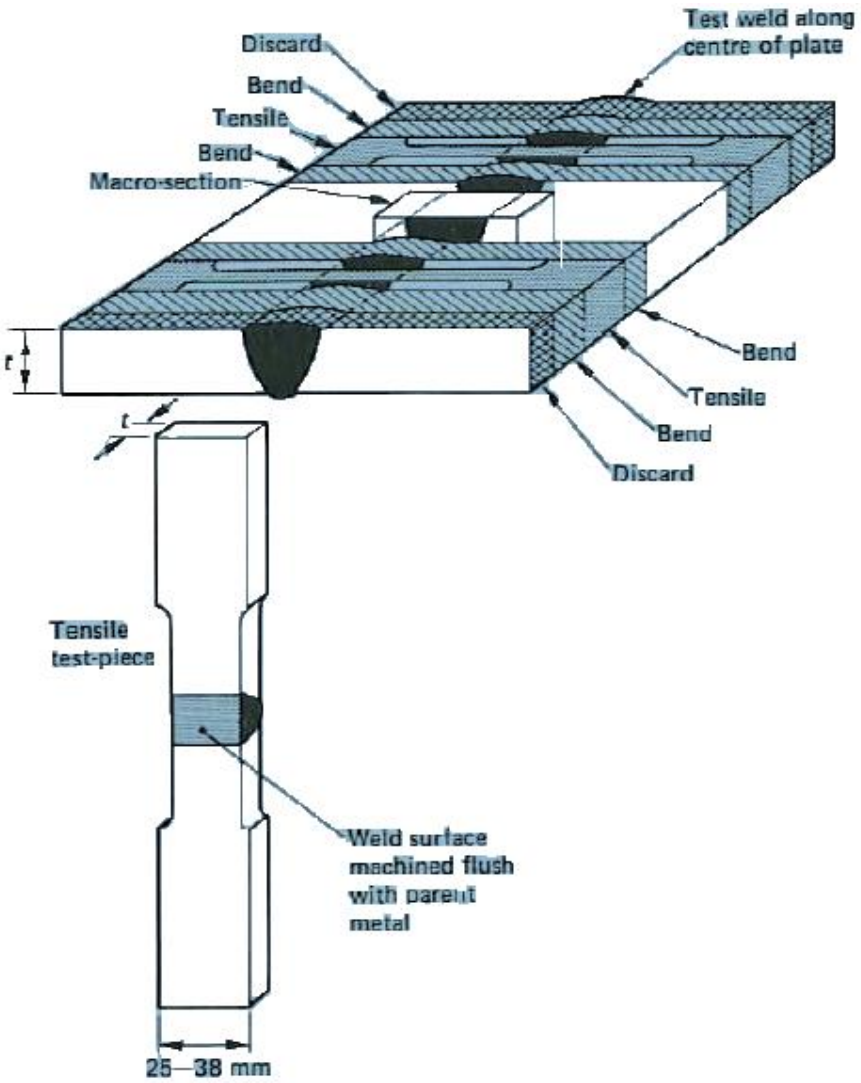


Figure 3.4.3 Method of cutting test-pieces from procedure approval plate

3.4.2 Testing Methods for Welded Joints

Two main testing methods are used to determine the presence of cracks, fusion defects, inclusions and pores.

3.4.2.6. Tensile testing

Tensile tests were performed according to international standard ISO 4136 2001 ASTM standard E8-04 [89], on aswelded specimens. The machined specimens were wetground flush in the longitudinal direction (LD) to remove all machining marks. An INSTRON™ testing machine equipped with *FASTTRACK2*™ software was used to axially stress specimens at a cross head speed of 3.0 mm/min. The dimension of the

specimens were as and. The ultimate tensile strength of welded specimens were collected for comparison and evaluation.

Table 3.4.2 Dimension of tensile test sample as standard EN 895[90]

Total length	Lt	Depends on test unit
Head width	b_1	b + 12
Width of parallel length	B	12 with a ≤ 2 25 with a > 2
Parallel length	Lc	≥ LS + 100
Radius of throat	R	≥ 25

3.4.2.7. Bending testing

It is used to determine the deformability of a weld, in bend testing, a 15 mm wide sample is cut so the weld is running across the width of the sample acording to the EUROPEAN STANDARD EN 910 [91]. The bend usually is made using a radiused plunger that pushes the sample down into a radiused female die. In this test, the specimen is put onto two supporting rollers and a former is pressed through between the rollers. The distance of the supporting rollers is Lf = d + 3a (former diameter + three times specimen thickness).

The backside of the specimen (tension side) is observed. If a surface crack develops, the test will be stopped and the angle to which the specimen could be bent is measured. A bending angle of 180° is reached, if the specimen is pressed through the supporting rollers without development of a crack.

3.4.2.8. Hardness measurements

In order to perform hardness measurements, machined specimens, in the welded condition, were wet-ground and polished. As-welded specimens were ground flush and polished to allow hardness measurements on the LT-LD plane.

Vickers micro-hardness and Vickers hardness tests were then performed according to the requirements of ASTM standards E92 and E384 [92,93]. An applied load of 100 grams and a holding time of 10 seconds were employed for the micro-hardness measurements in terms of HV0.5. A hardness profile from the centreline of the

weld, through HAZ, to the unaffected base metal was measured at 0.5 mm intervals for micro-hardness and at 5mm interval for Vicker hardness in terms of HV5.

3.4.2.4 Electrical Resistivity

Electrical resistivity measurements were performed using Foerster Sigma Test 2.069 equipment with measuring probe of 8 mm, at operating frequency of f =240 kHz. The Sigma Test 2.069 is an eddy current instrument that measures the electrical conductivity of non-ferromagnetic metals. Electrical resistivity is calculated as a reciprocal value of conductivity.

3.4.2.5 Corrosion testing

Machined specimens for corrosion testing, as-welded condition, were wet-ground. These specimens were cleaned and dried to remove dirt, oil and other residues from the surfaces.

3.4.2.5.1 NAMLT Test (ASTM G67)

Samples for NAMLT testing were prepared following ASTM G67 guidelines. The specimens were sawed and all the sawed surfaces were machined to the final dimensions 50 mm by 6 mm for all deformations.

According to standard ASTM-G67, the weight loss per unit area is the measuring unit by which the IGC susceptibility of the alloy is determined. If the metal loss is at or above 15 mg/cm^2, then the alloy is considered resistance to IGC.

3.4.2.5.2 ASSET Test (ASTM G66)

Samples for ASSET testing were prepared following ASTM G66 guidelines. The specimens were cut and all the surfaces were machined to the final dimensions 40 mm by 100 mm.

3.4.2.6 Metallographic observations

All samples for metallographic characterization were selected for optical microscopy for both macrostructure and microstructure to observe the initial grain structure. Small samples with a length of 15mm x 20mm in the rolling direction were cut, parallel to the rolling direction. The TD surface was polished by traditional metallographic procedure using silicon-carbon paper using 600 µm, 800 µm, 1200 µm

and 2000 μm grinding papers followed by polishing with 10, 3, and 1-0.5 microns diamond paste. Some samples which need to caculate the grain size were then etched in the Barker's reagent (200 ml distilled H_2O + 6 ml HBF4 (50wt%)) to reveal the microstructure. The microstructure was then studied using an optical microscope under polarized illumination.

3.4.2.6.1 Macrostructure of Welded Parts

It is a method of examination of large regions of the specimen surface or fractured section with the naked eye or under low magnification. All quality evaluations should begin on the macroscale using tests designed to survey the overall field in a simple and reliable manner.

A common macro test is weld cross section examination to reveal internal discontinuities, weld profile, weld passes and sequence, extent of penetration and the quality of weld. The macrostructural properties of a weldament can then be used as a component of weld procedure qualification or welder qualification.

3.4.2.6.2 Microstructure of Welded Parts

The microstructure development in the weldment depends on the solidification behavior of the weld pool. The principles of solidification control the size and shape of the grains, segregation, and the distribution of inclusions and porosity.

CHAPTER 4

4. Results

4.1. Work hardening and ductility of the tested alloys in cold rolling

4.1.1. Mechanical properties of the cold rolled material

Plot of engineering stress-starin curves of the as-received and cold rolled alloy sheets is shown in Figure 4.1.1.

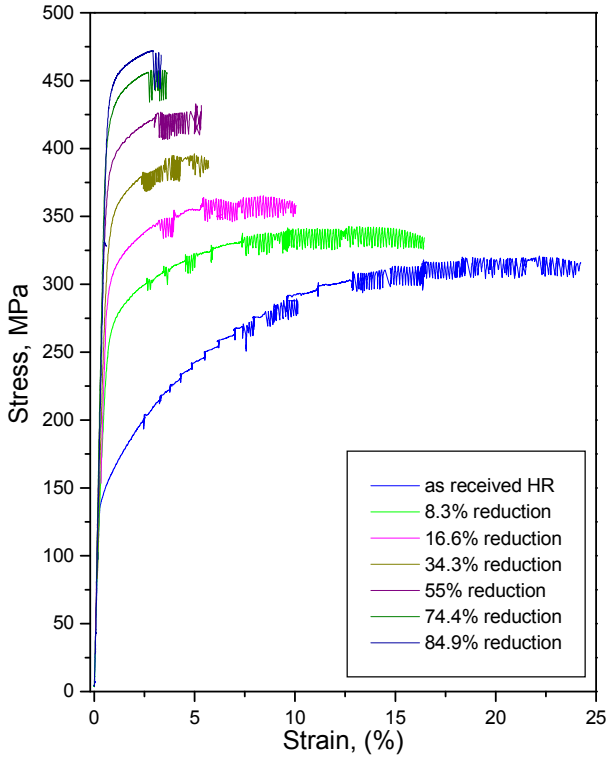


Figure 4.1.1 Engineering stress-strain curves of the material in as-received state and after cold rolling reductions in a range 8-85%

Table 4.1.1 Mechanical properties of as-received and cold rolled sheets

No.	Reduction [%]	Thickness of specimens	Yield strength [MPa]	Ultimate strength [MPa]	Elongation max [%]	Brinel Hardness [HB]
0	0.0	7.18	143.50	318.70	22.21	72
1	8.3	6.64	267.67	344.35	16.88	85
2	16.6	6.02	300.50	369.15	9.79	94
3	34.3	4.76	342.00	399.38	6.13	103
4	55.0	3.24	379.00	431.90	5.24	112
5	74.4	1.86	420.00	458.25	4.05	122
6	84.9	1.09	440.50	468.90	3.45	114

Average values of the yield strenght ($R_{0.2}$), ultimate tensile strenght (R_m) and elongation (ε) determined by the tensile test are given in Table 4.1.1 while their variation as a function of the cold rolling reduction is presented in Figure 4.1.2.

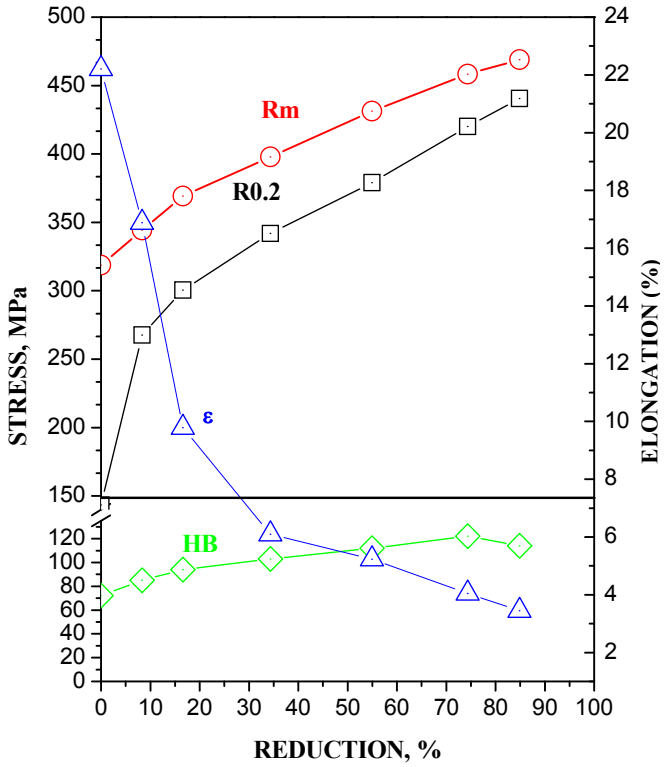


Figure 4.1.2 Plot of the average strength parameters, $R_{0.2}$ and Rm, elongation and hardness (HB) as a function of the cold reduction %.

The data show that, as expected, the increase in the cold rolling reduction from 0% to 85% resulted in a significant increase in strength, i.e. $R_{0.2}$ and R_m changed from 143.5MPa to 440.5MPa and from 318.7MPa to 468.9MPa, respectively. However, that was followed with reduction in the total elongation of the material from 22.2% to 3.4%.

Variation of the hardness (HB) as a function of the cold rolling reductions is also shown In Figure 4.1.2. Hardness shows same trend of increase as strength parameters.

4.1.2 Mechanical properties after the thermo-mechanical processing

4.1.2.1 Hardness (HB) of the material

In order to select optimal thermo-mechanical treatment, multiple parameters, i.e. cold rolling reduction, annealing temperature and time, were varied. Comprehensive data collected by a Brinell hardness test for all variants of the thermo-mechanical processing are shown in Figures 7.1.1 & 7.1.2 in Appendix 1. In this section are presented plots which show characteristic effect of each of parameters.

Effect of % cold reduction for the specimens annealed at different temperatures for 2 h is shown in Figure 4.1.3 Depending on the annealing temperature following trends were observed.

Hardness increased with increase of the % reduction from 16.7% to 35% for the specimens annealed at lower temperatures, 220-250 ˚C. Further increase in the reduction is characterized by plateau or slight increase in a hardness of the annealed sheets.

Hardness of the specimens deformed with reductions up to 35% increased during annealing at 260 ˚C, but further increase in the reduction give rise to softening during annealing. Annealing at 280 ˚C showed same trend, but softening started at even smaller reductions, i.e. 25%. Significant hardness drop with respect to the cold rolled state, like one of 65HB that occurred in specimen deformed by 42% reduction, is sign of recrystallization or complete recovery in the cold rolled sheets.

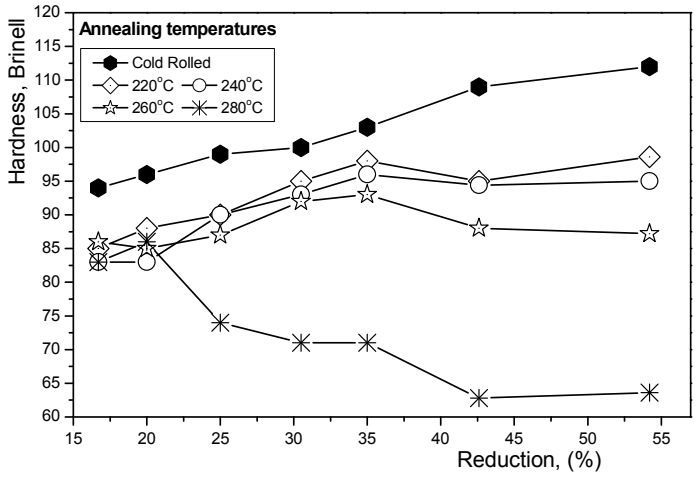


Figure 4.1.3 Hardness of the sheets cold rolled and annealed at 220-280 °C for 2h as a function of the % rolling reduction.

Effect of the annealing temperature on hardness for selected reductions is shown in Figure 4.1.4 Hardness of the specimens deformed by reductions less than 55% was almost constant for annealing temperatures in a range 220-260 ˚C. Annealing over 260 °C resulted in a steep drop in the harness for all reductions but for a sheets deformed 16.7%.

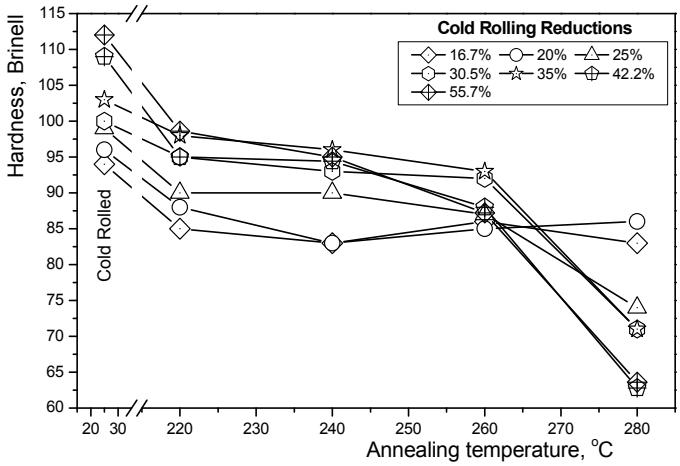


Figure 4.1.4 Hardness of the sheets cold rolled and annealed at 220-280 °C for 2h as a function of the annealing temperature.

Effect of annealing time on the hardness is shown for two reductions and whole range of annealing temperatures in Figure 4.1.5 Increasing the anneling time resulted in a hardenss decrease in general, but the effect was lesser than for other two processing variables.

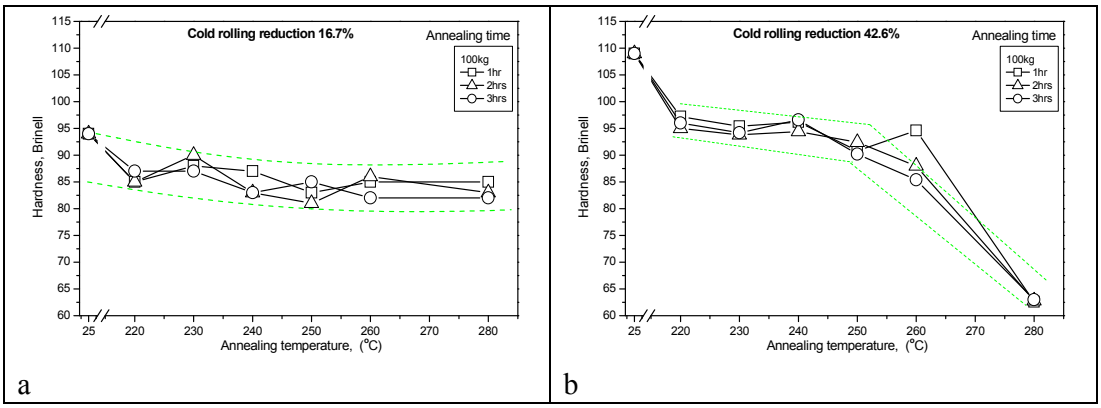


Figure 4.1.5 Effect of the annealing time on the hardness of the sheets deformed with 16.7% (a) and 42.6% (b) cold reduction and annealed in 220-280 °C temperature range.

4.1.2.2 Tensile properties

Results of the tensile tests performed on the alloy sheets that underwent complete thermo-mechanical processing, i.e. cold rolling and final annealing, are shown in Figures 4.1.6 and 4.1.7. Two sets of the specimens were characterized: in the first, alloy sheet was deformed with a low reduction of 16.7% while in the second group alloy

sheet underwent moderate deformation of 42%. Specimens underwent annealing in the whole range of annealing temperatures, 220-280 °C.

Following the same trend as the hardness, yield strength and ultimate tensile strength have not been significantly affected by the annealing temperature in the temperature range 220-260 °C. However, annealing at 280 °C resulted in significant decrease in the strength of the alloy (Figure 4.1.6).

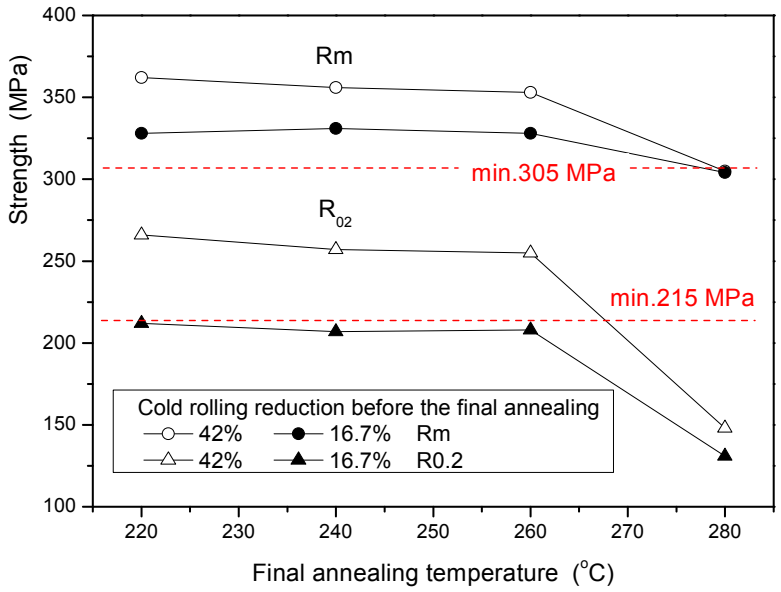


Figure 4.1.6 Effect of the final annealing temperature on the strength of the alloy. Annealing time was 2h. Prior the annealing specimens were deformed with 16.7% or 42% cold rolling reduction. (Red lines mark minimum strength parameters for attaining H321 state.

As the aim of this study was to develop schedule for attaining H321 state [77], the red lines in the plot represent the minimal strength values required by the standard ASTM B929/B 928M-04a. The results show (Figure 4.1.6) that yield strength of specimens deformed with 16.7% reduction did not meet the required minimum for any of the annealing temperatures. Specimens deformed with 42% reduction meet the requirements in terms of strength parameters (R_m and $R_{0.2}$) for the annealing temperature interval 220 °C - 260 °C and annealing time of 2 hours. Annealing at 280 °C for 2h caused a sudden drop in strength, most likely due to the occurrence of full recrystallization and grain growth.

An elongation showed rather sharp increase as the final annealing temperature increased from 260 °C to 280 °C. Specimens that underwent 16.7% cold reduction had greater elongation, but in all cases the elongation was greater than required by the standard [112].

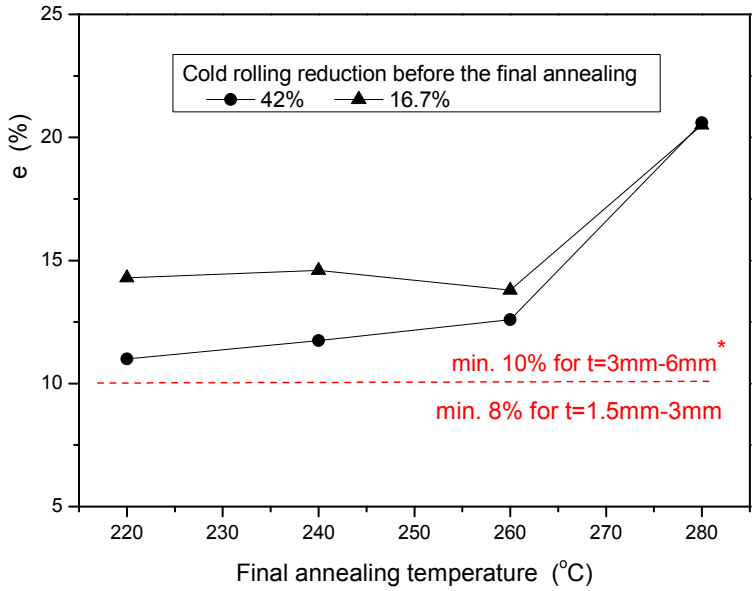


Figure 4.1.7 Effect of the final annealing temperature on the elongation. Annealing time was 2h. Prior the annealing specimens were deformed with 16.7% or 42% cold rolling reduction. (Red lines mark minimum strength parameters for attaining H321 state.

4.1.3 Electrical resistivity

Microstructural changes, occurring at different stages of the thermo-mechanical treatment, were followed up by electrical resistivity measurements. All plots of the measured electrical resistivity data for all processing variants are presented in Figures 7.1.3 & 7.1.4 in Appendix 1. In this section, as in the case on the hardness measurements, the presented plots show characteristic effect of % cold reduction, the annealing temperature and time on the electrical resistivity of the alloy sheet (Figure 4.1.8-Figure 4.1.10). Electrical resistivity of the material that underwent initial cold rolling and intermediate annealing of 3 h at 350° C was set as a referent state. That stage of the TMT corresponds to fully recrystallized microstructure, while Mg is bound into the Al-solid solution [94]. Subsequent cold work elevated electrical resistivity (Figure 4.1.8), due to an increase of dislocation's density and vacancy's concentration [106].

Extent of the prior cold work, i.e. % cold reduction, had a significant effect on the changes in the resistivity of the specimens annealed at all temperatures (Figure 4.1.8). While at deformations below 30%, the electrical resistivity was nearly constant for a given temperature, further increase in the thickness reduction (30-40 % range) lead to a steeper drop. With further increase in the % reduction, the resistivity reached plateau. The resistivity after the final annealing was at or below the referent level for all cold reductions and annealing temperatures. Decrease in the electrical resistivity below the referent, corresponding to fully recrystallized microstructure, points out that in addition to recovery/recrystallization processes precipitation took place during annealing in 220-260 °C temperature range. Considering the temperature range in question precipitation of Mg rich phase is the most likely.

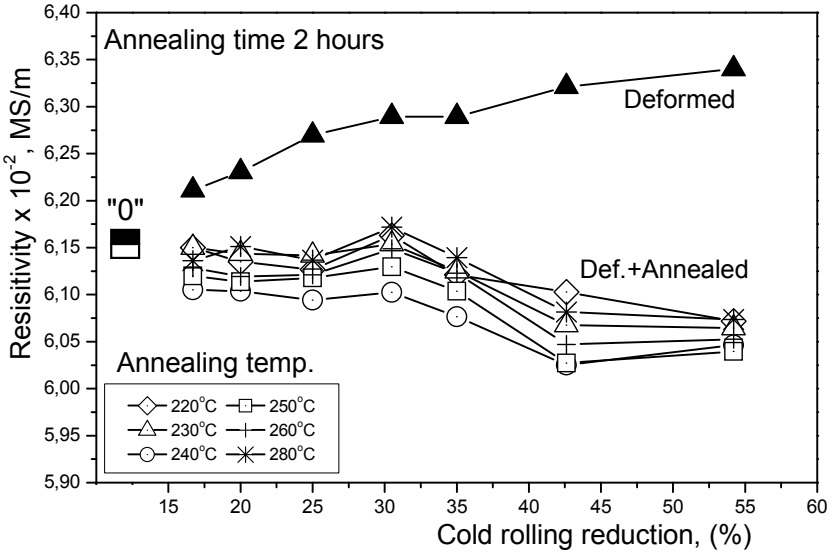


Figure 4.1.8 Electrical resistivity of the sheets cold rolled and annealed at 220-280 °C for 2h as a function of the % rolling reduction. "0" corresponds to the electrical resistivity of the specimens that underwent initial cold rolling and intermediate annealing.

Plot of the electrical resistivity change with annealing temperature (Figure 4.1.9) shows that the largest electrical resistivity drop, well below referent state occurs in the specimens annealed at 240 °C, indicating maximum precipitation of the Mg-rich phase. Although Mg solubility is lower at 220 °C than at 260 °C, the resistivity was higher due to kinetic limitation to the precipitation and recovery at the lower temperature.

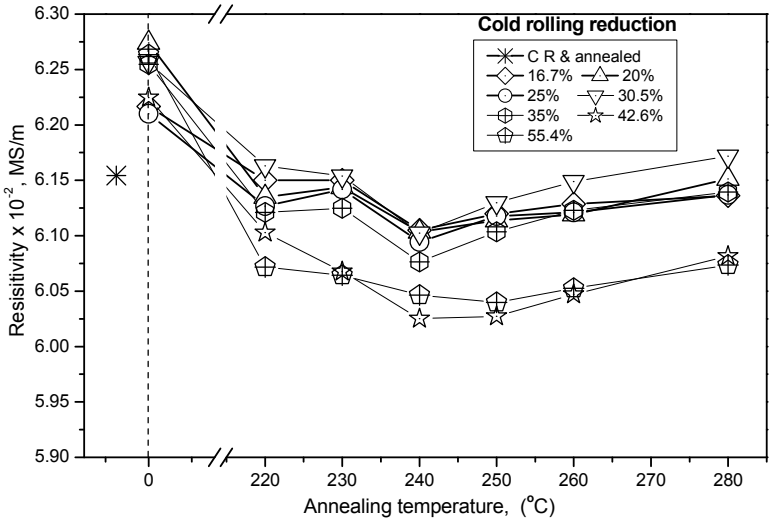
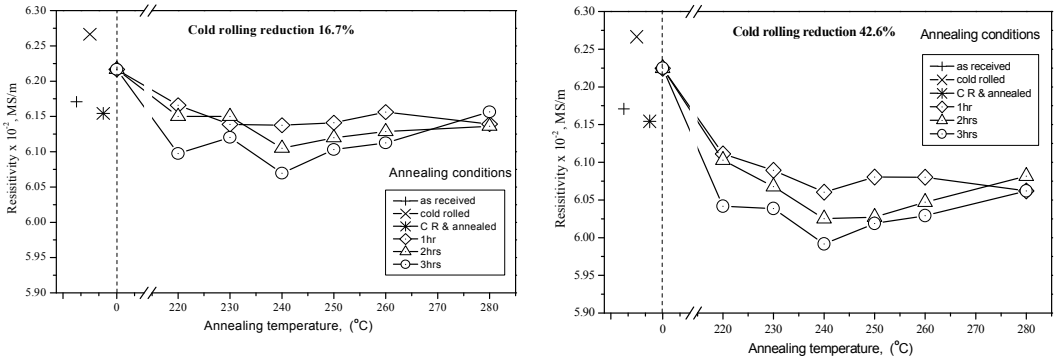


Figure 4.1.9 Electrical resistivity of the sheets cold rolled and annealed at 220-280 °C for 2h as a function of the annealing temperature. "0" corresponds to the electrical resistivity of the specimens that underwent initial cold rolling and intermediate annealing

The effect of annealing time on electrical resistivity is shown in Figure 4.1.10 In general, the resitistivity decreases with annealing time, but the effect is more pronauced at the lower temperatures while at 280 °C it is negligible.



a b

Figure 4.1.10 Effect of the annealing time on the electrical resistivity of the specimens deformed with 16.7% (a) and 42.6% (b) cold reduction and annealed in 220-280 °C temperature range

Sensitization treatment lead to further decrease in the electrical resistivity as shown in Figure 4.1.11 Decrease in the resistivity appears to be faster in the specimens that underwent high degree of cold reduction (42%). Observed trend could be in part be related to precipitation processes and in part to recovery.

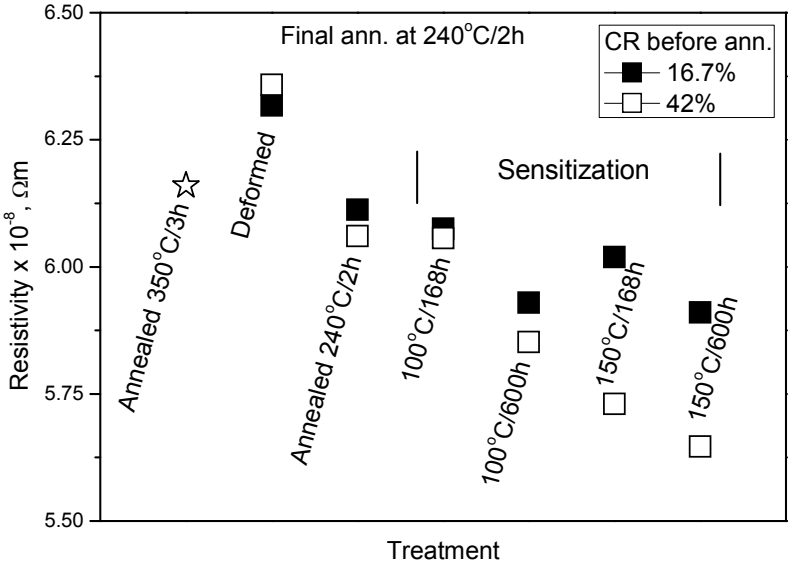


Figure 4.1.11 Electrical resistivity of the specimens deformed 16.7% and 42% at different stages of the thermo-mechanical processing and sensitization.

4.1.4 Corrosion Properties

4.1.4.1 Intergranular Corrosion – NAML Test

The effect of the thermo-mechanical processing on the IGC susceptibility (expressed as a mass loss in the NAML test) of the alloy is shown in Figure 4.1.12-Figure 4.1.14. It is evident that all processing parameters, % cold reduction, the annealing temperature and time, had influence on the IGC susceptibility. Extent of cold work affected the IGC susceptibility of the specimens that were subsequently annealed at the lower temperatures (220-240 °C). Increase in a thickness reduction decreased the IGC susceptibility and at 30-40 % thickness reduction steep decrease was observed. In the case of annealing at 240 °C, such increase in the amount of cold work lead to transition from IGC susceptible to IGC resistant state (Figure 4.1.12). The effect was negligible for the specimens that were annealed at a higher temperature (260 °C).

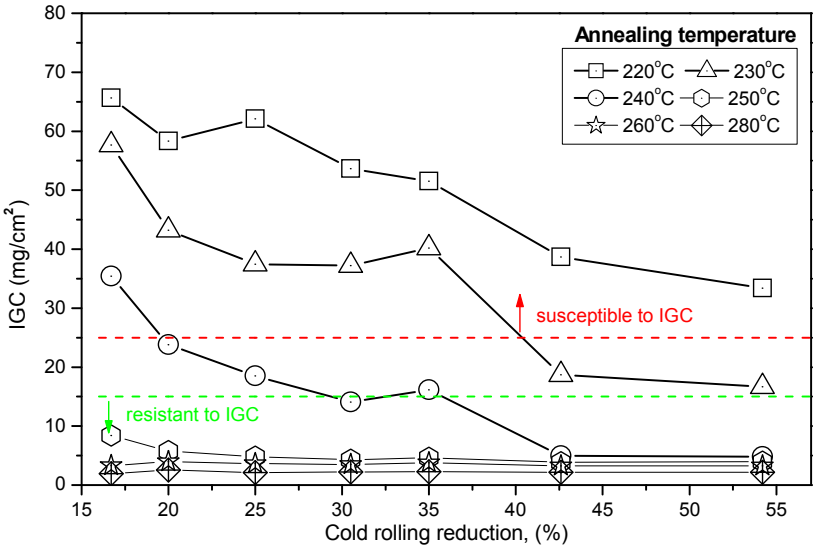


Figure 4.1.12 Intergranular corrosion susceptibility (IGC) determined by Nitric Acid Mass Loss Test (NAMLT) following the ASTM G67 standard as a function of the % cold rolling reduction.

Increasing the annealing temperature, in general, improved corrosion resistance (Figure 4.1.13). In the case of annealing at 240 °C, such increase in the amount of cold work lead to transition from IGC susceptible to IGC resistant state.

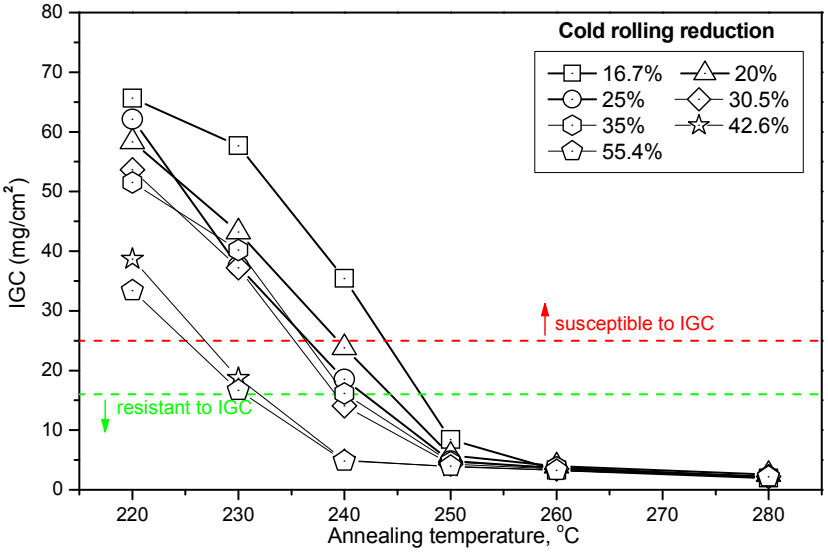
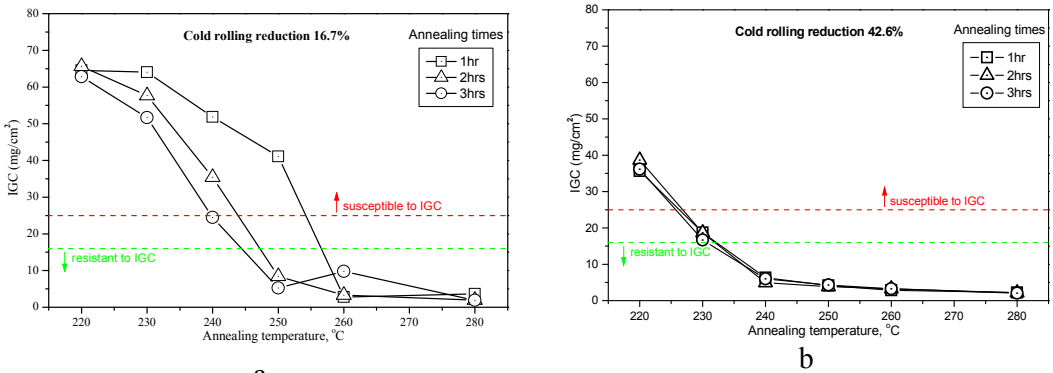


Figure 4.1.13 Intergranular corrosion susceptibility (IGC) determined by Nitric Acid Mass Loss Test (NAMLT) following the ASTM G67 standard as a function of the annealing temperature.

Increasing the annealing time, but in a lesser extent, improved corrosion resistance as can be seen in Figure 4.1.14. The effect is pronounced in 230-250 °C temperature range, while at lower and higher temperatures it is negligible. It is also more pronounced in the sheets deformed by the cold reduction 16.7-35% (Figure 4.1.14a and Appendix II), while at higher deformations it is negligible.

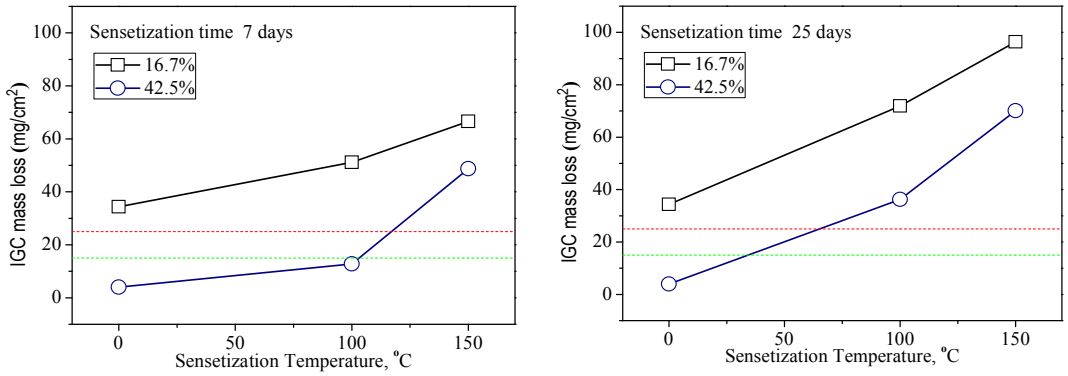
Complete data of the NAMLT testing are given in Figures 7.2.1 & 7.2.2 in Appendix II



a b

Figure 4.1.14 Effect of the annealing time on the IGC susceptibility of the specimens deformed with 16.7% (a) and 42.6% (b) cold reduction and annealed in 220-280 °C temperature range.

Results of the NAML test on sensitized specimens showed increase in the mass loss with respect to corresponding non-sensitized specimens (Figure 4.1.15). However, specimens deformed 42% and annealed for 2h at 240°C had mass loss of only 12.7587 mg/cm^2, i.e. below the lower IGC lower limit (IGC=15 mg/cm^2), after sensitization of seven days at 100 °C. That result is significant loss corresponding to sensitization of 7 days/ 100 °C is considered to correspond to mass loss in service lifetime of marine vessel.



a b

Figure 4.1.15 Effect of sensitization treatment on IGC susceptibility of alloy (a) 7 days and (b) 25 days

4.1.4.2 Exfoliation and Pitting Corrosion (G66 – ASSET TEST)

The complete results of testing for exfoliation and pitting corrosion as well as IGC susceptibility that were described in preceding character are shown in appendix II (Figures 7.2.3 – 7.2.6 & Tables 7.2.1 – 7.2.7) while for the selected states are shown in Table 4.1.2.

Table 4.1.2 Corrosion stability of the specimens deformed with a different cold rolling reductions and annealed for 2 hours in the temperature range 220-280 °C for three sets of specimens.

Condition	Cold Rolling %	$(m_1-m_2)/A$, mg/cm^2	IGC	Face	Exfoliation	Pitting
220°C/2h	17.6%	65.6632	Susceptible	1	N	N/A
				2	N	N/A
240°C/2h	30.5%	35.4337	Susceptible	1	N	N/A
				2	N	N/A
260°C/2h	42.6%	3.3193	Resistant – N	1	N	A
				2	N	N/A
280°C/2h	55.6%	1.9360	Resistant – N	1	N	A
				2	N	A
220°C/2h	17.6%	53.6610	Susceptible	1	A/B	A
				2	A/B	A
240°C/2h	30.5%	14.0963	Resistant – N	1	N	A
				2	N	A
260°C/2h	42.6%	3.4871	Resistant – N	1	N	A/B
				2	N	A/B
280°C/2h	55.6%	2.1992	Resistant – N	1	N	A
				2	N	A
220°C/2h	17.6%	38.6764	Susceptible	1	N	N/A
				2	N	N/A
240°C/2h	30.5%	4.9378	Resistant – N	1	A/B	A
				2	A/B	A
260°C/2h	42.6%	3.2572	Resistant – N	1	B	B
				2	B	B
280°C/2h	55.6%	2.1745	Resistant – N	1	B	B
				2	B	B
220°C/2h	17.6%	33.3820	Susceptible	1	C	A
				2	C	A
240°C/2h	30.5%	4.7990	Resistant – N	1	A/B	A
				2	A/B	A
260°C/2h	42.6%	3.2444	Resistant – N	1	N	B
				2	N	A/B
280°C/2h	55.6%	2.1898	Resistant – N	1	N	A/B
				2	N	A/B

NAMLT Intergranular Corrosion Testing (Susceptible if the mass loss < 25 mg/cm^2 Resistance-A if the mass loss > 25 mg/cm^2 and < 15 mg/cm^2 , Resistance-N if the mass loss > 15 mg/cm^2)
ASSET Tested Exfoliation Susceptible (A, B, C, D-Four Degrees of Exfoliation).
ASSET Pitting Corrosion Testing (N-No appreciable attack; A, B, C-Three Degrees of Pitting).

The results in Table 4.1.2 showed that while there is IGC susceptibility for certain states, material in states was graded a or A/B meaning that it showed little attack but for the specimen deformed 16.7% and annealed 2h at 240 °C which was graded C.

The rating of the sheets that underwent different thermo-mechanical processing according to different levels of exfoliation and pitting corrosion is shown in appendix 4b, while for the selected specimens is shown in Figure 4.1.16 and Figure 4.1.17.

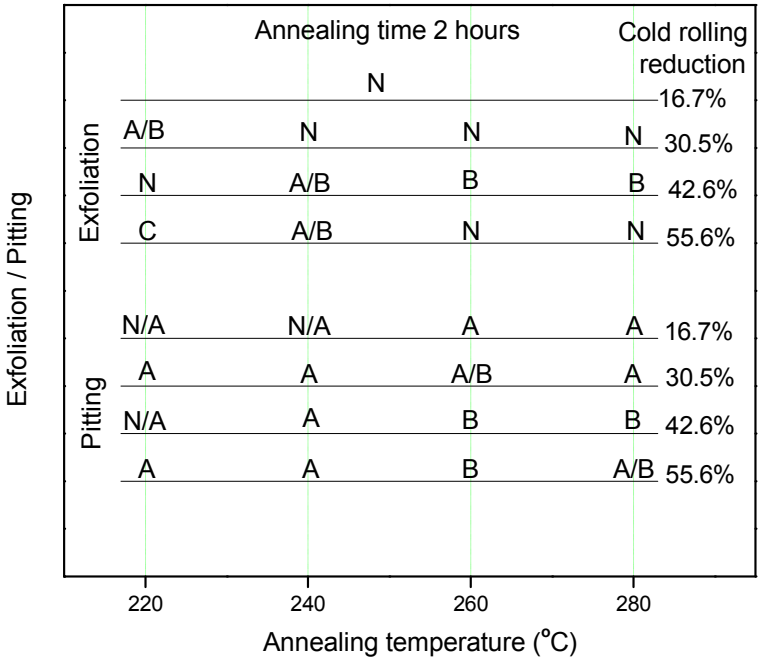


Figure 4.1.16 Variation in a response toward exfoliation and pitting corrosion as function of the cold rolling reduction and annealing temperature (Face 1).

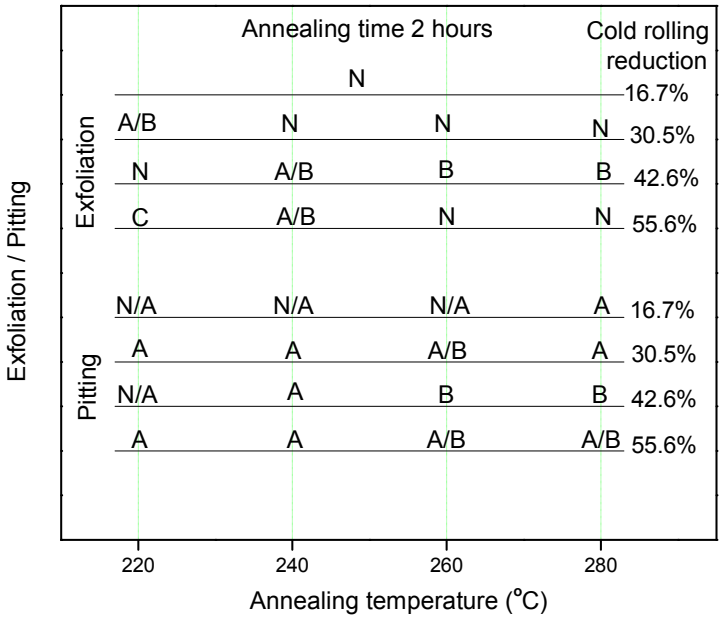


Figure 4.1.17 Variation in a response toward exfoliation and pitting corrosion as function of the cold rolling reduction and annealing temperature (Face 2).

The results from Figure 4.1.16 and Figure 4.1.17 show that unacceptable C level of exfoliation appeared after 54% deformation and low temperature annealing at 220°C, for all applied annealing times.

The most detrimental pitting corrosion susceptibility, described as C type surface appearance, was not recognized at all other figures. However, after higher degree of cold rolling reductions (42% and 54%) and higher final annealing temperatures (260°C and 280°C), B level of pitting susceptibility were identified in Figure 4.1.16 and Figure 4.1.17.

It should be noted that annealing time did not bring any significant exfoliation or pitting susceptibility variations in the range of applied annealing temperatures and deformation degrees.

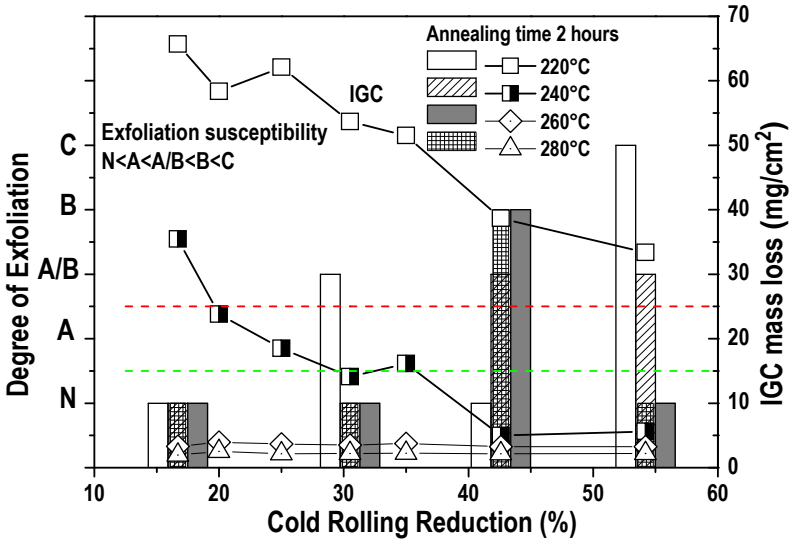


Figure 4.1.18 Ratings of different levels of exfoliation corrosion (according to ASTM G66 standard)

The appropriate data for the IGC susceptibility were also shown (square symbols). Values below the lower line (IGC=15 mg/cm^2) indicate IGC resistance, while above the upper line (IGC=25 mg/cm^2) indicate IGC susceptibility.

The results shown in Figure 4.1.19 indicate that unacceptable C level of exfoliation appeared after 54% deformation and low temperature annealing at 220°C, for all applied annealing times.

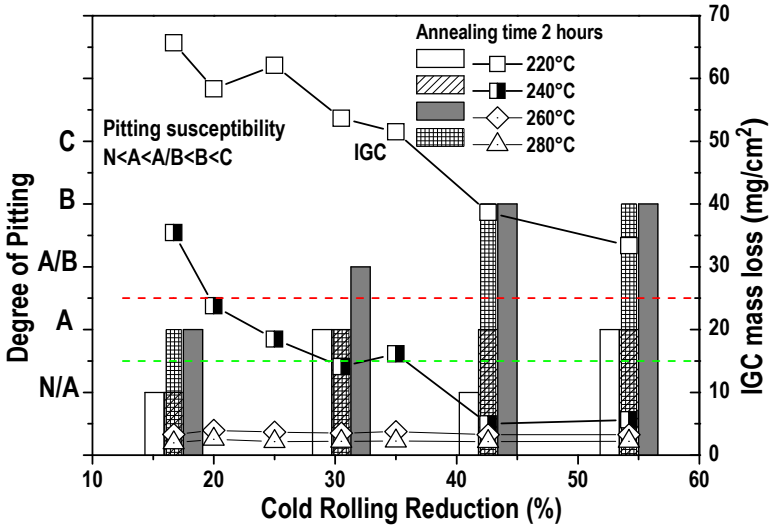
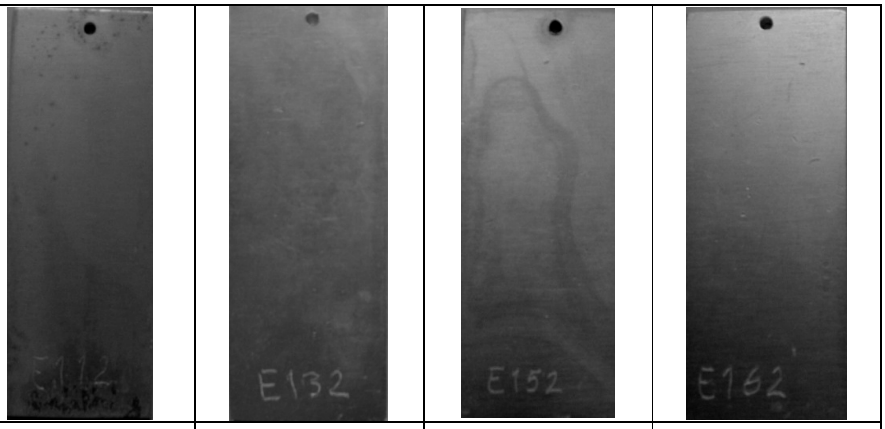


Figure 4.1.19 The degree of pitting corrosion (according to ASTM G66 standard) identified at samples cold rolled with different reductions (up to 55%) and subsequently annealed in the range of temperatures from 220°C to 280°C.

The most detrimental pitting corrosion susceptibility, described as C type surface appearance, was not recognized at all Figure 4.1.19. However, after higher degree of cold rolling reductions (42% and 54%) and higher final annealing temperatures (260°C and 280°C), B level of pitting susceptibility was identified.

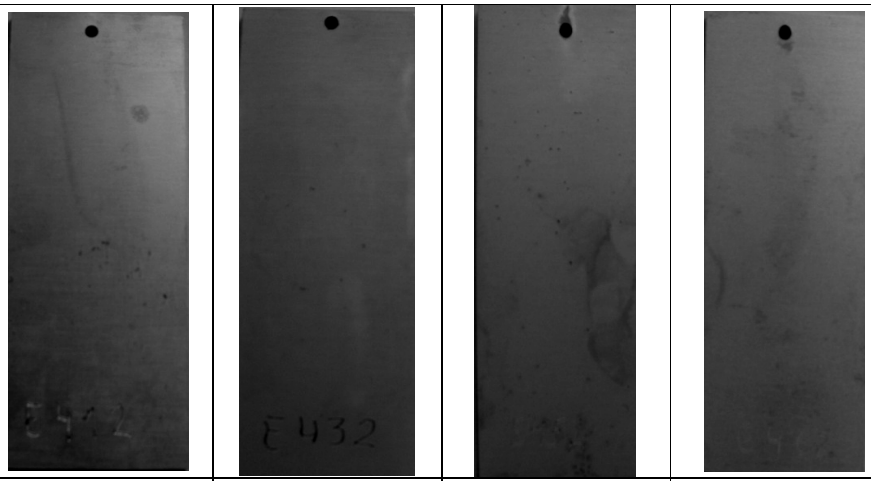
For all other samples exfoliation and pitting corrosion were within acceptable limits, and generally ranked as A and B, as can be seen in Figure 4.1.16 and Figure 4.1.17.

The photos of selected samples tested for exfoliation corrosion test are shown in and the rest are in appendix II (Figures 7.2.7).



220 °C	240 °C	260 °C	280 °C

(a) *16.7 % cold rolling deformation*



220 °C	240 °C	260 °C	280 °C

(b) *30.5 % cold rolling deformation*

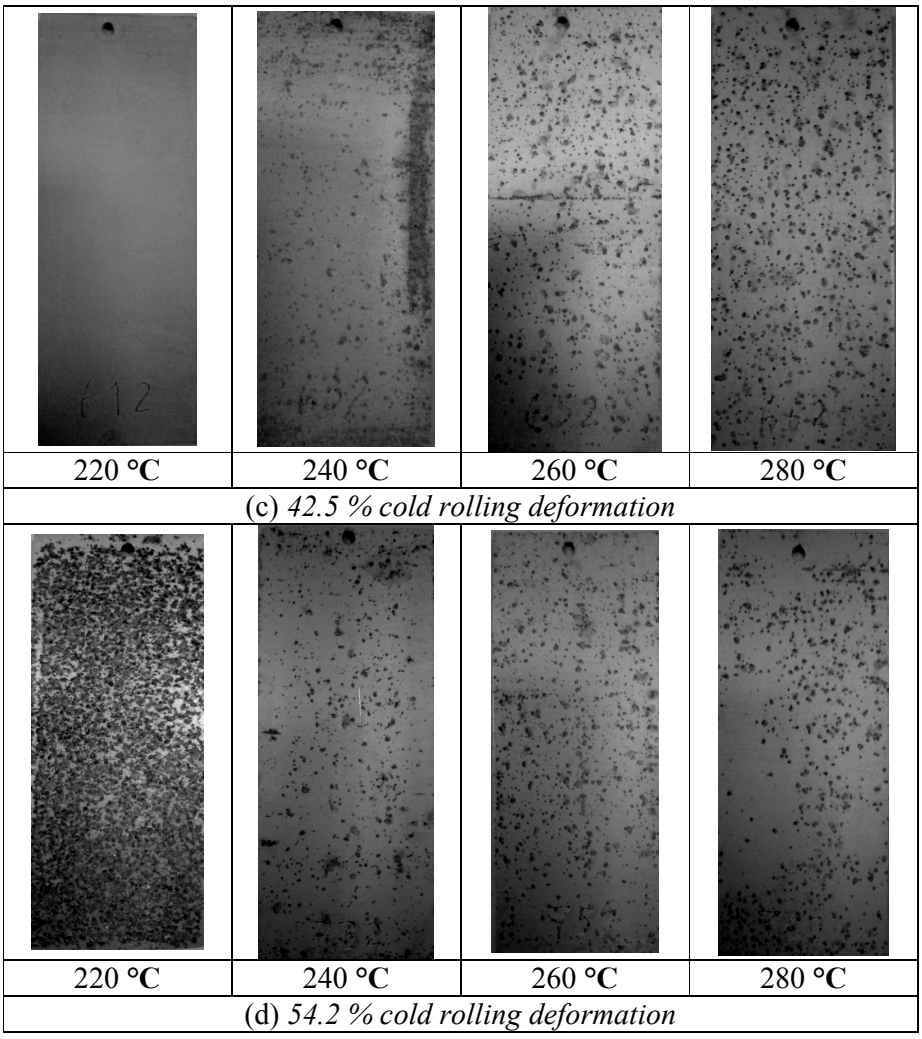
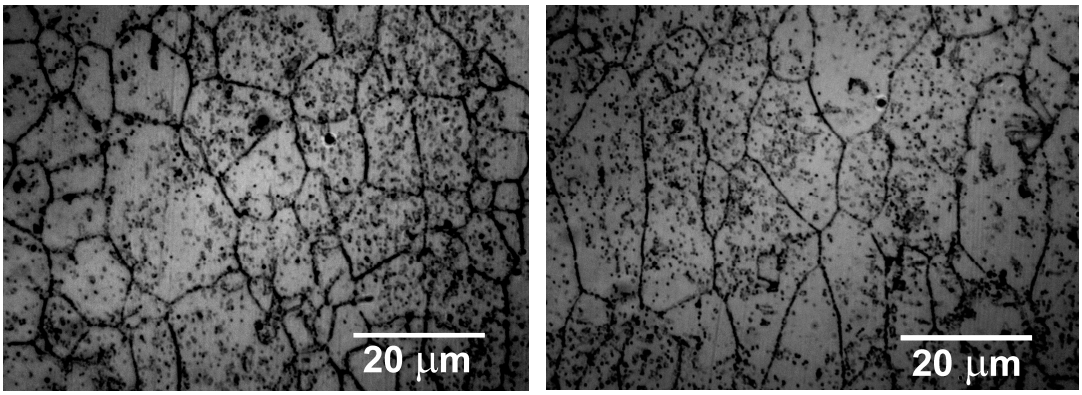


Figure 4.1.20 Samples surfaces after exfoliation and pitting testing for different cold rolling deformation and different annealing temperatures at annealing time 2 hours.

4.1.5 Microstructural characterization

4.1.5.1 Microstructure of the cold rolled sheets

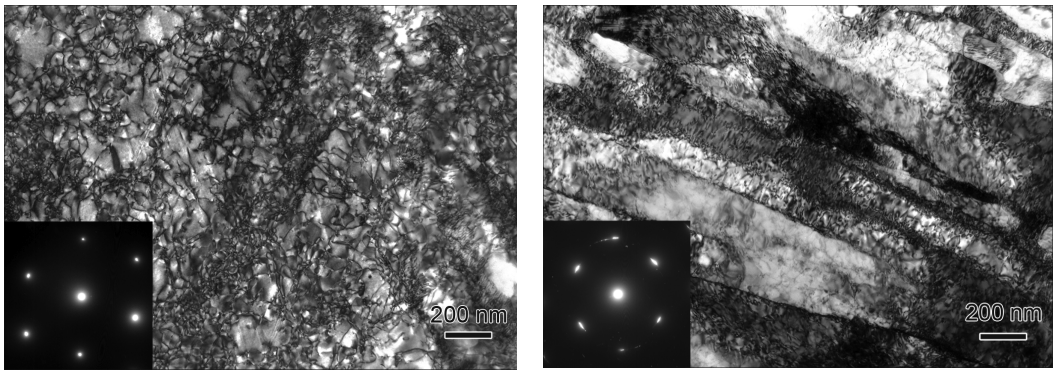
The microstructure of samples cold rolled to 16.7% and 42% and subsequently annealed at 240/2hrs are shown in Figure 4.1.21, rest of the samples are shown in Appendix III (Figure 7.3.1).



A B

Figure 4.1.21 Microstructure of samples cold rolled to 16.7% (a) and 42% (b) and subsequently annealed at 240°C/2h

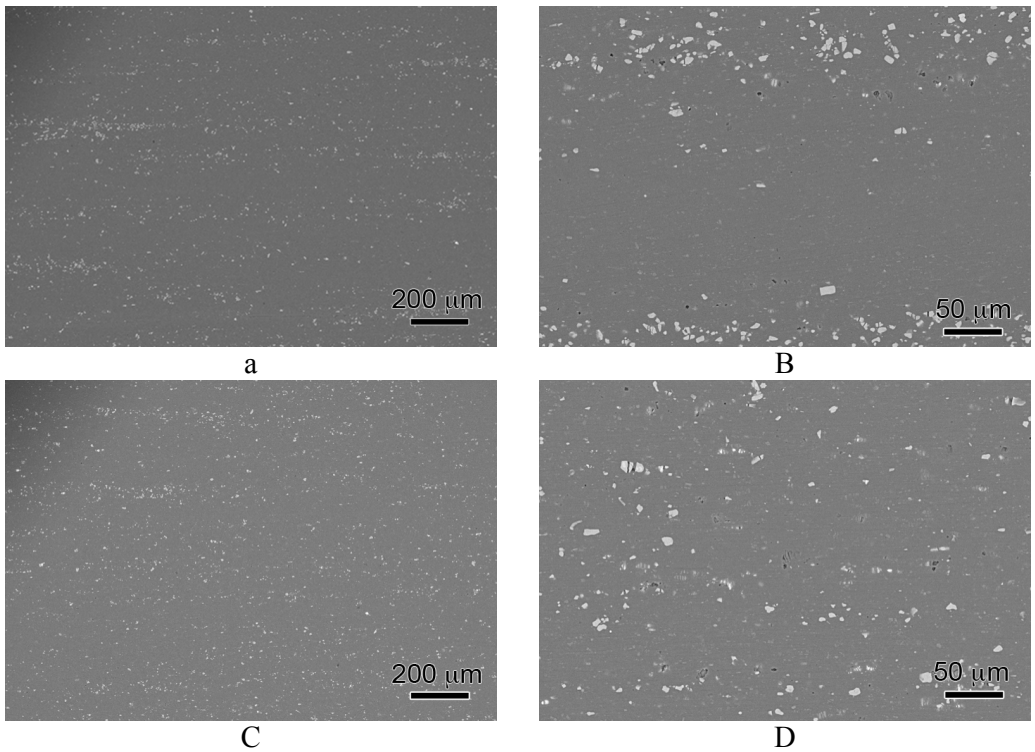
The precipitation of β-phase seems to be more abundant, as well as more homogenous across the grain interiors in samples deformed to 42%. There are more profuse of β-phase precipitations in a sample deformed to 42% with respect the 16.7% deformed one. Varied amount of the cold work produced distinct substructures of the specimens as characterization of the material deformed for 16% and 42% showed (Figure 4.1.22). Deformation of 16.7 % resulted in high dislocation density, but no organized substructure was developed (Figure 4.1.22 (a)). Only occasional subgrains were observed. In the inserted diffraction pattern spots from the area are sharp, confirming that fragmentation of the grains had not happened yet. Substructure of the specimen deformed 42% is characterized by high dislocation density and a number of interfaces created by fragmentation of the original grains during heavy deformation (Figure 4.1.22 (b)). Presence of microbands was confirmed by selected area diffraction patterns that shows splitting of the spots, indicating misorientation between microbands.



A B

Figure 4.1.22 Bright field TEM micrographs of the deformation substructure of: a) 16 % thickness reduction, 110]za.; b) 42 % thickness reduction, [110]za.

In addition, higher reductions resulted in more homogeneous deformation as well as distribution of the primary $Al_6(Mn,Fe)$ particles. In the case of the sheet cold rolled 16.7%, coarse broken constituent particles clustered in the bands with regions of lower particles density in between (Figure 4.1.23 (a) and (b)).



a B

C D

Figure 4.1.23 Back scattered SEM micrographs showing distribution of constituent particles after cold rolling. Bright particles are mostly $Al_6(Mn,Fe)$. (a) and (b) 16.7% cold reduction. (c) and (d) 42% cold reduction.

On the other hand higher reductions, such as 42%, the particles were uniformly distributed within a specimen (Figure 4.1.23 (c) and (d)).

4.1.5.2 Grain size

Micrographs of the grain microstructure after final annealing of the selected are shown in the Figure 4.1.24. Those four micrographs belong to the specimens deformed by minimum (16.7%) and maximum (54%) reductions as well as annealed at lowest (220 °C) and highest (280 °C). The micrographs show that the grains retain elongated morphology in a wide range of the processing parameters. According to the strength and hardness of the alloy, annealing at 280 °C lead to recrystallization, but never the less grain microstructure remained elongated in rolling direction.

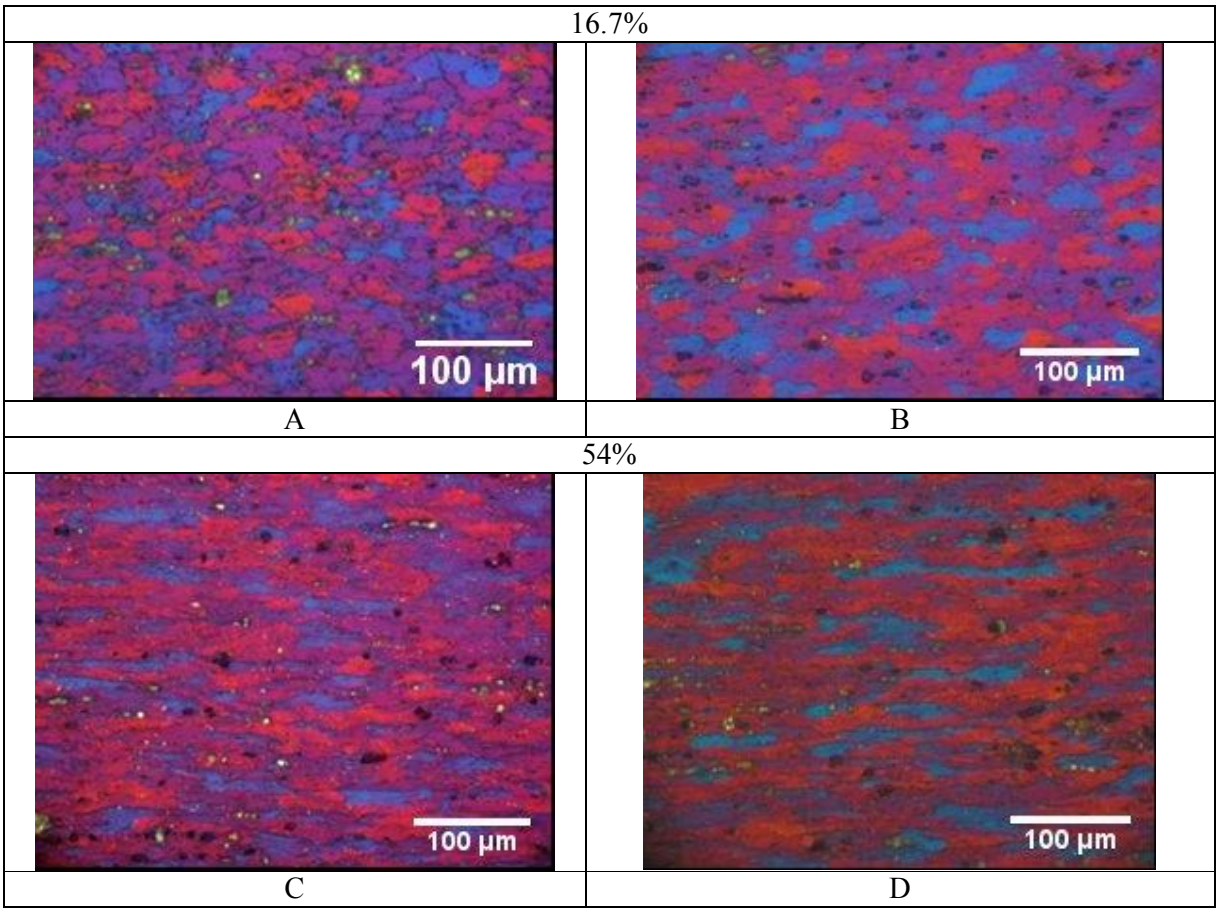


Figure 4.1.24 Grain microstructure of the specimens deformed to 16.7% (a & b) and 54% (c & d) and annealed at 220°C/2h and 280°C/2h, respectively.

Variation of an aspect ratio of the grains as function of the annealing temperature for three cold reductions is shown in Figure 4.1.25. The aspect ratio increased with the reduction. For 16.7% and 30% cold reduction the aspect ratio increased with the annealing temperature, while for the reduction of 54% scatter was too large to draw conclusion.

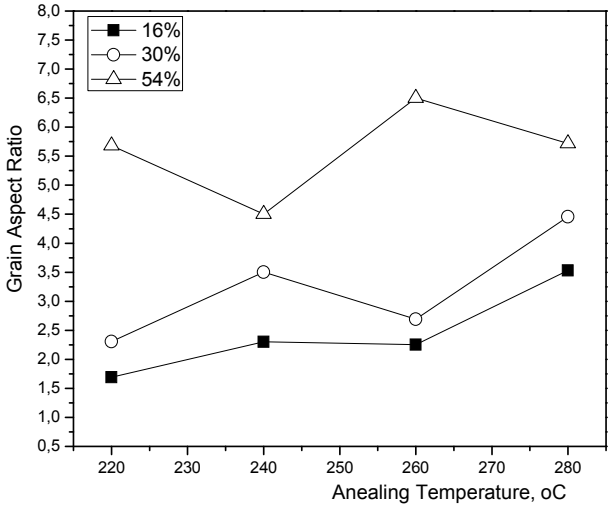


Figure 4.1.25 Mean grain size aspect ratio of the samples cold rolled to 16.7%, 30% and 54% and subsequently annealed in the temperature range 220°C-280°C for 2h.

4.1.5.3 Intergranular corrosion - microstructure

It is well known that precipitation of β-phase (Al_3Mg_2) at the grain boundaries is responsible for deterioration of the corrosion properties of Al-Mg alloys [107,108]. Precipitation of the β-phase (Al_3Mg_2) at the grain boundaries was revealed by etching with orthophosphoric acid and the results are shown in Figure 4.1.26.

Effect of the annealing temperature can be seen on the micrographs in Figure 4.1.26 (a-c) that show specimens deformed by 42.5% cold reduction and annealed at different temperatures. Specimen annealed at 260°C is characterized by discrete, dark precipitates vaguely delineating grain boundaries (Figure 4.1.26 (a)). Metallographic examination of the specimen annealed at 240°C revealed denser, but discrete particles delineating boundaries (Figure 4.1.26 (b)). Both states were IGC resistant region and were characterized by discrete precipitation along the grain boundaries. On the other hand, characterization of the specimen annealed at 220 °C showed faint, continuous

outlines of the grain boundaries indicating that precipitated grain boundary phase had morphology of a continuous film (Figure 4.1.27 (c)). That state was IGC susceptible.

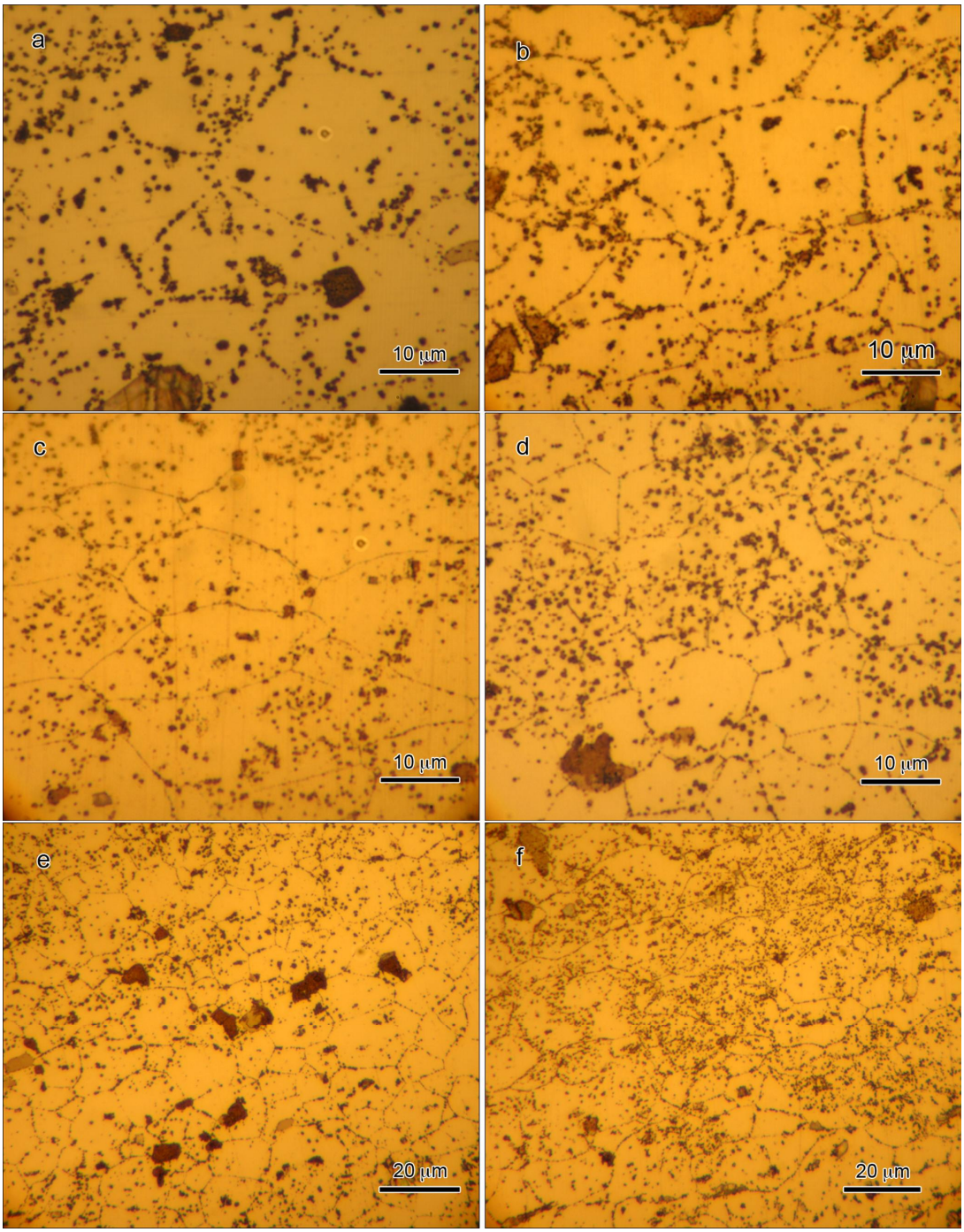


Figure 4.1.26 LOM micrographs of the microstructure after orthophosphoric acid etch: (a) 42% deformation and annealing 2h/260°C (IGC resistant); (b) 42% deformation and annealing 2h/240°C (IGC resistant); (c) 42% deformation and annealing 2h/220°C (IGC susceptible);

Effect of the precipitated grain boundary phase morphology on IGC susceptibility was further discerned during the study of the effect of the amount of cold work. Annealing at 240°C was particularly interesting since at that temperature transition from IGC susceptible to IGC resistant state was observed as the amount of cold work increased. In the IGC susceptible state, when the thickness reduction of the material was 16%, continuous outlines of the majority of grain boundaries indicated that the precipitated grain boundary phase formed a continuous film (Figure 4.1.26 (c)). Some grain boundaries were decorated by dark dots indicating discrete precipitates. Delineated grains tended to be polygonal, and grain boundaries were sharp and faceted (Figure 4.1.26 d and e).

In order to get some insight into the mechanism of the intergranular corrosion, surfaces of the IGS susceptible (16.7% deformation) and IGC resistant (42% deformation) specimens annealed at 240 °C were characterized in SEM after exposure to the nitric acid. Typical surfaces of the specimens deformed 16% (IGC susceptible) after immersion into the nitric acid for various times are shown in Figure 4.1.27 and Figure 4.1.28. After the immersion for 2h, corrosion of the surface corresponding to LT plane was non-uniform (Figure 4.1.27). Unbinding and fall out of grains was observed in the corroded areas. The attack of the acid was localized at the grain boundaries whereas the grain interiors appeared unaffected. In the areas in which flat surface layer had not been completely removed, polygonal grains were outlined by preferentially attacked grain boundaries (Figure 4.1.27.x (a)). Similar, non-uniform corrosion spreading of sensitized AA 5083 exposed to different corrosive environment, NaCl solution, was reported by Jain et al [109].

Extending the immersion time resulted in spreading of the corrosion throughout the surface. No remains of the flat surface layer were observed after the 24h in acid and multiple layers of grains got unbound and fell out (Figure 4.1.27b). Even after extended exposure to the corrosive environment, grain's surfaces stayed intact - smooth and faceted (Figure 4.1.28 (a)).

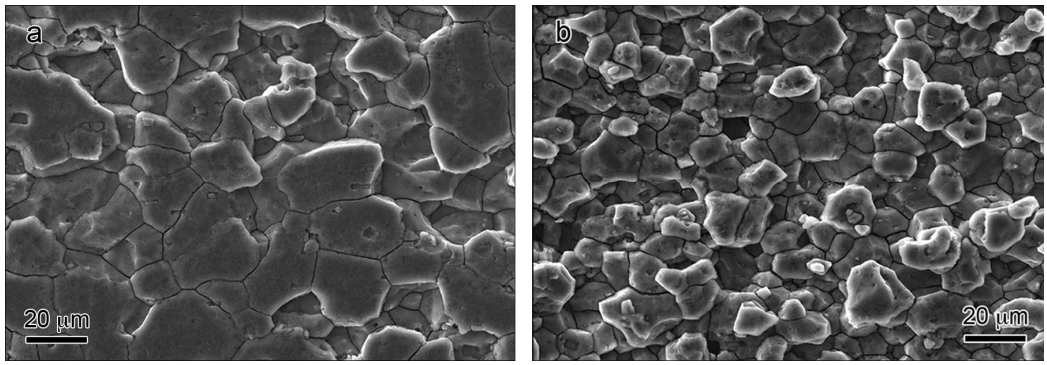


Figure 4.1.27 Secondary electron SEM micrographs showing morphology of the surface parallel to LT plane. Specimens were deformed 16% and annealed for 2h at 240°C (IGC susceptible). Specimens were immersed in the nitric acid for: (a) 2h - (b) 24h.

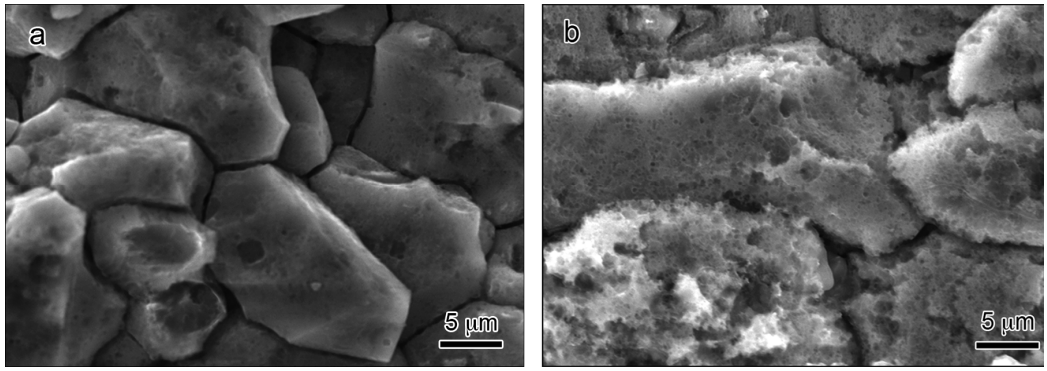


Figure 4.1.28 Secondary electron SEM micrographs of the surface morphology at higher magnifications: a) Specimen deformed 16 % and annealed for 2h at 240°C (IGC susceptible) after immersion 24h in the nitric acid. b) Specimen deformed 42% and annealed for 2h at 240°C

In contrast, in the specimens that underwent 42% thickness reduction (IGC resistant), both grain boundaries and grain interiors were corroded after the immersion into the nitric acid (Figure 4.1.28 (b) and Figure 4.1.29). Elongated grains and irregular outlines of grain boundaries characterized morphology of the surfaces in LT orientation (Figure 4.1.29). Rough, sponge like surface of the grains indicates that corrosion also took place in the grain interiors (Figure 4.1.28 (b)). Corrosion appeared to proceed layer by layer, and although more material was removed from the surface after 24h, no deepening and unbinding of the individual grains was observed.

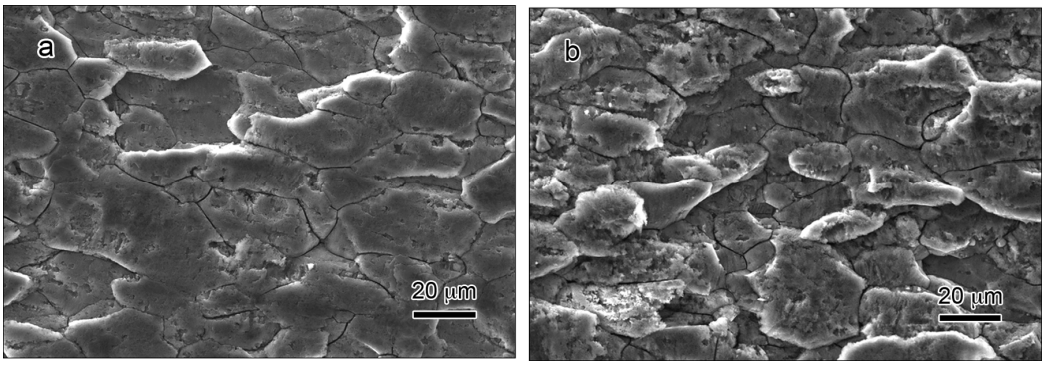


Figure 4.1.29 Secondary electron micrographs showing morphology of the surface parallel to LT plane. Specimens were deformed for 42% and annealed for 2h at 240°C (IGC resistant). Specimens were immersed in the nitric acid for: (a) 2h - Below surface layer of flat gra

4.1.6 Grain boundary phase

TEM characterization supported metallographic observations on morphology of β-phase (Al_3Mg_2). Thin, continuous or semi-continuous film was observed along the grain boundaries of the specimen deformed 16.7% and annealed 2h at 240°C (Figure 4.1.30 a and b). Thickness of the film was in the range 25-150 nm. Even occasionally observed discrete particles were elongated along the grain boundaries showing clear tendency toward grain boundary wetting. EDS characterization showed that the precipitated grain boundary phase is ternary Al-Mg-Zn and it contains small amounts of Cu (Figure 4.1.31(a)).

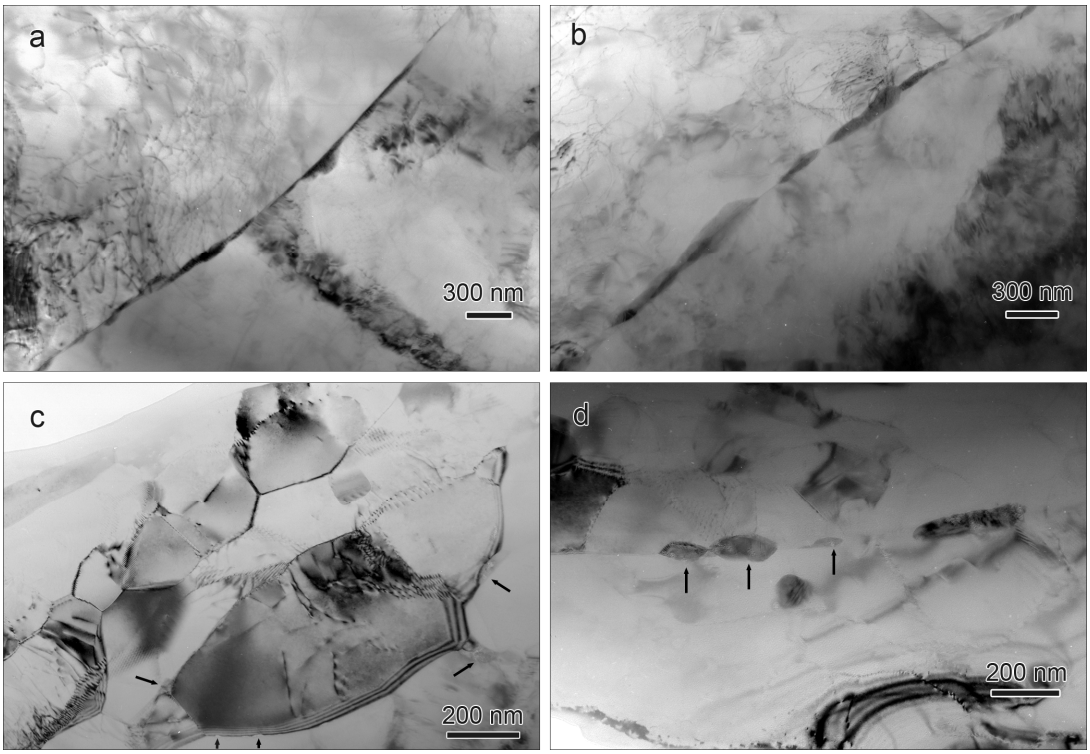


Figure 4.1.30 Bright field TEM micrographs of the precipitated β-phase at the grain boundaries: (a, b) Specimen deformed 16% and annealed 2h at 240°C (IGC susceptible state). The precipitated grain boundary phase forms continuous or semicontinuous film. (c, d) Specimen deformed 42% and annealed 2h at 240°C (IGC resistant state). Subgrains network was formed during annealing. The precipitated grain boundary phase is observed at the high angle grain boundaries and triple junctions while subgrain boundaries are precipitate free.

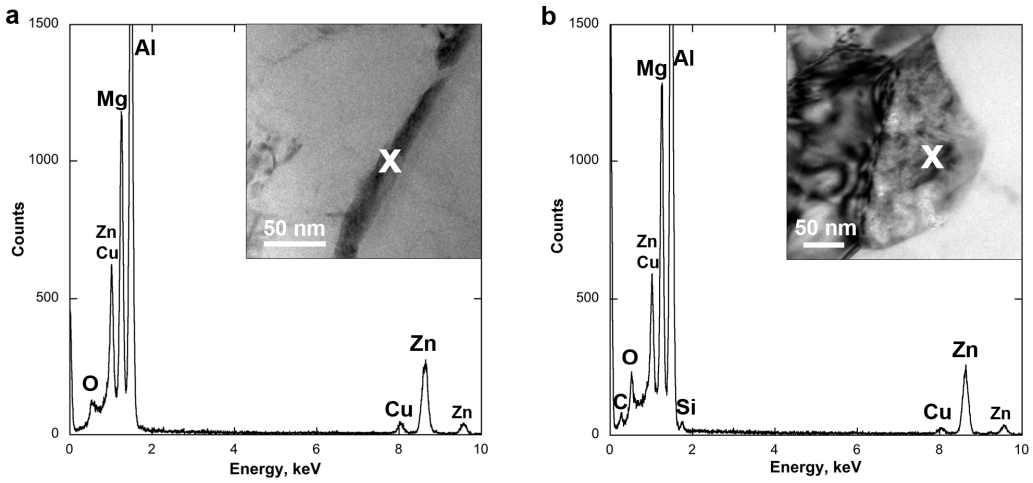


Figure 4.1.31 EDS spectra and corresponding bright field TEM micrographs of the precipitated grain boundary phases: (a) Specimen deformed 16% and annealed 2h at 240°C (IGC susceptible state). (b) Specimen deformed 42% and annealed 2h at 240°C (IGC resistant state).

When the cold rolling reduction of the material was 42% and the other processing parameters the same (IGC resistant state,), TEM characterization confirmed the presence of the discrete, lenticular particles at the grain boundaries (Figure 4.1.30 (d)). Precipitation showed a strong preference for the high angle grain boundaries as reported by other authors [110] while low-angle and subgrain boundaries are almost precipitate free (Figure 4.1.31 (c)). EDS spectra showed ternary Al-Mg-Zn compositional makeup of the grain boundary phase enriched with a small amount of Cu (Figure 4.1.31 (b). In addition to the grain boundaries, the precipitation also took place on secondary phase particles.

4.2 Welding Results

The designation of welded samples are shown in Table 4.2.1

Table 4.2.1 Desination of welded samples

Sample code	Welding process	Material type	Sample number
M1-1a	H116	MIG	1
M1-1b			2
MP1-1a		MIG-P	1
MP1-1b			2
T1-3a		TIG	1
T1-3b			2
TP1-3a		TIG-P	1
TP1-3b			2
M3-1a	H321	MIG	1
M3-1b			2
MP3-2a		MIG-P	1
MP3-2b			2
T3-1a		TIG	1
T3-1b			2
TP3-1a		TIG-P	1
TP3-1b			2

4.2.1 Radiographic Testing

A radiographic examination (X-ray) was used after welding to see if the joint does not contain defects (bubbles, cracks and inclusions). Radiographic testing of the weldments was done according to EN 1435-class B [111] standard in GOŜA INSTITUT using equipment Ind. Rentgen (Baltpost 200 kV), film AGFA D5 Pb 700mm and IQI type 10ISO 16 the picture estimated as per ISO 10042 [112] and the required quality is level B, the photos are shown in Appendix IV (Figures 7.4.1 & 7.4.2).

From photos shown in Appendix 7.3 there are some defects (porosities) in some places of samples, and these defects were avoided during the selection of material chosed for all tests. All chosed samples fulfill requirements for class C according to ISO 5817 [113].

4.2.2 Tensile Testing

Tensile test specimens were machined out of the base metal and welded samples according to ASME Sect. IX standard [114]. The mechanical behavior for 5083 H321 and

H116 of the base metal are shown in Table 4.2.2 and for welded samples are shown in Table 4.2.3.

Table 4.2.2 Mechanical behaviour of the base metal

	D mm	a mm	A mm^2	Fm N	Rp_{02} MPa	Rm MPa	At %
H116 T1	4.41	6.50	28.67	9574	222	334	15.68
H116 T2	4.41	6.52	28.75	9606	222	334	15.67
H116 L1	4.42	6.5	28.73	9969	262	347	13.21
H116 L2	4.4	6.49	28.56	9921	261	347	14.79
H321 T1	4.52	6.44	29.11	10604	260	364	15.99
H321 T2	4.53	6.52	29.54	10681	256	362	14.86
H321 L1	4.5	6.49	29.21	10865	262	372	13.91
H321 L2	4.45	6.5	28.93	10802	268	373	12.17

The results of yield strength for base metal are ranged from 222 to 268 MPa, and the ultimate tensile strength ranged to 362-373 MPa, while the percentage of elongation ranged to 12.17-15.99 %. Comparing the ultimate tensile strength properties of base metal with each other alloys of 5083H321 has higher strength properties than alloys 5083H116.

Table 4.2.3 Mechanical behaviour of welded samples

Sample code		Pm (N)	Rm (MPa)	Fracture position	Heat Input kJ/mm	Av. Rm (MPa)
H116	M1-1a	34400	314	HAZ	0.6985	290
	M1-1b	29320	267	HAZ		
	MP1-1a	31040	279	FL	0.51197	285
	MP1-1b	31800	291	FL		
	T1-3a	29800	272	HAZ	1.1138	275
	T1-3b	30580	279	FL		
	TP1-3a	27850	254	HAZ	1.0025	243
	TP1-3b	25400	232	FL		
H321	M3-1a	32640	298	FL	0.6826	291
	M3-1b	31135	284	FL		
	MP3-2a	31740	290	HAZ	0.51197	290
	MP3-2b	31570	289	HAZ		
	T3-1a	31040	280	FL	0.9237	285
	T3-1b	31800	290	HAZ		
	TP3-1a	30460	278	HAZ	0.7975	265
	TP3-1b	27700	253	HAZ		

Where:

a – Thickness of the specimens (= 4.4 mm)

b – Width of the specimens (for base metal = 6.5 mm and for welded samples = 24.9 mm)

L_0 - gauge length before application of force (for base metal = 50 mm and for welded samples = 59.14 mm).

Pm - maximum force - the greatest force which the test piece withstands during the test (N).

Rm - tensile strength - stress, corresponding to the maximum force Pm (MPa).

From Figure 4.2.1 the results of yield strength properties for all tested alloys after welding, by applying different welding conditions are ranged from 232 MPa to 314 MPa, and for H116 the tensile strength of MIG welded alloys are higher compared to alloy TIG by 9.9%, and also the pulse welded samples have lower values of strength compared with the convential welded samples by 11.2%, while also for H321 the tensile strength of MIG welded alloy are higher compared to alloy TIG by 5.3%, and also the pulse welded samples have lower values of strength compared with the convential welded samples by 7%. The value of Heat Input for MIG welding samples are higher than that of TIG welding samples and for MIG welding samples there was no clear difference between H116 and H321 whether for TIG welding samples the heat input of H116 is higher than H321. The pulse process doesn't have a clear affect.

Table 4.2.3 reveal that the failure in uniaxial tension was mostly positioned in the heat affected zone (HAZ) and in some cases passes also through the fusion line (FL). The results are presented graphically in Figure 4.2.1.

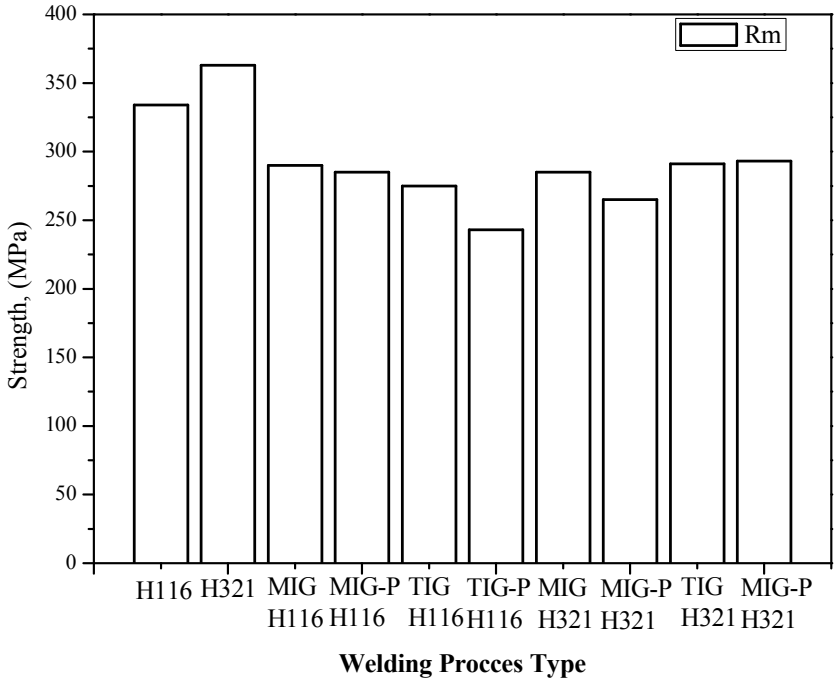


Figure 4.2.1 Comparison strength values with welded joints

4.2.3 Bending results

Bending test results of weldments are shown in Table 4.2.4

Table 4.2.4 Bending test results of the welded samples

Designation	Bending Around	Tensile Side	Fracture Angle	Fracture Position
M1-1b1	Face	Root	99	Fusion Line
M1-1b2	Root	Face	117	Fusion Line
MP1-1b1	Face	Root	88	Fusion Line
MP1-1b2	Root	Face	88	Fusion Line
T1-3a	Face	Root	157	HAZ
T1-3b	Root	Face	116	Fusion Line
TP1-3a	Face	Root	89	Weld Metal
TP1-3b	Root	Face	105	Weld Metal
M3-1b2	Face	Root	166	Fusion Line
M3-1b1	Root	Face	106	Fusion Line
MP3-2b2	Face	Root	110	Fusion Line
MP3-2b1	Root	Face	111	Fusion Line

T3-1a	Face	Root	132	Weld Metal
T3-1b	Root	Face	77	HAZ
TP3-1a	Face	Root	180	Without Fracture
TP-31b	Root	Face	108	HAZ

From Table 4.2.4 it is seen that all MIG welding specimens are fractured in Fusion Line while for TIG welding specimens the fracture position alter from place to other, and only TIG-pulse H321 specimen was not fractured after bended to 180°, the fracture angle for all samples are between 77 and 180, which may be accepted.

4.2.4 Hardness measurements

Micro hardness Vickers test was performed on the welded sample under a load of 300 g. The micro hardness was measured on an interval of 0.5 mm through the weld.

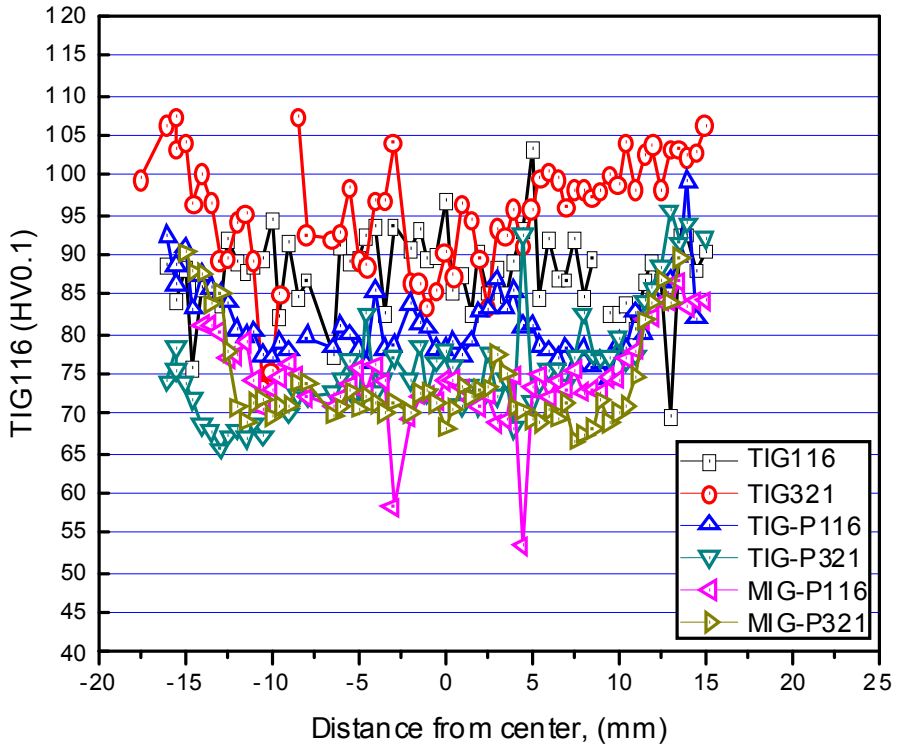


Figure 4.2.2 Micro-Hardness of the welded samples.

As shown in Figure 4.2.2, the micro-hardness values for all samples in weld metal returned a value between 68 and 97 HV0.1, and in HAZ the values are between 70 and 99 HV0.1, while in the base metal values are between 65 and 108 HV0.1. The transformation between the parent plate and HAZ occurred at distance of –16 to +13.5

mm from the centre of the weld, which correlated with the changes in the microstructure.

The results of Vickers hardness in terms of HV5 are shown in Figure 4.2.3.

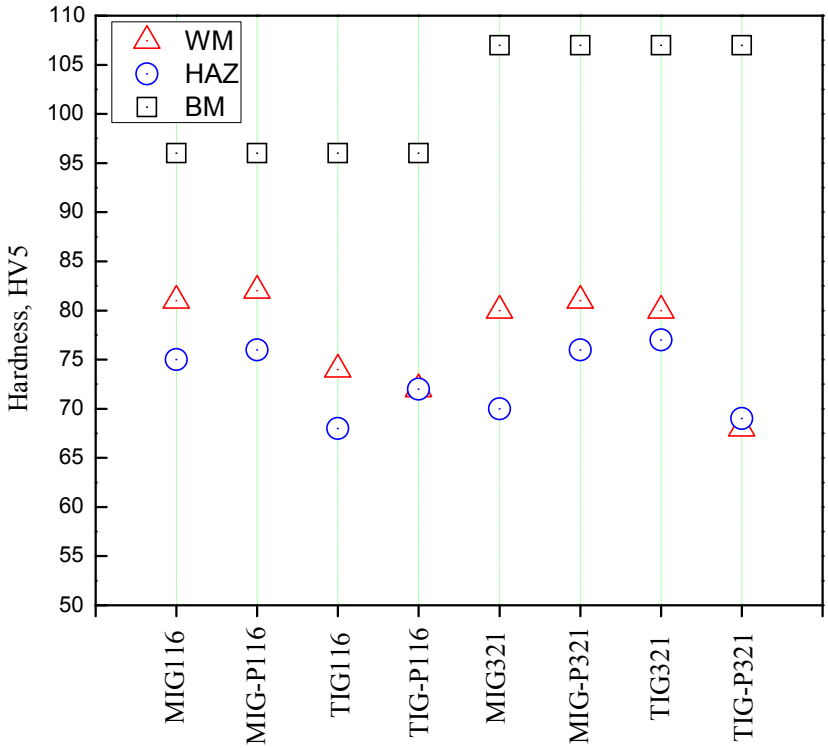


Figure 4.2.3 Vickers Hardness of the welded samples.

From Figure 4.2.3, the hardness values for H116 samples in weld metal returned a value between 72 and 82 HV5, and in HAZ the values are between 68 and 76 HV5, while in the base metal value is 96 HV5 and for H321 samples in weld metal returned a value between 68 and 81 HV5, and in HAZ the values are between 69 and 77 HV5, while in the base metal value is 107 HV5.

For base metal the hardness of H321 samples are higher than H116 samples by 10%. For HAZ the hardness of MIG samples are higher than that of TIG samples, also the pulse process decreases the hardness.

4.2.5 Electrical Resistivity

The electrical resistivity changes in the samples treated by different welding procedures are shown in Figure 4.2.4 and Figure 4.2.5.

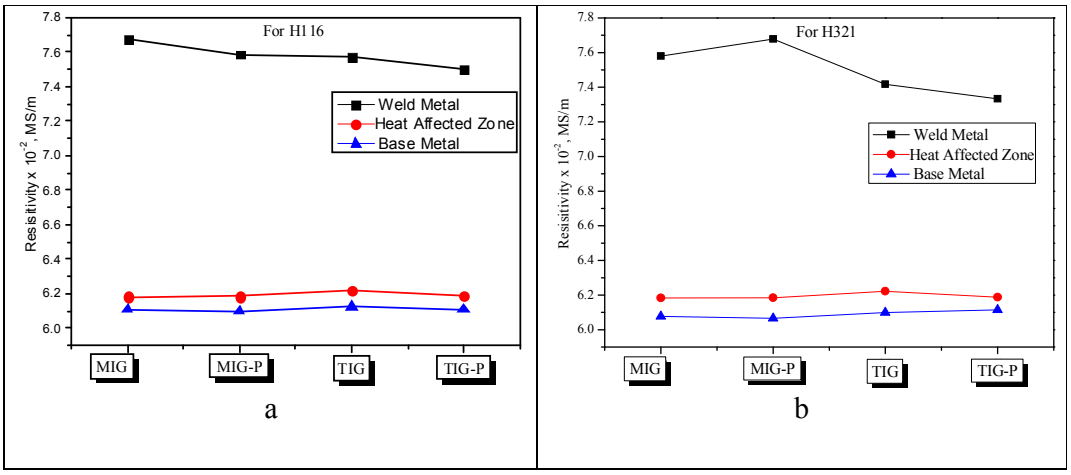


Figure 4.2.4 Electrical resistivity variation for different welding process.

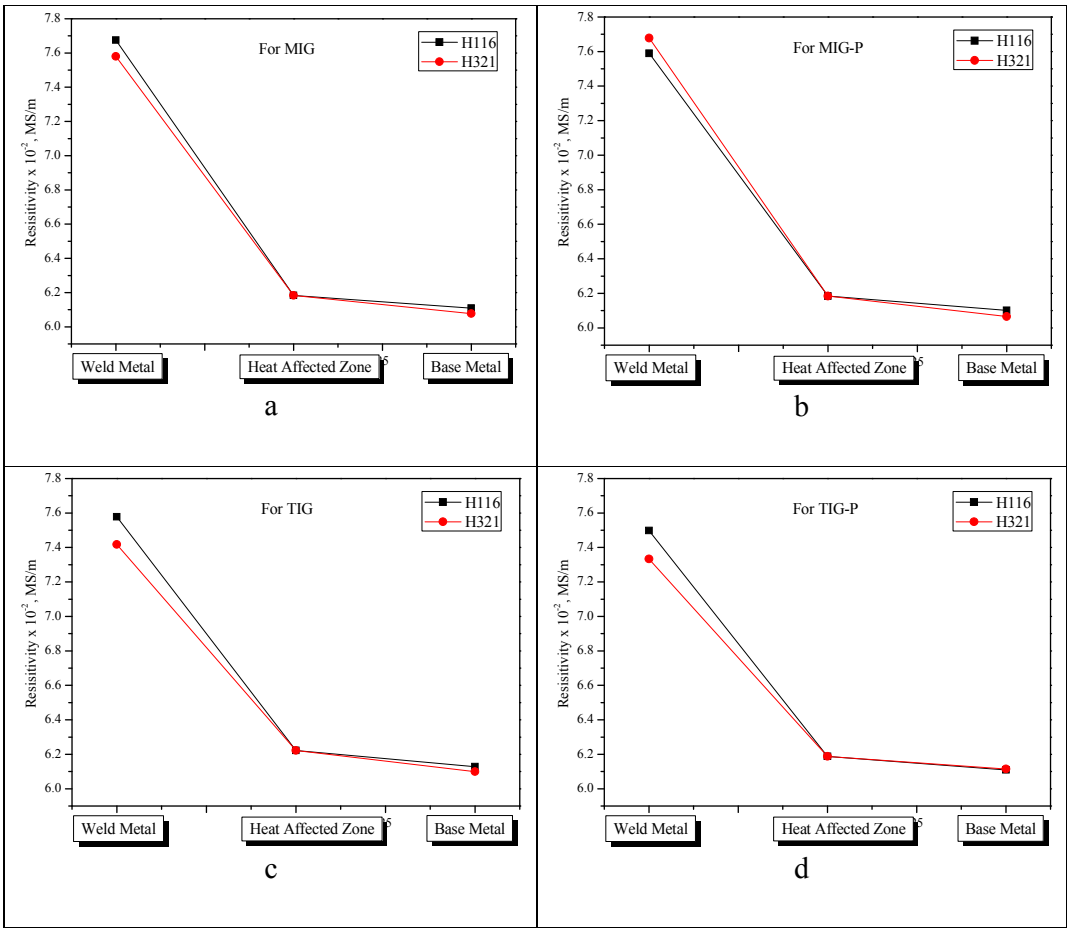


Figure 4.2.5 Electrical resistivity variation for different welding process.

From the Figure 4.2.4 and Figure 4.2.5 it is clear that the electrical resistivity of weld metal is higher than the electrical resistivity of base metal and heat affected zone

for all welding processes and for both materials. Also type of welding process doesn't affect the electrical resistivity.

4.2.6 Corrosion test results

4.2.6.1 Intergranular Corrosion

Figure 4.2.6 shows the ratio of mass loss per surface area of the tested samples.

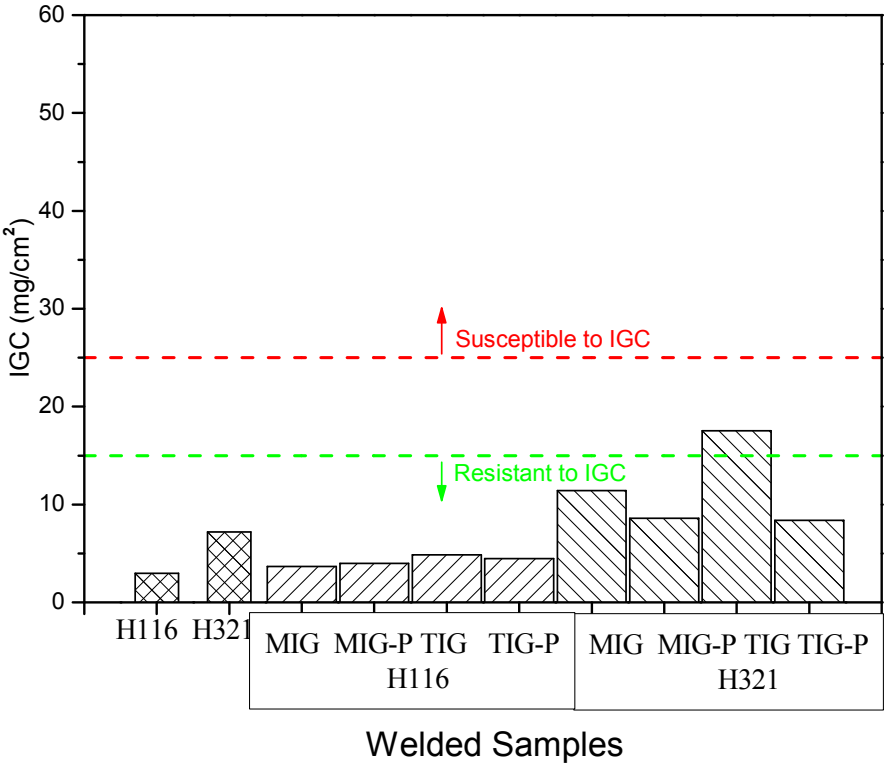


Figure 4.2.6 Results of Intergranular Corrosion (G67) testing for different welded samples

From Figure 4.2.6 it can be seen that the mass losses of all samples are below resistant region (15 mg/cm^2), except for TIG H321 the mass loss is between the resistant regions and the susceptible region (15 mg/cm^2 and 25 mg/cm^2), also the H116 material is more resistant than H321.

4.2.6.2 Exfoliation and Pitting Corrosion

The surface appearance of the specimens following the exfoliation immersion testing for 24 h is shown in figure 4.2.7. Generally, the weld regions and the parent alloy are almost free from exfoliation corrosion, indicating similarity in the corrosion behavior of the parent alloy and the weld regions.

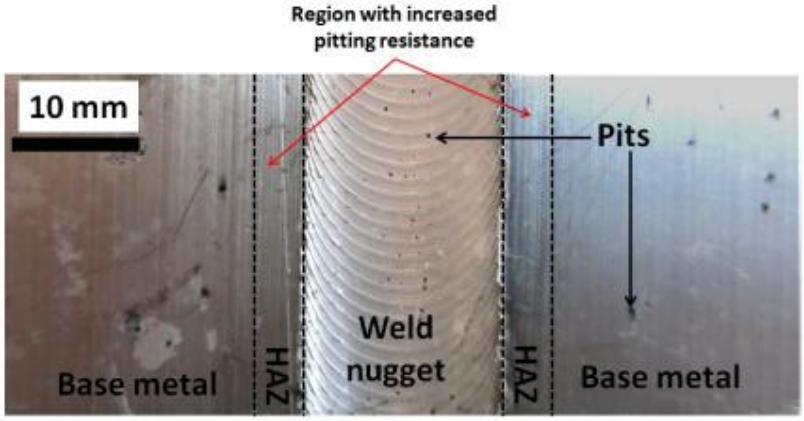
Table 4.2.5 Corrosion stability for welded Samples.

Condition	Material	$(m_1-m_2)/A$, mg/cm^2	IGC	Face	Exfoliation	Pitting
H116	Base Metal	2.9702	Resistant – N	1	A	N
				2	A	N
H321		7.1933	Resistant – N	1	A	N
				2	A	N
H116	MIG	3.6677	Resistant – N	1	A	B
				2	A	B
	MIG-P	3.9857	Resistant – N	1	A	N
				2	A	N
	TIG	4.8592	Resistant – N	1	A	N
				2	A	N
	TIG-P	4.4585	Resistant – N	1	A	A
				2	A	A
H321	MIG	11.4033	Resistant – N	1	A	A
				2	A	A
	MIG-P	8.6052	Resistant – N	1	A	B
				2	A	B
	TIG	17.5168	Resistant – A	1	A	N
				2	A	N
	TIG-P	8.3729	Resistant – N	1	A	B
				2	A	B

NAMLT Intergranular Corrosion Testing (Susceptible if the mass loss < 25 mg/cm^2 Resistance-A if the mass loss > 25 mg/cm^2 and < 15 mg/cm^2, Resistance-N if the mass loss > 15 mg/cm^2)
ASSET Tested Exfoliation Susceptible (A, B, C, D-Four Degrees of Exfoliation).
ASSET Pitting Corrosion Testing (N-No appreciable attack; A, B, C-Three Degrees of Pitting)

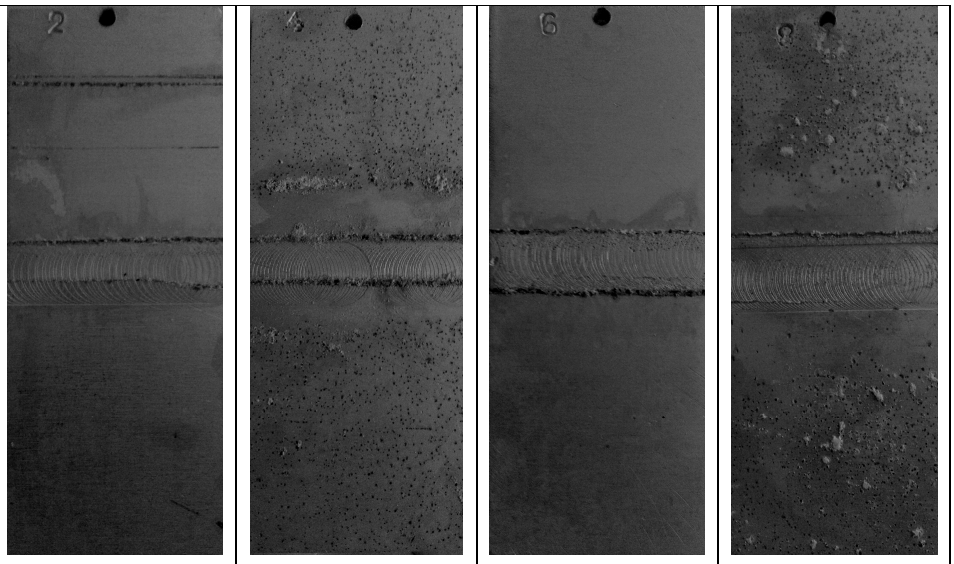
As it can be seen in Figure 4.2.6 all alloys are resistant to intergranular corrosion, while for exfoliation and pitting corrosion all alloys are of grade A, A/B or N/A which means a little attack is detected and all the samples are resistant to corrosion.

In Figure 4.2.7 and Figure 4.2.8 photos of welded samples are shown and all the observed pits are highlighted with black dots. Moreover, from the figure the improved resistance to pitting corrosion in the heat affected zone may be observed. Also, the etched layer close to the fusion zone should be noted.



	a.	b.	c.	d.
Exfoliation	A	A	A	A
Pitting	A	A	B	A

Figure 4.2.7 Exfoliation and pitting corrosion of H116 samples (a.) TIG, (b.) TIG Pulse, (c.) MIG (d.) MIG Pulse



	a.	b.	c.	d.
Exfoliation	A	A	A	A
Pitting	A	B	A	B

Figure 4.2.8 Exfoliation and pitting corrosion of H321 samples (a.) TIG, (b.) TIG Pulse, (c.) MIG (d.) MIG Pulse

The photos in Figure 4.2.7 and Figure 4.2.8 show that the WM and HAZ are clear without corrosion (Exfoliation or Pitting) only a little in the fusion line which is acceptable according to ASSET test. But there was some amount of pitting corrosion of type B in the base metal of the pulse welded samples.

4.2.7 Metallographic observations results

4.2.7.1 Macrostructure of Welded Parts

Macrographs were produced using a Meiji EMZ TR optical microscope, with oblique illumination. The electro-etched surface had sufficient relief under such lighting to show the macrostructure of the weld regions. Images were captured using a video camera and printed with a video printer. The photo and the macro-photo of the joint are shown in Figure 4.2.9 & Figure 4.2.10.

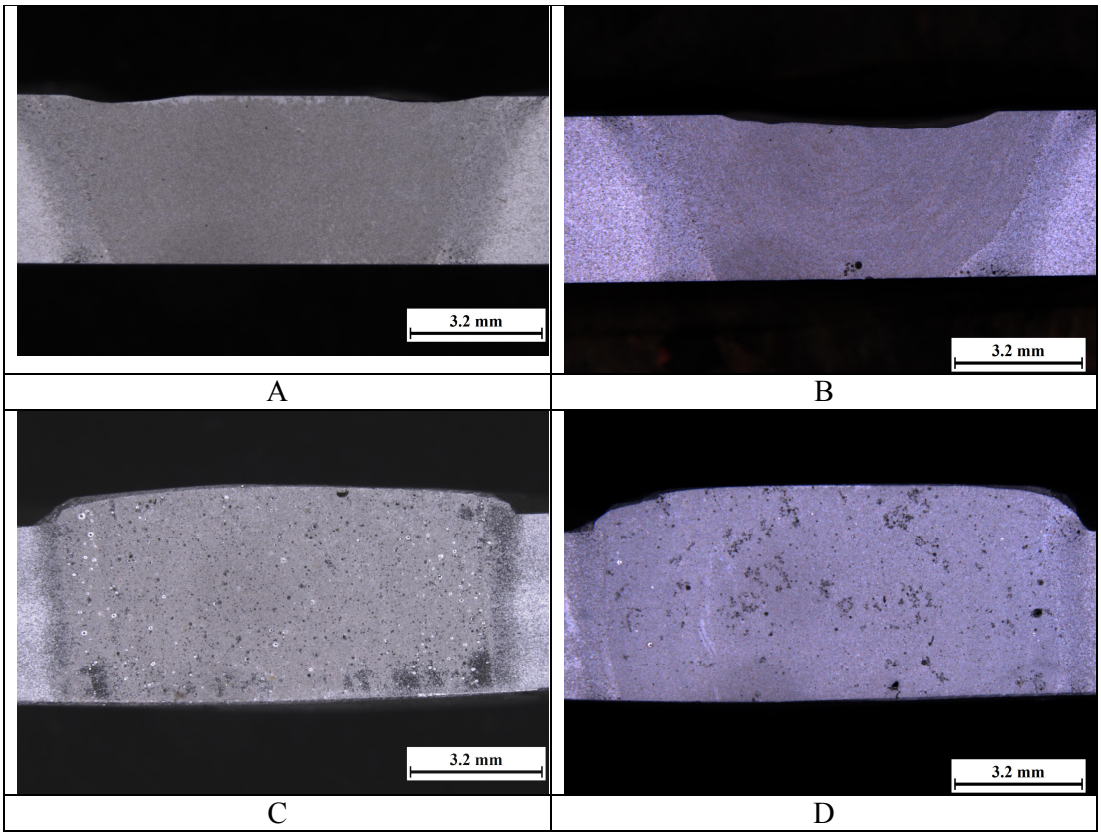
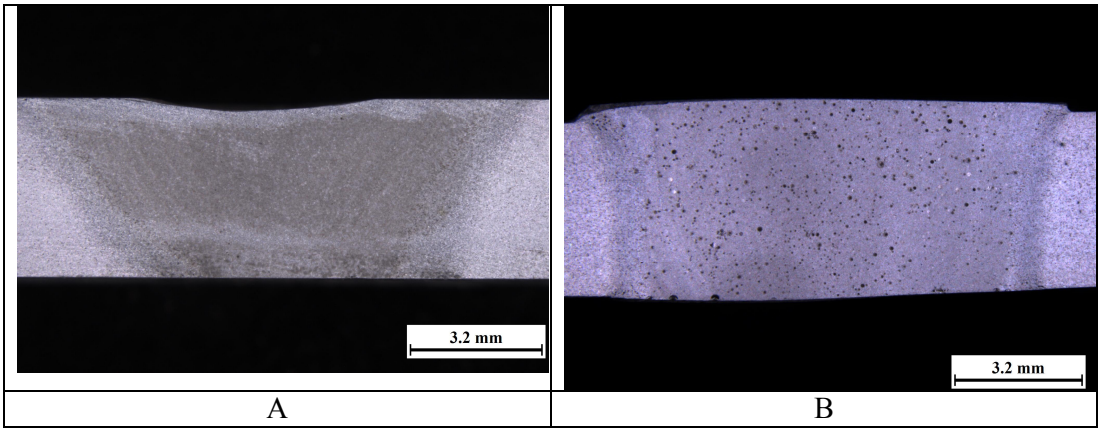
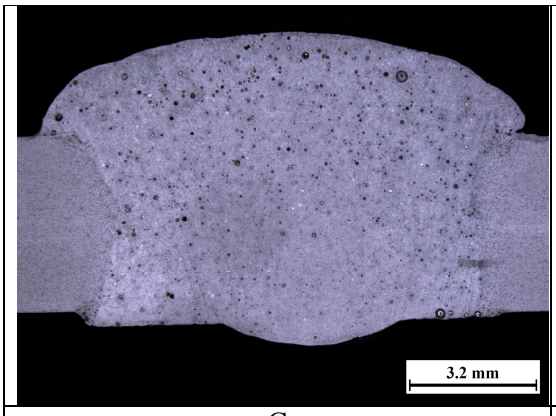


Figure 4.2.9 Macrographs of 5083H116 : (a) TIG welded, (b) TIG-Pulse welded, (c.) MIG (d.) MIG Pulse.

Figure 4.2.9 shows the macrostructure of welded joints after welding. Observation of macrostructure has shown, that the width of the heat affected zone (HAZ) is relatively small, no inhomogeneities were found in the joint. It can be seen from the figure also that for TIG welded specimens there is no porosities and all the zones are clear, while for MIG welded specimens there are some porosities





C D

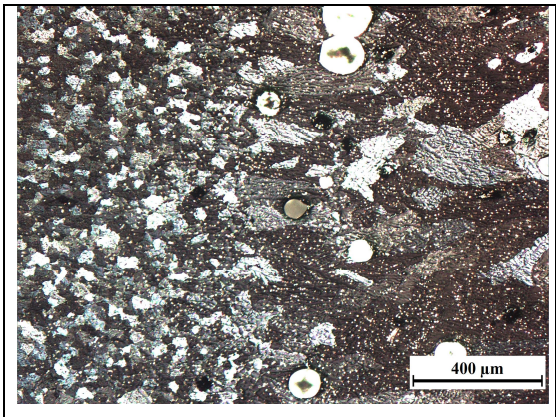
Figure 4.2.10 Macrographs of 5083H321 : (a) TIG welded, (b) TIG-Pulse welded, (c) MIG welded, (d) MIG-Pulse welded.

When observing from cross section of the weld joint, there was no significant difference of the fusion zone profile between all zones.

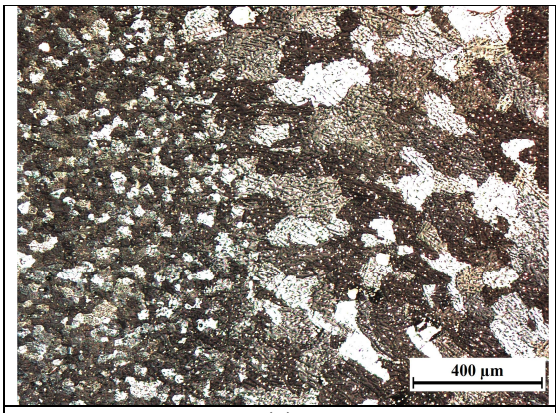
The macrostructure is shown in the Figure 4.2.9 and Figure 4.2.10. Weld dilution is uniform. A hint of porosity is observed in all samples. In MIG welded samples the weld dilution is high weld and also the bead width is high. Weld penetration is almost the same for all sample and there is more weld deposition in the weld area.

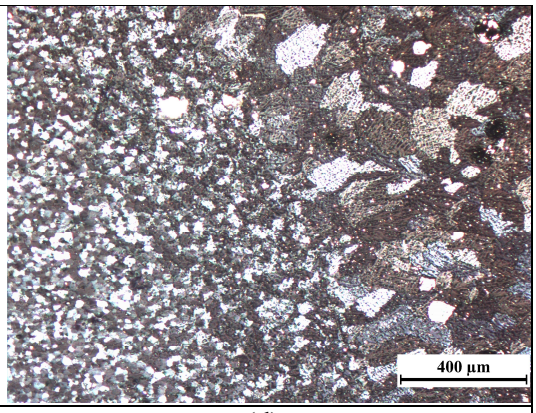
4.2.7.2 Microstructure of Welded Parts

Microstructure of base metal, weld metal and HAZ of the selected samples are shown in Figure 4.2.11, while for other samples the figures are shown in Appendix III (Figures 7.4.3 – 7.4.10).



(a) (b)



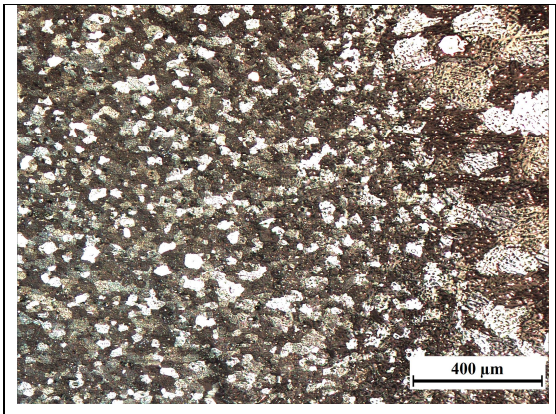


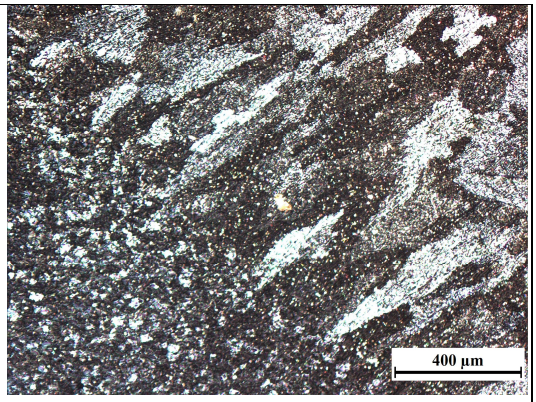
(c)	(d)

(a) H116, MIG	(b) H321, MIG	(c) H116, MIG Pulse	(d) H321, MIG Pulse

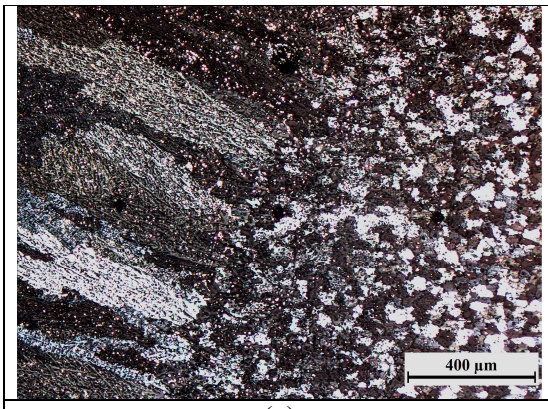
Figure 4.2.11 Microstructure of Base Metal, Weld Metal and Heat Affected Zone of etched 5083 samples MIG welded

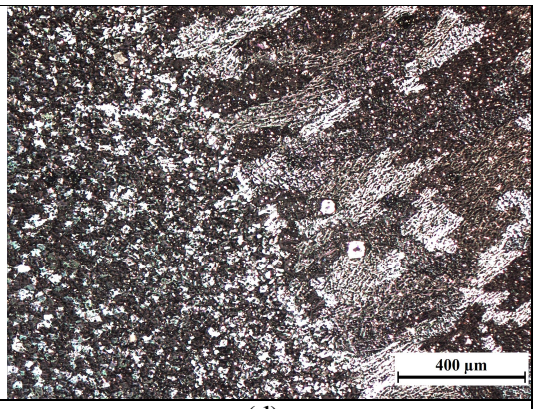
The welded joint shows typically cast dendritic structure. The microstructure of the fusion zone near the weld is composed of equiaxed grain which are disparate in size, and some columnar grains along the direction of heat radiation. While fine equiaxed grains exist in the fusion zone near base metal with a relatively uniform size. With coarsening of grains in the HAZ to different degree, the most remarkable coarsening appears near the fusion zone. The base 5083 Al alloy is entirely composed of fully recrystallized structure.





(a)	(b)





(c)		(d)	
(a) H116, TIG	(b) H321, TIG	(c) H116, TIG Pulse	(d) H321, TIG Pulse

Figure 4.2.12 Microstructure of Base Metal, Weld Metal and Heat Affected Zone of etched 5083 samples TIG welded

The typical microstructure of the polished samples of weld metal, fusion line and heat affected zone are shown in Figure in Appendix.

CHAPTER 5

5. Discussion

5.1 Thermo-mechanical processing

5.1.1 Mechanical properties

Degradation of the corrosion properties of Al-Mg alloys containing 4-5 wt% Mg, such as AA 5083 alloy, in certain enviroments limits their application as a material of choice for structural components of marine vehicles. The extent of susceptibility toward different forms of corrosion depends on environment, materials chemistry, fabrication and thermo-mechanical processing.

Table 5.1.1 Properties of the AA 5083 required by ASTM standard for H321 state.

Composition Specification (%)					(single values are maxima except as noted)					
Alloy	Si	Fe	Cu	Mn	Mg	Cr	Zn	Ti	Others	
5083	0.40	0.40	0.10	0.10-1.0	4.0-4.9	0.05-0.25	0.25	0.15	0.05	0.15

Mechanical Property Specification			(single values are minima except as noted)			
Alloy & Temper	Spec.	Tensile Strength (MPa)	Yield Strength 0.2% Proof (MPa)	Elongation (% in 50mm) minimum for sheet or plate thicknesses shown		
				All gauges (Note 2)	5.0-12.5mm	6.31-80.0mm
5083-H116	B928M	305 min(1)	215 min(1)	10		
5083-H321	B928M	305-385(1)	215 min(1)	12-10		

1. Properties for H116 and H321 reduced at thickness over 40mm, tensile strength 285MPa min and yield strength 200MPa min.
2. Elongations specified for H116 and H321 vary slightly depending on gauge. Measurement gauge length also varies. Refer to ASTM B928M for details.

In order to develop optimal thermo-mechanical regime for the studied Zn modified Al-5.1wt%Mg-0.7wt%Mn alloy plates that would provide desired combination of mechanical and corrosion properties (Table 5.1.1.) the effect of multiple processing parameters was evaluated.

The stress–strain curves (Figure 4.1.1) and the data given in Table 4.1.1 for the as received material demonstrate that with increasing the percentage of deformation up to 85%, the hardness, yield and ultimate tensile strengths increased rapidly (HB 75 - 120), (YS 140-440MPa) and (UTS 318-470MPa), respectively, reflecting rather high degree of work hardening ability.

After the as received material was processed to 3.0-2.34 mm (see Figure 3.2.1) with the finial cold rolling deformation 16%-54% and final annealing at the temperature range of 220°C-280°C for 1-3hr, the hardness was rather decreasing by increasing temperature, especially after annealing of 250°C, unless recrystallization come into play (Figure 4.1.2). Also, after annealing at higher temperatures as 260°C or 280°C, the pre-deformation increase brought also a hardness drop due to favorizing the recrystallization process.

For selected samples the tensile properties shown in Figure 4.1.6, revealed that the strength parameters, R_m and $R_{0.2}$ depend on the degree of cold rolling and temperature of the final annealing. The YS of 16.7% deformed samples do not meet the minimum required by the standard ASTM B929/B 928M-04a, while the 42% deformed samples meet the requirements in terms of strength parameters (R_m and $R_{0.2}$) for the annealing temperature interval 220°C-260°C for annealing time of 2 hours. Annealing at 280°C/2h causes a sudden drop of strength due to the occurrence of recrystallization and grain growth, what is also recognized clearly in the hardness drop.

The elongations achieved for both reductions and final annealings are in the range of acceptable values (changed from 11% to 20% for the 42% pre-deformed samples and from 14% to 20% for 16.7% pre-deformed samples) according the ASTM B929/B 928M-04a standard where it was specified to 10%.

5.2. Corrosion Resistance and Microstructure

5.2.1. Intergranular Corrosion

The corrosion testing of the studied alloy plates revealed that, in addition to the final annealing temperature, significant effect on the IGC susceptibility had the amount of

previous cold work (Figures 4.1.12 and 4.1.13). Varied amount of the cold work produced IGC susceptible and IGC resistant states, although post-anneal conditions, such as 2h at 240°C, were the same. There is a clear distinction between substructures of the specimens that underwent different amount of the cold work as characterization of the material deformed for 16% and 42% showed (Figure 4.1.22). Deformation of 16 % resulted in high dislocation density, but no organized substructure was developed (Figure 4.1.22a). Only occasional subgrains were observed. Substructure of the specimen deformed 42% is characterized by high dislocation density and a number of interfaces created by fragmentation of the original grains during heavy deformation (Figure 4.1.22b). In addition, higher reductions resulted in more homogeneous deformation as well as distribution of the primary $Al_6(Mn,Fe)$ particles (Figure 4.1.23). Such microstructures set the stage for the precipitation during final annealing at 220°C-260 °C.

Deformation substructure did not affect morphology of the grain boundary precipitation during annealing at the higher temperatures, 260-280°C, and the lowest, 220°C, temperature. However, at the intermediate annealing temperature, 240°C, it is evident that the cold work and resulting deformation substructure affected precipitation morphology (Figures 4.1.26 and 4.1.30). Considering that a nearly continuous coverage of the grain boundaries was observed in heavily deformed material annealed at the lowest annealing temperature, 220°C, and in the material that underwent smaller amount of deformation and annealed at the intermediate temperature, 240°C, morphology and distribution of the precipitated grain boundary phases (Figures 4.1.26 and 4.1.30) appears to be controlled by kinetic parameters. For annealing conditions of 2h at 240°C, certain deformation substructure, such that can facilitate precipitation process through the excess of fast diffusion paths – pipe and grain boundary diffusion as well as the presence of additional nucleation sites like fine dispersion of intermetallic particles, was necessary for precipitation of the discrete precipitates. At the higher temperature, 260°C, discrete precipitates (Figure 4.1.26a) were formed regardless of pre-existing deformation substructure, indicating that there were no kinetic constraints to the precipitation mechanism.

Table 5.2.1 Average Composition of the Precipitated Grain Boundary Phases and Aluminum Matrix (Weight Percent) from EDS Data.[106]

	% Red.	Mg	Al	Mn	Cu	Zn	Mg/Zn
Grain boundary precipitation	16	23.84 ± 6.01	64.25 ± 10.39	0	1.46 ± 0.57	10.4 ± 4.51	2.16 ± 0.30
	42	22.20 ± 5.70	0.51 ± 0.39	0	0.51 ± 0.39	11.30 ± 5.30	2.13 ± 0.47
Matrix (s.s.)	16	4.27 ± 0.42	94.86 ± 0.71	0.11 ± 0.08	0	0.20 ± 0.07	-
	42	3.78 ± 0.16	95.13 ± 0.96	0.16 ± 0.28	0	0.16 ± 0.13	-

While the amount of cold work had an effect on the precipitated grain boundary phases morphology during precipitation at 240°C, EDS analysis showed that in the both cases, at 16% and 42% thickness reductions, precipitated grain boundary phases were ternary Al-Mg-Zn enriched with a small amount of Cu (Figure 4.1.31). From EDS spectra, it was not possible to determine exact stoichiometry of the precipitate, due to the strong Al signal from the underlying Al matrix. However, Mg/Zn ratio appears to be similar for the specimens deformed 16% (IGC susceptible state) and 42% (IGC resistant state) (Table 5.1.1).

In standard Al-Mg alloys like AA 5083, annealing below 300°C should result in precipitation of β-phase (Al_3Mg_2) [95,107]. However, investigations of Carroll et al. [23] showed that low level Zn additions (0.58-0.7 wt%) in AA 5083 resulted in the replacement of the β-phase by a ternary Al-Mg-Zn τ-phase. Furthermore, Cu, at the level as low as 0.073wt%, segregated toward the grain boundaries and was incorporated into the grain boundary phase [108]. The results of this work show that at even lower levels of 0.5wt% Zn and 0.013wt% Cu, in the high Mg (5.1wt%) aluminium alloy, the precipitated grain boundary phases contained both Zn and Cu (Figure 4.1.31). Al-Mg-Zn τ-phase has better corrosion properties than the β-phase [23], so there is a possibility that the variation of the phase composition of the grain boundary precipitates is responsible for the observed difference in IGC susceptibility. On the other hand, lack of significant difference in the chemistry of the precipitates, ternary Al-Mg-Zn characterizes both IGC susceptible (16% red.+ 2h/240°C) and IGC resistant (42% red.+ 2h/240°C) states, suggests that the precipitates morphology and distribution are critical factors for the IGC susceptibility.

Chemical composition of the aluminium matrix, as determined by EDS, showed lower content of Mg and Zn in the solid solution of IGC resistant (42% red.+ 2h/240°C) specimens than of the IGC susceptible (16% red.+ 2h/240°C) specimens (Table 5.1.1). Apparently, larger amount of Mg and Zn precipitated out of solid solution in the IGC resistant state. Such finding is in an agreement with the results of the electrical resistivity measurements (Figure 4.1.8).

While the increase in the electrical resistivity above referent level of the specimens that underwent cold work is related to the increase of density of the lattice defects, the causes of the resistivity decrease observed after the final annealing are more complex as both recovery and precipitation processes occurred during the treatment. After the final anneal of 2h at 240 °C, total change in the resistivity of the specimens underwent 42 % reduction (IGC resistant state) is larger ($\Delta\rho=0.29\times10^{-8}$ Ωm) than of the specimens with 16 % reduction (IGC susceptible state) ($\Delta\rho=0.11\times10^{-8}$ Ωm). Even with respect to the referent state, the resistivity change is $\Delta\rho=0.12\times10^{-8}$ Ωm and $\Delta\rho=0.05\times10^{-8}$ Ωm for 42 % (IGC resistant state) and 16 % (IGC susceptible state), respectively. In the temperature range of the final anneal, 220-280 °C, expected precipitation processes are limited to the reactions involving formation Mg rich phases. Based on the method described in [109] and assuming that the electrical resistivity drop below the referent state is mostly due the precipitation of Mg and Zn out of solid solution, leads to a rough estimate of the volume fraction of the precipitated phase of 0.5 % and 1.3 %, for the specimens annealed 2 h at 240 °C and deformed 16 % (IGC susceptible state) and 42 % (IGC resistant state), respectively.

More extensive precipitation in the specimen deformed 42 % (IGC resistant state) is in an agreement with the optical microscopy observations (Figures 4.1.26 e and f) that coarser and more profuse precipitation occurred in the specimens deformed 42%. Abundance of the Mg rich precipitation in grain interiors of the specimens deformed 42% is likely to be due to finer and more uniformly distributed $Al_6(Mn,Fe)$ particles that act as nucleation sites for the precipitation and higher density of the crystal defects that provide fast diffusion paths similar to observations by Goswami et al. [43] and Zhu et al. [110] in AA5083. Massive precipitates at the interfaces of the intermetallic particles were also observed by TEM. Precipitation in grain's interiors decreases content of Mg and Zn solutes in the solid solution and hence decreases electrical resistivity but does

not contribute toward IGC susceptibility. Such observations support the thesis that morphology of the grain boundary precipitation and precipitate distribution are determining factor for the IGC susceptibility, even if the larger amount of corrosion prone phase was precipitated out of solid solution. The coverage of the grain boundaries by the continuous and semi-continuous film of ternary Al-Mg-Zn phase enriched with small amounts of Cu appears to be the key feature of IGC susceptible states, while the discrete precipitation at the grain boundaries is the main characteristic of IGC resistant states.

Such conclusion is further supported by observations of the surface morphologies after the immersion into the nitric acid during the NAML test. Unaffected grain interiors, corrosion confined to the grain boundaries that results in grain fall out appear to be the signature of the IGC susceptible states while corrosion of both grain boundaries and grain interiors is characteristic of IGC resistant states (Figures 4.1.27-29). Similar morphological features were also observed in the 5083 alloy that underwent different thermo-mechanical regimes [49]. In general, cause of corrosion in Al-Mg alloys is a large difference between corrosion potential of anodic β-phase and Al-matrix. Corrosion of the grain boundaries as well as the grain interiors in IGC resistant specimens indicates lower potential difference between them, than in the case of IGC susceptible state in which grain boundaries were solely attacked. According to some early models [111], precipitation within grains actually decreased potential difference between the matrix and anodic grain boundaries covered with the β-phase, decreasing the driving force for the preferential corrosion/ attack on the grain boundaries.

5.2.2. Exfoliation and Pitting Corrosion

It has been shown [112,113] that the grain structure developed through different thermo-mechanical treatments can have an important role in development of the exfoliation corrosion. The major influence is related to the grain aspect ratio or the grain flatness that can provide a specific long – surface path for IGC, and formation of corrosion products with a higher specific volume than the matrix in a few surface layers. In that way the expansion tendency introduces compressive stress that are able to lift the surface grains and form surface blisters.

In this work, harmful C-level exfoliation was observed only after 54% cold rolling deformation and subsequent low temperature annealing as 220°C (Figure

4.1.18). In that case, the recovery degree was low or absent, as it is indicated by the unchanged hardness level during annealing at 220°C with respect to the cold rolled state (Figure 4.1.3). Microstructural characterization revealed highly elongated grains (Figure 4.1.24) with the aspect ratio about 5.7 (Figure 4.1.25). In samples with a lower grain aspect ratio of ~ 2.3 after 30% deformation, or ~ 1.7 after 16.7% deformation, unacceptable exfoliation level of the attack was not observed or even the exfoliation was completely absent (Figures 4.1.18). Such observations point out on the importance of the grain flatness in appearance of exfoliation type corrosion. It should also be emphasized that, although in the specimens deformed 16.7% the general IGC susceptibility was the highest (Figure 4.1.13), the grain flattening was sufficiently low, so the exfoliation could not develop, i.e. it was graded as A-B. Apparently, the grain flatness was a dominant parameter in developing the exfoliation corrosion, which is not necessarily correlated to IGC susceptibility.

The grain aspect ratio increased with increasing the annealing temperature (Figure 4.1.24), but detrimental level of exfoliation attack was not observed. It was assumed that general IGC susceptibility was reduced in such extent so appearance of exfoliation appearance or any other type of intercrystalline corrosion was supressed. Therefore, the specimens deformed 54% with unrecrystallized structure and the grain aspect ratio of 5.5, i.e. after annealing at 220°C, were prone to the exfoliation while the recrystallized structure with a same grain aspect ratio of 5.7, i.e. after annealing at 280°C) was completely resistant to exfoliation as the IGC was suppressed too. As in the case of IGC susceptibility, the change in propensity toward the exfoliation is related to the morphology of precipitated β-phase i.e. the change of continuous coverage after the low temperature annealing to a discontinuous discrete β – phase morphology after the higher temperature annealing such as 260°C and 280°C. Therefore, the exfoliation corrosion control in practice, should be considered in a limited range of structure states which are also fully resistant to IGC. However, according to our results the tendency to exfoliation type of corrosion in all circumstances was related to a flattened grain structure, i.e. it was suppressed in case of structure with a grain aspect ratio below some critical value.

On the other hand, lowering the grain aspect ratio or having a structure with less elongated grains, the pitting type corrosion is thought to be the active process of intercrystalline corrosion [112,113]. In this experiment unacceptable C level pitting was

not detected (Figure 4.1.19) due to the fact that an equiaxed grain structure did not develop during the thermo-mechanical processing (Figure 4.1.24). The appearance of a severe but not harmful level of B pitting corrosion, observed in specimens deformed 40%-50% and annealed at 260°C and 280°C and (Figures 4.1.19 & 4.1.21), could be related to the recovery or recrystallization process manifested by the hardness drop (Figure 4.1.3). However, development of less flattened grain structure, which could enable the pitting by the progress of the intercrystalline corrosion over the shorter paths around the grains [112,113], was not observed.

Based on the results shown in Figure 4.1.19 it is difficult to correlate the degree of pitting susceptibility and a general intercrystalline corrosion (IGC) as the pitting was even stronger for the samples showing high IGC resistance.

5.3. Welding and Weldability

The indicator for weldability of Aluminium alloys are decreasing of mechanical properties susceptibility to cracks and decreasing of corrosion resistance.

5.3.1. Tensile properties test

The achieved mechanical properties of base metal for both materials H116 & H321 matching the properties of the 5083 alloys in H116/H321 conditions (YSmin=215/220MPa, UTSmin=305 MPa and emin= 10%, EN485-2:1999).

Figure 4.2.1 reveal that the failure in uniaxial tension was mostly positioned in the heat affected zone (HAZ) and in some cases passes also through the fusion line (FL). So, the HAZ appeared to be weaker than weld Metal (WM) in the base material, indicating that the heat input during welding was low enough to keep the HAZ harder than the WM. That problem of weaker HAZ in respect the surrounding material is known, but until now was not found a reliable way to improve the fracture resistance of the HAZ.

It can be seen that the specimens has offered better mechanical properties for the welding joint, the tensile strength was more than 230 MPa. Thus, the joint strength is approximately equivalent to that of the base material, which proved the welding parameters to be feasible. In most cases, the elastic limit or yield point is not clearly defined on the stress/strain curves for aluminum alloys. For this reason the point of departure from the elastic range has to be defined arbitrarily. The failure for the tensile test occurred at the heat affected zone and fusion line. Furthermore, the tensile test can ensure that the minimum strength requirements, as there are defined by the ASME Sec IX standards, are met after welding. For AA welds, the minimum strength prerequisite is the same with that of the parent metal, set at 270 MPa for the AA 5083. The obtained value is less about 4.5 % of the limit value.

The fusion line of these aluminum alloys is typically the weakest part of the joint and is the location of failure when the joint is loaded in tension. This is in contrast to most heat-treatable aluminum alloys, where the heat affected zone often is the weakest link.

5.3.2. Bending test

All the results of bending test recorded up to 180° bending angle fulfils the requirements of classification institutions ASME and are acceptable taking in our mind the high

strength of alloys. Welded joints with TIG have better bending properties compared to MIG due to the differences of mechanical properties. For all cases bending test specimens were used for assessments of susceptibility to hot cracks, the maximum values of hot cracks length were 6% which means that the resistance were good according to criterion of FISCO test.

5.3.3. The hardness

It shows that the hardness in the weld zone was greater than that in the heat affected zone (HAZ), as well as in the base metal, irrespective of thermal frequency. In Figure 4.2.2, it can be observed that the values of micro hardness tests vary between 65 and 108 HV0.1, and a softening is apparent for the HAZ area. The hardness values are generally scattered, so that it is very difficult to discern a HAZ. This can be attributed mainly to recrystallization in the weld and HAZ that had taken place during welding.

5.3.4. Electrical resistivity

Electrical resistivity was high in weld metal as shown in figure 4.2.5, indicating that the amount of main alloying elements (Cu and Mg) increases in solid solution.
As can be seen from the figure, the fusion zone in the MIG welded samples display the lowest conductivity due to the microstructure containing substantial amounts of Mg in solid solution. Moreover, for both set of welds, the electrical conductivity is observed to increase with increasing distance from the weld. As a result, the concentration of solute atoms in solid solution decreases with increasing distance from the weld. This increase is explained by re-precipitation of hardening precipitates which increases the mobility of electrons. Such observations are important when the susceptibility towards pitting corrosion is to be evaluated.

5.3.5. Corrosion Resistance

5.3.5.1. Intergranular Corrosion (G67 – NAML TEST):

The specimens are expected to be resistance to IGC. This is because of reducing the precipitation of magnesium rich phase at the grain boundaries and the grains interior, hence, most of the grain boundaries are free of the β- phase, consequently the resistance of the alloy to IGC is likely to be high.

It can be seen that there is no significant change in the ratio of mass loss over the different welding process. The range of mass losses difference is within 6 mg/cm^2 and

in addition all the results are in the non-susceptible range of material to intergranular corrosion considered to be <25 mg/cm^2. This small variation in mass loss suggests that it is important to study the microstructure of alloys to understand what is so significant about this alloy that makes it resistant to IGC.

5.3.5.2. Exfoliation and Pitting Corrosion (G66 – ASSE TEST)

The heat affected zone of both the MIG welded and TIG welded samples displayed increased resistance towards exfoliation and pitting corrosion. Moreover, the samples increased pitting resistance was observed even in the base metal close to the HAZ, such increased corrosion resistance for this region was unexpected and an obvious explanation could not be found. However, four possible suggestions for this increased corrosion resistance are listed below:

1. Favorable microstructure.
2. Thermal oxidation of oxide layer close to the weld.
3. Galvanic effects from the weld metal (MIG welded samples).
4. Selective corrosion of excess metal.

Moreover, it should be noted that the first explanation is believed to be the most probable due to extensive variations in the microstructure during the welding cycle.

The filler metal used during MIG welding was an Al-Mg alloy containing 4.8 wt % Mg. As a result, highly anodic Al_3Mg_2 precipitates are expected to form in the weld metal. As a result, selective dissolution of these particles are expected when exposed to a corrosive environment. Moreover, as the weld metal displayed corrosion potential more negative than the base metal, some galvanic effects during corrosion testing is expected. As a result, the base material in the HAZ close to the weld metal is expected to experience some protection from the weld metal, which acts as a sacrificial anode.

5.3.6. Metallographic observations

5.3.6.1. Macrostructure of Welded Parts

After the visual inspection of the plates, MIG and TIG welded joints were determined to be acceptable as no surface cracks and discontinuities were detected.

Investigations have shown that the distortion rates of fusion welded specimens, measured for MIG were higher than for TIG welded specimens, with 1.1 mm distortion rate. The results were within the acceptable limits.

5.3.6.2. Microstructure of Welded Parts

A metallographic examination of the base metal presents a granular structure slightly stretched out (Figure 4.2.11). The size of the grains varies between 20 and 40 μm.

The microstructure of the fusion zone is greatly different from base metal. Due to its high strength and hardness.

Metallographic study of the different regions of the weld shows that the Heat Affected Zone (HAZ) has a coarse grain structure than the base metal (Figure 4.2.11). This is due to thermal cycle caused by welding. While, the weld metal microstructure consists of columnar, epitaxial grains with a cellular or columnar-dendritic substructure (Figure 4.2.12).

Porosity forms during solidification due to the abrupt drop in hydrogen solubility during solidification. Porosity can best be avoided by minimizing hydrogen pickup during welding. This can be accomplished through proper joint preparation, use of high-grade shielding gas as argon with low-dew-point, and careful storage of filler wire (that is, protection from exposure to moisture and oil).

CHAPTER 6

6 Conclusions

6.1 For the as received material with increasing the percentage of deformation up to 85%, the hardness, yield and ultimate tensile strengths increased rapidly, reflecting rather high degree of work hardening ability, while after processing the hardness was rather decreasing by increasing temperature, especially after annealing of 250°C, unless recrystallization come into play, also, after annealing at higher temperatures the pre-deformation increase brought also a hardness drop due to the recrystallization process.

6.2 For selected samples the tensile properties revealed that the strength parameters depend on the degree of cold rolling and temperature of the final annealing. Annealing at 280°C/2h causes a sudden drop of strength due to the occurrence of recrystallization and grain growth.

6.3 The increase in electrical resistivity with the applied cold rolling deformation is a result of increased concentration of dislocations and vacancies (formed at the intersections of dislocations multiplied during the deformation. Both, dislocations and vacancies contribute to the scattering of electrons, as well as the solute elements or grain boundaries, raising the electrical resistivity. However, the electrical resistivity was changed non-monotonically with the increase of annealing temperature or in function of the applied pre-annealing cold rolling reductions.

6.4 Electrical resistivity measurements combined with microstructural characterization and EDS analysis pointed out that IGC resistance of the studied alloy was controlled by morphology and distribution of ternary Al-Mg-Zn precipitates, and not by their amount. The wetting of the grain boundaries by continuous and semicontinuous film was characteristic of all IGC susceptible states, while formation of discrete precipitates at the grain boundaries was characteristic of all IGC resistant states.

6.5 The presence of 0.5 wt % Zn in the studied alloy resulted in precipitation of ternary Al-Mg-Zn phase enriched with small amounts of Cu during annealing 2 hours at 240 °C, as shown by EDS analysis. The extent of prior cold work did not influence the chemical composition of precipitated Al-Mg-Zn phase. However, the degree of cold work did affect the morphology and distribution of precipitate d Al-Mg-Zn phase. There is a clear correlation between the morphology of the grain boundary precipitation and IGC resistance. In the case of annealing 2 hours at 240 °C, a lower degree of prior cold deformation resulted in an IGC susceptible state due to wetting of grain boundaries by precipitation of continuous and semi continuous film of Al-Mg-Zn phase. Higher cold deformation improved corrosion response after subsequent annealing at 240 °C by creation of a microstructure that favors ternary Al-Mg-Zn phase precipitation as discrete particles at grain boundaries and in grain interiors.

6.6 The exfoliation and pitting corrosion appearance was considered in a Zn modified 5083 type alloy sheet, after applying different thermo-mechanical treatments. The as received 5083 type hot rolled plates were laboratory processed by different cold rolling deformations (15% - 54%) and final heat treatments (220°C - 280°C for 1h, 2h and 3h). Exfoliation and pitting corrosion testing was performed according to ASTM G66 standard.

6.7 The results have shown that exfoliation or pitting type of corrosion can be significantly affected by applying different thermo-mechanical treatments. It was found that exfoliation corrosion developed after ~ 50% cold rolling deformation and low temperature annealing at 220°C and 230°C. Pitting corrosion was less agressive and tend to be active after higher cold rolling deformations (40% - 50%) and higher annealing temperatures (260°C and 280°C) when the grain morphology is supposed to change, lowering the flattness in the recovery process.

6.8 The relationship between general intergranular corrosion susceptibility, defined by a mass loss, and the ratings of different levels of exfoliation and pitting corrosion should be established.

6.9 Obviously, the question of the relation of general IGC susceptibility, expressed as a mass loss, to the exfoliation or pitting appearance need some further examinations and improved understanding of the influence of basic thermo-mechanical treatment

parameters and the appropriate structure features. In any case, the final relevance of exfoliation or pitting corrosion, in practice, should be considered in a limited range of structure states which are fully resistant to IGC.

6.10 The heat input of pulse process samples are lower than the convential processes which is expected since the main advantage of pulse process is to decrease the heat input. The degradation of heat input is more signifant for MIG processes (25-27%) than TIG processes (10-13%), thats because TIG process has lower effecency and MIG processes are more effective.

6.11 The decreasing in strenght in specimens welded by TIG process for alloy 5083H321 is higher than MIG process, while the maximum degradation is for TIG-P process (27%) and for 5083H116 is (23%), then the MIG process is more convenient for welding both materials because there are no big changes in strength and heat input.

6.12 Weldability of both materials (5083H116 & 5083H321) taking into account mechanical properties (tensile strength, bending and hardness), corrosion resistance, metallography and resistance against the cracks are acceptable welding for all welding processes (TIG, TIG-P, MIG & MIG-P).

6.12 Some problems with porosity need to extend research using the highest quality of shielded gas and choosing the optimal parameters of welding conditions (current, voltage, etc), but no critical values of hot cracks length were detected even when use the very stringent condition which were used for FISCO test.

6.13 A more detailed analysis of weldability seeks more tests, but it can be concluded that the alloys 5083H116 & 5083H321 can be applied for welded structures.

CHAPTER 8

---

8 References

[1]- A. Kelkar, R. Roth, and J. Clark, "Automobile Bodies: Can Aluminum Be an Economical Alternative to Steel?" *Journal of Materials (JOM)*, vol. 53, pp. 28-32, 2001.

[2]- W. S. Miller, L. Zhuang, J. Bottema, A. J. Witterbrood, P. De Smet, A. Haszler, and A. Vieregge, "Recent Development in Aluminium Alloys for the Automotive Industry," *Materials Science and Engineering A*, vol. 280, pp. 37-49, 2000.

[3]- G. Mathers, The Welding of Aluminium and its Alloys. England: CRC Press, 2002.

[4]- Aqueous processes and passive films, Edited by J.C Scully, Published; London; New York: Academic Press (1983).

[5]- Corrosion Mechanisms in Theory and Practice, 2nd Edition, Edited by Philippe Marcus, Published by Marcel Dekker, Inc. (2002).

[6]- Corrosion Engineering, Mars G. Fontana, Third Edition, Published by mcgraw-hill international (1987).

[7]- Analytical Characterization of Aluminum, Steel, and Superalloys edited by D. Scott MacKenzie, George E. Totten, published by Taylor & Francis, 2006

[8]- Springer Handbook of Mechanical Engineering, Volume 10, edited by Karl-Heinrich Grote, Erik K. Antonsson

[9]- Concise Metals Engineering Data Book, By Joseph R. Davis, ASM International, the natural information society, 1997

[10]- BS EN 515 : 1993 Aluminum and aluminum alloys - Wrought products - Temper designations

[11]- S. Court, K. Gatenby and D. Lloyd, Materials Science and Engineering A 319-321 (2001), pp. 443- 447.

[12]- Mondolfo, L.F.: Aluminium Alloys: Structure and Properties, Boston, Butterworths, 1976.

[13]- Hatch, J.E.: Aluminium: Properties and Physical Metallurgy, ASM, Metals Park, Ohio, 1984.

[14]- T. Radetić, M. Popović, E. Romhanji, “Microstructure evolution of a modified AA5083 aluminum alloy during a multistage homogenization treatment”, Materials Characterization 65, (2012), 16-27, ISSN: 1044-5803

[15]- A. Halap, T. Radetić, M. Popović, E. Romhanji, “Study of homogenization treatments of cast 5xxx series Al-Mg-Mn alloy modified with Zn”, Light Metals 2012 Edited by: Carlos E. Suarez, TMS (The Minerals, Metals & Materials Society) (2012), pp. 387-392

[16]- V. Ocenasek and M. Slamova, Material Characterization 47 (2001), pp. 157-162.

[17]- S.Kang, J.Kim & H.Kim, Material Science Forum 519-521 (2006),pp. 847-852.
[18]- Aluminum, Vol. I. Properties, Physical Metallurgy and Phase Diagrams, Edited by Kent R. Van Hom, Published by the American Society for Metals (1967).
[19]- Sheasby, P.G., and Pinner, R., The surface treatment of aluminum and its alloys. 6th ed. Vol. 1. 2001: Finishing Publications Ltd.
[20]- Osman, M. M., Engler, O., Karhausen, K., & McLaren, A. (2002). *The influence of homogenization heat treatment on microstructure development in Al-Mg-Mn alloy AA5454*. Paper presented at 8th International Conference on Aluminum Alloys, Cambridge, UK.
[21]- E. Nes: Aluminum, 52, 1976, pp. 560.
[22]- E. Nes: Acta Met, 24, 1976, pp. 391.
[23]- Handbook of Corrosion Data, Second Edition (1995) by Bruce D. Criag
[24]- Carrol and C. Breslin, British Corrosion Journal 26 (1991), pp. 255-259.
[25]- Corrosion Resistance of Aluminum and Magnesium Alloys, Edited by Edward Ghali, Published by John Wiley & Sons, Inc., Hoboken, New Jersey (2010).
[26]- Davis, J.R., ed. Corrosion of aluminum and aluminum alloys. 1999, ASM International. 1-43.
[27]- N. Idusuyi and O. Oluwole, International Journal of Science and Technology 2 (8) 2012, pp. 561-566.
[28]- H. Ezuber, A. El-Houd and F. El-Shawesh, Materials and Design 29 (4) 2008, pp. 801-805.
[29]- N. Birbilis and R. Buchheit, Electrochemical Society 152 (4) 2005, pp. 140-151.
[30]- R. Buchheit, Electrochemal Society 142 (11) 1995, pp. 3994-3996.
[31]- M. Trueba and S. Trasatti, Materials Chemistry and Physics 121 (2010), pp. 523-533.
[32]- A. Davoodi, J. Pan, C. Leygraf and S. Norgren, Electrochemical Society 155 (5) 2008, pp. 211-218.
[33]- A. Balle, M. Bethencourt, F. Botana, M. Cano and M. Marcos, Corrosion Sience 45 (2003), pp. 161-180.
[34]- W. Zhang and G. Frankel, Electrochemical Acta, 48 (2003), pp. 1193-1210.
[35]- A. Davenport, Y. Yuan, R. Ambat, B. Connolly, M. Strangwood, A. Afseth and G. Scamans, Material Science Forum 519-521 (2006), pp. 641-646.
[36]- X. Liu, G. Frankel, B. Zoofan, and S. Rokhlin, Electrochemical Society 153 (2) 2006, pp. 42-51.
[37]- A. Beck and P. Sperry, In Fundamental Aspect of Stress Corrosion Cracking (1969), pp. 513-525.
[38]- D. Mcnaughtan, M. Worsfold and M. Robinson, Corrosion Science 45 (2003), pp. 2377-2389.
[39]- K. Osamura and T. Ogura: Metall. Trans. A, 1984, vol. 15A, pp. 835-842; M.J.
[40]- Starink and A.-M. Zahra: Phil. Mag. A, 1997, vol. 76A, pp. 701-714; M.J.
[41]- Starink and A.-M. Zahra: Acta Mater., 1998, vol. 46, pp. 3381-3397
[42]- J.L. Searles, P.I. Gouma and R.G. Buchheit: Metall. Mater. Trans. A, 2001, vol. 32A, pp. 2859-2867
[43]- R. Goswami, G. Spanos, P.S. Pao and R.L. Holtz: Mater. Sci. Eng. A, 2010, vol. 527A, pp. 1089-1095
[44]- M. Popović, T. Radetić, and E. Romhanji: in ICAA13: 13th International Conference on Aluminum Alloys
[45]- H. Welland, A.D. Rollett and W.A. Cassada, eds., John Wiley & Sons, Inc., Hoboken, NJ, USA, 2012, pp. 363–368

[46]- H.-C. Jiang, L.-Y. Ye, and X.-M. Zhang: Trans. Nonferrous Met. Soc., 2013, vol. 23, pp. 3553-60

[47]- Starink, M.J. and A.M. Zahra, beta ' and beta precipitation in an Al-Mg alloy studied by DSC and TEM. Acta Materialia, 1998. 46(10): p. 3381-3397.

[48]- Sieniawski, R., Filip, R., and Ziaja, W., The effect of microstructure on the mechanical properties of two-phase titanium alloys. Materials & Design, 1997. 18(4/6): p. 361-363.

[49]- J.C. Chang, T.H. Chuang, Stress-corrosion Cracking Susceptibility of the Superplasticaly Formed 5083 Aluminum Alloy in 3.5 pct NaCl Solution, Metall. Mater. Trans. A 30 (1999) 3191–319916-21

[50]- L. Tan, T.R. Allen, Effect of thermomechanical treatment on the corrosion of AA5083, Corros. Sci. 52 (2010) 548–554

[51]- A. Halap, T. Radetić, M. Popović, E. Romhanji, Influence of the Thermo - mechanical Treatment on the Intergranular Corrosion Susceptibility of Zn-Modified Al-5.1 Wt Pct Mg-0.7 Wt Pct Mn Alloy Sheet, Metall. Mater. Trans. A 45 (2014) 4572–4579

[52]- Stefano Ferraris, The Fifth International Forum on Aluminum Ships Aluminum Alloys in Third Millennium Shipbuilding: Materials, Technologies, Perspectives

[53]- Aluminum in Shipbuilding http://www.aluminumleader.com/en/around/transport/ship

[54]- G.E. Thompson, Surface Characteristics of Aluminum and Alloys, Training Aluminum Application Technologies, Lecture 5101.

[55]- F. Admas, L. Vaeck and R. Barrett, Spectrochemical Acta Part B: Atomic Spectroscopy 60 (1) 2005, pp. 13-26.

[56]- Http://www.nptel.iitm.cc.in/courses/webcourse-contents/iit-roorkee/manufacturing-processes/welding/lecture10.htlm

[57]- Guidelines To Gas Metal Arc Welding (GMAW), USA, 2007−02 www.Millerwelds.com/pdf/mig_handbook.pdf. Retrieved on 24th Jan, 2007

[58]- Mike Y. Nakata, Principal Investigator, Aluminum Welding, Final Report January 1984

[59]- R. Scoot Funderburk `Key Concepts in Welding Engineering´ Welding Innovation .Vol. xvi, No.1 and 2, 1999.

[60]- http://en.wikipedia.org/wiki/welding#_note-30

[61]- K. Shimizu, R. Furneaux, G. Thompson, G. Wood, A. Gotoh and Kobayashi, Oxidation of Metals 35 (5/6) 1991, pp. 427-439.

[62]- Light Alloys from Traditional Alloys to Nanocrystals, Fourth Edition, Edited by I.J. Polmear, Published by Elsevier (2006).

[63]- G. Thompson, Material Science Forum 217-222 (1996), pp. 95-106.

[64]- S. Umoren and M. Solomon, The Arabian Journal For Science and Engineering 35 (2a) 2010, pp. 115-129.

[65]- Applied Welding Engineering Processes, Codes and Standards, Edited by Ramesh Singh, Published by Elesvier Inc. (2012).

[66]- Weld Metal Properties For Extra High Strength Steels, Kenneth Kåkansson, Phd Thesis 2002, The Royal Institute of Technology (Kth), Department of Production Engineering.

[67]- Lean, P.P.; Gil, L. & Ureå, A. (2003). Dissimilar Welds Between Unreinforced AA6082 and AA6092/Sic/25p Composite by Pulsed-MIG Arc Welding Using Unreinforced Filler Alloys (Al-5Mg and Al-5Si), J.Mat. Pro.Tec., Vol. 143-144, pp.846-850

[68]- Czechowski, M. (2004). Corrosion Fatigue of Gma Al-Mg Alloy, Advances In Materials Science, Vol. 4, No. 2004, pp. 16-24.

[69]- Praveen, P. & Yarlagadda, P.K.D.V. (2005). Meeting Challenges In Welding of Aluminum Alloys Through Pulse Gas Metal Arc Welding, J.Mat.Proc.Tec., Vol. 164-165, pp. 1106-1112

[70]- Olson, D.L.; Siewert, T.A.; Liu, S.; Edwards, G.R. 2007, Welding, Brazing, and Soldering, ASM International, USA

[71]- Wilcox, D.V.; Adkins, H.; Dickerson, P.B.; Hasemeyer, E.A. & Lockwood, L. (1972). Welding Aluminum, In: Welding Aluminum, 6th edn, American welding society, Florida, pp. 69.2-69.4-69.25

[72]- Maddox, S.J. (1991). Fatigue Strength of Welded Structures, In: Fatigue Strength of Welded Structures, 2nd Edn, Abington Publishing, Cambrige, England, pp. 19-27-30-36, 38- 43, 66-70

[73]- Davis, J.R. (1998). Aluminum and Aluminum Alloys, 4th edn, ASM International, USA

[74]- Corrosion of Aluminum, Edited by C. Vargel, Published by Elsevier (2004).

[75]- Maggiolino, S. & Schmid, C.(2008). Corrosion resistance in FSW and in MIG welding techniques of AA6xxx, J.Mat.Proc.Tec., vol. 197, no. 1-3, pp. 237-240

[76]- Marine Aluminum Plate - ASTM Standard Specification B 928 and The Events Leading to Its Adoption.Harold Bushfield

[77]- Raghavan V. Al-Mg-Mn (Aluminum-Magnesium-Manganese). J Phase Equilib Diffus 2009;30:626–9.

[78]- J.A.van der Hoeven, L.Zhuang, B.Schepers, P.De Smet, J.P. Baekelandt, Aluminum 78 (2002) 750-754.

[79]- Oguocha INA, Adigun OJ, Yannacopoulos S. Effect of sensitization heat treatment on properties of Al–Mg alloy AA5083-H116. J Mater Sci 2008;43:4208–14.

[80]- ASTM, "E8 Standard Test Methods of Tension Testing of Metallic Materials, „Annual Book or ASTM Standards, American Society for Testing and Materials, Vol. 3.01

[81]- S.I. Vooijs, S.B. Davenport, I. Todd, and S. Van Der Zwaag. Monitoring the precipitation reactions in a cold-rolled Al-Mn-Mg-Cu alloy using thermoelectric power and electrical resistivity measurements. Philosophical Magazine A 2001;81:1–2059–2072.

[82]- Popović M, Romhanji E. Characterization of microstructural changes in an Al-6.8wt.% Mg alloy by electrical resistivity measurements. Materials Science and Engineering: A 2008;492:460–7.

[83]- Li YJ, Arnberg L. Solidification structures and phase selection of iron-bearing eutectic particles in DC-cast AA5182 alloy. Acta Materialia 2004;52:2673-81.

[84]- ASTM G67-04 Standard Test Method for Determining the Susceptibility to Intergranular Corrosion of 5xxx Series Aluminum Alloys by Mass Loss after Exposure to Nitric Acid (NAMLT).

[85]- ASTM G66-99 Standard Test Method for Visual Assessment of Exfoliation Corrosion Susceptibility of 5xxx Series Aluminum Alloys Test (ASSET).

[86]- M.C. Carroll, P.I. Gouma, M.J. Mills, G.S. Daehn and B.R. Dunbar: Effects of Zn Additions on the Grain Boundary Precipitation and Corrosion of Al-5083. Scripta Materialia 2000;42:pp 335–340.

[87]- R.H. Jones, D.R. Baer, M.J. Danielson and J.S. Vetrano. Role of Mg in the Stress Corrosion Cracking of an Al-Mg Alloy. Metall and Mat Trans A 2001;32:1700–11.

[88]- ASTM E340-2002 Standard Test Method for Macroetching Metals and Alloys
[89]- ISO 4136:2001 Destructive tests on welds in metallic materials -- Transverse tensile test
[90]- BS EN 895-1995 Destructive tests on welds in metallic materials
[91]- BS EN 910:1996 Destructive tests on welds in metallic materials. Bend tests
[92]- ASTM E92-82(2003)e2, Standard Test Method for Vickers Hardness of Metallic Materials
[93]- ASTM E384 - 11e1, Standard Test Method for Knoop and Vickers Hardness of Materials
[94]- ASTM B345 / B345M - 11 Standard Specification for Aluminum
[95]- T.B. Massalski, J.L. Murray, L.H. Bennett and H. Baker: Binary Alloy Phase Diagrams, ASM International, Metals Park, Ohio, 1984, vol. 1, pp. 129-131.
[96]- Popović M, Romhanji E. Characterization of microstructural changes in an Al-6.8wt.% Mg alloy by electrical resistivity measurements. Materials Science and Engineering: A 2008;492:460–7.
[97]- S. Jain et al., "Spreading of Intergranular Corrosion on the Surface of Sensitized Al-4.4Mg Alloys: A general Finding," Corrosion Science, 59 (2012) 136-147.
[98]- EN 1435-class B:2007, Non-destructive testing of welds Radiographic testing of welded joints.
[99]- ISO 10042, Arc-welded joints in aluminum and its alloys
[100]- ISO 5817, Fusion-welded joints in steel, nickel, titanium and their alloys
[101]- ASME Section. IX standard, Welding classification
[102]- T. Radetic´, A. Halap, M. Popovic´, and E. Romhanji: in Light Metals 2014: Proc. TMS 2014 Annual Meeting, J. Grandfield, eds., John Wiley and Sons, Hoboken, NJ, 2014, pp. 297–302.
[103]- Y.K. Yang and T.R. Allen: Metall. Mater. Trans. A, 2013, vol. 44A, pp. 5226–23.
[104]- M.C. Carroll, P.I. Gouma, G.S. Daehn, and M.J. Mills: Mater. Sci. Eng. A, 2001, vols. A319–A321, pp. 425–28.
[105]- S.A. Court, K.P. Hicklin, D.J. Lloyd, The Ageing and Thermal Recovery Behavior of Al-Mg-Cu Alloys, Mater. Sci. Forum 396-402 (2002) 1031–1036.
[106]- T. Radetic´, A. Halap, M. Popovic´, and E. Romhanji: in Light Metals 2014: Proc. TMS 2014 Annual Meeting, J. Grandfield, eds., John Wiley and Sons, Hoboken, NJ, 2014, pp. 297–302.
[107]- Y.K. Yang and T.R.Allen: Metall. Mater. Trans. A,2013,vol. 44A, pp. 5226-23.
[108]- M. C. Carroll, R. G. Buchheit, G. S. Daehn, and M. J. Mills: Mater. Sci. Forum, 2002, vol. 1443, pp. 396-402.
[109]- Osorio, W.R., Freire, C.M., and Gacia, A., The role of macrostructural morphology and grain size on the corrosion resistance of Zn and Al castings. Materials Science and Engineering 2005. A 402: p. 22-32.
[110]- Y. Zhu, D.A. Cullen, S. Kar, M.L. Free, and L.F. Allard: Metall. Mater. Trans. A, 2012, vol. 43A, pp. 4933-4939.
[111]- E. Romhanji, M. Popović, Problems and prospect of Al-Mg alloys application in marine constructions, Journal of Metallurgy 12/4 (2006) 297-307.
[112]- Robinson Mj, Jackson Nc, British Corrosion Journal, 34 (1999) 45–49
[113]- Robinson Mj, Jackson Nc, Corrosion Science, 41 (1999) 1013–1028

CHAPTER 7

7 Appendix

7.1 Appendix I (Mechanical properties)

The Brinell hardness variation with cold rolling reduction and subsequent annealing condition are given in Figure 7.1.1.

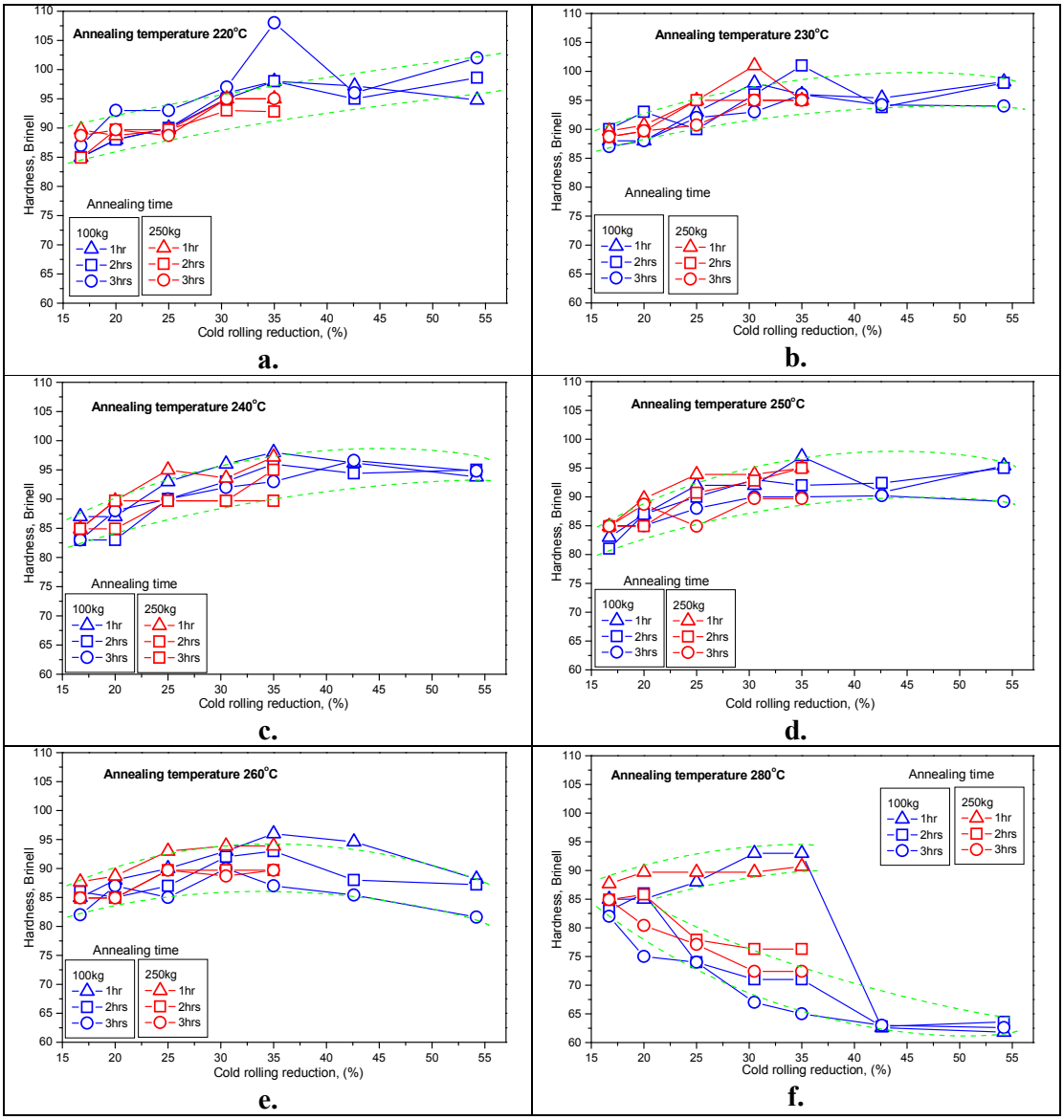


Figure 7.1.1 Hardness variation with cold rolling reduction for different annealing temperatures and different annealing time.

(Mechanical properties) Hardness continue

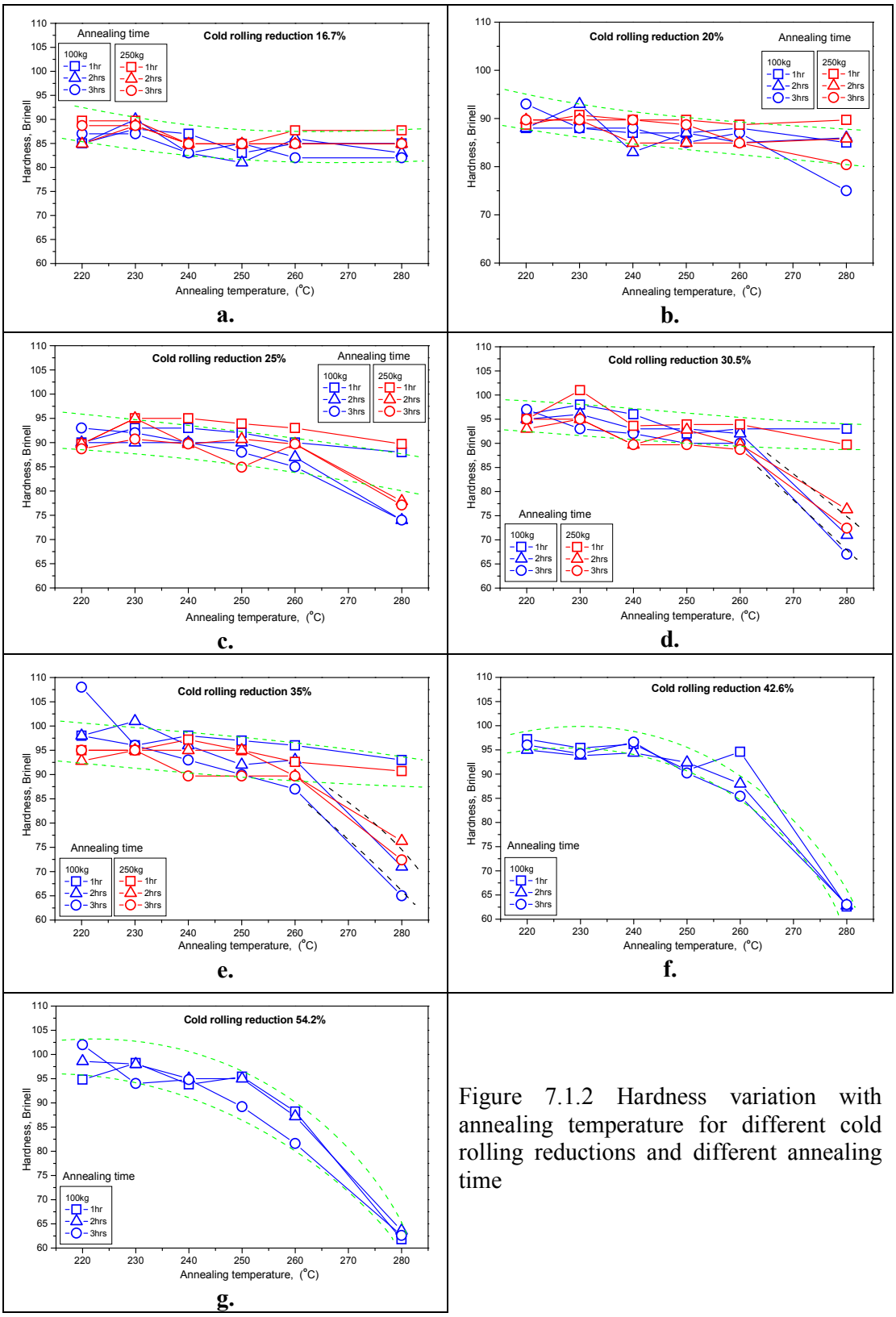


Figure 7.1.2 Hardness variation with annealing temperature for different cold rolling reductions and different annealing time

Electrical resistivity

Electrical resistivity measurements made at the samples after different cold rolling reductions (15% - 55%), annealing temperatures (220°C - 280°C) and annealing times (1h, 2h and 3h). The results are shown in Figure 7.1.3 and Figure 7.1.4.

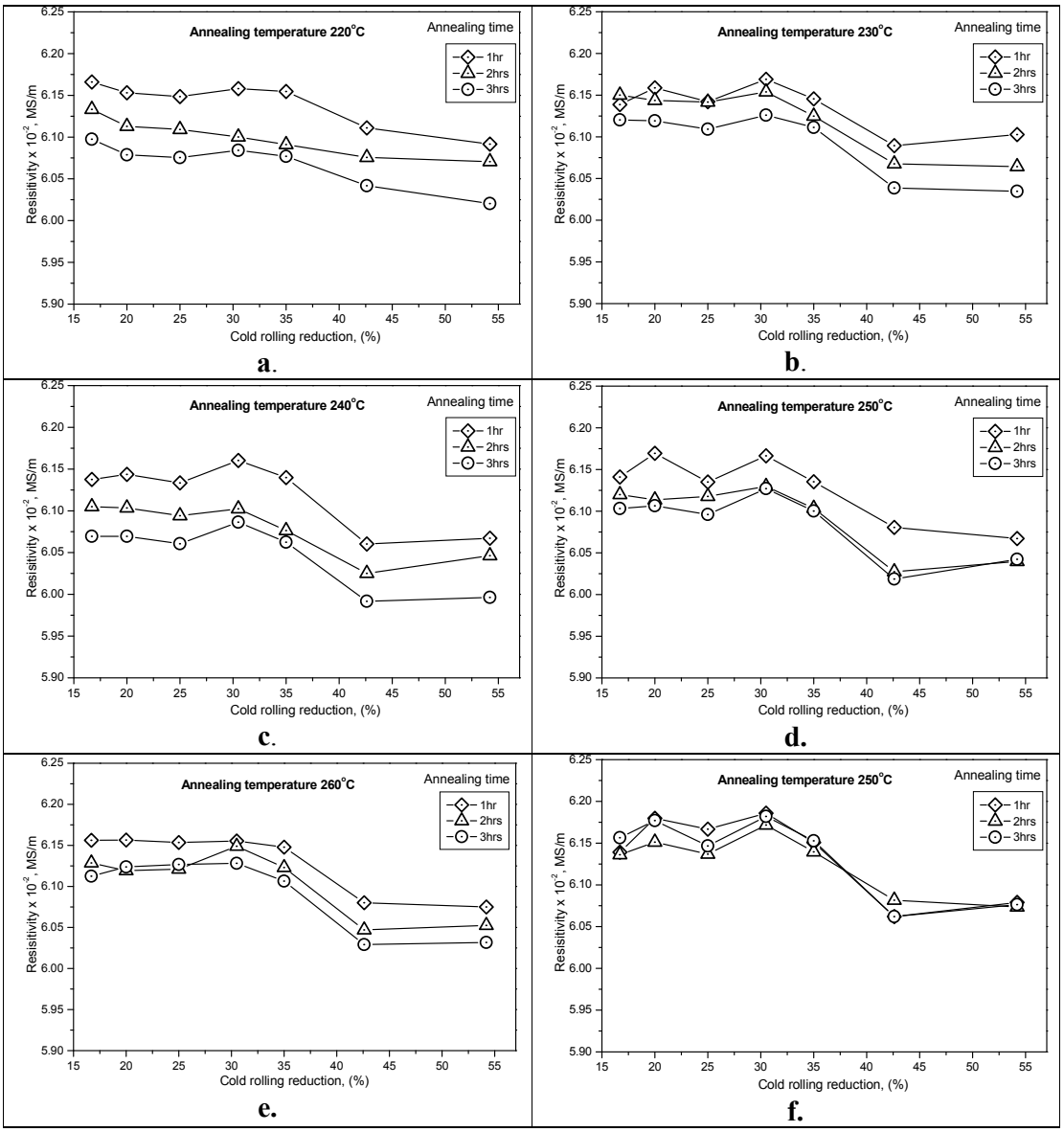


Figure 7.1.3 Electrical resistivity variation with cold rolling reduction for different annealing temperatures and annealing times.

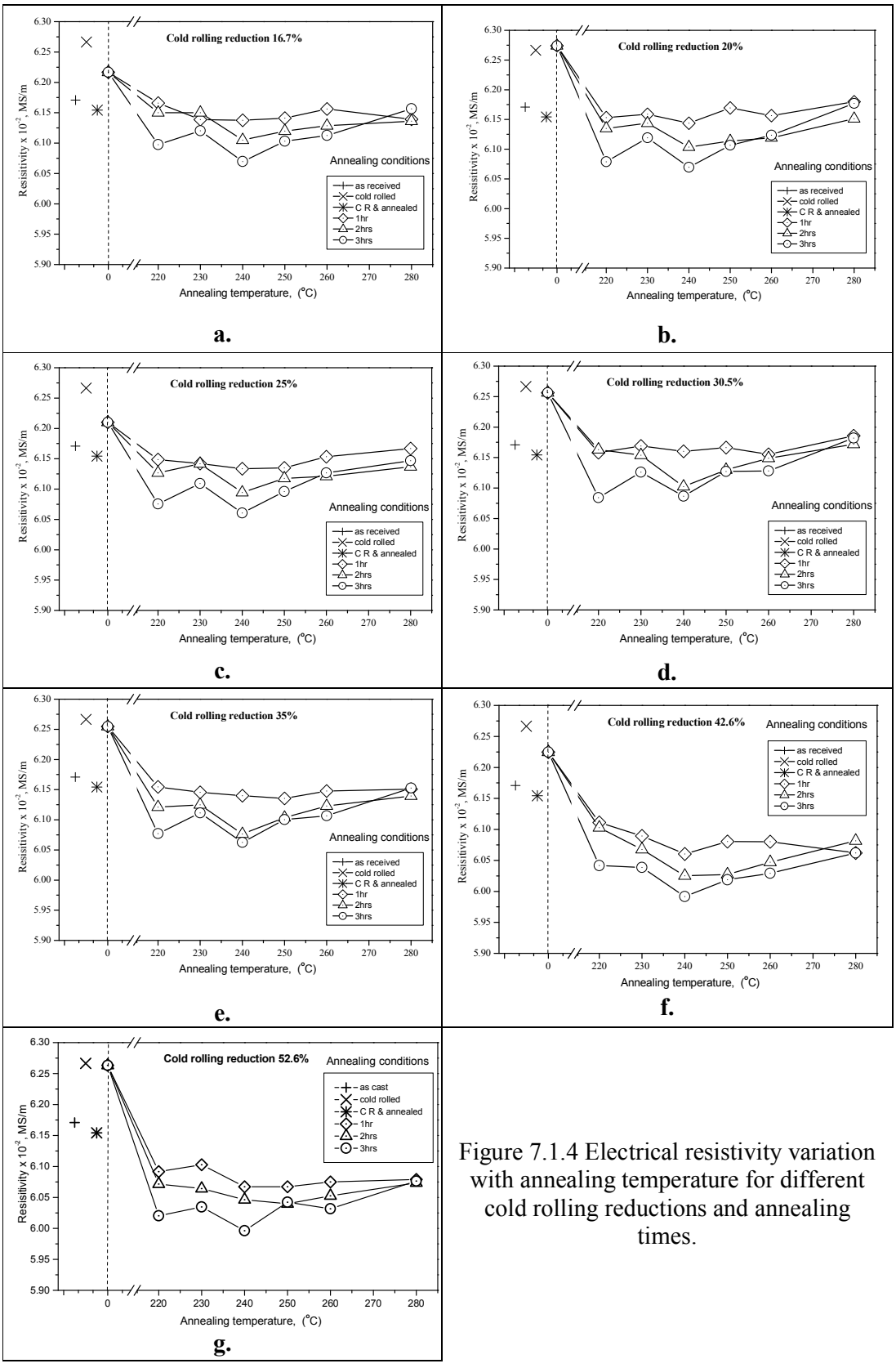


Figure 7.1.4 Electrical resistivity variation with annealing temperature for different cold rolling reductions and annealing times.

7.2 Appendix II Corrosion

The IGC susceptibility (expressed as a mass loss in the NAML test) variation with cold rolling deformation and subsequent annealing conditions is shown in Figure 7.2.1a-c, which shows the ratio of mass loss per surface area of the tested alloys.

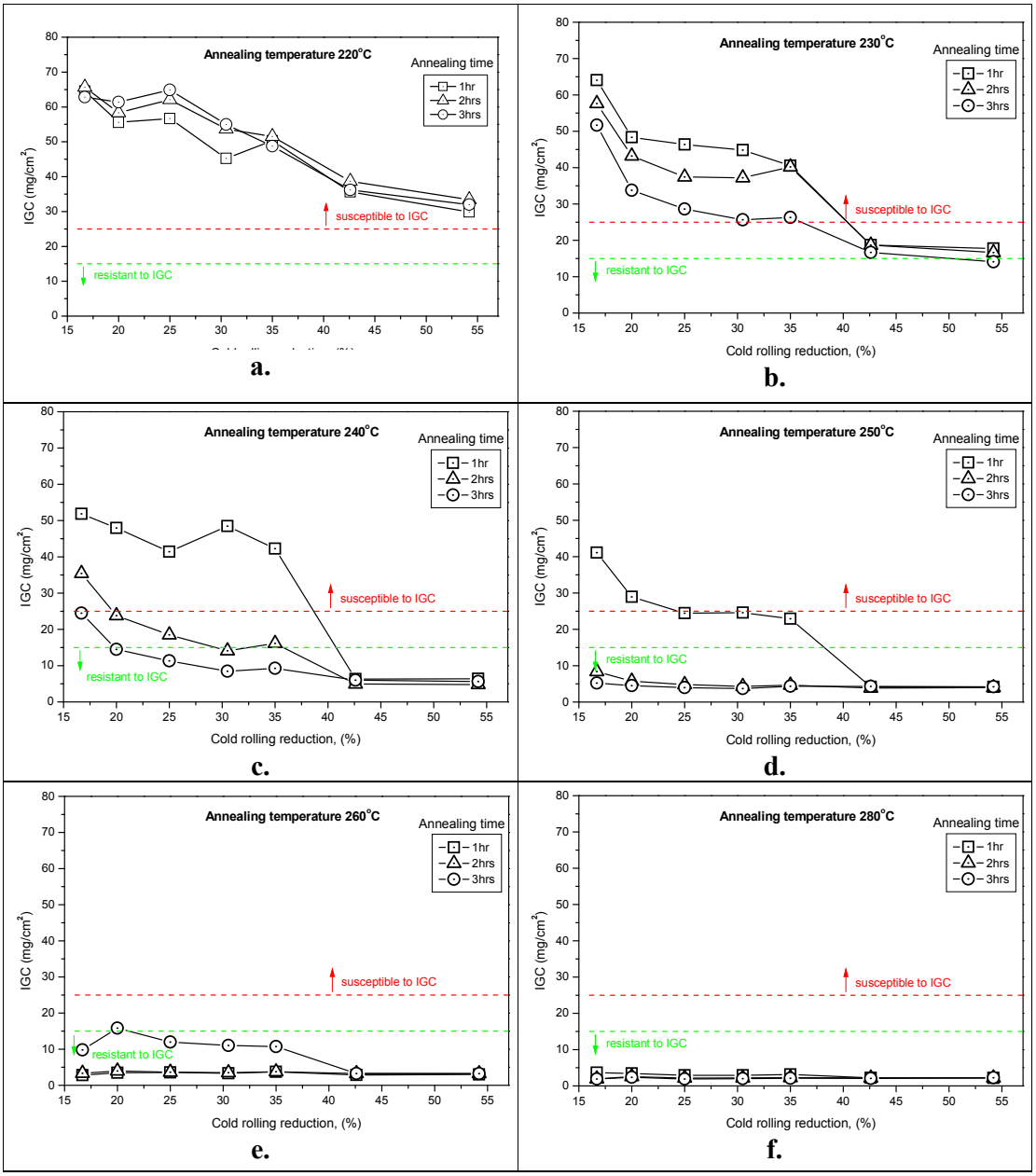


Figure 7.2.1 Intergranular Corrosion variation with cold rolling reduction for different annealing time and different annealing temperatures.

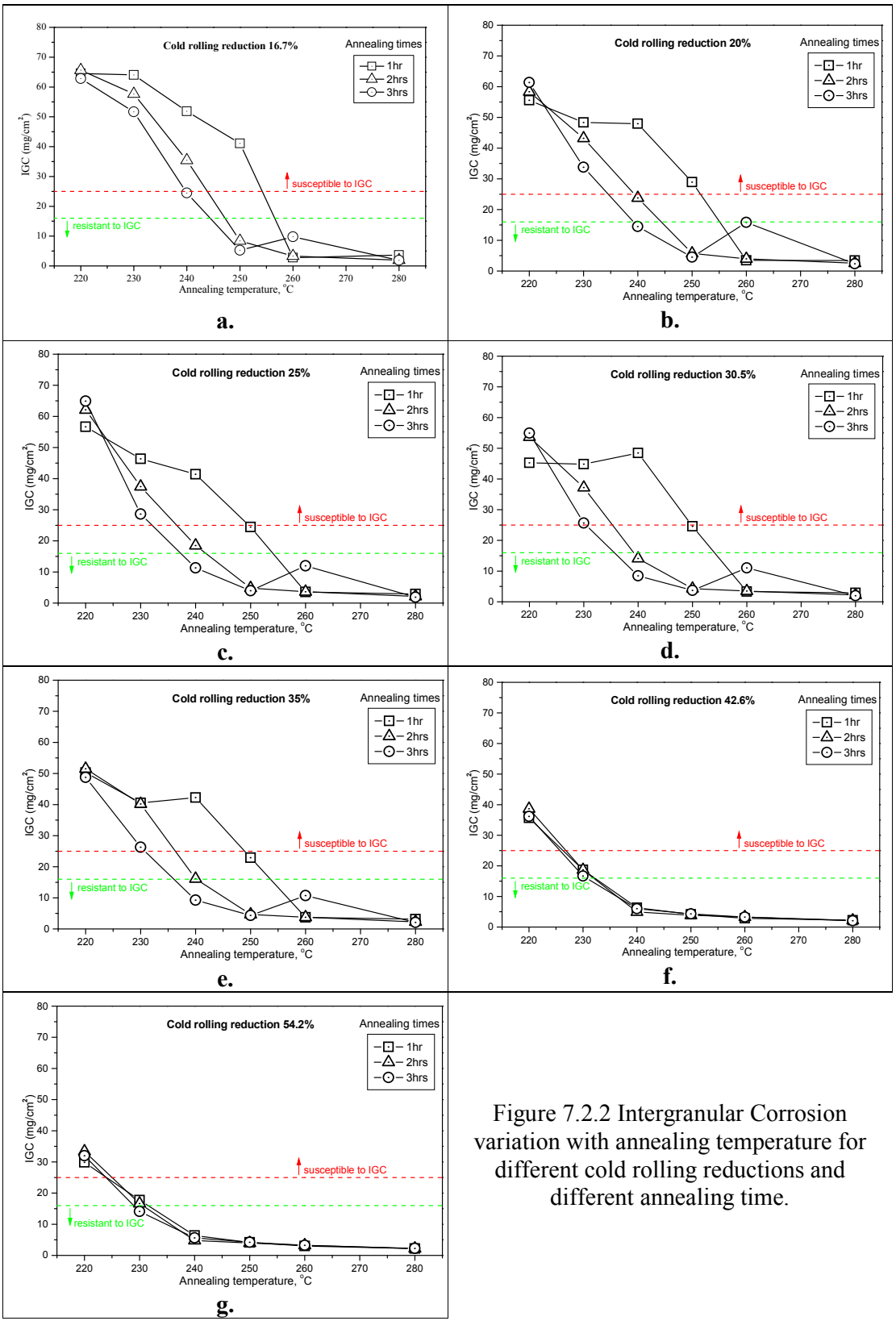


Figure 7.2.2 Intergranular Corrosion variation with annealing temperature for different cold rolling reductions and different annealing time.

The results of Exfoliation and Pitting corrosion for all alloys and the results of previously determined general IGC susceptibility of the tested alloy, expressed as a mass loss per unit area, defined according to ASTM G66 & G67 standard, were shown in Table 7.2.1-7.

Table 7.2.1 Corrosion stability after 17.6% deformation, different final annealing and time.

Condition	Code	$(m_1-m_2)/A$, mg/cm^2	IGC	Face	Exfoliation	Pitting
220°C/1h	111	64.5614	Susceptible	1	N	N/A
				2	N	N/A
220°C/2h	112	65.6632	Susceptible	1	N	N/A
				2	N	N/A
220°C/3h	113	62.8110	Susceptible	1	N	N/A
				2	N	N/A
230°C/1h	121	64.0580	Susceptible	1	N	A/B
				2	N	A/B
230°C/2h	122	57.6423	Susceptible	1	N	N/A
				2	N	N/A
230°C/3h	123	51.6705	Susceptible	1	N	A
				2	N	N/A
240°C/1h	131	51.8397	Susceptible	1	N	N/A
				2	N	N/A
240°C/2h	132	35.4337	Susceptible	1	N	N/A
				2	N	N/A
240°C/3h	133	24.4773	Susceptible	1	N	A
				2	N	N/A
250°C/1h	141	41.1053	Susceptible	1	N	A
				2	N	A
250°C/2h	142	8.3929	Resistant – N	1	N	A
				2	N	A
250°C/3h	143	5.2290	Resistant – N	1	N	A
				2	N	N/A
260°C/1h	151	2.8038	Resistant – N	1	N	N/A
				2	N	A
260°C/2h	152	3.3193	Resistant – N	1	N	A
				2	N	N/A
260°C/3h	153	9.7925	Resistant – N	1	N	A
				2	N	A
280°C/1h	161	3.6353	Resistant – N	1	N	A
				2	N	A
280°C/2h	162	1.9360	Resistant – N	1	N	A
				2	N	A
280°C/3h	163	1.8817	Resistant – N	1	N	A
				2	N	A

NAMLT Intergranular Corrosion Testing (Susceptible if the mass loss < 25 mg/cm^2 Resistance-A if the mass loss > 25 mg/cm^2 and < 15 mg/cm^2 , Resistance-N if the mass loss > 15 mg/cm^2)
ASSET Tested Exfoliation Susceptible (A, B, C, D-Four Degrees of Exfoliation).
ASSET Pitting Corrosion Testing (N-No appreciable attack; A, B, C-Three Degrees of Pitting).

Table 7.2.2 Corrosion stability after 20% deformation, different final annealing and time.

Condition	Code	(m1-m2)/A, mg/cm2	IGC	Face	Exfoliation	Pitting
220°C/1h	211	55.5724	Susceptible	1	N	A
				2	N	A
220°C/2h	212	58.3416	Susceptible	1	A/B	A
				2	A/B	A
220°C/3h	213	61.3700	Susceptible	1	A/B	A/B
				2	A/B	A/B
230°C/1h	221	48.3490	Susceptible	1	N	A
				2	N	A
230°C/2h	222	43.1957	Susceptible	1	N	A
				2	A/B	A/B
230°C/3h	223	33.7788	Susceptible	1	N	A
				2	N	A/B
240°C/1h	231	47.9567	Susceptible	1	N	A
				2	A/B	A/B
240°C/2h	232	23.7915	Resistant – A	1	N	A
				2	A/B	A
240°C/3h	233	14.4854	Resistant – N	1	N	A
				2	A/B	A/B
250°C/1h	241	28.9416	Susceptible	1	N	A
				2	A/B	A/B
250°C/2h	242	5.7462	Resistant – N	1	A/B	A/B
				2	A/B	A/B
250°C/3h	243	4.5218	Resistant – N	1	N	A
				2	A/B	A/B
260°C/1h	251	3.4634	Resistant – N	1	N	A
				2	N	A
260°C/2h	252	3.9600	Resistant – N	1	A/B	A/B
				2	A/B	A/B
260°C/3h	253	15.8318	Resistant – A	1	N	A
				2	N	A
280°C/1h	261	3.4284	Resistant – N	1	N	A
				2	N	A
280°C/2h	262	2.5418	Resistant – N	1	A/B	A/B
				2	A/B	A/B
280°C/3h	263	2.3643	Resistant – N	1	A/B	A/B
				2	A/B	A/B

NAMLT Intergranular Corrosion Testing (Susceptible if the mass loss < 25 mg/cm^2 Resistance-A if the mass loss > 25 mg/cm^2 and < 15 mg/cm^2 , Resistance-N if the mass loss > 15 mg/cm^2)
ASSET Tested Exfoliation Susceptible (A, B, C, D-Four Degrees of Exfoliation).
ASSET Pitting Corrosion Testing (N-No appreciable attack; A, B, C-Three Degrees of Pitting).

Table 7.2.3 Corrosion stability after 25% deformation, different final annealing and time.

Condition	Code	$(m_1-m_2)/A$, mg/cm^2	IGC	Face	Exfoliation	Pitting
220°C/1h	311	56.6595	Susceptible	1	N	N/A
				2	N	N/A
220°C/2h	312	62.1083	Susceptible	1	N	A
				2	A/B	A/B
220°C/3h	313	64.8966	Susceptible	1	B	A/B
				2	B	B
230°C/1h	321	46.3713	Susceptible	1	N	A
				2	N	A
230°C/2h	322	37.4463	Susceptible	1	N	A
				2	A/B	A
230°C/3h	323	28.5925	Susceptible	1	N	N/A
				2	N	N/A
240°C/1h	331	41.4144	Susceptible	1	N	A
				2	A/B	A/B
240°C/2h	332	18.4990	Resistant – A	1	A/B	A
				2	B	A/B
240°C/3h	333	11.3117	Resistant – N	1	N	A
				2	A/B	A/B
250°C/1h	341	24.4490	Resistant – A	1	N	N/A
				2	N	A
250°C/2h	342	4.8202	Resistant – N	1	N	N/A
				2	N	A
250°C/3h	343	3.9693	Resistant – N	1	N	N/A
				2	N	N/A
260°C/1h	351	3.5668	Resistant – N	1	N	N/A
				2	N	N/A
260°C/2h	352	3.6492	Resistant – N	1	N	N/A
				2	N	N/A
260°C/3h	353	11.9727	Resistant – N	1	N	N/A
				2	N	A
280°C/1h	361	2.9019	Resistant – N	1	N	A
				2	N	A
280°C/2h	362	2.1396	Resistant – N	1	N	A
				2	N	A
280°C/3h	363	1.8990	Resistant – N	1	N	A
				2	A	A

NAMLT Intergranular Corrosion Testing (Susceptible if the mass loss < 25 mg/cm^2 Resistance-A if the mass loss > 25 mg/cm^2 and < 15 mg/cm^2 , Resistance-N if the mass loss > 15 mg/cm^2)
ASSET Tested Exfoliation Susceptible (A, B, C, D-Four Degrees of Exfoliation).
ASSET Pitting Corrosion Testing (N-No appreciable attack; A, B, C-Three Degrees of Pitting).

Table 7.2.4 Corrosion stability after 30.5% deformation, different final annealing and time.

Condition	Code	$(m_1-m_2)/A$, mg/cm^2	IGC	Face	Exfoliation	Pitting
220°C/1h	411	45.2521	Susceptible	1	N	A
				2	N	A
220°C/2h	412	53.6610	Susceptible	1	A/B	A
				2	A/B	A
220°C/3h	413	54.9482	Susceptible	1	A/B	A
				2	A/B	A
230°C/1h	421	44.8304	Susceptible	1	N	A
				2	N	A
230°C/2h	422	37.2101	Susceptible	1	N	A
				2	N	A
230°C/3h	423	25.6536	Susceptible	1	N	A
				2	A/B	A/B
240°C/1h	431	48.4597	Susceptible	1	N	A
				2	A/B	A
240°C/2h	432	14.0963	Resistant – N	1	N	A
				2	N	A
240°C/3h	433	8.4670	Resistant – N	1	N	A
				2	N	A
250°C/1h	441	24.5918	Resistant – A	1	N	A
				2	N	A
250°C/2h	442	4.2911	Resistant – N	1	A/B	A/B
				2	A/B	A/B
250°C/3h	443	3.7162	Resistant – N	1	A/B	A
				2	A/B	A
260°C/1h	451	3.3216	Resistant – N	1	A/B	A
				2	A/B	A
260°C/2h	452	3.4871	Resistant – N	1	N	A/B
				2	N	A/B
260°C/3h	453	11.0254	Resistant – N	1	N	A
				2	N	A
280°C/1h	461	2.9003	Resistant – N	1	N	A
				2	N	A
280°C/2h	462	2.1992	Resistant – N	1	N	A
				2	N	A
280°C/3h	463	1.9808	Resistant – N	1	N	A
				2	N	A

NAMLT Intergranular Corrosion Testing (Susceptible if the mass loss < 25 mg/cm^2 Resistance-A if the mass loss > 25 mg/cm^2 and < 15 mg/cm^2 , Resistance-N if the mass loss > 15 mg/cm^2)
ASSET Tested Exfoliation Susceptible (A, B, C, D-Four Degrees of Exfoliation).
ASSET Pitting Corrosion Testing (N-No appreciable attack; A, B, C-Three Degrees of Pitting).

Table 7.2.5 Corrosion stability after 35% deformation, different final annealing and time.

Condition	Code	$(m_1-m_2)/A$, mg/cm^2	IGC	Face	Exfoliation	Pitting
220°C/1h	511	50.2764	Susceptible	1	A/B	A
				2	N	A
220°C/2h	512	51.5094	Susceptible	1	N	N/A
				2	A/B	A
220°C/3h	513	48.7454	Susceptible	1	N	A
				2	A/B	A
230°C/1h	521	40.5406	Susceptible	1	A/B	A
				2	A/B	A
230°C/2h	522	40.1890	Susceptible	1	N	A
				2	N	A
230°C/3h	523	26.2848	Susceptible	1	A/B	A/B
				2	A/B	A/B
240°C/1h	531	42.2444	Susceptible	1	A/B	A/B
				2	N	A/B
240°C/2h	532	16.1330	Resistant – A	1	N	N/A
				2	N	N/A
240°C/3h	533	9.2670	Resistant – N	1	A/B	A/B
				2	N	A
250°C/1h	541	22.9104	Resistant – A	1	N	A
				2	N	A
250°C/2h	542	4.6464	Resistant – N	1	N	A/B
				2	N	A
250°C/3h	543	4.3422	Resistant – N	1	N	N/A
				2	N	N/A
260°C/1h	551	3.7306	Resistant – N	1	N	A
				2	N	A
260°C/2h	552	3.7668	Resistant – N	1	N	A
				2	N	A
260°C/3h	553	10.7274	Resistant – N	1	N	N/A
				2	N	N/A
280°C/1h	561	3.1405	Resistant – N	1	N	A/B
				2	N	A/B
280°C/2h	562	2.2573	Resistant – N	1	A/B	A/B
				2	A/B	A/B
280°C/3h	563	2.1081	Resistant – N	1	N	A
				2	N	A/B

NAMLT Intergranular Corrosion Testing (Susceptible if the mass loss < 25 mg/cm^2 Resistance-A if the mass loss > 25 mg/cm^2 and < 15 mg/cm^2 , Resistance-N if the mass loss > 15 mg/cm^2)
ASSET Tested Exfoliation Susceptible (A, B, C, D-Four Degrees of Exfoliation).
ASSET Pitting Corrosion Testing (N-No appreciable attack; A, B, C-Three Degrees of Pitting).

Table 7.2.6 Corrosion stability after 42.6% deformation, different final annealing and time.

Condition	Code	$(m_1-m_2)/A$, mg/cm^2	IGC	Face	Exfoliation	Pitting
220°C/1h	611	35.6563	Susceptible	1	N	N/A
				2	N	N/A
220°C/2h	612	38.6764	Susceptible	1	N	N/A
				2	N	N/A
220°C/3h	613	36.1674	Susceptible	1	N	N/A
				2	N	N/A
230°C/1h	621	18.7051	Resistant – A	1	N	N/A
				2	N	N/A
230°C/2h	622	18.6849	Resistant – A	1	N	N/A
				2	N	N/A
230°C/3h	623	16.6852	Resistant – A	1	N	N/A
				2	N	N/A
240°C/1h	631	6.2983	Resistant – N	1	A/B	A
				2	A/B	A
240°C/2h	632	4.9378	Resistant – N	1	A/B	A
				2	A/B	A
240°C/3h	633	4.9878	Resistant – N	1	A/B	A
				2	A/B	A
250°C/1h	641	4.1572	Resistant – N	1	A/B	A/B
				2	N	A/B
250°C/2h	642	3.8605	Resistant – N	1	A/B	A/B
				2	N	A
250°C/3h	643	4.3089	Resistant – N	1	A/B	A
				2	N	A
260°C/1h	651	2.8642	Resistant – N	1	B	B
				2	B	B
260°C/2h	652	3.2572	Resistant – N	1	B	B
				2	B	B
260°C/3h	653	3.2635	Resistant – N	1	B	B
				2	B	B
280°C/1h	661	2.2173	Resistant – N	1	B	B
				2	B	B
280°C/2h	662	2.1745	Resistant – N	1	B	B
				2	B	B
280°C/3h	663	2.0440	Resistant – N	1	B	B
				2	B	B

NAMLT Intergranular Corrosion Testing (Susceptible if the mass loss < 25 mg/cm^2 Resistance-A if the mass loss > 25 mg/cm^2 and < 15 mg/cm^2 , Resistance-N if the mass loss > 15 mg/cm^2)
ASSET Tested Exfoliation Susceptible (A, B, C, D-Four Degrees of Exfoliation).
ASSET Pitting Corrosion Testing (N-No appreciable attack; A, B, C-Three Degrees of Pitting).

Table 7.2.7 Corrosion stability after 54.2% deformation, different final annealing and time.

Condition	Code	$(m_1-m_2)/A$, mg/cm^2	IGC	Face	Exfoliation	Pitting
220°C/1h	711	29.8470	Susceptible	1	C	A
				2	C	A
220°C/2h	712	33.3820	Susceptible	1	C	A
				2	C	A
220°C/3h	713	31.9915	Susceptible	1	C	A
				2	C	A
230°C/1h	721	17.7350	Resistant – A	1	C	A
				2	C	A
230°C/2h	722	16.6478	Resistant – A	1	C	A
				2	C	A
230°C/3h	723	14.1034	Resistant – N	1	C	A
				2	C	A
240°C/1h	731	6.3854	Resistant – N	1	N	A/B
				2	N	A/B
240°C/2h	732	4.7990	Resistant – N	1	A/B	A
				2	A/B	A
240°C/3h	733	5.6199	Resistant – N	1	N	A
				2	N	A
250°C/1h	741	4.1601	Resistant – N	1	N	A
				2	N	A
250°C/2h	742	3.9612	Resistant – N	1	N	A
				2	N	A
250°C/3h	743	4.2137	Resistant – N	1	N	A
				2	N	A
260°C/1h	751	3.0000	Resistant – N	1	N	B
				2	N	A/B
260°C/2h	752	3.2444	Resistant – N	1	N	B
				2	N	A/B
260°C/3h	753	3.2300	Resistant – N	1	N	B
				2	N	B
280°C/1h	761	2.2053	Resistant – N	1	N	B
				2	N	B
280°C/2h	762	2.1898	Resistant – N	1	N	A/B
				2	N	A/B
280°C/3h	763	2.2530	Resistant – N	1	N	B
				2	N	A/B

NAMLT Intergranular Corrosion Testing (Susceptible if the mass loss < 25 mg/cm^2 Resistance-A if the mass loss > 25 mg/cm^2 and < 15 mg/cm^2 , Resistance-N if the mass loss > 15 mg/cm^2)
ASSET Tested Exfoliation Susceptible (A, B, C, D-Four Degrees of Exfoliation).
ASSET Pitting Corrosion Testing (N-No appreciable attack; A, B, C-Three Degrees of Pitting).

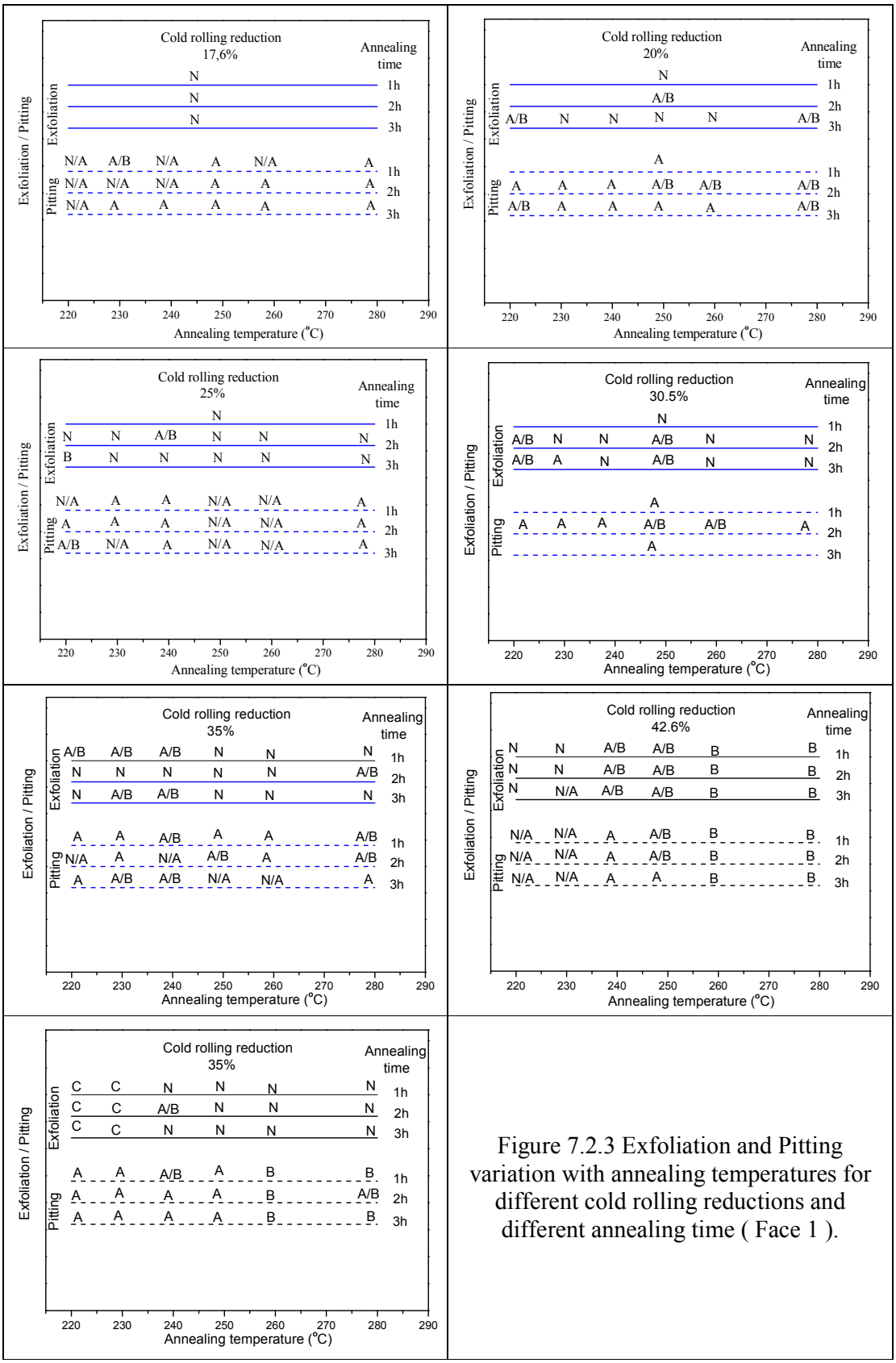


Figure 7.2.3 Exfoliation and Pitting variation with annealing temperatures for different cold rolling reductions and different annealing time (Face 1).

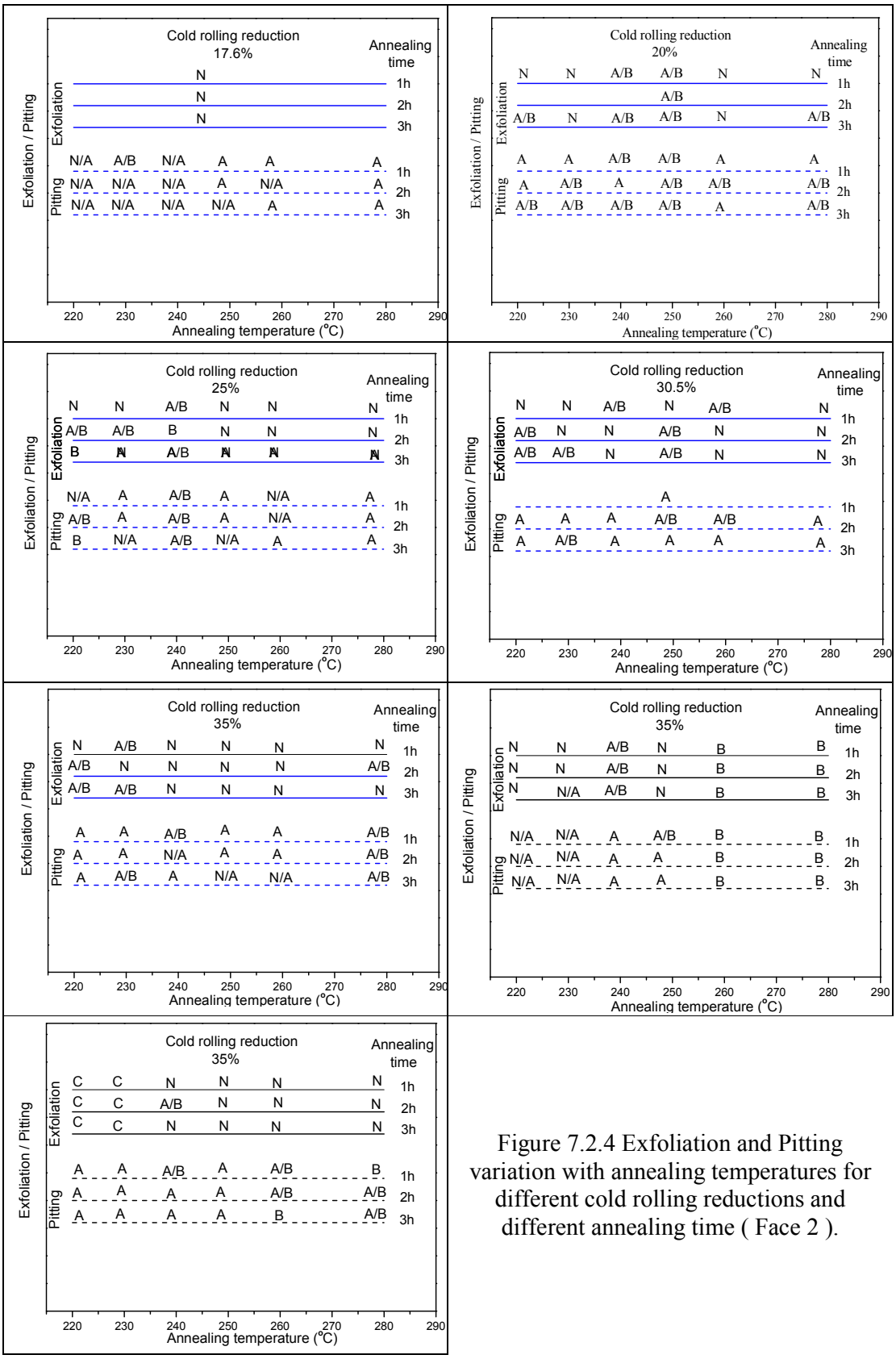


Figure 7.2.4 Exfoliation and Pitting variation with annealing temperatures for different cold rolling reductions and different annealing time (Face 2).

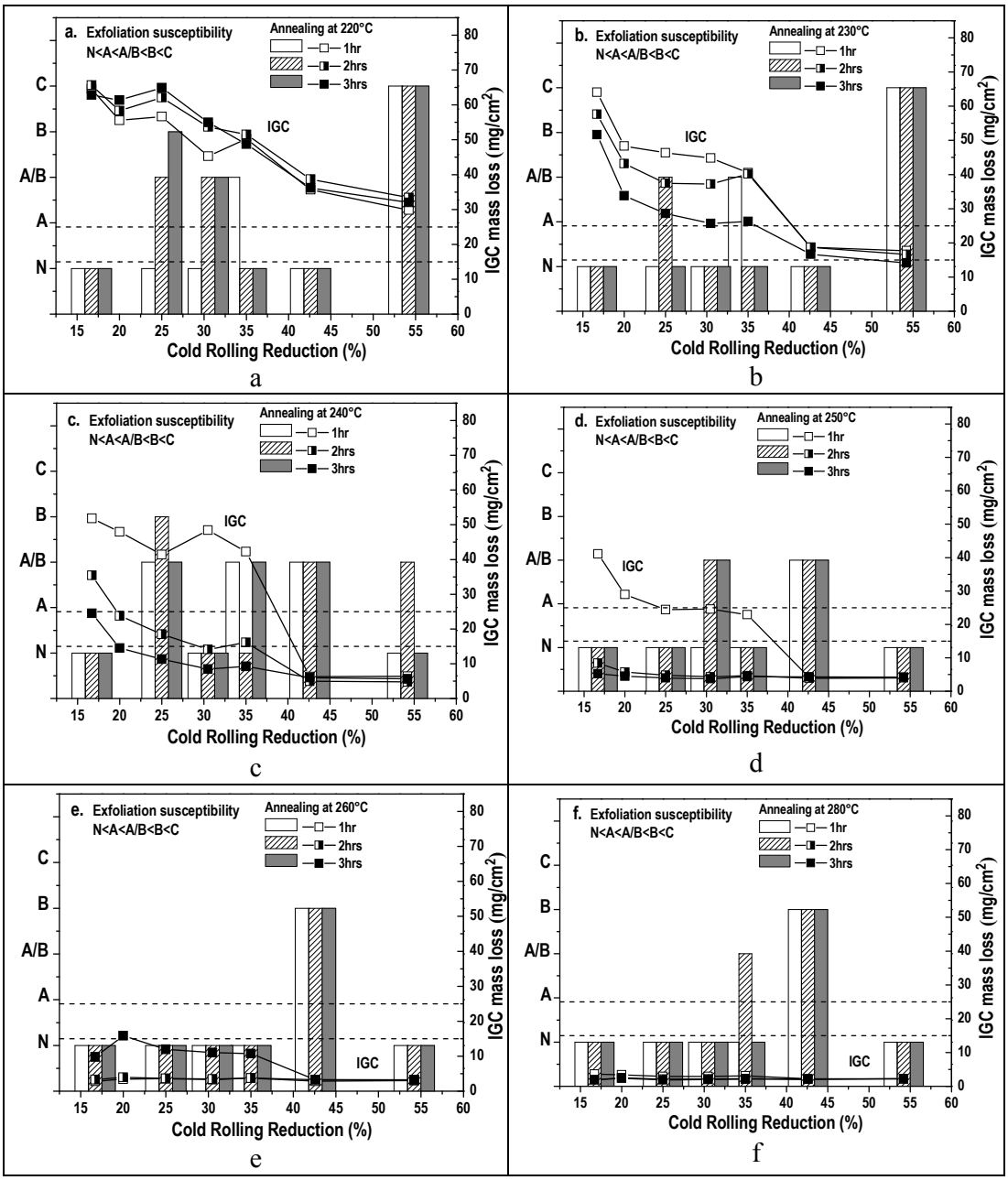


Figure 7.2.5 Ratings of different levels of exfoliation corrosion (according to ASTM G66 standard)

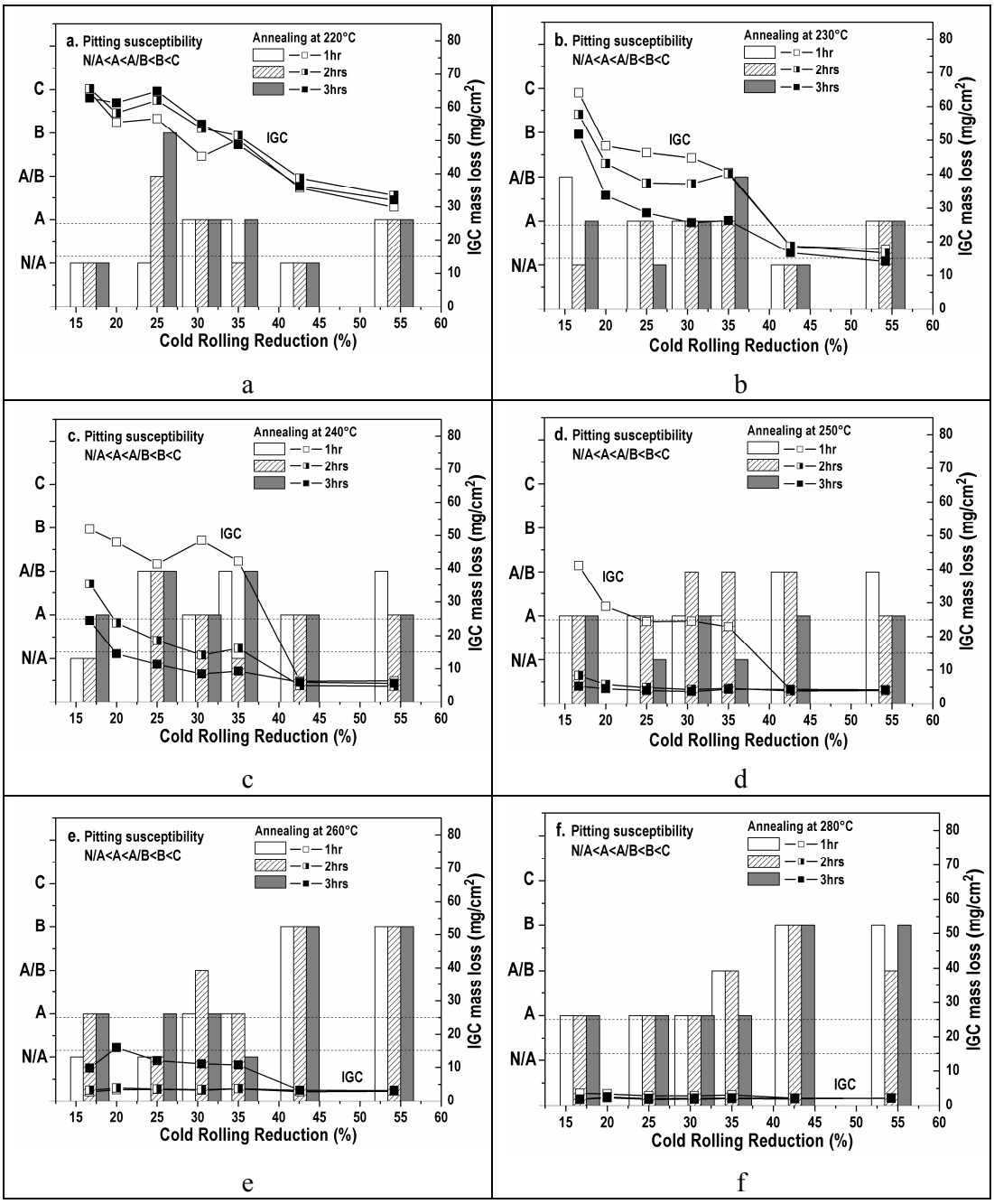
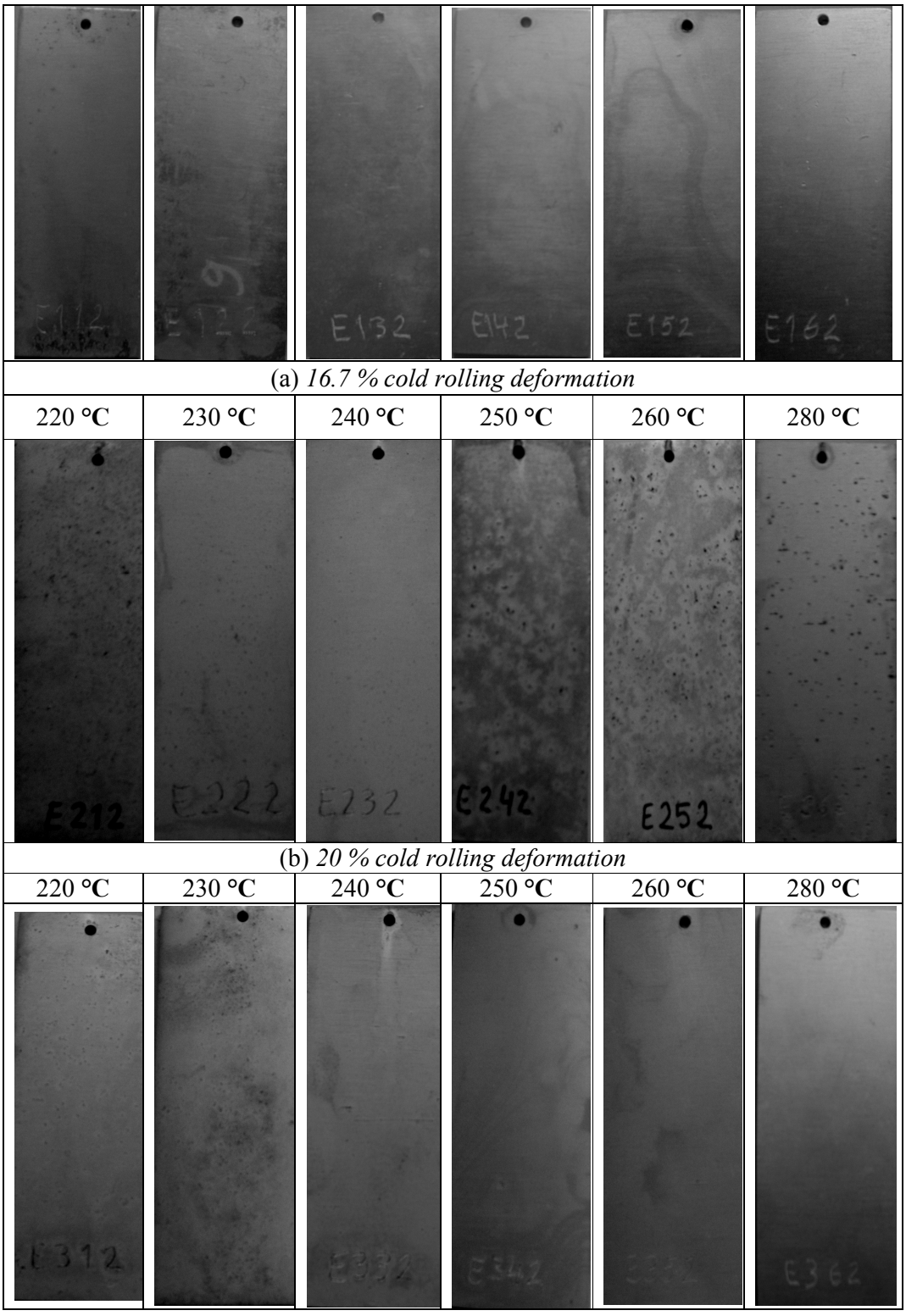


Figure 7.2.6 The degree of pitting corrosion (according to ASTM G66 standard) identified at samples cold rolled with different reductions (up to 55%) and subsequently annealed in the range of temperatures from 220°C to 280°C.

The photos of some samples tested for exfoliation corrosion test are shown in Figure 7.2.7.



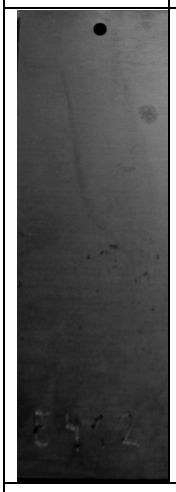
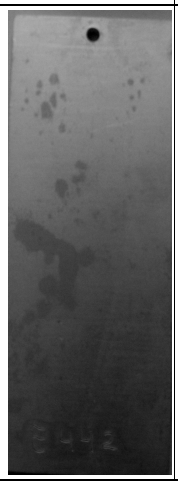
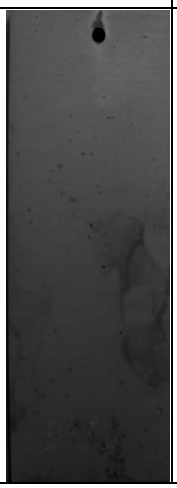
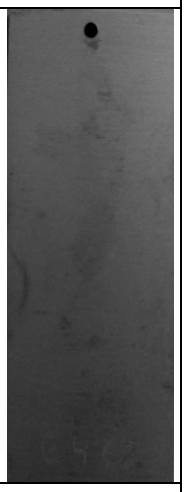
(a) *16.7 % cold rolling deformation*

220 °C	230 °C	240 °C	250 °C	260 °C	280 °C

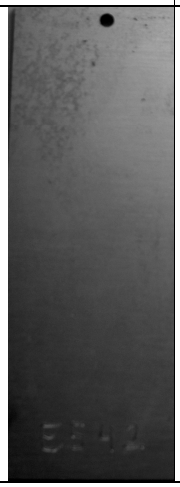
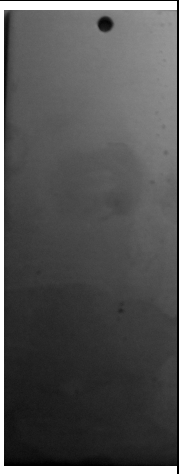
(b) *20 % cold rolling deformation*

220 °C	230 °C	240 °C	250 °C	260 °C	280 °C

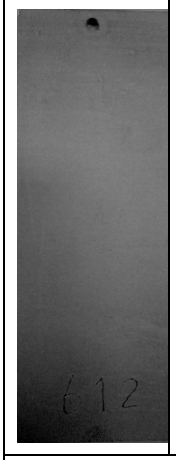
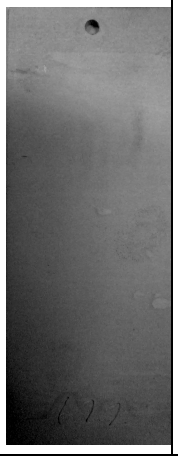
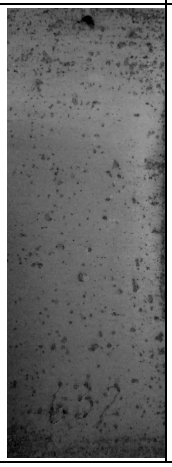
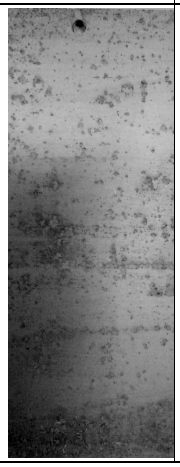
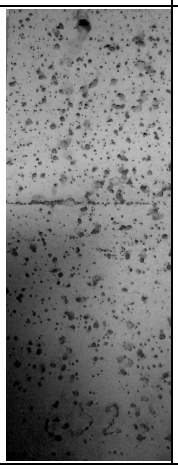
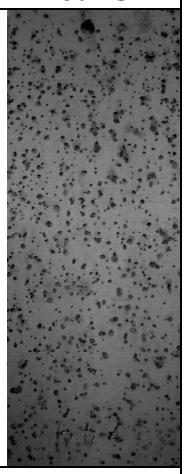
(c) *25 % cold rolling deformation*

220 °C	230 °C	240 °C	250 °C	260 °C	280 °C
					

(d) *30.5 % cold rolling deformation*

220 °C	230 °C	240 °C	250 °C	260 °C	280 °C
					

(e) *35 % cold rolling deformation*

220 °C	230 °C	240 °C	250 °C	260 °C	280 °C
					

(f) *42.5 % cold rolling deformation*

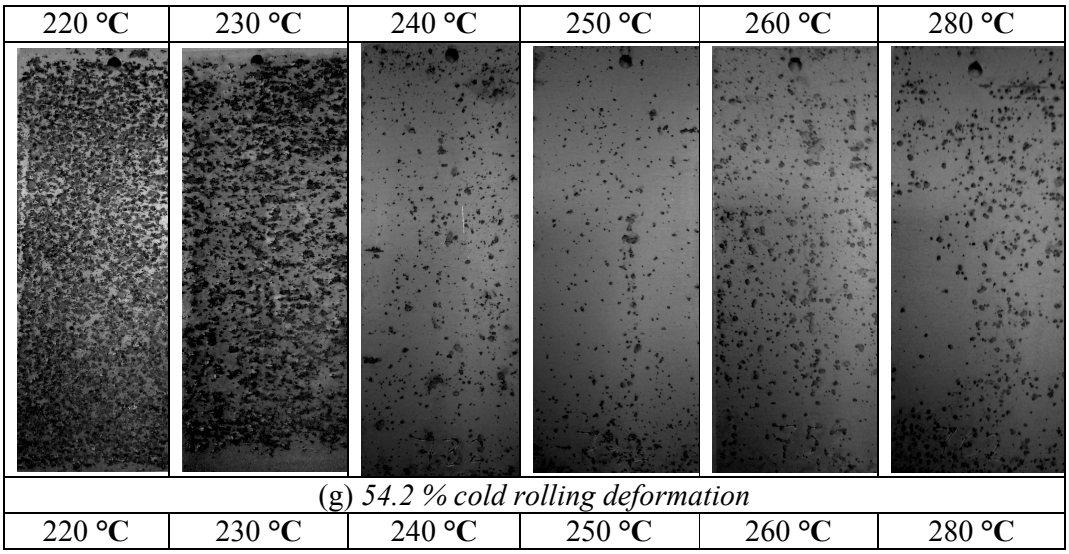
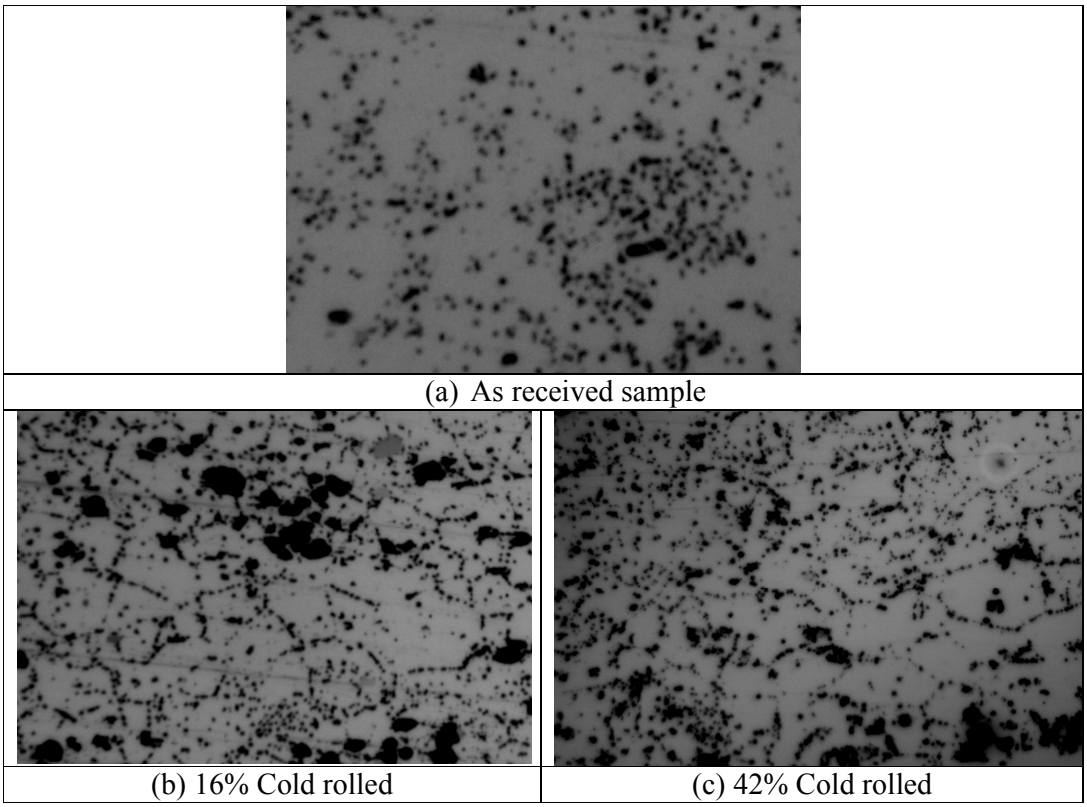
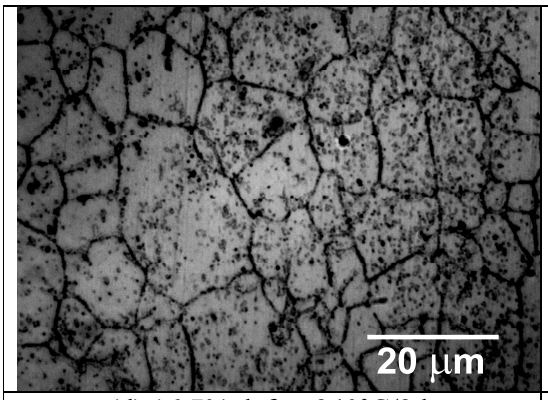


Figure 7.2.7 Samples surfaces after exfoliation and pitting testing for different cold rolling deformation and different annealing temperatures at annealing time 2 hours

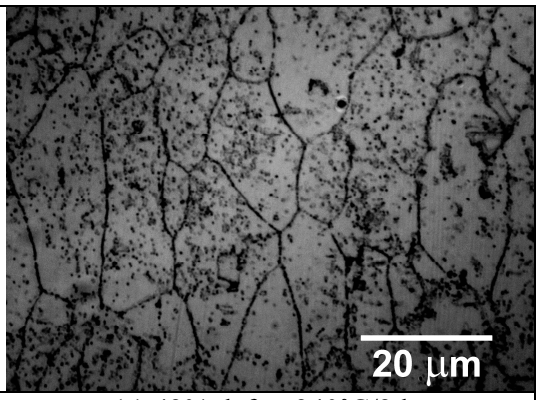
7.3 Appendix III Optical Microscope

The microstructure of samples cold rolled to 16.7% and 42% and subsequently annealed at 240/2hrs are shown in Figure 7.3.1.

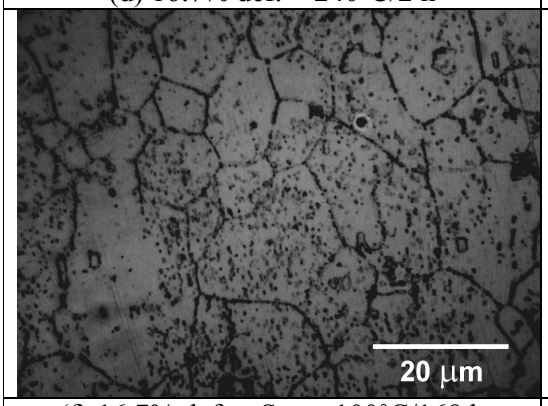




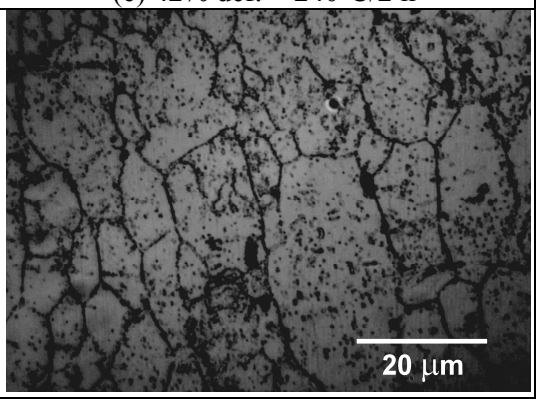
(d) 16.7% def. + 240˚C/2 h



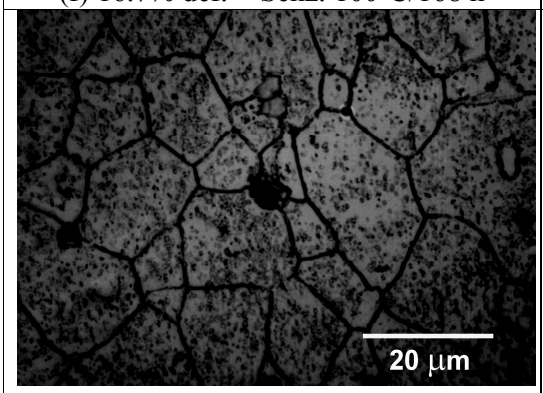
(e) 42% def. + 240˚C/2 h



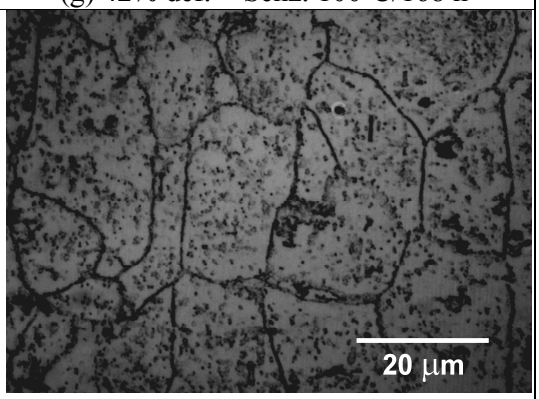
(f) 16.7% def. + Senz. 100˚C/168 h



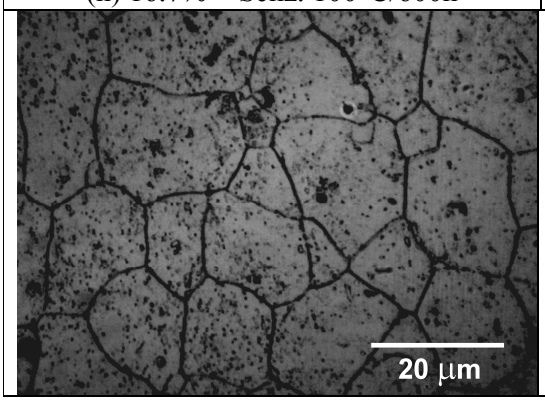
(g) 42% def. + Senz. 100˚C/168 h

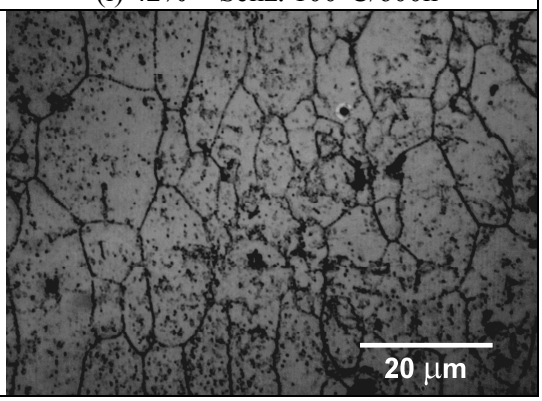


(h) 16.7% + Senz. 100°C/600h



(i) 42% + Senz. 100°C/600h





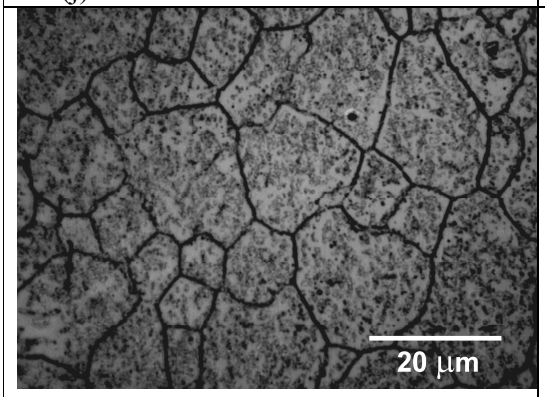
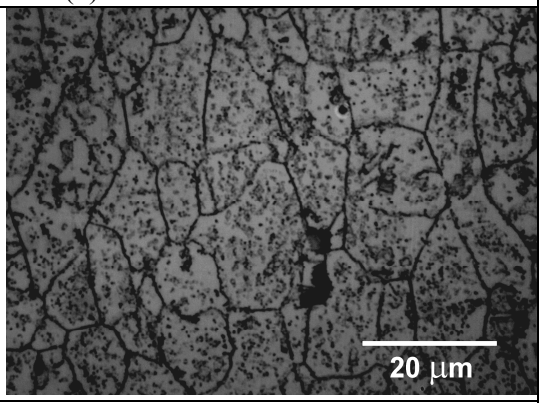
(j) 16.7% def + senz. 150˚C/168 h	(k) 42% def + senz. 150˚C/168 h
	
(l) 16.7% def + senz. 150˚C/600 h	(m) 42% def + senz. 150˚C/600 h

Figure 7.3.1 Optical images of 5083-H321 samples

a Annealed 350°C/3hrs

b Specimen deformed 16.7% c Specimen deformed 42%

d Specimen deformed 16.7% and annealed 2h at 240°C

e Specimen deformed 42% and annealed 2h at 240°C

f Specimen deformed 16.7% and annealed 2h at 240°C+ sensitized 100°C/7days

g Specimen deformed 42% and annealed 2h at 240°C+ sensitized 100°C/7days

h Specimen deformed 16.7% and annealed 2h at 240°C+ sensitized 150°C/7days

i Specimen deformed 42% and annealed 2h at 240°C+ sensitized 150°C/7days

j Specimen deformed 16.7% and annealed 2h at 240°C+ sensitized 100°C/25days

k Specimen deformed 42% and annealed 2h at 240°C+ sensitized 100°C/25days

l Specimen deformed 16.7% and annealed 2h at 240°C+ sensitized 150°C/25days

m Specimen deformed 42% and annealed 2h at 240°C+ sensitized 150°C/25days

Figure 7.3.1 shows at longer sensitisation times, β precipitation increased, after 25 days at 150^{o}C, a continuous film of β precipitates was formed at grain boundaries. Different microstructures represent differing degrees of sensitization ranging from highly susceptible to resistant. The treatments that provide high resistance are those that produce microstructures either free of precipitate distributed along grain boundaries or with precipitate distributed evenly within the grains.

7.4 Appendix IV Welding

Radiographic Testing

A radiographic examination (X-ray) was used after welding to see if the joint does not contain defects (bubbles, cracks and inclusions). Radiographic testing of the weldments was done according to EN 1435-class B:2007 standard in GOŜA INSTITUT using equipment Ind. Rentgen (Baltpost 200 kV), film AGFA D5 Pb 700mm and IQI type 10ISO 16 the picture estimated as per ISO 10042:2005 and the required quality is level B, the photos are shown in the Figures 7.4.1 & 7.4.2.

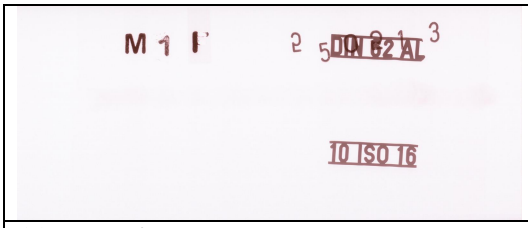
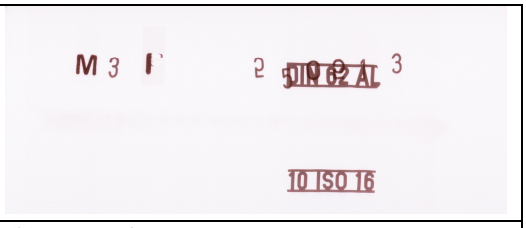
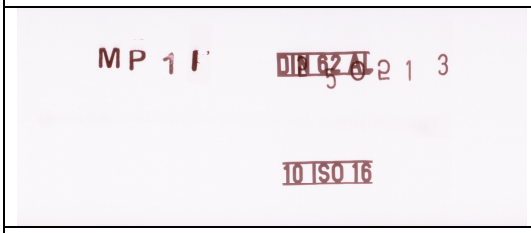
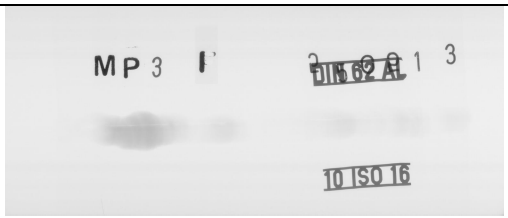
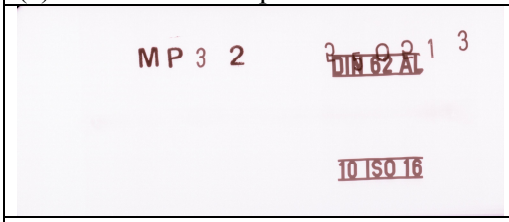
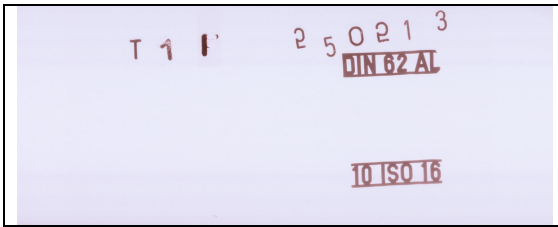
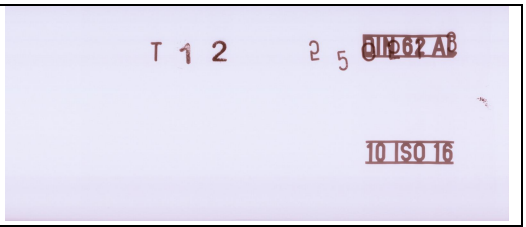
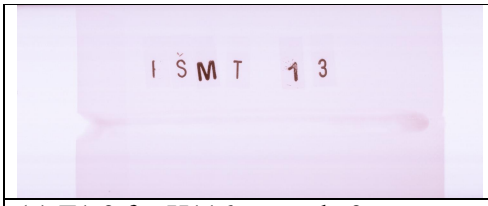
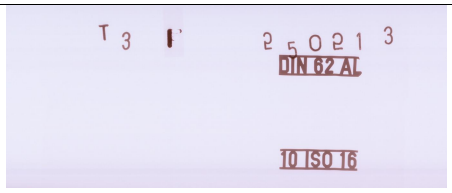
<table>
<tr><td></td><td></td></tr>
<tr><td>(a) M1-1 for H116</td><td>(b) M3-1 for H321</td></tr>
<tr><td></td><td></td></tr>
<tr><td>(c) MP1-1for H116 pulse weled</td><td>(d) MP3-1for H321 pulse weled sample 1</td></tr>
<tr><td></td><td></td></tr>
<tr><td>(e) MP3-2 for H321 pulse weled sample 2</td><td></td></tr>
</table>

Figure 7.4.1 X-ray radiogragh image of MIG welded specimens

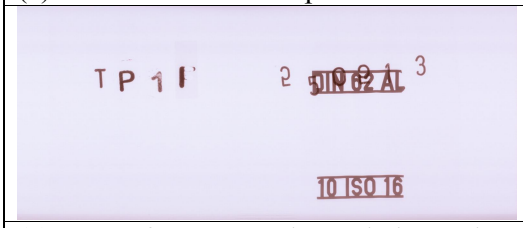
<table>
<tr><td></td><td></td></tr>
<tr><td>(a) T1-1 for H116 sample 1</td><td>(b) T1-2 for H116 sample 2</td></tr>
</table>



(c) T1-3 for H116 sample 3



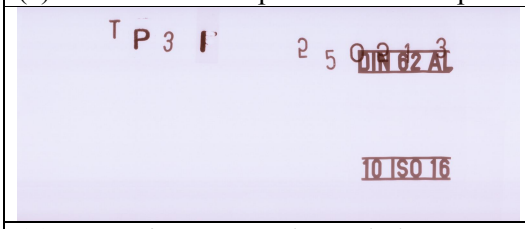
(d) T3-1 for H321



(e) TP1-1 for H116 pulse weled sample 1



(f) TP1-3 for H116 pulse weled sample 3



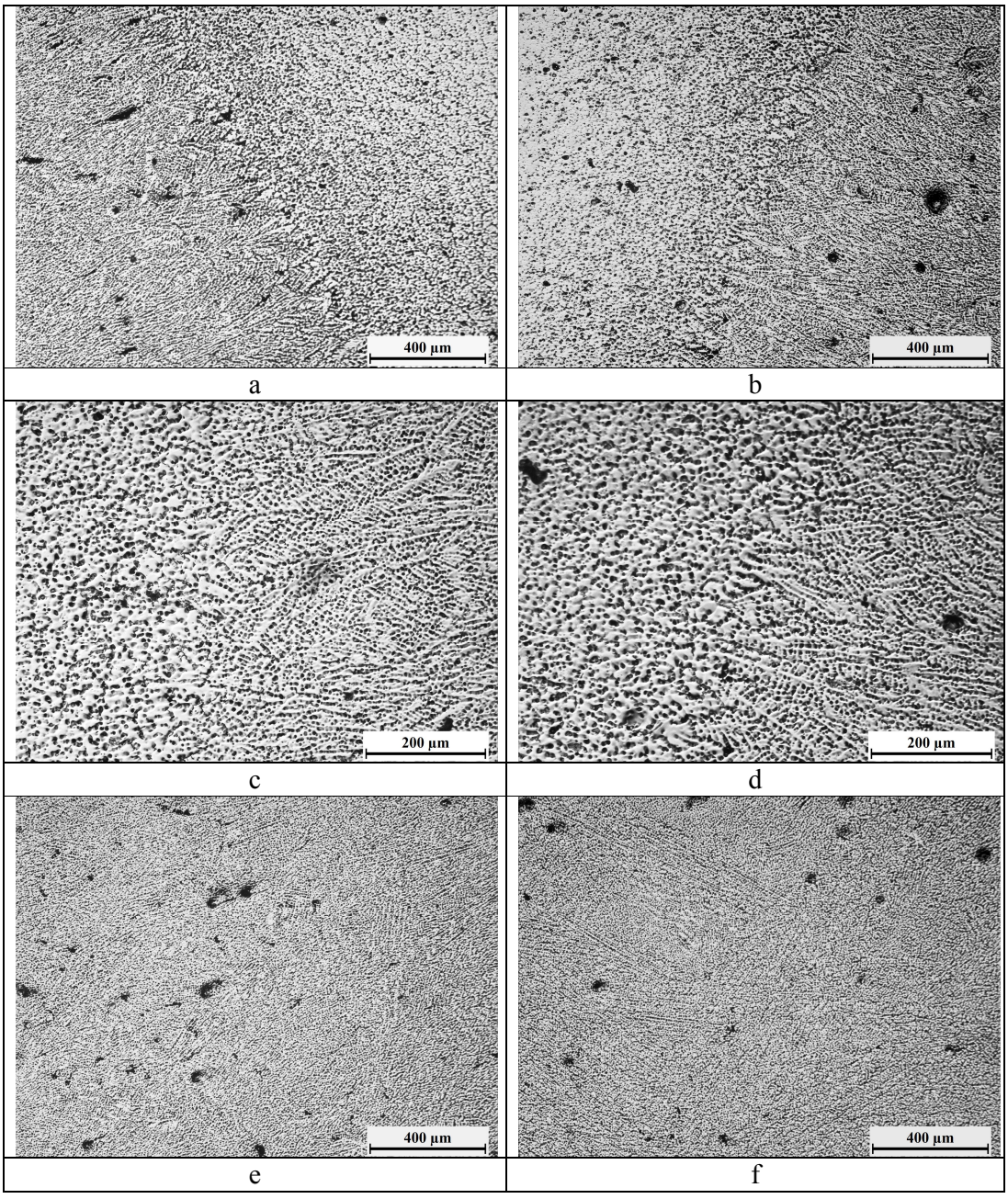
(g) TP3-1 for H321 pulse weled

Figure 7.4.2 X-ray radiogragh image of TIG welded specimens

From photos shown there are some defects in some places of samples, and these defects were avioded during the selection of material chosed for all tests.

Microstructure of Welded Parts

Figure 7.4.3 shows the microstructure of samples TIG welded, the microstructure was mainly composed of coarse dendrite grains and precipitations distributed at the grain boundaries. It indicated that the recrystallization occurred close to the fusion zone during welding process.



a b c d e f

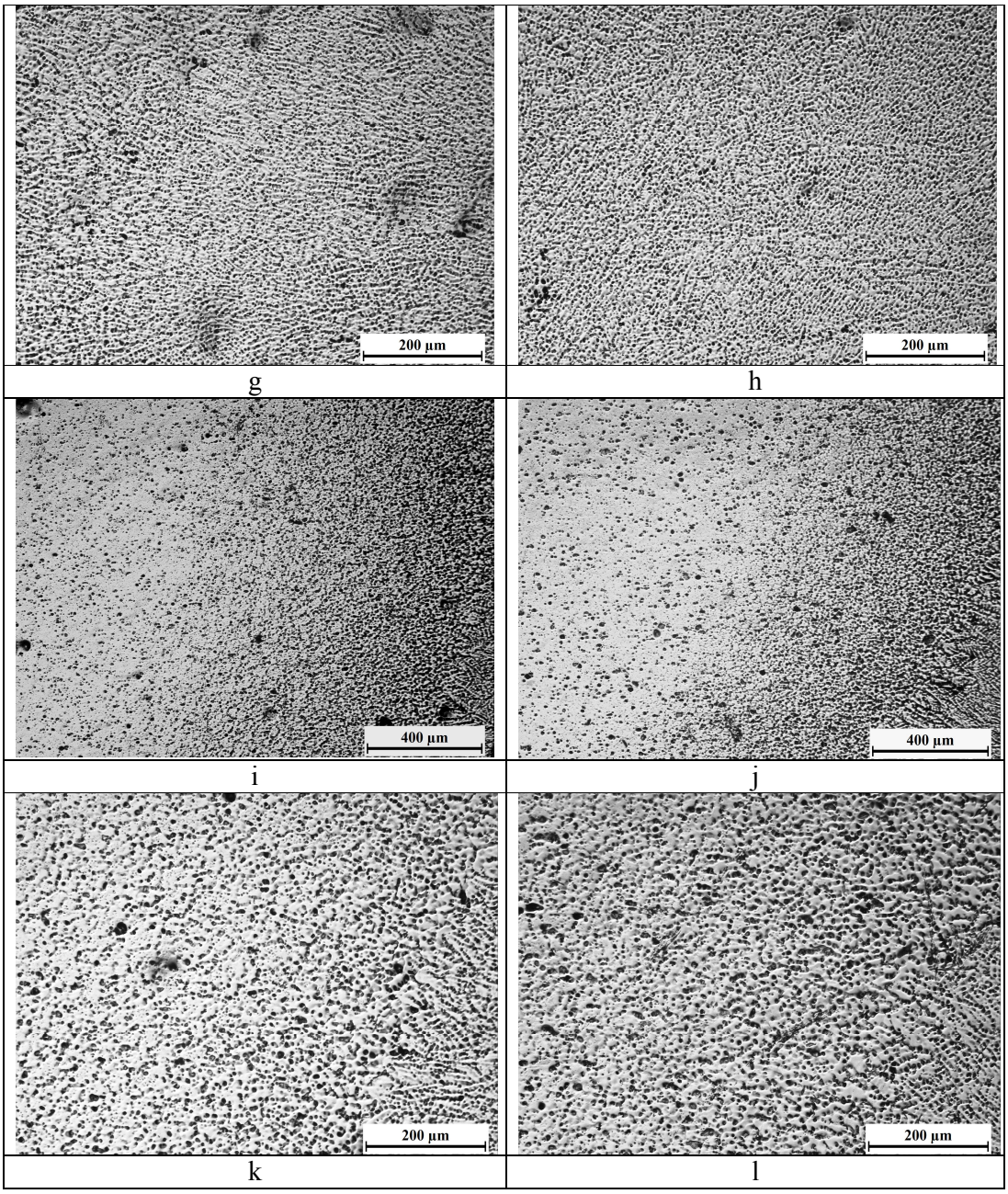
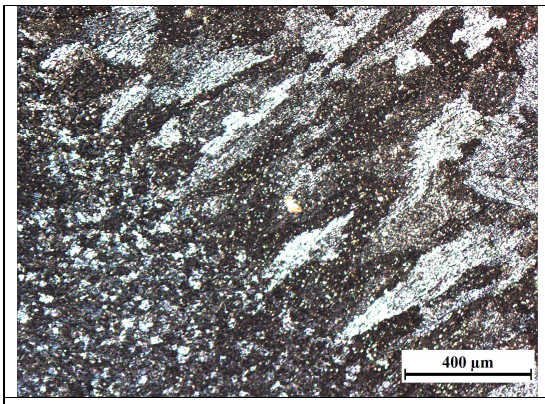
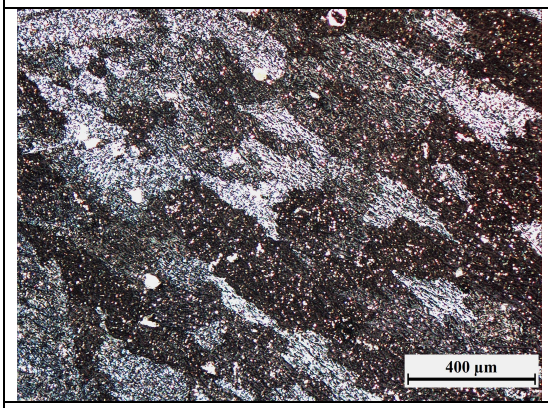


Figure 7.4.3 Micrographs of polished 5083H116 & H321 samples TIG welded (a) H116 BM, 50X, (b) H321 BM, 50X, (c) H116 BM, 100X, (d) H321 BM, 100X, (e) H116 WM, 50X, (f) H321 WM, 50X. (g) H116 WM, 100X, (h) H321 WM, 100X, (i) H116 HAZ, 50X, (j) H321 HAZ, 50X, (k) H116 HAZ, 100X, (l) H321 HAZ, 100X.



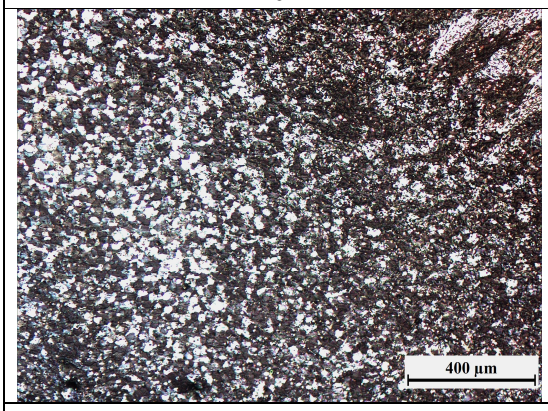
a

b



c

d



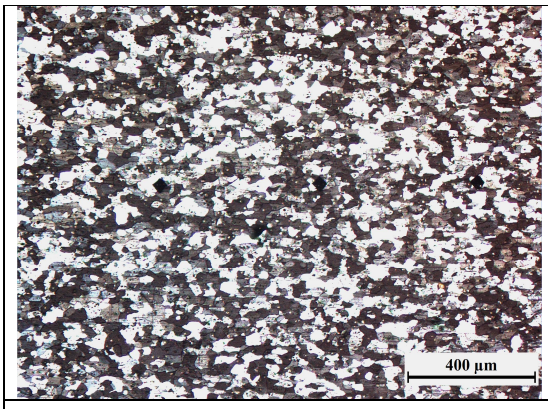
e

f

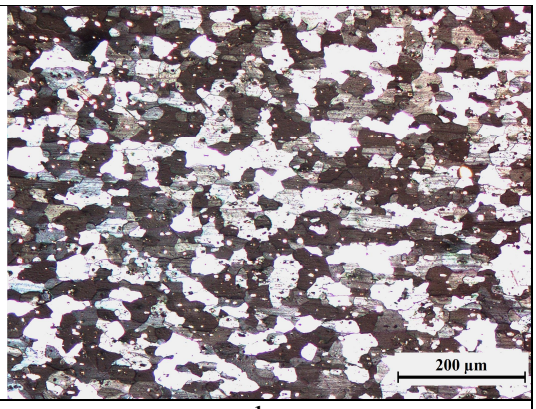
Figure 7.4.4 Micrographs of Etced 5083H321 & H116 samples TIG welded
(a) BM, 50X, (b) BM, 50X, (c) WM, 50X,
(d) WM, 50X, (e) HAZ, 50X. (f) HAZ, 50X.

Metallographic study of the different regions of the weld shows that the Heat Affected Zone (HAZ) has a coarse grain structure than the base metal "figure 4.2.14".

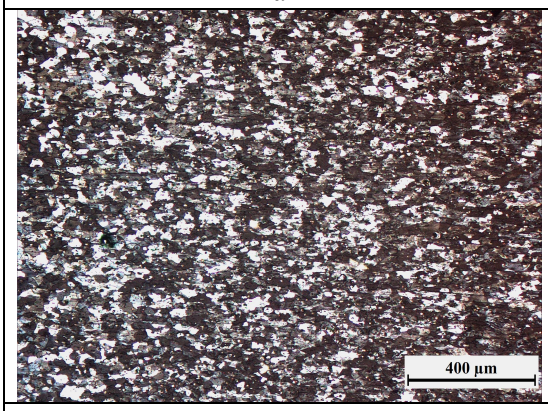
Figure 4.2.14: all the grains have been affected by the heat, but those on the left, nearer to the weld, have become much more equiaxed in comparison to those on the right (x150), position 7 in Figure 4.2.14



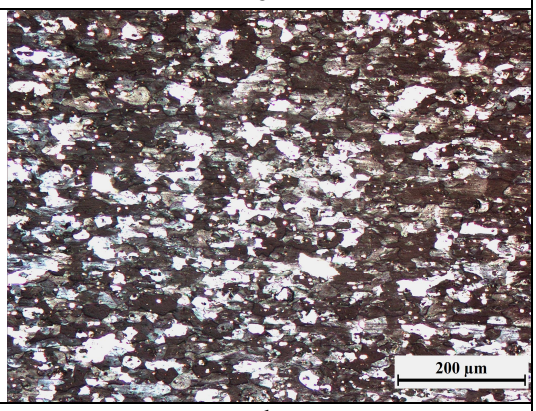
a



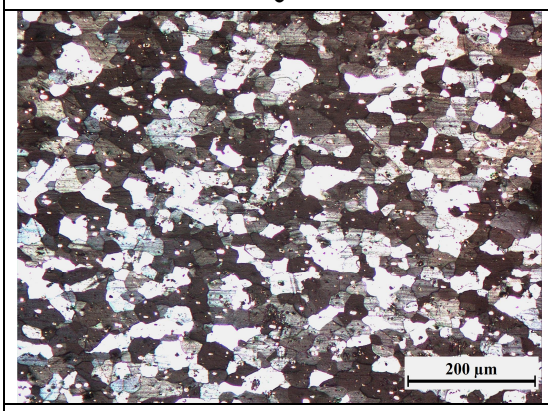
b



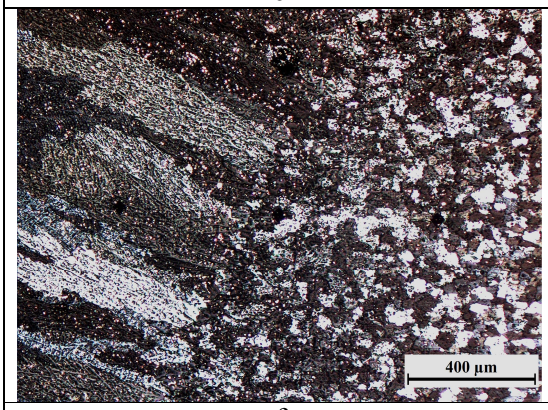
c



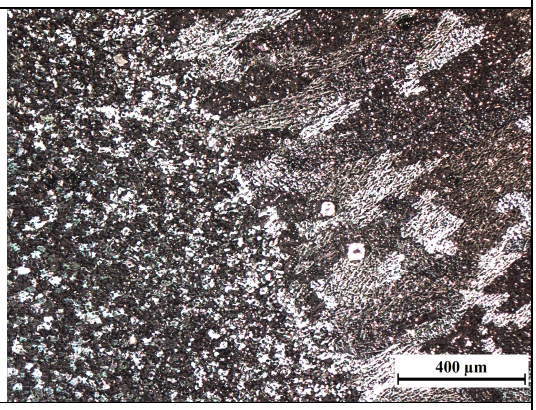
d



e



f



g

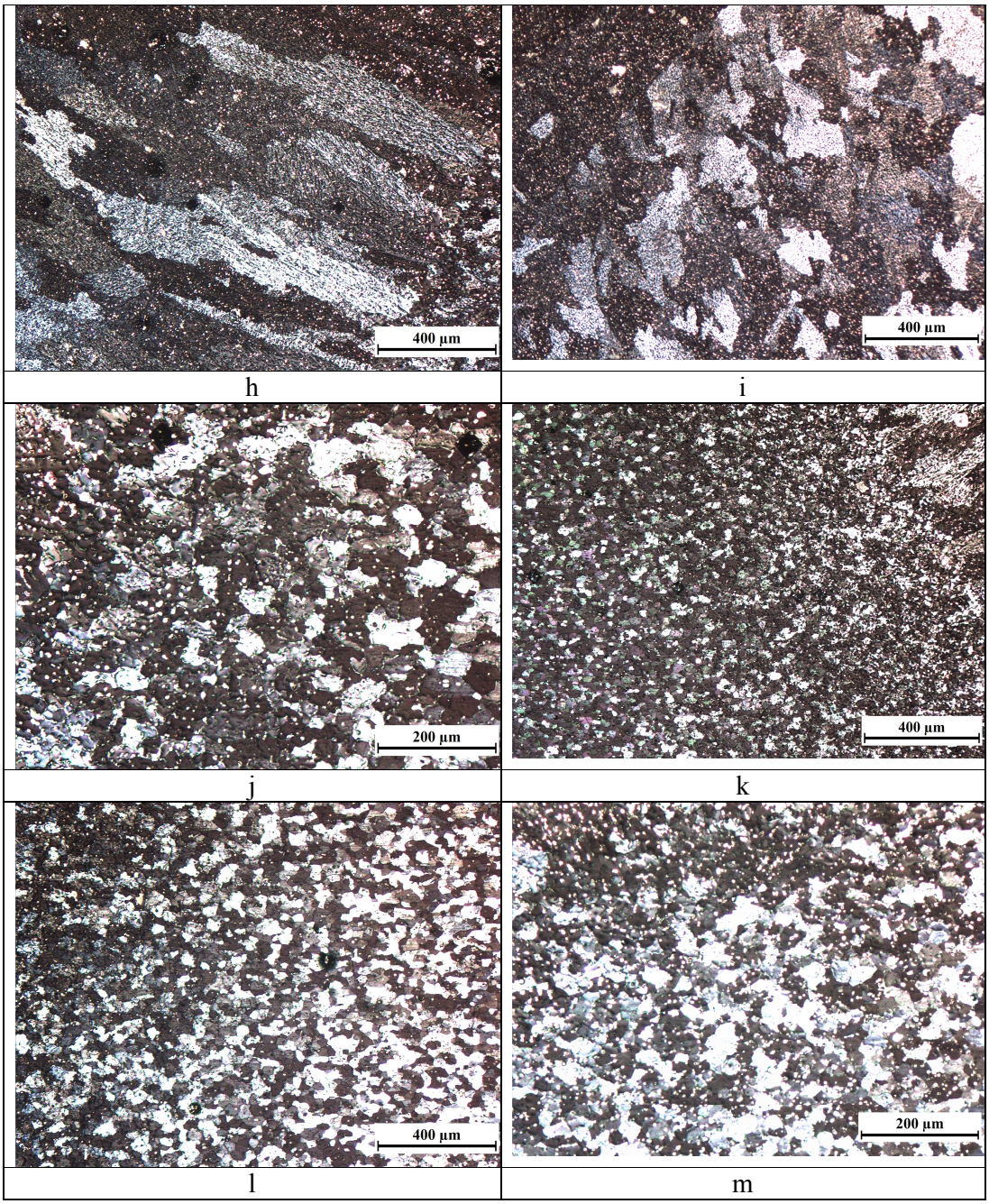
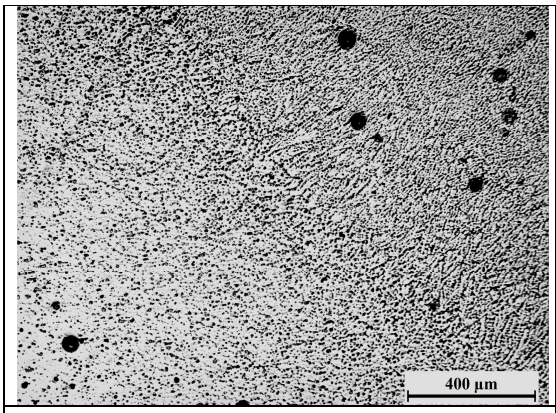


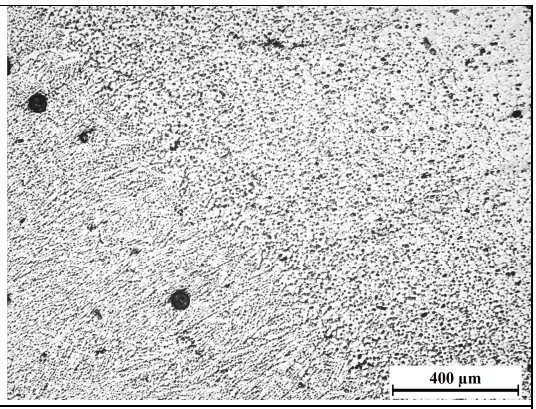
Figure 7.4.5 Micrographs of etched 5083H116 samples TIG Pulse welded

H116

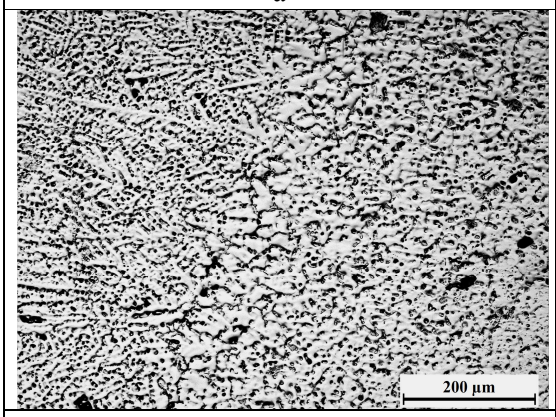
(a) 10mm from center, 50X, (b) 10mm from center, 100X,
(c) 12mm from center, 50X, (d) 12mm from center, 100X,
(e) 6 mm from center, 100X,
(f) H116, BM, 50X, (h) H116, WM, 50X,
(g) H321, BM, 50X, (j) H321, WM, 50X,
(j) H116, HAZ, 50X, (l) H116, HAZ, 100X,
(k) H321, HAZ, 50X, (m) H321, HAZ, 100X,



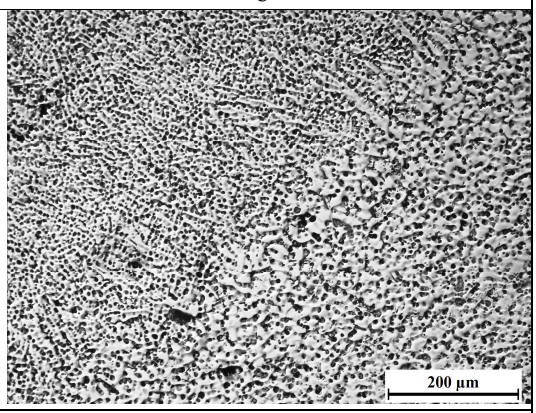
a



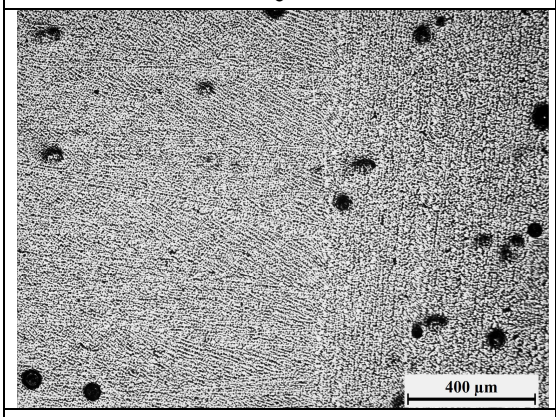
b



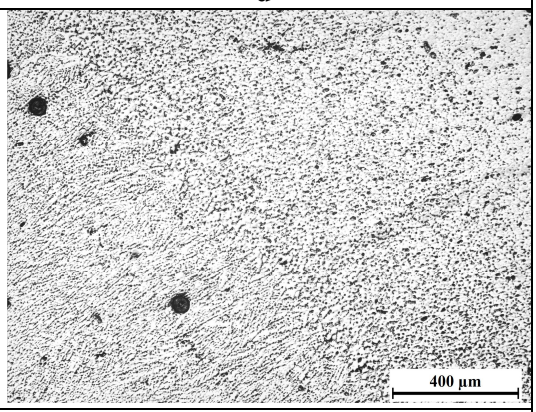
c



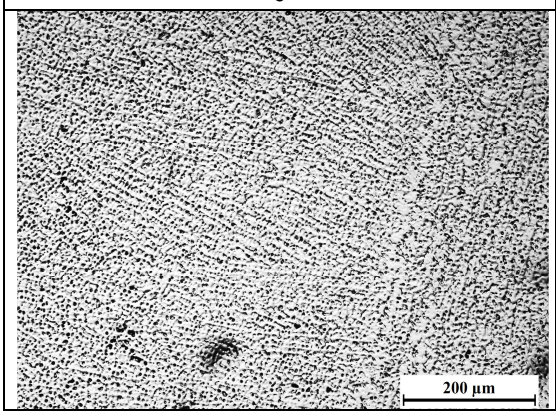
d

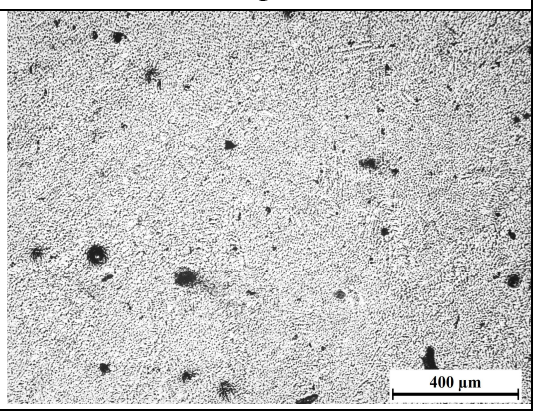


e



f





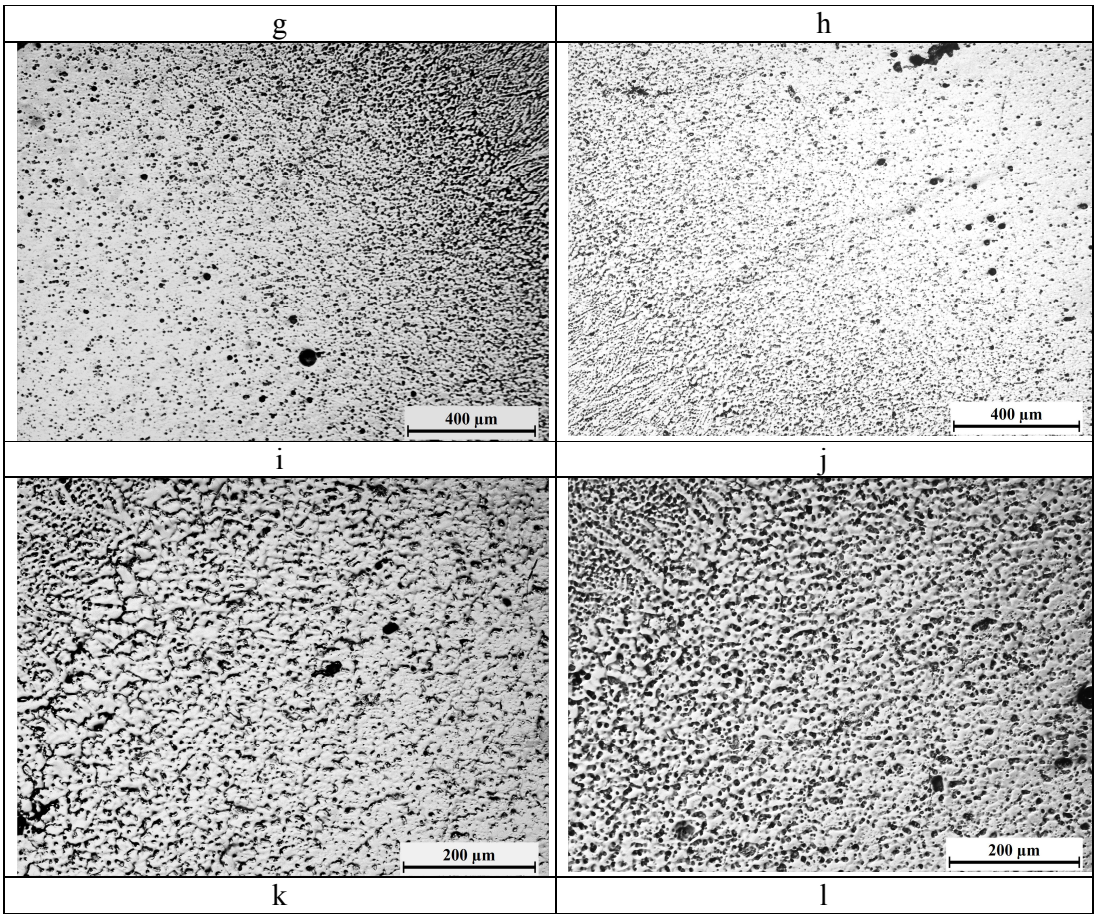


Figure 7.4.6 Micrographs of polished 5083H116 & H321 samples TIG Pulse welded (a) H116 BM, 50X, (b) H321 BM, 50X, (c) H116 BM, 100X, (d) H321 BM, 100X, (e) H116 WM, 50X, (f) H321 WM, 50X. (g) H116 WM, 100X, (h) H321 WM, 100X, (i) H116 HAZ, 50X, (j) H321 HAZ, 50X, (k) H116 HAZ, 100X, (l) H321 HAZ, 100X.

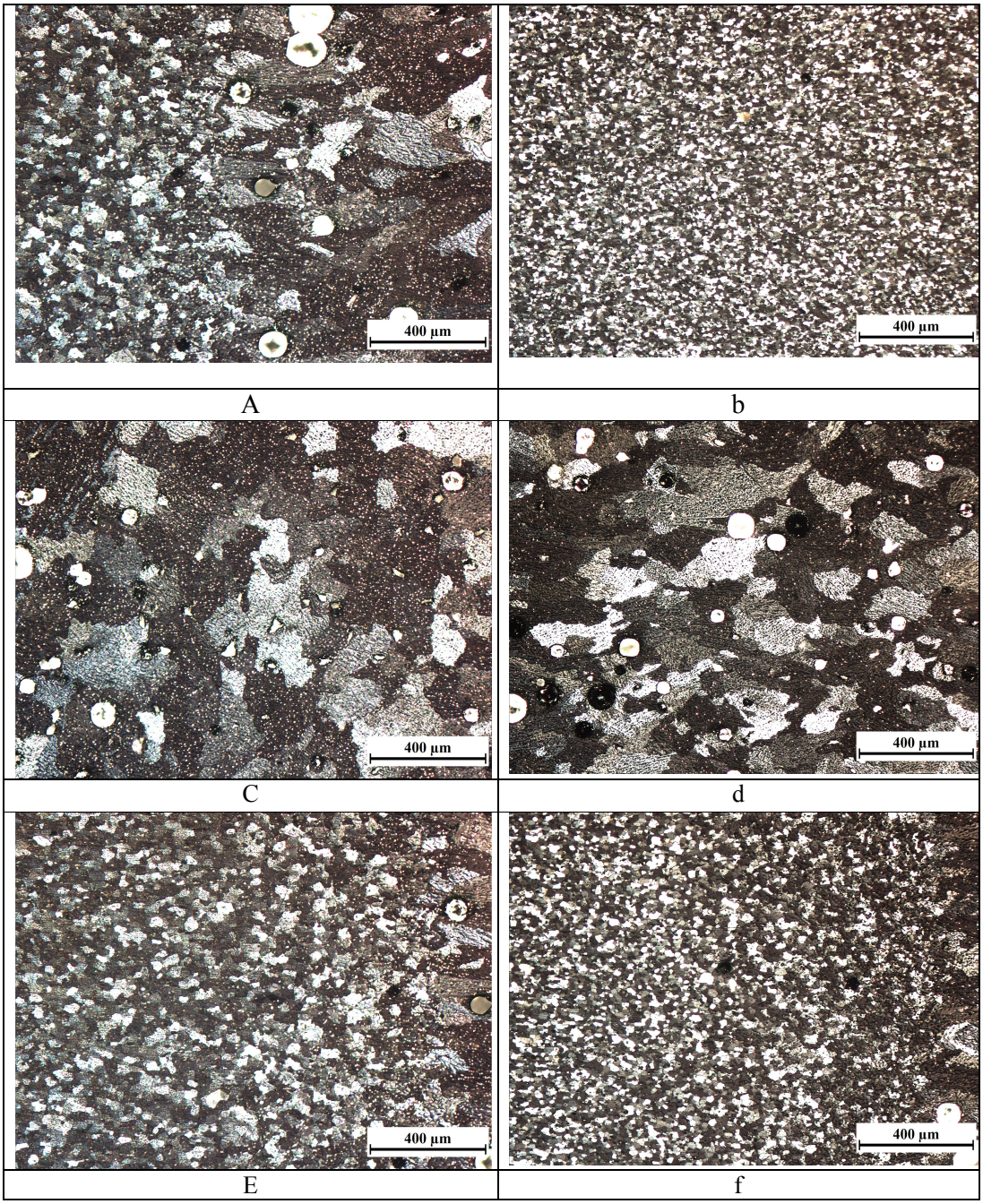


Figure 7.4.7 Micrographs of etched 5083 H116 & H321 samples MIG welded (a) H116, BM, 50X, (b) H321, BM, 50X, (c) H116, WM, 50X, (d) H321, WM, 50X, (e) H116, HAZ, 50X, (e) H321, HAZ, 50X,

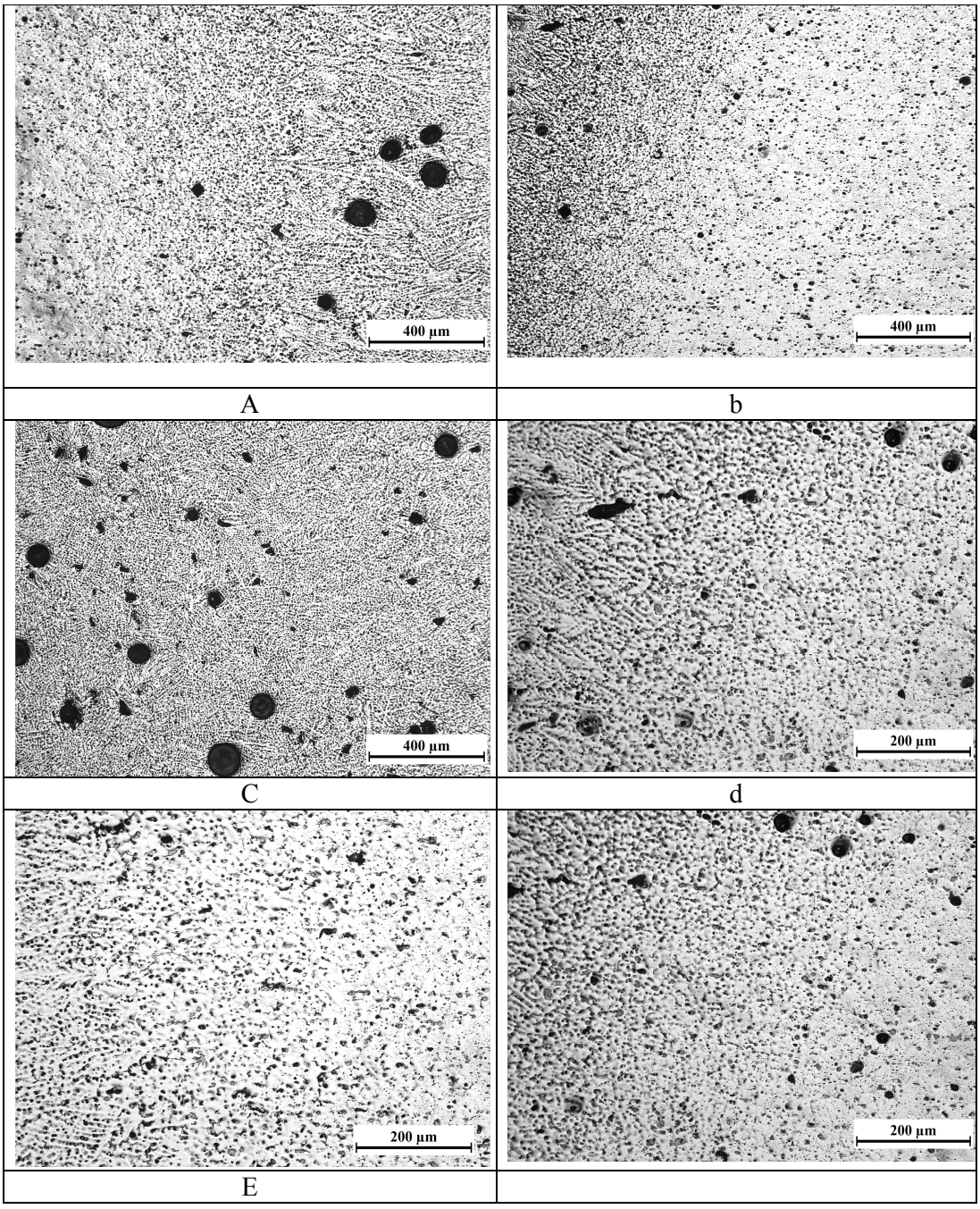


Figure 7.4.8 Micrographs of Polished 5083 H116 & H321 samples MIG welded (a) H116, BM, 50X, (b) H321, BM, 50X, (c) H116, WM, 50X, (d) H321, WM, 100X, (e) H116, HAZ, 100X, (f) H321, HAZ, 100X.

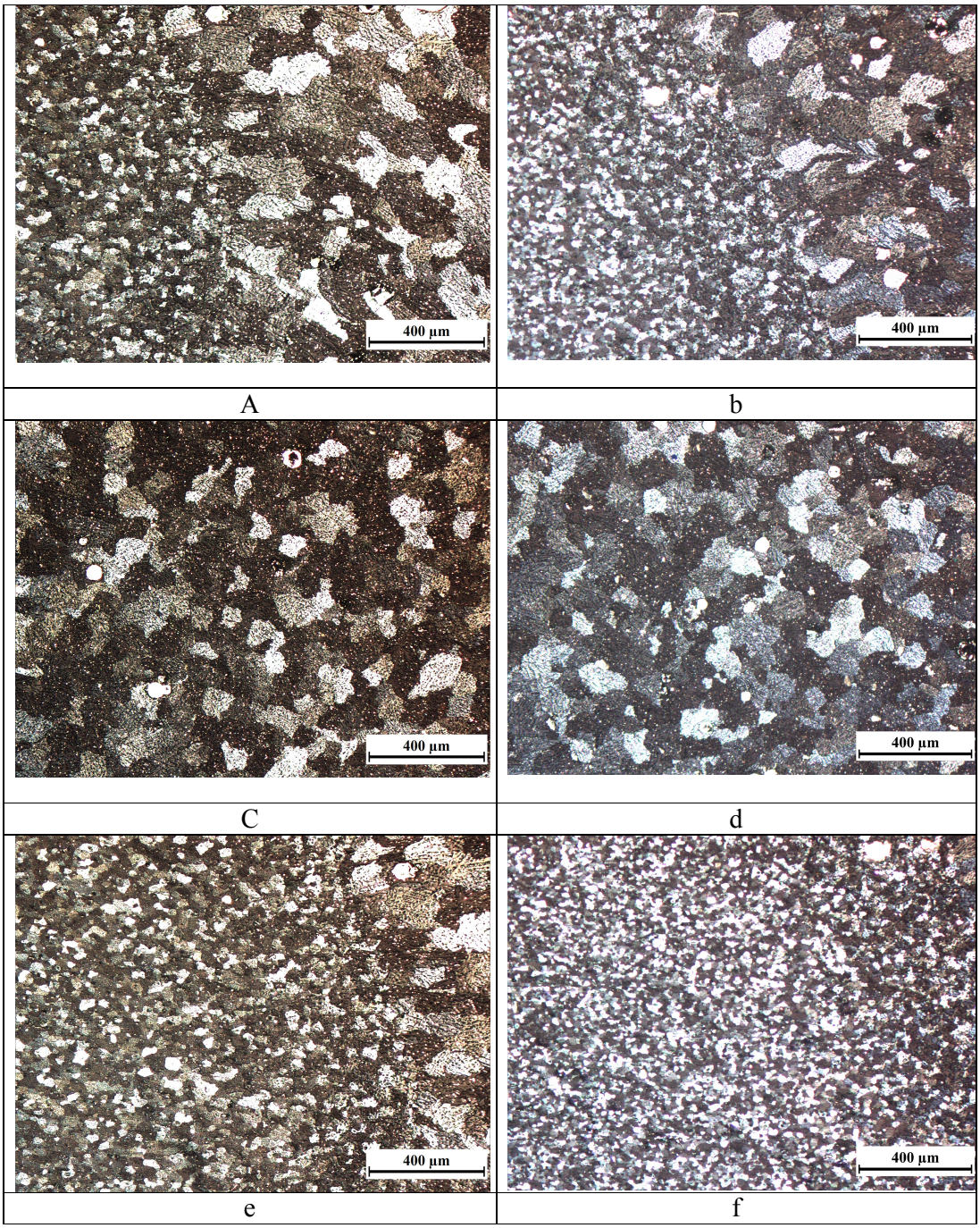
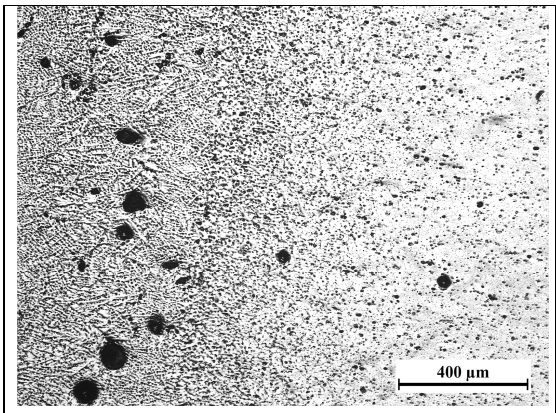
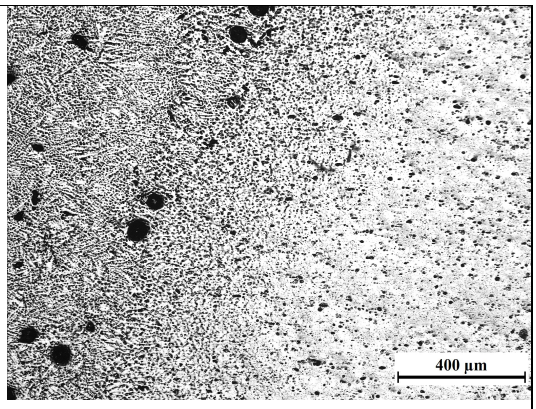


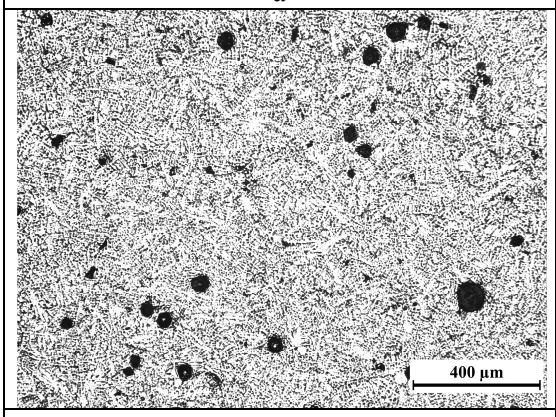
Figure 7.4.9 Micrographs of etched 5083 H116 & H321 samples MIG-Pulse welded (a) H116, WM, 50X, (b) H321, WM, 50X, (c) H116, BM, 50X, (d) H321, BM, 50X, (e) H116, HAZ, 50X. (f) H321, HAZ, 50X.



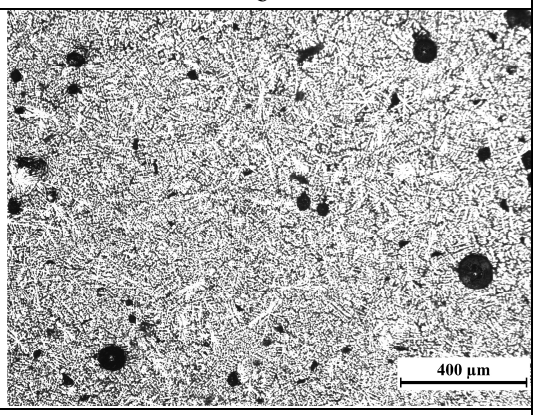
a



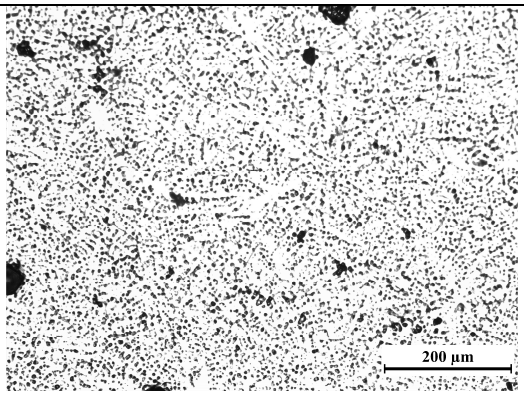
b



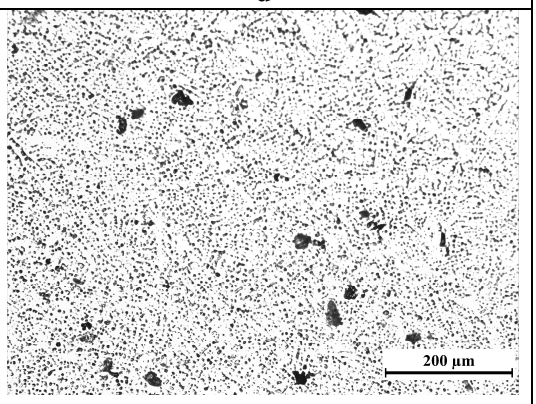
c



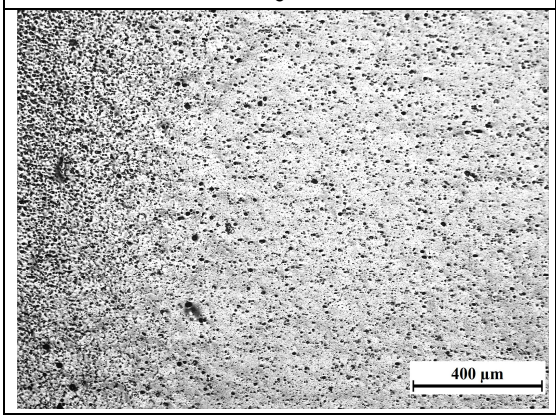
d

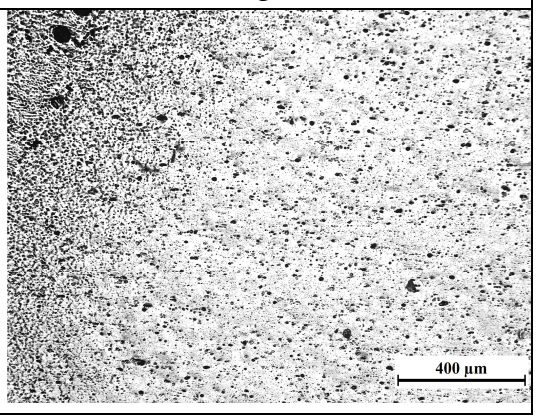


e



f





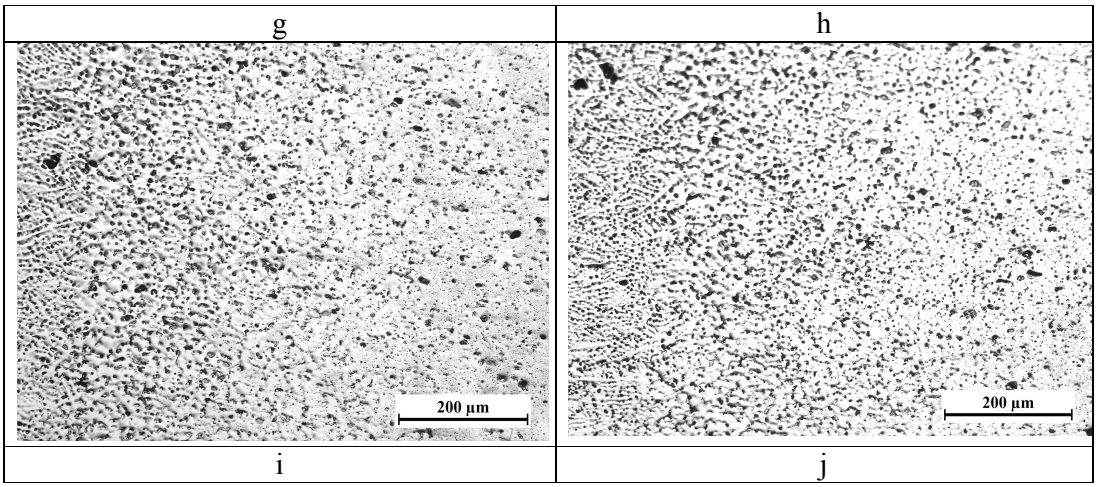


Figure 7.4.10 Micrographs of Polished 5083H116 samples MIG-Pulse welded (a) H116, BM, 50X, (b) H321, BM, 50X, (c) H116, WM, 50X, (d) H321, WM, 50X, (e) H116, WM, 100X, (f) H116, WM, 100X, (g) H116, HAZ, 50X, (h) H116, HAZ, 50X, (i) H116, HAZ, 100X, (j) H116, HAZ, 100X,

7.4 Appendix V Papers published as a result of this thesis

Journal papers:

1- Study of Homogenization Treatments of Cast 5XXX Series Al-Mg-Mn Alloy Modified with Zn, Halap Akram, Radetić Tamara, Popović Miljana and Romhanji Endre, Light Metals 2012, Edited by: Carlos E. Suarez, TMS (The Minerals, Metals & Materials Society), vol. Pp 387-392.

2- Influence of the Thermomechanical Treatment on the Intergranular Corrosion Susceptibility of Zn-Modified Al-5.1 Wt % Mg-0.7 Wt % Mn Alloy Sheet, A. Halap, T. Radetić, M. Popović, E. Romhanji, Metall. Mater. Trans. A 45 (2014) 4572–4579.

Conference Proceedings:

1- Exfoliation and Pitting Corrosion Susceptibility in a Modified 5083 Type Aluminium Alloy, Akram Halap, Miljana Popović, Veselin Vaščić, Tamara Radetić, Endre Romhanji, 1st Metallurgical & Materials Engineering Congress of South-East Europe (MME SEE 2013) 194-201.

Биографија

AKRAM ARIEBI M. HALAP РОЂЕН ЈЕ 25.06.1968.ГОД. У МЕСТУ ZWARA У ЛИБИЈИ. ОСНОВНУ И СРЕДЊУ ШКОЛУ ЗАВРШИО ЈЕ У ЛИБИЈИ. ПОСЛЕДИПЛОМСКЕ СТУДИЈЕ ПОХАЂАО ЈЕ НА ТЕХНОЛОШКО-МЕТАЛУРШКОМ ФАКУЛТЕТУ У БЕОГРАДУ У ПЕРИОДУ 1997-2000.ГОД. У ТОКУ МАГИСТАРСКИХ СТУДИЈА ПОЛОЖИО ЈЕ 10 ИСПИТА СА ПРОСЕЧНОМ ОЦЕНОМ 9.10 И УСПЕШНОМ ЈЕ ОДБРАНИО МАГИСТАРСКУ ТЕЗУ.

IZJAVA

SA PUNOM ODGOVORNOŠĆU IZJAVLJUJEM DA PREDLOŽENU TEMU POD OVIM NAZIVOM NISAM PRIJAVIO NA BILO KOJOJ USTANOVI U ZEMLJI ILI INOSTRANSTVU

AKRAM ARIEBI M. HALAP

Прилог 1.

Изјава о ауторству

Потписани-а AKRAM ARIEBI M. HALAP

број уписа _____

Изјављујем

да је докторска дисертација под насловом

СТРУКТУРА И ЗАВАРЉИВОСТ Al-Mg ЛЕГУРА ВИСОКЕ ЧВРСТОЋЕ ЗА БРОДОГРАДЊУ

- резултат сопственог истраживачког рада,
- да предложена дисертација у целини ни у деловима није била предложена за добијање било које дипломе према студијским програмима других високошколских установа,
- да су резултати коректно наведени и
- да нисам кршио/ла ауторска права и користио интелектуалну својину других лица.

У Београду, 12.11.2014

Потпис докторанда

_____

Прилог 2.

Изјава о истоветности штампане и електронске верзије докторског рада

Име и презиме аутора AKRAM ARIEBI M. HALAP

Број уписа _____

Студијски програм: СТРУКТУРА И ЗАВАРЉИВОСТ Al-Mg ЛЕГУРА ВИСОКЕ ЧВРСТОЋЕ ЗА БРОДОГРАДЊУ

Наслов рада _ Ментор: Prof. Endre Romhanji

Потписани : AKRAM ARIEBI M. HALAP

изјављујем да је штампана верзија мог докторског рада истоветна електронској верзији коју сам предао/ла за објављивање на порталу Дигиталног репозиторијума Универзитета у Београду.

Дозвољавам да се објаве моји лични подаци везани за добијање академског звања доктора наука, као што су име и презиме, година и место рођења и датум одбране рада.

Ови лични подаци могу се објавити на мрежним страницама дигиталне библиотеке, у електронском каталогу и у публикацијама Универзитета у Београду.

Потпис докторанда

У Београду, 12.11.2014

_____

Прилог 3.

Изјава о коришћењу

Овлашћујем Универзитетску библиотеку „Светозар Марковић“да у Дигитални репозиторијум Универзитета у Београду унесе моју докторску дисертацију под насловом:

СТРУКТУРА И ЗАВАРЉИВОСТ Al-Mg ЛЕГУРА ВИСОКЕ ЧВРСТОЋЕ ЗА БРОДОГРАДЊУ

која је моје ауторско дело.

Дисертацију са свим прилозима предао/ла сам у електронском формату погодном за трајно архивирање.

Моју докторску дисертацију похрањену у Дигитални репозиторијум Универзитета у Београду могу да користе сви који поштују одредбе садржане у одабраном типу лиценце Креативне заједнице (Creative Commons) за коју сам се одлучио/ла.

1. Ауторство
2. Ауторство - некомерцијално
3. Ауторство – некомерцијално – без прераде
4. Ауторство – некомерцијално – делити под истим условима
5. Ауторство – без прераде
6. Ауторство – делити под истим условима

(Молимо да заокружите само једну од шест понуђених лиценци, кратак опис лиценци дат је на полеђини листа).

У Београду, 12.11.2014

Потпис докторанда

_____